UNIVERSITY OF SOUTHERN QUEENSLAND

COMPACT APPROXIMATION STENCILS BASED ON INTEGRATED RADIAL BASIS FUNCTIONS FOR FLUID FLOWS

A dissertation submitted by

THUY-TRAM HOANG-TRIEU

B.Eng., (Hon.), Tomsk Polytechnic University, Russia, 2008

Engineer, (Hon.), Tomsk Polytechnic University, Russia, 2009

For the award of the degree of

Doctor of Philosophy

2014

Dedication

To my family

Certification of Dissertation

I certify that the idea, experimental work, results and analyses, software and conclusions reported in this dissertation are entirely my own effort, except where otherwise acknowledged. I also certify that the work is original and has not been previously submitted for any other award.

Thuy-Tram HOANG-TRIEU	Date
ENDORSEMENT	
Prof. Nam MAI–DUY, Principal supervisor	Date
Dr. Canh–Dung TRAN, Co-supervisor	Date
Prof. Thanh TRAN–CONG, Co-supervisor	Date

Acknowledgements

It would not have been possible to write this thesis without the help and support of the kind people around me.

Above all, I would like to express my special appreciation and thanks to my supervisors, Prof. Nam Mai-Duy, Dr. Canh-Dung Tran and Prof. Thanh Tran-Cong, for their insightful guidance and indispensable suggestions. I am deeply grateful for their helps and their patience over the past years.

I would like to acknowledge the University of Southern Queensland (USQ) for the PhD Scholarship and the Computational Engineering and Science Research Centre (CESRC) for the financial supplement.

I would like to thank Dr. Lan Mai-Cao for introducing me to an opportunity to study at CESRC, USQ.

I would also like to thank my friends for their encouragement over the past years.

Finally, I am deeply grateful to my parents, my sister and my husband for their unequivocal support, love and encouragement.

Abstract

This research project is concerned with the development of compact local integrated radial basis function (CLIRBF) stencils and its verification in the simulation of Newtonian and non-Newtonian fluid flows governed by the streamfunction-vorticity formulation. In the CLIRBF stencils, nodal values of the governing equations at selected nodes on a stencil are also incorporated into the IRBF approximations with the help of integration constants to enhance their accuracy. The proposed CLIRBF stencils overcome some of the weaknesses of the local RBF stencils (low order accuracy) and the global RBF approximations (full system matrices).

Four main research tasks are carried out

- Development of CLIRBF stencils for approximating the field variables and their derivatives.
- Incorporation of CLIRBF stencils into two formulations for discretisation of ordinary/partial differential equation (ODEs/PDEs), namely point collocation and subregion collocation.
- Discretisation of fourth-order elliptic ODEs/PDEs, sets of two second-order PDEs representing fourth-order PDEs, and second-order ODEs/PDEs.
- Discretisation of transient problems, where time derivatives are approximated using the Crank-Nicolson/Adams Bashforth scheme.

The proposed CLIRBF stencils are verified in a wide range of problems: (i) ODEs/PDEs with analytic solutions; (ii) heat transfer problems; (iii) Newtonian fluid flows (Burger's equations, lid-driven cavity flows, natural convection in rectangular and nonrectangular domains); and viscoelastic fluid flows (Poiseuille flows and corrugated tube flows of Oldroyd-B fluid).

Numerical verifications show that (i) compact local forms are generally much more accurate than local forms and much more efficient than global forms; and (ii) the CLIRBF-based point/subregion collocation methods yield highly accurate results using relatively coarse grids.

Papers resulting from the Research

Journal papers

1. Hoang-Trieu, T.-T., Mai-Duy, N., and Tran-Cong, T. (2011). Compact local stencils employed with Integrated RBFs for fourth-order differential problems. *SL: Structural Longevity*, 6(2):93–108

2. Hoang-Trieu, T.-T., Mai-Duy, N., and Tran-Cong, T. (2012). Several compact local stencils based on Integrated RBFs for fourth-order ODEs and PDEs. *CMES Computer Modeling in Engineering and Sciences*, 84(2):171–203.

3. Hoang-Trieu, T.-T., Mai-Duy, N.,Tran, C. -D., and Tran-Cong, T. (2013). A finite-volume method based on compact local integrated radial basis function approximations for second-order differential problems. *CMES Computer Modeling in Engineering and Sciences*, 91(6):485–516.

4. Pham-Sy, N., Tran, C. -D., Hoang-Trieu, T.-T., Mai-Duy, N., and Tran-Cong, T. (2013). Compact local IRBF and domain decomposition method for solving PDEs using a distributed termination detection based parallel algorithm. *CMES Computer Modeling in Engineering and Sciences*, 92(1):1–31.

5. Mai-Duy, N., Thai-Quang, N., Hoang-Trieu, T.-T., and Tran-Cong, T. (2013). A compact 9 point stencil based on integrated RBFs for the convection-diffusion equation. *Applied Mathematical Modelling*, 235:302–321.

6. Hoang-Trieu, T.-T., Mai-Duy, N.,Tran, C. -D., and Tran-Cong, T. Compact local IRBF stencils for viscoelastic fluid flows. *(to be submitted).*

7. Hoang-Trieu, T.-T., Mai-Duy, N.,Tran, C. -D., and Tran-Cong, T. Compact local IRBF stencils for transient problems. *(to be submitted).*

Conference papers

1. Hoang-Trieu, T.-T., Mai-Duy, N., Tran, C.-D., and Tran-Cong, T. (2012). Compact local integrated RBF stencil based on finite volume formulation for second-order differential problems. *4th International Conference on Computational Methods (ICCM 2012)*, 25-28/Nov/2012, Gold Coast, Australia.

2. Pham-Sy, N., Tran, C. -D., Hoang-Trieu, T.-T., Mai-Duy, N., and Tran-Cong, T. (2012) Development of parallel algorithm for boundary value problems using compact local integrated RBFN and domain decomposition. *4th International Conference on Computational Methods (ICCM 2012)*, 25-28/Nov/2012, Gold Coast, Australia.

Table of Contents

Acronyms and Abbreviations

BEM	Boundary Element Method
CDS	Central Difference Scheme
CFD	Computational Fluid Dynamics
CLIRBF	Compact Local Integrated Radial Basis Function
CLIRBF-FVM	Compact Local Integrated Radial Basis Function-FiniteVolume Method
CLIRBF-PCM	Compact Local Integrated Radial Basis Function-Point Collocation Method
CLS	Compact Local Stencil
CM	Convergence measure
DQM	Differential Quadrature Method
DRBF	Differential Radial Basis Function
FD	Finite Difference
FDM	Finite Difference Method
FEM	Finite Element Method
FVM	Finite Volume Method
GE	Governing Equation
IRBF	Integrated Radial Basis Function
MQ	Multiquadric
ODE	Ordinary Differential Equation
PDE	Partial Differential Equation
RBF	Radial Basis Function
RBFN	Radial Basis Function Network
SCHOS	Single Cell High Order Scheme
SD	Spectral Difference
SM	Spectral Method

UCM	Upper-Convected Maxwell
UDS	Upwind Difference Scheme
WENO	Weighted Essentially Non-Oscillatory

List of Tables

List of Figures

Chapter 1

Introduction

This chapter aims to give an introduction to the present thesis. It starts with the motivation of the proposed research. Then, brief overviews of the basic equations governing the motion of Newtonian and non-Newtonian fluids, and numerical schemes used for the simulation of fluid flows are given. Next, we review integrated radial basis functions (IRBF), which are used to construct the proposed compact stencils, and present the main objectives of the research. The chapter will end with an outline of the thesis.

1.1 Motivation

Computational Fluid Dynamics (CFD) deals with the computer simulation of fluid flows, where the motion of a fluid is described mathematically, e.g., in the form of ODEs and PDEs. A physical/engineering process can be investigated theoretically, experimentally and by computer simulations. Doing experiments and measurements is a traditional approach, and it has been widely used with varying degrees of success. However, this approach suffers from time consuming, high cost, large measurement error, etc. and has limitations - for examples, the size of problems should be small and the obtained information is rather limited. These drawbacks are eliminated in computer simulations (e.g. the problem can now be of small or large size, etc.). Since the late 1960s, the development and application of CFD to all aspects of fluid dynamics have been growing massively (Moin and Kim, 1997). The quality of simulation results depends on the accuracy of the numerical method used. There are numerous numerical methods developed, which can be classified into low order and high order methods, or finite-element-based and meshless/grid-based methods. Each group has its own strengths and weaknesses. High-order methods have the ability to produce accurate results using relatively coarse discretisations, while low-order methods result in sparse system matrices that can be solved efficiently. Meshless/grid-based methods are much more efficient in modelling complex geometries than finite-element-based methods.

Radial basis function networks (RBFNs) have emerged as a powerful tool in numerical analysis. It has been proved that RBFNs have an universal approximation

capability (Park and Sandberg, 1991). Originally, RBFNs were used for function approximation and classification. Then, RBFNs were extended to a variety of applications, e.g. the solution of ordinary differential equations/ partial differential equations (ODEs/PDEs) (Kansa and Hon, 2000). They have been used with success in solving heat transfer problems (Zerroukat et al., 1998), fluid flow problems (Sadat and Couturier, 2000; Kosec and Sarler, 2011), time-dependent problems (Kansa et al., 2004), fluid-structure interaction analyses (Ngo-Cong et al., 2012b), Darcy flows (Kosec and Sarler, 2008), hyperbolic problems (Islam et al., 2013), etc. - this list is not meant to be exhaustive. RBFNs are a flexible simulation method as they can be used with Cartesian grids or meshless discretisations, and employed in local or global forms derived from the differentiation or integration process. We will develop approximation stencils based on RBFNs for fluid flows, where the benefits of low cost (by means of Cartesian grids), sparse system matrices (using small stencils) and high order accuracy (integrated RBFs and compact form) of the existing numerical schemes are exploited.

1.2 Governing equations

1.2.1 Newtonian and non-Newtonian fluids

Fluids are substances whose deformation easily occurs under external shear forces. Indeed, applying a very small force is able to result in the fluid motion. Fluids can be recognised everywhere in human life, e.g. breathing, blood, wind, rain, etc., and also in many industrial disciplines, such as aerospace, automotive, food processing and chemical processing. An understanding of the behaviour of fluids allows us to control effectively their effects in flow processes.

Fluids can be divided into Newtonian and non-Newtonian. If the behaviour of a fluid is linear, one has a Newtonian fluid; otherwise, a non-Newtonian fluid. Viscoelastic is the term used to describe the coexistence of elastic and viscous properties in a fluid. Viscoelastic fluid is an example of non-Newtonian fluids. Because of the mixture, viscoelastic fluids exhibit many interesting phenomena, which are totally different from those associated with Newtonian fluids.

There are different fluid flow regimes, ranging from creeping, through laminar to turbulent. The laminar regime is characterised by the smooth motion of a fluid, while the turbulent regime tends to produce chaotic eddies, vortices and other flow instabilities. At speeds that are low enough, the creeping flow is observed. As the speed is increased, the flow is then said to be laminar. Further increases in speed may cause the instability in the fluid, which corresponds to a turbulent regime. A dimensionless quantity, called the Reynolds number Re, can be used to characterise these regimes. Creeping flow is the flow at $Re = 0$, laminar flow occurs at low Reynolds numbers, and turbulent flow occurs at high Reynolds numbers. When dealing with the flow at high Reynolds numbers, the non-linear term in the governing equation will be dominant, which makes the numerical solution difficult to converge, and special care is needed.

It has been recognised that the simulation of non-Newtonian fluid flows is much

more challenging than that of Newtonian fluid flows (Keunings, 1990; Walters and Webster, 2003). Constitutive equations relating stress to rate of strain are nonlinear for non-Newtonian fluids, and consequently, their solutions are obtained normally in a more complex manner than those associated with the Newtonian case (Walters and Webster, 2003; Barnes et al., 1989; Macosko, 1994; Grillet et al., 1999). For viscoelatic fluids, a dimensionless quantity, called the Weissenberg number We, is used to measure the relative importance of the elastic and viscous effects.

1.2.2 Conservation laws

The motion of any fluid is described by the equations of conservation of mass, momentum and energy. Consider an incompressible fluid, whose density is constant. The conservation of mass can be described as

$$\nabla \cdot \mathbf{v} = 0, \qquad \mathbf{x} \in \Omega, \tag{1.1}$$

where $\mathbf{v}$ is the velocity vector, $\mathbf{x}$ the position vector, and Ω the domain of interest.

The conservation of momentum (equation of motion) is given by

$$\rho \frac{D\mathbf{v}}{Dt} = (\nabla \cdot \boldsymbol{\sigma}) + \rho \mathbf{g}, \qquad \mathbf{x} \in \Omega, \tag{1.2}$$

where t is the time, ρ the density, $\boldsymbol{\sigma}$ the total stress tensor, $\mathbf{g}$ the force per unit mass due to gravity, and D/Dt the material or substantial derivative (Tanner, 2000; Reddy and Gartling, 1994),

$$\frac{D}{Dt} = \frac{\partial}{\partial t} + \mathbf{v} \cdot \nabla \tag{1.3}$$

The total stress tensor $\boldsymbol{\sigma}$ for a fluid at rest is $\boldsymbol{\sigma} = -p\mathbf{I}$, in which p is called the hydrostatic pressure, and $\mathbf{I}$ is the identity tensor. When dealing with fluids in motion, the total stress tensor is decomposed into two parts: $\boldsymbol{\sigma} = -p\mathbf{I} + \boldsymbol{\tau}$, where $\boldsymbol{\tau}$ is the extra stress tensor. Equation (1.2) can thus be rewritten as

$$\rho \frac{D\mathbf{v}}{Dt} = -\nabla p + (\nabla \cdot \boldsymbol{\tau}) + \rho \mathbf{g}, \qquad \mathbf{x} \in \Omega. \tag{1.4}$$

For simplicity, without loss of generality, one may combine the pressure and gravity terms into the so-called "modified pressure": $\nabla P = \nabla p - \rho \mathbf{g}$.

1.2.3 Constitutive equations

The constitutive equation describes the relation between force and deformation in fluid. Constitutive equations are usually written in terms of extra stress tensor $\boldsymbol{\tau}$ and strain rate tensor. The simplest constitutive equation is in the case of Newtonian fluids

$$\boldsymbol{\tau} = 2\eta_0 \mathbf{D}, \tag{1.5}$$

where η_0 is the constant viscosity, and $2\mathbf{D}$ is the rate of deformation tensor, defined as $2\mathbf{D} = \left(\nabla\mathbf{v}^T + \nabla\mathbf{v}\right)$.

Many differential constitutive models have been developed. Below is a brief review of some constitutive models.

Upper-Convected Maxwell (UCM) model

$$\boldsymbol{\tau} + \lambda_1 \overset{\nabla}{\boldsymbol{\tau}} = 2\eta_0\mathbf{D}, \tag{1.6}$$

where λ_1 is the characteristic relaxation time of the fluid and the upper-convected derivative $\overset{\nabla}{[]}$ is defined as

$$\overset{\nabla}{[]} = \frac{\partial []}{\partial t} + \mathbf{v}\cdot\nabla[] - (\nabla\mathbf{v})^T\cdot[] - []\cdot\nabla\mathbf{v}. \tag{1.7}$$

Oldroyd-B model

$$\boldsymbol{\tau} + \lambda_1 \overset{\nabla}{\boldsymbol{\tau}} = 2\eta_0\left(\mathbf{D} + \lambda_2 \overset{\nabla}{\mathbf{D}}\right), \tag{1.8}$$

where λ_2 is the characteristic retardation time of the fluid. Let α be the ratio of the retardation time to the relaxation time ($\alpha = \lambda_2/\lambda_1$). The Oldroyd-B model will reduce to UCM when $\alpha = 0$.

The extra stress tensor $\boldsymbol{\tau}$ can also be decomposed into two components, namely solvent and polymeric contributions

$$\boldsymbol{\tau} = 2\eta_s\mathbf{D} + \boldsymbol{\tau}_v, \tag{1.9}$$

where η_s is the solvent viscosity and $\boldsymbol{\tau}_v$ is the elastic stress

$$\boldsymbol{\tau}_v + \lambda_1 \overset{\nabla}{\boldsymbol{\tau}}_v = 2\eta_p\mathbf{D}, \tag{1.10}$$

in which η_p is the polymeric viscosity. Note that $\eta_0 = \eta_s + \eta_p$, $\eta_s = \alpha\eta_0$, and $\eta_p = (1-\alpha)\eta_0$. If the value of η_s in equation (1.9) is set to zero (i.e. $\boldsymbol{\tau} = \boldsymbol{\tau}_v$), the Oldroyd-B model reduces to a UCM model. Further details can be found in (Covas et al., 1995) and (Phan-Thien and Tanner, 1977).

Giesekus-Leonov model

$$\boldsymbol{\tau}_v + \lambda_1 \overset{\nabla}{\boldsymbol{\tau}}_v - \frac{\lambda_1}{2\eta_p}\{\boldsymbol{\tau}_v\cdot\boldsymbol{\tau}_v\} = 2\eta_p\mathbf{D}. \tag{1.11}$$

Phan-Thien Tanner (PTT) model 1

$$\exp\left(\frac{\lambda_1\varepsilon}{\eta_p}\mathrm{tr}(\boldsymbol{\tau}_v)\right)\boldsymbol{\tau}_v + \lambda_1 \overset{\nabla}{\boldsymbol{\tau}}_v + \xi\lambda_1\{\mathbf{D}\cdot\boldsymbol{\tau}_v + \boldsymbol{\tau}_v\cdot\mathbf{D}\} = 2\eta_p\mathbf{D}, \tag{1.12}$$

where ε and ξ are the material parameters, and 'tr' denotes the trace operation.

Phan-Thien Tanner (PTT) model 2

$$\left(1 + \frac{\lambda_1\varepsilon}{\eta_p}\mathrm{tr}(\boldsymbol{\tau}_v)\right)\boldsymbol{\tau}_v + \lambda_1 \overset{\nabla}{\boldsymbol{\tau}}_v + \xi\lambda_1\{\mathbf{D}\cdot\boldsymbol{\tau}_v + \boldsymbol{\tau}_v\cdot\mathbf{D}\} = 2\eta_p\mathbf{D}. \tag{1.13}$$

In this project, we restrict our attention to Newtonian fluids and Oldroyd-B fluids in two dimensional flows. There are three popular forms of the governing equations, based either on velocity-pressure, or streamfunction-vorticity $(\psi - \omega)$ or streamfunction (ψ). Advantages of the $(\psi - \omega)$ formulation over the $(\mathbf{v} - p)$ one are that (i) the number of equations to be solved are reduced due to the elimination of the pressure variable, and thus reducing the computational effort; and (ii) the continuity equation is automatically satisfied. However, one needs to derive a boundary condition for ω from the given boundary conditions, and also to compute the velocities and pressure after solving the system of discrete equations. Advantages of the (ψ) formulation over the $(\psi-\omega)$ one are that (i) the number of equations are further reduced; and (ii) there is no intermediate variable. However, one needs to deal with the approximation of high-order derivatives and the imposition of double boundary conditions. Further details can be found in (Quartapelle, 1993). Some detailed forms of the governing equations are given below, with our focus on the streamfunction-vorticity formulation which is mainly used in the following chapters.

Newtonian fluids:

In Cartesian coordinates, the governing equations for Newtonian fluids take the form

$$\frac{\partial v_x}{\partial x} + \frac{\partial v_y}{\partial y} = 0, \tag{1.14}$$

$$\rho\left(\frac{\partial v_x}{\partial t} + v_x\frac{\partial v_x}{\partial x} + v_y\frac{\partial v_x}{\partial y}\right) = -\frac{\partial P}{\partial x} + \eta_0\left(\frac{\partial^2 v_x}{\partial x^2} + \frac{\partial^2 v_x}{\partial y^2}\right), \tag{1.15}$$

$$\rho\left(\frac{\partial v_y}{\partial t} + v_x\frac{\partial v_y}{\partial x} + v_y\frac{\partial v_y}{\partial y}\right) = -\frac{\partial P}{\partial y} + \eta_0\left(\frac{\partial^2 v_y}{\partial x^2} + \frac{\partial^2 v_y}{\partial y^2}\right). \tag{1.16}$$

By introducing

$$x^* = \frac{x}{L}, \quad y^* = \frac{y}{L}, \quad t^* = \frac{t}{L/V},$$
$$p^* = \frac{P}{\rho V^2}, \quad v_x^* = \frac{v_x}{V}, \quad v_y^* = \frac{v_y}{V},$$

where L and V are the flow characteristic length and velocity, respectively, the governing equations in dimensionless form are obtained

$$\frac{\partial v_x^*}{\partial x^*} + \frac{\partial v_y^*}{\partial y^*} = 0, \tag{1.17}$$

$$\frac{\partial v_x^*}{\partial t^*} + v_x^*\frac{\partial v_x^*}{\partial x^*} + v_y^*\frac{\partial v_x^*}{\partial y^*} = -\frac{\partial p^*}{\partial x^*} + \frac{1}{Re}\left(\frac{\partial^2 v_x^*}{\partial x^{*2}} + \frac{\partial^2 v_x^*}{\partial y^{*2}}\right), \tag{1.18}$$

$$\frac{\partial v_y^*}{\partial t^*} + v_x^*\frac{\partial v_y^*}{\partial x^*} + v_y^*\frac{\partial v_y^*}{\partial y^*} = -\frac{\partial p^*}{\partial y^*} + \frac{1}{Re}\left(\frac{\partial^2 v_y^*}{\partial x^{*2}} + \frac{\partial^2 v_y^*}{\partial y^{*2}}\right), \tag{1.19}$$

in which $Re = \rho V L/\eta_0$ is the Reynolds number.

They can be reformulated to produce the following streamfunction-vorticity for-

mulation

$$\frac{\partial^2\psi}{\partial x^2}+\frac{\partial^2\psi}{\partial y^2}=-\omega, \tag{1.20}$$

$$\frac{\partial\omega}{\partial t}+\left(\frac{\partial\psi}{\partial y}\frac{\partial\omega}{\partial x}-\frac{\partial\psi}{\partial x}\frac{\partial\omega}{\partial y}\right)=\frac{1}{Re}\left(\frac{\partial^2\omega}{\partial x^2}+\frac{\partial^2\omega}{\partial y^2}\right), \tag{1.21}$$

where the streamfunction $\psi(x,y,t)$ is defined with the property: $v_x=\dfrac{\partial\psi}{\partial y}$ and $v_y=-\dfrac{\partial\psi}{\partial x}$, and ω is the vorticity, $\omega=\dfrac{\partial v_y}{\partial x}-\dfrac{\partial v_x}{\partial y}$.

In cylindrical coordinates (axi-symmetric), the governing equations for Newtonian fluids are of the form

$$\frac{1}{r}\frac{\partial}{\partial r}\left(rv_r\right)+\frac{\partial v_z}{\partial z}=0, \tag{1.22}$$

$$\rho\left(\frac{\partial v_r}{\partial t}+v_r\frac{\partial v_r}{\partial r}+v_z\frac{\partial v_r}{\partial z}\right)=-\frac{\partial p}{\partial r}+\eta_0\left[\frac{\partial}{\partial r}\left(\frac{1}{r}\frac{\partial}{\partial r}\left(rv_r\right)\right)+\frac{\partial^2 v_r}{\partial z^2}\right], \tag{1.23}$$

$$\rho\left(\frac{\partial v_z}{\partial t}+v_r\frac{\partial v_z}{\partial r}+v_z\frac{\partial v_z}{\partial z}\right)=-\frac{\partial p}{\partial z}+\eta_0\left[\frac{1}{r}\frac{\partial}{\partial r}\left(r\frac{\partial v_z}{\partial r}\right)+\frac{\partial^2 v_z}{\partial z^2}\right]. \tag{1.24}$$

Their dimensionless form is

$$\frac{1}{r^*}\frac{\partial}{\partial r^*}\left(r^*v_r^*\right)+\frac{\partial v_z^*}{\partial z^*}=0, \tag{1.25}$$

$$\frac{\pi Re}{2}\left(\frac{\partial v_r^*}{\partial t^*}+v_r^*\frac{\partial v_r^*}{\partial r^*}+v_z^*\frac{\partial v_r^*}{\partial z^*}\right)=-\frac{\partial p^*}{\partial r^*}+\left[\frac{\partial}{\partial r^*}\left(\frac{1}{r^*}\frac{\partial}{\partial r^*}\left(r^*v_r^*\right)\right)+\frac{\partial^2 v_r^*}{\partial z^{*2}}\right], \tag{1.26}$$

$$\frac{\pi Re}{2}\left(\frac{\partial v_r^*}{\partial t^*}+v_r^*\frac{\partial v_z^*}{\partial r^*}+v_z^*\frac{\partial v_z^*}{\partial z^*}\right)=-\frac{\partial p^*}{\partial z^*}+\left[\frac{1}{r^*}\frac{\partial}{\partial r^*}\left(r^*\frac{\partial v_z^*}{\partial r^*}\right)+\frac{\partial^2 v_z^*}{\partial z^{*2}}\right]. \tag{1.27}$$

where

$$r^*=\frac{r}{R},\quad z^*=\frac{z}{R},\quad t^*=\frac{t}{Q/R^3},$$
$$p^*=\frac{P}{\eta_0 Q/R^3},\quad v_r^*=\frac{v_r}{Q/R^2},\quad v_z^*=\frac{v_z}{Q/R^2},$$

and $Re=\dfrac{2\rho Q}{\pi R\eta_0}$ is the Reynolds number.

The streamfunction-vorticity formulation in cylindrical coordinates becomes

$$\frac{1}{r}\left(\frac{\partial^2\psi}{\partial r^2}+\frac{\partial^2\psi}{\partial z^2}-\frac{1}{r}\frac{\partial\psi}{\partial r}\right)=-\omega, \tag{1.28}$$

$$\frac{\pi Re}{2}\left(\frac{\partial\omega}{\partial t}+v_z\frac{\partial\omega}{\partial z}+v_r\frac{\partial\omega}{\partial r}-\frac{v_r}{r}\omega\right)=\frac{\partial^2\omega}{\partial r^2}+\frac{1}{r}\frac{\partial\omega}{\partial r}-\frac{\omega}{r^2}+\frac{\partial^2\omega}{\partial z^2}, \tag{1.29}$$

where $v_r=-\dfrac{1}{r}\dfrac{\partial\psi}{\partial z}$ and $v_z=\dfrac{1}{r}\dfrac{\partial\psi}{\partial r}$, and $\omega=\dfrac{\partial v_r}{\partial z}-\dfrac{\partial v_z}{\partial r}$.

Hereafter, to simplify the notation, we will drop the superscript '*' in the dimensionless equations.

Oldroyd-B fluids:

In Cartesian coordinates, the dimensionless form of the governing equations for Oldroyd-B fluids is

$$\frac{\partial^2\psi}{\partial x^2}+\frac{\partial^2\psi}{\partial y^2}+\omega=0, \tag{1.30}$$

$$Re\left(\frac{\partial\omega}{\partial t}+v_x\frac{\partial\omega}{\partial x}+v_y\frac{\partial\omega}{\partial y}\right)=\left(\frac{\partial^2\tau_{xy}}{\partial x^2}-\frac{\partial^2\tau_{xy}}{\partial y^2}-\frac{\partial^2\left(\tau_{xx}-\tau_{yy}\right)}{\partial x\partial y}\right)+\alpha\left(\frac{\partial^2\omega}{\partial x^2}+\frac{\partial^2\omega}{\partial y^2}\right), \tag{1.31}$$

$$\tau_{xx}+We\left(\frac{\partial\tau_{xx}}{\partial t}+v_x\frac{\partial\tau_{xx}}{\partial x}+v_y\frac{\partial\tau_{xx}}{\partial y}-2\frac{\partial v_x}{\partial x}\tau_{xx}-2\frac{\partial v_x}{\partial y}\tau_{xy}\right)=2(1-\alpha)\frac{\partial v_x}{\partial x}, \tag{1.32}$$

$$\tau_{xy}+We\left(\frac{\partial\tau_{xy}}{\partial t}+v_x\frac{\partial\tau_{xy}}{\partial x}+v_y\frac{\partial\tau_{xy}}{\partial y}-\frac{\partial v_x}{\partial y}\tau_{yy}-\frac{\partial v_y}{\partial x}\tau_{xx}\right)=(1-\alpha)\left(\frac{\partial v_x}{\partial y}+\frac{\partial v_y}{\partial x}\right), \tag{1.33}$$

$$\tau_{yy}+We\left(\frac{\partial\tau_{yy}}{\partial t}+v_x\frac{\partial\tau_{yy}}{\partial x}+v_y\frac{\partial\tau_{yy}}{\partial y}-2\frac{\partial v_y}{\partial x}\tau_{xy}-2\frac{\partial v_y}{\partial y}\tau_{yy}\right)=2(1-\alpha)\frac{\partial v_y}{\partial y}, \tag{1.34}$$

where $Re=\dfrac{\rho VL}{\eta_0}$ is the Reynolds number, $We=\lambda_1\dfrac{V}{L}$ is the Weissenberg number, and L and V are the flow characteristic length and velocity, respectively.

In cylindrical coordinates, the dimensionless form of the governing equations for

Oldroyd-B fluids, flowing in a tube with circular cross sections, is

$$\frac{1}{r}\left(\frac{\partial^2\psi}{\partial r^2}+\frac{\partial^2\psi}{\partial z^2}-\frac{1}{r}\frac{\partial\psi}{\partial r}\right)+\omega=0, \tag{1.35}$$

$$\frac{\pi Re}{2}\left(\frac{\partial\omega}{\partial t}+v_z\frac{\partial\omega}{\partial z}+v_r\frac{\partial\omega}{\partial r}-\frac{v_r}{r}\omega\right)=\alpha\left(\frac{\partial^2\omega}{\partial r^2}+\frac{1}{r}\frac{\partial\omega}{\partial r}-\frac{\omega}{r^2}+\frac{\partial^2\omega}{\partial z^2}\right)$$
$$+\frac{\partial^2\tau_{rr}}{\partial r\partial z}-\frac{\partial^2\tau_{rz}}{\partial r^2}+\frac{\partial^2\tau_{rz}}{\partial z^2}+\frac{1}{r}\left(\frac{\partial\tau_{rr}}{\partial z}-\frac{\partial\tau_{\theta\theta}}{\partial z}\right)-\frac{\partial^2\tau_{zz}}{\partial r\partial z}+\frac{1}{r^2}\tau_{rz}-\frac{1}{r}\frac{\partial\tau_{rz}}{\partial r}, \tag{1.36}$$

$$\tau_{rr}+We\left(\frac{\partial\tau_{rr}}{\partial t}+v_r\frac{\partial\tau_{rr}}{\partial r}+v_z\frac{\partial\tau_{rr}}{\partial z}-2\frac{\partial v_r}{\partial r}\tau_{rr}-2\frac{\partial v_r}{\partial z}\tau_{rz}\right)$$
$$=2(1-\alpha)\frac{\partial v_r}{\partial r}, \tag{1.37}$$

$$\tau_{rz}+We\left(\frac{\partial\tau_{rz}}{\partial t}+v_r\frac{\partial\tau_{rz}}{\partial r}+v_z\frac{\partial\tau_{rz}}{\partial z}+\frac{v_r}{r}\tau_{rz}-\frac{\partial v_z}{\partial r}\tau_{rr}-\frac{\partial v_r}{\partial z}\tau_{zz}\right)$$
$$=(1-\alpha)\left(\frac{\partial v_r}{\partial z}+\frac{\partial v_z}{\partial r}\right), \tag{1.38}$$

$$\tau_{zz}+We\left(\frac{\partial\tau_{zz}}{\partial t}+v_r\frac{\partial\tau_{zz}}{\partial r}+v_z\frac{\partial\tau_{zz}}{\partial z}-2\frac{\partial v_z}{\partial r}\tau_{rz}-2\frac{\partial v_z}{\partial z}\tau_{zz}\right)$$
$$=2(1-\alpha)\frac{\partial v_z}{\partial z}, \tag{1.39}$$

$$\tau_{\theta\theta}+We\left(\frac{\partial\tau_{\theta\theta}}{\partial t}+v_r\frac{\partial\tau_{\theta\theta}}{\partial r}+v_z\frac{\partial\tau_{\theta\theta}}{\partial z}-2\frac{v_r}{r}\tau_{\theta\theta}\right)=2(1-\alpha)\frac{v_r}{r}, \tag{1.40}$$

where $Re=\dfrac{2\rho Q}{\pi R\eta_0}$ and $We=\lambda_1\dfrac{Q}{R^3}$ are the Reynolds number and the Weissenberg number, respectively, R is the radius of the tube and Q is the flow rate.

1.3 Conventional simulation methods

Solving the governing equations in fluid mechanics is very challenging. Only a few simple fluid flows can be solved analytically/exactly. Using discretisation methods appears to be a practical way to obtain a solution. Techniques used include finite-difference methods (FDMs), finite-element methods (FEMs), boundary-element methods (BEMs), finite-volume methods (FVMs), spectral methods (SMs), differential quadrature methods (DQMs), and radial basis function networks (RBFNs). FDMs are considered as the oldest discretisation scheme. They were applied to simulate fluid flows as early as 1933 (Thom, 1933). The methods are easy to set up and produce sparse system matrices (Conte and Dames, 1958; Smith, 1985; Gupta and Manohar, 1979; Bjrstad, 1983). The main drawback of FDMs lies in the handling of non-rectangular domains. If one uses "irregular" boundary nodes in the FD formulations, it will significantly deteriorate the accuracy of their approximations (Osswald and Hernandez-Ortiz, 2006). If one uses coordinate transformations to obtain a computational domain of rectangular shape, the solution procedure becomes complicated - it is impossible to conduct it for flows with free surfaces or similar complex geometries. FDM simulations reported in the literature are mainly concerned with Newtonian fluids. There are relatively

few FDM publications in Computational Rheology, where only flows with simple geometries are considered. On the other hand, FEMs, BEMs and FVMs can accurately handle problems with complex geometries. For these techniques, generating a mesh and re-meshing are known to be a time-consuming process (Pastor et al., 1991) and the solution appears to converge very slowly in high gradient regions (Emdadi et al., 2008). FEMs have been used in solving transient problems (Bishko et al., 1999; Wapperom et al., 2000), and non-Newtonian fluid flows (Rasmussen, 1999; Yurun and Crochet, 1995; Fan et al., 1999; Sun et al., 1999). In FVMs, physical quantities such as mass, momentum and energy are exactly conserved over any control volume, and thus over the whole domain of interest. Therefore, even with a coarse grid, FVMs can give a solution that exhibits the exact integral balance (Eymard et al., 2000). BEMs can be used to solve linear and nonlinear problems, where one can avoid taking the variables at interior nodes as the unknowns in the discretisation system. This feature comes straightforwardly for solving linear problems, but for non-linear problems, to make it occur, some extra treatments need be implemented. BEMs generate a full matrix and do not work well for highly nonlinear flows (Tanner and Xue, 2002).

Based on their order of convergence, numerical methods can be classified into low order and high order. Low-order methods are referred to as methods of first and second orders of convergence, e.g. traditional FDMs, FEMs, FVMs, and BEMs. Their approximations are widely based on linear functions. The main advantages of these methods are their simplicity, which results in fast implementation, and robustness (the robustness means that one can always get a solution, even though it may not be very accurate). However, one needs to use a large number of grid points to represent the approximate solution and thus requiring large computational resources. Most of problems in practice are large scale; low rates of convergence may hinder low-order methods from being useful.

Numerical methods with accuracy better than $O(h^2)$ are called high-order methods. High-order methods have been increasingly used in CFD to effectively resolve complex flow features. Apart from the well-known spectral methods, many other high-order methods have been proposed - examples include DQMs, compact FD schemes (Lele, 1992), spectral volume (SV) methods (Wang, 2002), spectral difference (SD) methods (Liu et al., 2006), weighted essentially non-oscillatory (WENO) schemes (Liu et al., 1994), discontinuous Galerkin method (Persson, 2013) and RBFNs (Kansa, 1990; Haykin, 1999). These methods are capable of providing high accuracy with relatively coarse grids. Therefore, to obtain a similar level of accuracy, high-order methods normally require much less computational cost than low-order methods. On the other hand, high order methods are often complicated to understand and code, and are less robust in comparison with low-order methods. Applications of high-order methods for flows in complex geometries are still limited. Take SMs, which have become more popular in the computation of continuum mechanics problems in recent years, for example. SMs have the ability to provide an exponential rate of convergence in solving problems whose solutions are sufficiently smooth and their domains are of rectangular shape. Pilitsis and Beris (Pilitsis and Beris, 1989) have developed a mixed pseudospectral finite difference method for the solution of non-Newtonian fluid flows. In (Momeni-Masuleh and Phillips, 2004), the spectral technique has

been presented for the flow of viscoelastic fluids through an undulating tube in the transformed coordinates system, and highly accurate results are obtained. There are several ways proposed in the literature to handle irregularly shaped domains, including domain decompositions, coordinate transformations, fictitious domains and meshless approximations (Bueno-Orovio et al., 2006). It is noted that the access of nodes in meshless approximations and Cartesian-grid-based approximations are much faster than the node access in approximations based on unstructured meshes (Liu et al., 2006).

Numerical methods can also be classified into global and local. For the former, the value of a derivative at a point is computed from the values of the field variable at all nodes in the domain. Such approximations can result in better accuracy, as shown in spectral methods, DQMs and RBFNs. However, global methods are geometrically less flexible and more complicated to implement. They provide dense matrices whose condition numbers grow rapidly as the number of nodes are increased. Handling the fully populated matrices becomes very costly in the case of large scale problems. For local methods, such as FDMs, FEMs and FVMs, the approximation of a derivative at a point involves the neighbouring nodal points only. They can provide resultant sparse coefficient matrices, and thus, their solution are more efficient. Local methods, on the other hand, converge slowly with grid/mesh refinement and cannot yield highly accurate results. Many efforts have been put in the improvement of accuracy for local methods. Using local approximations compactly is an attractive prospect.

1.4 Integrated radial basis function methods

Radial basis function networks are a powerful concept, which is essential to this project. Derived from the biological sciences, they can be considered as universal approximation schemes (Haykin, 1999). The application of RBFNs for the numerical solution of partial differential equations (PDEs) was first reported by Kansa (1990) (Kansa, 1990). A function $f(\mathbf{x})$ can be represented by RBFs as

$$f(\mathbf{x}) = \sum_{i=1}^{N} w_i g_i(\mathbf{x}), \tag{1.41}$$

where $\mathbf{x}$ is the position vector, N is the number of RBFs, $\{w_i\}_{i=1}^{N}$ is the set of network weights, and $\{g_i(\mathbf{x})\}_{i=1}^{N}$ is the set of RBFs. The RBFs can be written in a general form as $g_i(\mathbf{x}) = g_i\left(\|\mathbf{x} - \mathbf{c}_i\|\right)$, where $\|\cdot\|$ denotes the Euclidean norm and $\{\mathbf{c}_i\}_{i=1}^{N}$ is a set of the RBF centers. There are some common types of RBFs, including

- Multiquadrics function (MQ)

$$g_i(\mathbf{x}) = \sqrt{r^2 + a_i^2}, \quad a_i > 0, \tag{1.42}$$

- Inverse multiquadrics function

$$g_i(\mathbf{x}) = \frac{1}{\sqrt{r^2 + a_i^2}}, \quad a_i > 0, \tag{1.43}$$

- Gaussians function

$$g_i(\mathbf{x}) = \exp\left(-\frac{r^2}{a_i^2}\right), \quad a_i > 0, \tag{1.44}$$

where a_i is usually referred to as the width of the ith basis function and $r = \|\mathbf{x} - \mathbf{c}_i\| = \sqrt{(\mathbf{x} - \mathbf{c}_i) \cdot (\mathbf{x} - \mathbf{c}_i)}$.

Some RBFs, such as the above mentioned, are shown to possess spectral convergence rate. Thus, they fall into a class of high order methods. RBF collocation methods need only a set of discrete points – instead of a set of elements – throughout a volume to approximate the field variables. Thus, they can be regarded as truly meshless methods. Originally, RBF approximations were constructed globally. Advantages of global RBF schemes include (i) fast convergence (spectral accuracy for some RBFs such as the multiquadric and Gaussian functions); (ii) meshless nature and (iii) simple implementation. Unlike other high order methods, RBFNs are capable of handling domains with non-rectangular boundaries. To overcome the problem of fully populated matrices and their high condition numbers of global methods, local RBF methods were developed (Franke, 1982; Shu et al., 2003; Kosec and Sarler, 2008; Bourantas et al., 2010). A much larger number of nodes can be now employed; but, their solution accuracy is significantly reduced (Lee et al., 2003). Compact local RBF schemes have been implemented, e.g. (Mai-Duy and Tran-Cong, 2011), to enhance the numerical accuracy of local forms.

RBF approximations can be obtained from the differentiation process (differentiated RBFs (DRBFs)) or the integration process (integrated RBFs (IRBFs)). In DRBFs, the function to be approximated is first decomposed into RBFs, and its derivatives are then calculated by differentiating RBFs

$$u(\mathbf{x}) = \sum_{i=1}^{N} w_i g_i(\mathbf{x}), \tag{1.45}$$

$$\frac{\partial^k u(\mathbf{x})}{\partial \eta^k} = \sum_{i=1}^{N} w_i^{[\eta]} h_{[\eta]i}^{(k)}(\mathbf{x}), \tag{1.46}$$

where η denotes a component of the position vector $\mathbf{x}$ (e.g. η can be x for 1D problems, and x or y for 2D problems), superscript (k) denotes the order of the derivatives of u, and $h_{[\eta]i}^{(k)}(\mathbf{x}) = \dfrac{\partial^k g_i(\mathbf{x})}{\partial \eta^k}$.

In IRBFs (Mai-Duy and Tran-Cong, 2001), highest-order derivative(s) in the ODE/PDE are approximated by RBFs, and lower-order derivatives and the de-

pendent variable itself are then obtained by integrating RBFs

$$\frac{\partial^k u(\mathbf{x})}{\partial \eta^k} = \sum_{i=1}^{N} w_i^{[\eta]} g_i(\mathbf{x}) = \sum_{i=1}^{N} w_i^{[\eta]} I_{[\eta]i}^{(k)}(\mathbf{x}), \tag{1.47}$$

$$\frac{\partial^{k-1} u(\mathbf{x})}{\partial \eta^{k-1}} = \sum_{i=1}^{N} w_i^{[\eta]} I_{[\eta]i}^{(k-1)}(\mathbf{x}) + C_1^{[\eta]}, \tag{1.48}$$

$$\cdots$$

$$u(\mathbf{x}) = \sum_{i=1}^{N} w_i^{[\eta]} I_{[\eta]i}^{(0)}(\mathbf{x}) + \frac{\eta^{k-1}}{(k-1)!} C_1^{[\eta]} + \frac{\eta^{k-2}}{(k-2)!} C_2^{[\eta]} + \cdots + C_k^{[\eta]}, \tag{1.49}$$

where $I_{[\eta]i}^{(k-1)}(\mathbf{x}) = \int I_{[\eta]i}^{(k)}(\mathbf{x}) d\eta$, $\cdots$, $I_{[\eta]i}^{(0)}(\mathbf{x}) = \int I_{[\eta]i}^{(1)}(\mathbf{x}) d\eta$; and $C_1^{[\eta]}, C_2^{[\eta]}, \cdots, C_k^{[\eta]}$ are the "constants" of integration, which will be constants for 1D problems, functions in one variable for 2D problems, and in two variables for 3D problems. These functions are unknown and can be approximated as linear combinations of basis functions.

The purposes of using integration (a smoothing operator) to construct the approximants are to avoid the reduction in convergence rate caused by differentiation and to improve the numerical stability of a discrete solution. It has been found that the integration constants are very helpful in the implementation of multiple boundary conditions (Mai-Duy, 2005; Mai-Duy and Tanner, 2005b; Mai-Duy and Tran-Cong, 2006) and non-overlapping domain decompositions (Mai-Duy and Tran-Cong, 2008b). Numerical results showed that IRBFs yield better accuracy than DRBFs (Mai-Duy and Tran-Cong, 2001, 2003; Mai-Duy, 2005; Mai-Duy and Tanner, 2005b).

1.5 Objectives of the research

This research project is concerned with the development of powerful approximation stencils for the discretisation of partial differential equations (PDEs) governing the motion of fluids. The proposed stencils are based on several recent advances in computational fluid dynamics and computational mechanics, including the integral approximation formulation, radial basis functions (RBFs) and compact approximations. The main objectives of this research are

- to build up compact local integrated RBF (CLIRBF) stencils for the approximation of a function and its derivatives up to fourth order
- to introduce CLIRBF stencils into the point collocation formulation for the discretisation of second-order elliptic equations and biharmonic equations
- to introduce CLIRBF stencils into the sub-region collocation formulation for the discretisation of second-order elliptic equations
- to build up a numerical procedure based on CLIRBF stencils and point collocation for the simulation of Newtonian fluid flows
- to build up a numerical procedure based on CLIRBF stencils and sub-region collocation for the simulation of Newtonian fluid flows

- to build up a numerical procedure based on CLIRBF stencils and point collocation for the simulation of viscoelastic fluid flows

1.6 Outline of the Thesis

The remaining of the thesis is organised as follows.

- Chapter 2 deals with the development of several CLIRBF stencils for solving fourth-order ODEs and PDEs in point collocation. Test problems, governed by the biharmonic equation and its equivalent set of two Poisson equations, are considered.
- Chapter 3 deals with the incorporation of CLIRBF stencils into the point-collocation formulation for the simulation of flows of a Newtonian fluid. Test problems, whose solutions involve very steep gradients, are considered. Governing equations employed are the convection-diffusion equation and the streamfunction-vorticity formulation.
- Chapter 4 deals with the incorporation of CLIRBF stencils into the subregion-collocation formulation for the simulation of flows of a Newtonian fluid. Two numerical integration schemes to evaluate volume integrals, namely the middle point rule and 3-point Gaussian quadrature rule, are employed. Several test problems including natural convection in an annulus, where the governing equations are taken in the streamfunction-vorticity formulation, are considered.
- Chapter 5 is concerned with the application of CLIRBF stencils for simulating steady state viscoelastic flows. Poiseuille flows and corrugated tube flows of Oldroyd-B fluids are considered.
- Chapter 6 is concerned with the use of CLIRBF stencils in transient problems. Hyperbolic and parabolic equations are considered.
- Chapter 7 concludes the thesis with a summary and possible directions for future research.

Chapter 2

Compact local IRBF stencils and point collocation for high-order differential problems

Our first concern is about high-order ODEs/PDEs, which govern many applications in engineering. New compact local stencils based on IRBFs for the discretisation of fourth-order ODEs and PDEs will be presented in this chapter. Five types of compact stencils - 3-node and 5-node for 1D problems and 5×5-node, 13-node and 3×3 -node for 2D problems - are implemented. In the case of 3-node stencil and 3×3-node stencil, nodal values of the first derivative(s) of the field variable are treated as additional unknowns (i.e. 2 unknowns per node for 3-node stencil and 3 unknowns per node for 3×3-node stencil). The integration constants arising from the construction of IRBFs are exploited to incorporate into the local IRBF approximations (i) values of the governing equation (GE) at selected nodes for the case of 5-, 5×5- and 13-node stencils, and (ii) not only nodal values of the governing equation but also nodal values of the first derivative(s) for the case of 3-node stencil and 3×3-node stencil. There are no special treatments required for grid nodes near the boundary for 3-node stencil and 3×3-node stencil. The proposed stencils, which lead to sparse system matrices, are numerically verified through the solution of several test problems.

2.1 Introduction

Fourth-order differential problems occur widely in practice. Typical examples include the deformation of thin plates, the equilibrium of an elastic rectangular plate, and the solution of Stokes flow of a viscous fluid; they are governed by the biharmonic equation. Various numerical methods have been developed for solving the fourth-order problems, such as finite-difference-based methods (Conte and Dames, 1958; Gupta and Manohar, 1979; Bjrstad, 1983; Altas et al., 1998), spectral methods (Bernardi et al., 1992; Heinrichs, 1992; Bialecki and Karageorghis, 2010), global and local RBF methods (Chantasiriwan, 2007), and global integrated RBFs/Chebyshev polynomials methods (Mai-Duy and Tanner, 2005b; Mai-Duy and Tran-Cong, 2006; Mai-Duy and Tanner, 2007; Mai-Duy et al.,

2009b), and Galerkin schemes (Mai-Duy et al., 2009a). Global RBF methods are more accurate but less efficient than local RBF methods (please see Section 1.4 for a detailed discussion).

This chapter is concerned with the development of local IRBF stencils in compact form for the solution of fourth-order ODEs and PDEs. The following two strategies (e.g. (Stephenson, 1984; Altas et al., 1998)) are studied in the context of local compact IRBF stencils.

The first strategy employs relatively large stencils (i.e. 5 nodes for 1D fourth-order problems, and 13 nodes or 5×5 nodes for 2D fourth-order problems). For this approach, only nodal values of the field variable on a stencil are treated as unknowns. It is noted that, when compared with second-order problems, there are more nodes used on a stencil (i.e. 2 additional nodes for 1D problems, and 4 and 16 additional nodes for 2D problems).

The second strategy employs relatively small stencils (i.e. 3 nodes for 1D problems and 3×3 nodes for 2D problems). For this approach, not only nodal values of the field variable on a stencil but also nodal values of its first derivative at selected nodes are treated as unknowns. Advantages of this strategy include (i) the number of nodes employed here does not increase when compared with the case of second-order problems; (ii) there are no special treatments required for grid nodes near the boundary; (iii) boundary derivative values can be imposed easily and accurately; and (iv) first derivative values are obtained directly from the final system of algebraic equations.

Furthermore, in both strategies, we also incorporate nodal values of the governing equation at selected nodes on a stencil into the IRBF approximations. Numerical results will show that such an incorporation can significantly enhance the solution accuracy.

The remainder of the chapter is organised as follows. Section 2 is a brief review of IRBFs. The proposed compact local stencils based on IRBFs are presented for 1D problems in Section 3 and for 2D problems in Section 4. Numerical examples, including the simulation of lid-driven cavity flows, are given in Section 5 to demonstrate the attractiveness of the proposed stencils. Section 6 concludes the chapter.

2.2 Brief review of integrated RBFs

Consider a continuous function $u(\mathbf{x})$ where $\mathbf{x}$ is the position vector. Such a function can be approximated using IRBF schemes of second and fourth orders.

2.2.1 Second-order integrated RBF scheme

In this scheme, the second-order derivatives of the function u are decomposed into a set of RBFs

$$\frac{\partial^2 u(\mathbf{x})}{\partial \eta^2} = \sum_{i=1}^{N} w_i^{[\eta]} I_{[\eta]i}^{(2)}(\mathbf{x}), \tag{2.1}$$

where η denotes a component of the position vector $\mathbf{x}$ (e.g. η can be x for 1D problems, and x or y for 2D problems), $\{w_i\}_{i=1}^{N}$ is the set of RBF coefficients which are unknown, and $\left\{I_i^{(2)}(\mathbf{x})\right\}_{i=1}^{N}$ is the set of RBFs. Expression (2.1) is then integrated to obtain approximate expressions for lower order derivatives and the function itself as follows.

$$\frac{\partial u(\mathbf{x})}{\partial \eta} = \sum_{i=1}^{N} w_i^{[\eta]} I_{[\eta]i}^{(1)}(\mathbf{x}) + C_1, \tag{2.2}$$

$$u(\mathbf{x}) = \sum_{i=1}^{N} w_i^{[\eta]} I_{[\eta]i}^{(0)}(\mathbf{x}) + \eta C_1 + C_2, \tag{2.3}$$

where C_1 and C_2 are "constants of integration" with respect to η, which are to be treated as the additional RBF coefficients. In (2.1)-(2.3), the superscript (.) is used to indicate the associated derivative order.

Collocating (2.1)-(2.3) at a set of nodal points $\{\mathbf{x}_i\}_{i=1}^{N}$ yields

$$\widehat{\frac{\partial^2 u}{\partial \eta^2}} = \mathcal{H}_\eta^{(2)} \widehat{w}_\eta, \tag{2.4}$$

$$\widehat{\frac{\partial u}{\partial \eta}} = \mathcal{H}_\eta^{(1)} \widehat{w}_\eta, \tag{2.5}$$

$$\widehat{u} = \mathcal{H}_\eta^{(0)} \widehat{w}_\eta, \tag{2.6}$$

where the notation '$\widehat{\ }$' is used to denote a vector, $\mathcal{H}^{(.)}$ is the RBF coefficient matrix in the RBF space and $\widehat{w}_\eta$ is the RBF vector of coefficients, including the integration constants.

2.2.2 Fourth-order integrated RBF scheme

In this scheme, the fourth-order derivatives of the function u are decomposed into a set of RBFs as

$$\frac{\partial^4 u(\mathbf{x})}{\partial \eta^4} = \sum_{i=1}^{N} w_i^{[\eta]} I_{[\eta]i}^{(4)}(\mathbf{x}). \tag{2.7}$$

Approximate expressions for lower order derivatives and the function itself are then obtained through integration as

$$\frac{\partial^3 u(\mathbf{x})}{\partial \eta^3} = \sum_{i=1}^{N} w_i^{[\eta]} I_{[\eta]i}^{(3)}(\mathbf{x}) + C_1, \tag{2.8}$$

$$\frac{\partial^2 u(\mathbf{x})}{\partial \eta^2} = \sum_{i=1}^{N} w_i^{[\eta]} I_{[\eta]i}^{(2)}(\mathbf{x}) + \eta C_1 + C_2, \tag{2.9}$$

$$\frac{\partial u(\mathbf{x})}{\partial \eta} = \sum_{i=1}^{N} w_i^{[\eta]} I_{[\eta]i}^{(1)}(\mathbf{x}) + \frac{\eta^2}{2} C_1 + \eta C_2 + C_3, \tag{2.10}$$

$$u(\mathbf{x}) = \sum_{i=1}^{N} w_i^{[\eta]} I_{[\eta]i}^{(0)}(\mathbf{x}) + \frac{\eta^3}{6} C_1 + \frac{\eta^2}{2} C_2 + \eta C_3 + C_4. \tag{2.11}$$

Collocating (2.7)-(2.11) at a set of nodal points $\{\mathbf{x}_i\}_{i=1}^{N}$ yields

$$\widehat{\frac{\partial^4 u}{\partial \eta^4}} = \mathcal{H}_\eta^{(4)} \widehat{w}_\eta, \tag{2.12}$$

$$\widehat{\frac{\partial^3 u}{\partial \eta^3}} = \mathcal{H}_\eta^{(3)} \widehat{w}_\eta, \tag{2.13}$$

$$\widehat{\frac{\partial^2 u}{\partial \eta^2}} = \mathcal{H}_\eta^{(2)} \widehat{w}_\eta, \tag{2.14}$$

$$\widehat{\frac{\partial u}{\partial \eta}} = \mathcal{H}_\eta^{(1)} \widehat{w}_\eta, \tag{2.15}$$

$$\widehat{u} = \mathcal{H}_\eta^{(0)} \widehat{w}_\eta. \tag{2.16}$$

For the approximations of integration constants used in (2.1)-(2.3) and (2.7)-(2.11), the reader is referred to (Mai-Duy and Tran-Cong, 2003, 2010) for further details.

In this study, the multiquadric (MQ) function is chosen as the basis function as

$$I_i^{(4)}(x) = \sqrt{(x - c_i)^2 + a_i^2} \quad \text{for 1D problems,} \tag{2.17}$$

$$I_i^{(4)}(\mathbf{x}) = \sqrt{(x - c_{ix})^2 + (y - c_{iy})^2 + a_i^2} \quad \text{for 2D problems,} \tag{2.18}$$

where c_i (for 1D problems) or $(c_{ix}, c_{iy})^T$ (for 2D problems) and a_i are the MQ centre and width, respectively. The width of the ith MQ can be determined according to the following relation

$$a_i = \beta d_i, \tag{2.19}$$

where β is a factor ($\beta > 0$) and d_i is the distance from the ith centre to the nearest neighbour. It was observed in (Kansa, 1990) that, as the RBF width increases, the numerical error of the RBF solution reduces and the condition number of the interpolant grows. At large values of β, one needs to pay special attention as the solution becomes unstable. Reported values of β vary from, typically, 1 for global IRBF methods to a wide range of $2-200$ for local and compact local IRBF

methods. For the latter, one can vary the value of β and/or refine the spatial discretisation to enhance the solution accuracy.

In the following sections, to simplify the notations, we will drop the subscript η used in (2.12)-(2.16) for 1D problems, and use (i, j) to represent a grid node located at (x_i, y_j) in a global 2D grid, $\mathbf{x}_k$ to represent a grid node k in a local 2D stencil, and $\mathcal{M}(i, :)$ to denote the ith row of the matrix $\mathcal{M}$.

2.3 Proposed compact local IRBF stencils for fourth-order ODEs

Our sample of fourth-order ODEs is taken as

$$\frac{d^4u}{dx^4} + \frac{d^2u}{dx^2} = f(x), \tag{2.20}$$

where $x_A \leq x \leq x_B$ and $f(x)$ is some given function. The boundary conditions prescribed here are of Dirichlet type, i.e. u and du/dx given at both x_A and x_B.

We discretise the problem domain using a set of N discrete nodes $\{x_i\}_{i=1}^N$, and utilise fourth-order IRBF schemes to represent the field variable u.

2.3.1 Compact local 5-node stencil (5-node CLS)

Consider a grid node x_i and its associated 5-node stencil $[x_1^i, x_2^i, x_3^i, x_4^i, x_5^i]$ ($x_i \equiv x_3^i$).

The conversion system, which represents the relation between the RBF space and the physical space, is established from the following equations

$$\begin{pmatrix} \widehat{u} \\ \widehat{e} \end{pmatrix} = \underbrace{\begin{bmatrix} \mathcal{H}^{(0)} \\ \mathcal{K} \end{bmatrix}}_{\mathcal{C}} \widehat{w}, \tag{2.21}$$

where $\mathcal{C}$ is the conversion matrix, $\widehat{w} = (w_1, w_2, w_3, w_4, w_5, C_1, C_2, C_3, C_4)^T$, $\widehat{u} = (u_1, u_2, u_3, u_4, u_5)^T$, $\widehat{u} = \mathcal{H}^{(0)}\widehat{w}$ are equations representing nodal values of u over the stencil, $\mathcal{H}^{(0)}$ is a 5×9 matrix that is obtained from collocating (2.11) at grid nodes of the stencil, $\widehat{e} = \mathcal{K}\widehat{w}$ are equations representing extra information that can be the ODE (2.20) at selected nodes, and du/dx at x_A and x_B. Solving (2.21) results in

$$\widehat{w} = \mathcal{C}^{-1} \begin{pmatrix} \widehat{u} \\ \widehat{e} \end{pmatrix}. \tag{2.22}$$

If the number of extra information values are less than or equal to 4, the obtained conversion matrix in (2.21) is not overdetermined owing to the presence of the integration constants. In this case, the extra information is thus imposed in an exact manner. By substituting (2.22) into (2.7)-(2.11), values of u and its

derivatives at an arbitrary point x on the stencil are calculated in the physical space as

$$\frac{d^4u(x)}{x^4} = \left[\begin{array}{cccccccc} I_1^{(4)}(x), & \ldots, & I_5^{(4)}(x), & 0, & 0, & 0, & 0 \end{array}\right] \mathcal{C}^{-1} \left(\begin{array}{c} \widehat{u} \\ \widehat{e} \end{array}\right), \tag{2.23}$$

$$\frac{d^3u(x)}{dx^3} = \left[\begin{array}{cccccccc} I_1^{(3)}(x), & \ldots, & I_5^{(3)}(x), & 1, & 0, & 0, & 0 \end{array}\right] \mathcal{C}^{-1} \left(\begin{array}{c} \widehat{u} \\ \widehat{e} \end{array}\right), \tag{2.24}$$

$$\frac{d^2u(x)}{dx^2} = \left[\begin{array}{cccccccc} I_1^{(2)}(x), & \ldots, & I_5^{(2)}(x), & x, & 1, & 0, & 0 \end{array}\right] \mathcal{C}^{-1} \left(\begin{array}{c} \widehat{u} \\ \widehat{e} \end{array}\right), \tag{2.25}$$

$$\frac{du(x)}{dx} = \left[\begin{array}{cccccccc} I_1^{(1)}(x), & \ldots, & I_5^{(1)}(x), & x^2/2, & x, & 1, & 0 \end{array}\right] \mathcal{C}^{-1} \left(\begin{array}{c} \widehat{u} \\ \widehat{e} \end{array}\right), \tag{2.26}$$

$$u(x) = \left[\begin{array}{cccccccc} I_1^{(0)}(x), & \ldots, & I_5^{(0)}(x), & x^3/6, & x^2/2, & x, & 1 \end{array}\right] \mathcal{C}^{-1} \left(\begin{array}{c} \widehat{u} \\ \widehat{e} \end{array}\right), \tag{2.27}$$

where $x_1^i \leq x \leq x_5^i$. In what follows, we present two ways to construct the final system of algebraic equations, namely Implementation 1 and Implementation 2.

Implementation 1: The final system is generated by

(i) the collocation of the ODE (2.20) at $\{x_3, x_4, \ldots, x_{N-2}\}$ using (2.23) and (2.25) with $x = x_i$, in which $\widehat{e} = \mathcal{K}\widehat{w}$ is employed to represent values of (2.20) at x_2^i and x_4^i, i.e.

$$\left(\begin{array}{c} f\left(x_2^i\right) \\ f\left(x_4^i\right) \end{array}\right) = \left[\begin{array}{c} \mathcal{G}(2,:) \\ \mathcal{G}(4,:) \end{array}\right] \widehat{w}, \tag{2.28}$$

where $\mathcal{G} = \mathcal{H}^{(4)} + \mathcal{H}^{(2)}$, and

(ii) the imposition of du/dx at x_A and x_B using (2.26) with $x = x_1$ and $x = x_N$.

Implementation 2: The final system is generated by collocating the ODE (2.20) at $\{x_4, x_5, \ldots, x_{N-3}\}$ and $\{x_2, x_3, x_{N-2}, x_{N-1}\}$. For the former, the collocation process is similar to that of Implementation 1. For the latter, special treatments for the imposition of first derivative boundary conditions are required. Collocations of the ODE (2.20) at $\{x_2, x_3\}$ and $\{x_{N-2}, x_{N-1}\}$ are based on the stencils of nodes x_3 and x_{N-2}, respectively, with the following modified extra information vectors

$\widehat{e} = (du(x_1^i)/dx, f(x_4^i))^T$ for the stencil of x_3,
$\widehat{e} = (f(x_2^i), du(x_5^i)/dx)^T$ for the stencil of x_{N-2}.

Both implementations lead to a system matrix of dimensions $(N-2) \times (N-2)$. We define the sparsity as the percentage of zero entries relative to the total matrix entries. For example, the use of grid node $N = 31$ leads to a system matrix of dimension 29×29 with the sparsity of 83.82%.

2.3.2 Compact local 3-node stencil (3-node CLS)

Consider a grid node x_i ($i = \{2, 3, \ldots, N-1\}$) with its associated 3-node stencil $[x_1^i, x_2^i, x_3^i]$ ($x_i \equiv x_2^i$).

Unlike the **5-node CLS**, nodal values of the first derivative of the field variable are also treated here as unknowns. There are thus two unknowns, namely u and du/dx, per node.

We form the conversion system as follows.

$$\begin{pmatrix} \widehat{u} \\ \widehat{du} \\ \widehat{e} \end{pmatrix} = \underbrace{\begin{bmatrix} \mathcal{H}^{(0)} \\ \mathcal{H}^{(1)} \\ \mathcal{K} \end{bmatrix}}_{\mathcal{C}} \widehat{w}, \tag{2.29}$$

where $\mathcal{C}$ is the conversion matrix, $\widehat{u} = (u_1, u_2, u_3)^T$, $\widehat{du} = (du(x_1^i)/dx, du(x_3^i)/dx)^T$, $\widehat{w} = (w_1, w_2, w_3, c_1, c_2, c_3, c_4)^T$, $\widehat{u} = \mathcal{H}^{(0)}\widehat{w}$ is a set of three equations representing nodal values of u over the stencil, $\widehat{du} = \mathcal{H}^{(1)}\widehat{w}$ is a set of two equations representing nodal values of the first derivative at x_1^i and x_3^i, and $\widehat{e} = \mathcal{K}\widehat{w}$ is a set of equations which can be used to incorporate more information into the approximations.

Solving (2.29) results in

$$\widehat{w} = \mathcal{C}^{-1} \begin{pmatrix} \widehat{u} \\ \widehat{du} \\ \widehat{e} \end{pmatrix}. \tag{2.30}$$

It can be seen that the IRBF approximations for the field variable and its derivatives can now be expressed in terms of not only nodal values of u at the three grid nodes of the stencil but also nodal values of du/dx at the two extreme nodes of the stencil.

The two unknowns at the central point of the stencil (x_2^i) require the establishment of two algebraic equations. This can be achieved by collocating the ODE (2.20) at x_2^i and collocating the first derivative at x_2^i

$$f(x_2^i) = \mathcal{G}(2,:)\mathcal{C}^{-1} \begin{pmatrix} \widehat{u} \\ \widehat{du} \\ \widehat{e} \end{pmatrix}, \tag{2.31}$$

$$\frac{du(x_2^i)}{dx} = \mathcal{H}^{(1)}(2,:)\,\mathcal{C}^{-1} \begin{pmatrix} \widehat{u} \\ \widehat{du} \\ \widehat{e} \end{pmatrix}, \tag{2.32}$$

where $\mathcal{G} = \mathcal{H}^{(4)} + \mathcal{H}^{(2)}$.

The above process leads to a determined final system with $(N-2)$ equations for the ODE, and $(N-2)$ equations for the first derivative du/dx, with $(N-2)$ unknowns for the field variable u and $(N-2)$ unknowns for du/dx at the interior nodes. The sparsity of the final system is 90.76% with the grid node of $N = 31$ used.

In the case that $\widehat{e}$ is used to represent the governing equation (GE) (2.20) at x_1^i

and x_3^i, i.e.

$$\underbrace{\begin{pmatrix} f(x_1^i) \\ f(x_3^i) \end{pmatrix}}_{\widehat{e}} = \begin{pmatrix} \mathcal{G}(1,:) \\ \mathcal{G}(3,:) \end{pmatrix} \widehat{w}, \tag{2.33}$$

we name the corresponding stencil a **3-node CLS with GE**.

In the case that $\widehat{e}$ is simply set to null, we call it a **3-node CLS without GE**.

2.4 Proposed compact local IRBF stencils for fourth-order PDEs

Consider a 2D fourth-order differential problem governed by the biharmonic equation

$$\frac{\partial^4 u}{\partial x^4} + 2\frac{\partial^4 u}{\partial x^2 y^2} + \frac{\partial^4 u}{\partial y^4} = f(x,y) \tag{2.34}$$

on a rectangular domain ($x_A \leq x \leq x_B$, $y_C \leq y \leq y_D$), and subject to Dirichlet boundary conditions (i.e. u and $\partial u/\partial n$ given at the boundaries (n the normal direction)).

The problem domain is represented by a Cartesian grid of $N_x \times N_y$ as shown in Figure 2.1. We employ fourth-order IRBF schemes for compact local 5×5-node and 13-node stencils, and second-order IRBF schemes for compact local 3×3-node stencils.

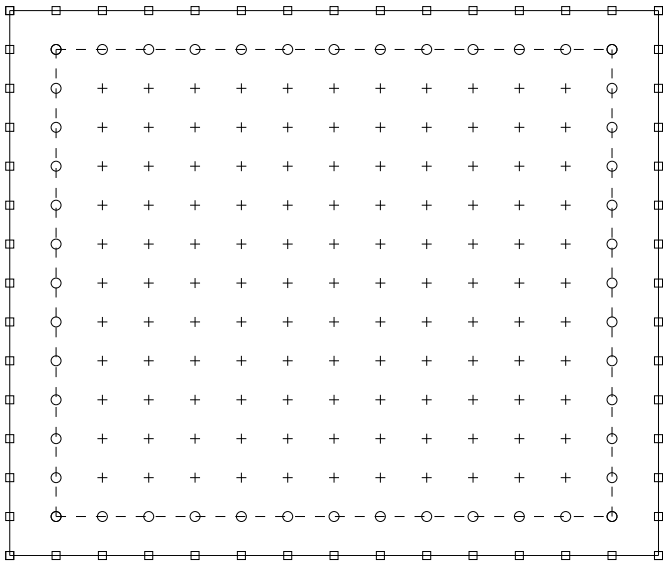

Figure 2.1 A problem domain and a typical discretisation. Legends square, circle and plus are used to denote the boundary nodes, the interior nodes next to the boundary and the remaining interior nodes, respectively.

2.4.1 Compact local 5×5-node stencil (5×5-node CLS)

Consider a grid node (i, j) and its associated 5×5-node stencil. The stencil is locally numbered from bottom to top and from left to right (node $(i, j) \equiv$ node 13) (Figure 2.2).

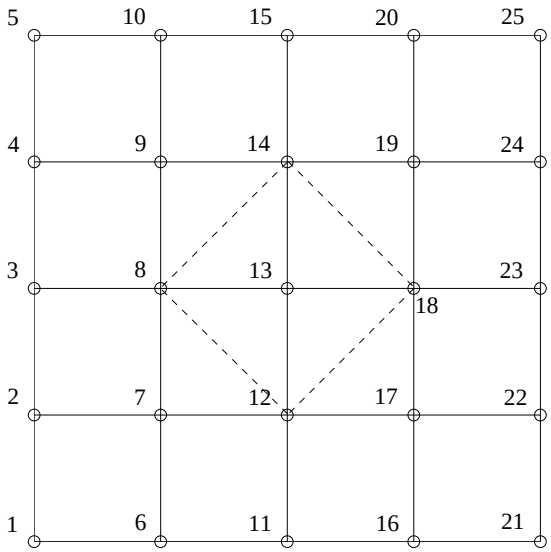

Figure 2.2 A schematic representation of the proposed 5×5-node stencil associated with node (i, j). Over the stencil, nodes are locally numbered for bottom to top and left to right, where $13 \equiv (i, j)$. Nodal values of the governing equation used as extra information are placed on a diamond shape.

The solution procedure here is similar to that for 1D problems. However, the 2D problem formulation involves more terms and requires special treatments for interior "corner" nodes.

The conversion system is constructed as

$$\begin{pmatrix} \widehat{u} \\ \widehat{0} \\ \widehat{e} \end{pmatrix} = \underbrace{\begin{bmatrix} \mathcal{H}_x^{(0)}, & \mathcal{O} \\ \mathcal{H}_x^{(0)}, & -\mathcal{H}_y^{(0)} \\ \mathcal{K}_x, & \mathcal{K}_y \end{bmatrix}}_{\mathcal{C}} \begin{pmatrix} \widehat{w}_x \\ \widehat{w}_y \end{pmatrix}, \tag{2.35}$$

where the subscripts x and y denote the quantity associated with the integration process in the x and y direction, respectively; $\widehat{0}$ and $\mathcal{O}$ are a vector and a matrix of zeros, respectively; equations $\widehat{u} = \mathcal{H}_x^{(0)}\widehat{w}_x$ are employed to collocate the variable u over the stencil; equations $\mathcal{H}_x^{(0)}\widehat{w}_x - \mathcal{H}_y^{(0)}\widehat{w}_y = \widehat{0}$ are employed to enforce nodal values of u obtained from the integration with respect to x and y to be identical; and equations $\mathcal{K}_x\widehat{w}_x + \mathcal{K}_y\widehat{w}_y = \widehat{e}$ are employed to represent extra information that can be values of the PDE (2.20) at selected nodes on the stencil and first-order derivative boundary conditions. In (2.35), $\mathcal{C}$ is the conversion matrix, $\widehat{u}$ and $\widehat{0}$ are vectors of length 25; $(\widehat{w}_x, \widehat{w}_y)^T$ is the RBF coefficient vector of length 90, and $\mathcal{O}, \mathcal{H}_x^{(0)}, \mathcal{H}_y^{(0)}, \mathcal{K}_x$ and $\mathcal{K}_y$ are matrices (the first three are of dimensions 25×45, while for the last two, their dimensions are dependent on the number of extra information values imposed and typically vary between 4×45 to 6×45). Solving

(2.35) yields

$$\begin{pmatrix} \widehat{w}_x \\ \widehat{w}_y \end{pmatrix} = \mathcal{C}^{-1} \begin{pmatrix} \widehat{u} \\ \widehat{0} \\ \widehat{e} \end{pmatrix}. \tag{2.36}$$

We present two ways, namely Implementation 1 and Implementation 2, to form the final set of algebraic equations.

Implementation 1: The final system is composed of two sets of equations. The first set is obtained by collocating the PDE at interior nodes (i, j) with $(3 \leq i \leq N_x - 2$ and $3 \leq j \leq N_y - 2)$ and the second set is obtained by imposing first derivative boundary conditions at boundary nodes $(i = 1,\ 2 \leq j \leq N_y - 1)$, $(i = N_x,\ 2 \leq j \leq N_y - 1)$, $(3 \leq i \leq N_x - 2,\ j = 1)$ and $(3 \leq i \leq N_x - 2,\ j = N_y)$.

Implementation 2: First derivative boundary conditions are incorporated into the conversion system and the final system is formed by collocating the PDE only at all interior nodes.

Some implementation notes:

1. In constructing the approximations for stencils, the cross derivative $\partial^4 u/\partial x^2 \partial y^2$ is computed through the following relation (Mai-Duy and Tanner, 2005a), which requires the approximation of second-order pure derivatives only,

$$\begin{aligned} \frac{\partial^4 u}{\partial^2 x \partial^2 y} &= \frac{1}{2}\left(\frac{\partial^2}{\partial x^2}\left(\frac{\partial^2 u}{\partial y^2}\right) + \frac{\partial^2}{\partial y^2}\left(\frac{\partial^2 u}{\partial x^2}\right)\right) \\ &= \frac{1}{2}\left(\mathcal{H}_x^{(2)}\left[\mathcal{H}_x^{(0)}\right]^{-1}\left(\mathcal{H}_y^{(2)}\widehat{w}_y\right) + \mathcal{H}_y^{(2)}\left[\mathcal{H}_y^{(0)}\right]^{-1}\left(\mathcal{H}_x^{(2)}\widehat{w}_x\right)\right). \end{aligned} \tag{2.37}$$

2. For stencils whose central points are interior nodes (i, j) with $3 < i < N_x - 2$ and $3 < j < N_y - 2$, we construct $\widehat{e} = \mathcal{K}_x\widehat{w}_x + \mathcal{K}_y\widehat{w}_y$ through the collocation of the PDE (2.34) at four nodes placed in the diamond (i.e $(i-1, j), (i, j-1), (i, j+1)$ and $(i+1, j)$) as shown in Figure 2.2. The extra information vector can thus be expressed in the form

$$\begin{pmatrix} f(\mathbf{x}_8) \\ f(\mathbf{x}_{12}) \\ f(\mathbf{x}_{14}) \\ f(\mathbf{x}_{18}) \end{pmatrix} = \begin{bmatrix} \mathcal{G}_x(8,:), \mathcal{G}_y(8,:) \\ \mathcal{G}_x(12,:), \mathcal{G}_y(12,:) \\ \mathcal{G}_x(14,:), \mathcal{G}_y(14,:) \\ \mathcal{G}_x(18,:), \mathcal{G}_y(18,:) \end{bmatrix} \begin{pmatrix} \widehat{w}_x \\ \widehat{w}_y \end{pmatrix}, \tag{2.38}$$

where

$$\mathcal{G}_x = \mathcal{H}_x^{(4)} + \mathcal{H}_y^{(2)}\left[\mathcal{H}_y^{(0)}\right]^{-1}\mathcal{H}_x^{(2)},$$

and

$$\mathcal{G}_y = \mathcal{H}_y^{(4)} + \mathcal{H}_x^{(2)}\left[\mathcal{H}_x^{(0)}\right]^{-1}\mathcal{H}_y^{(2)}.$$

3. For stencils whose central points are $(3, 3)$, $(3, N_y - 2)$, $(N_x - 2, 3)$ and $(N_x - 2, N_y - 2)$, the extra information vector is comprised of four nodal values of the derivative boundary condition and two nodal values of the PDE. For example, in

the case of $(3,3)$, we form $\widehat{e} = \mathcal{K}_x \widehat{w}_x + \mathcal{K}_y \widehat{w}_y$ as

$$\begin{pmatrix} \dfrac{\partial u(\mathbf{x}_2)}{\partial x} \\ \dfrac{\partial u(\mathbf{x}_3)}{\partial x} \\ \dfrac{\partial u(\mathbf{x}_6)}{\partial y} \\ \dfrac{\partial u(\mathbf{x}_{11})}{\partial y} \\ f(\mathbf{x}_{14}) \\ f(\mathbf{x}_{18}) \end{pmatrix} = \begin{bmatrix} \mathcal{H}_x^{(1)}(2,:), & \mathcal{O} \\ \mathcal{H}_x^{(1)}(3,:), & \mathcal{O} \\ \mathcal{O}, & \mathcal{H}_y^{(1)}(6,:) \\ \mathcal{O}, & \mathcal{H}_y^{(1)}(11,:) \\ G_x(14,:), & G_y(14,:) \\ G_x(18,:), & G_y(18,:) \end{bmatrix} \begin{pmatrix} \widehat{w}_x \\ \widehat{w}_y \end{pmatrix}. \tag{2.39}$$

4. For stencils whose central points are $(i = 3,\ 3 < j < N_y - 2)$, $(i = N_x - 2,\ 3 < j < N_y - 2)$, $(3 < i < N_x - 2,\ j = 3)$ and $(3 < i < N_x - 2,\ j = N_y - 2)$, the extra information vector is comprised of one nodal value of the derivative boundary condition and three nodal values of the PDE. For example, in the case of $(i = 3,\ 3 < j < N_y - 2)$, we form $\widehat{e} = \mathcal{K}_x \widehat{w}_x + \mathcal{K}_y \widehat{w}_y$ as

$$\begin{pmatrix} \dfrac{\partial u(\mathbf{x}_3)}{\partial x} \\ f(\mathbf{x}_{12}) \\ f(\mathbf{x}_{14}) \\ f(\mathbf{x}_{18}) \end{pmatrix} = \begin{bmatrix} \mathcal{H}_x^{(1)}(3,:), & \mathcal{O} \\ G_x(12,:), & G_y(12,:) \\ G_x(14,:), & G_y(14,:) \\ G_x(18,:), & G_y(18,:) \end{bmatrix} \begin{pmatrix} \widehat{w}_x \\ \widehat{w}_y \end{pmatrix}. \tag{2.40}$$

Both Implementation 1 and Implementation 2 lead to a final system matrix of dimensions $(N_x - 2)(N_y - 2) \times (N_x - 2)(N_y - 2)$. The sparsity of the final system is 93.64% with the given grid of 21×21.

2.4.2 Compact local 13-node stencil (13-node CLS)

Figure 2.3 shows a schematic outline of a compact local 13-node stencil. The construction of the final system matrix using **13-node CLS** is similar to that with **5×5-node CLS**. Since the present stencil involves 13 nodes rather than 25 nodes, a sparsity level of the system matrix increases (96.52% with the given grid of 21×21) and its solution is thus more efficient. However, one can expect that **13-node CLS** is less accurate than **5×5-node CLS**.

2.4.3 Compact local 3×3-node stencil (3×3-node CLS)

A **3×3-node CLS** is constructed through a coupled set of two Poisson equations

$$\frac{\partial^2 \nu}{\partial x^2} + \frac{\partial^2 \nu}{\partial y^2} = f(x,y), \tag{2.41}$$

$$\frac{\partial^2 u}{\partial x^2} + \frac{\partial^2 u}{\partial y^2} = \nu, \tag{2.42}$$

which represents the biharmonic equation (2.34).

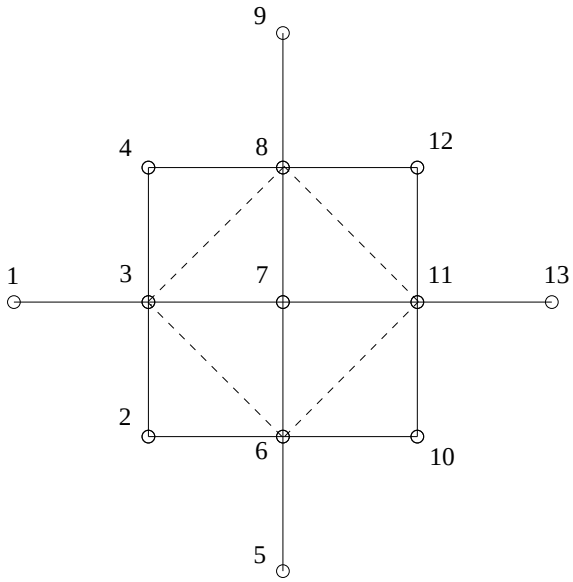

Figure 2.3 A schematic representation of the proposed 13-node stencil associated with node (i, j). Over the stencil, nodes are locally numbered for bottom to top and left to right, where $7 \equiv (i, j)$. Nodal values of the governing equation used as extra information are placed on a diamond shape.

Consider a grid node (i, j) $(2 \leq i \leq N_x - 1, 2 \leq j \leq N_y - 1)$ and its associated 3×3-node stencil $\begin{bmatrix} \mathbf{x}_3 & \mathbf{x}_6 & \mathbf{x}_9 \\ \mathbf{x}_2 & \mathbf{x}_5 & \mathbf{x}_8 \\ \mathbf{x}_1 & \mathbf{x}_4 & \mathbf{x}_7 \end{bmatrix}$ $((i, j) \equiv \mathbf{x}_5)$.

Discretisation of equation (2.41)

Over a 3×3-node stencil, we construct the conversion system as

$$\begin{pmatrix} \widehat{\nu} \\ \widehat{0} \\ \widehat{e}^{[\nu]} \end{pmatrix} = \underbrace{\begin{bmatrix} \mathcal{H}_x^{(0)}, & \mathcal{O} \\ \mathcal{H}_x^{(0)}, & -\mathcal{H}_y^{(0)} \\ \mathcal{K}_x^{[\nu]}, & \mathcal{K}_y^{[\nu]} \end{bmatrix}}_{\mathcal{C}^{[\nu]}} \begin{pmatrix} \widehat{w}_x^{[\nu]} \\ \widehat{w}_y^{[\nu]} \end{pmatrix}, \tag{2.43}$$

where $\widehat{\nu}$ and $\widehat{0}$ are vectors of length 9, $(\widehat{w}_x^{[\nu]}, \widehat{w}_y^{[\nu]})^T$ is the vector of length 30, $\mathcal{H}_x^{(0)}, \mathcal{H}_y^{(0)}$ are the matrices of dimensions 9×15, and equations $\widehat{e}^{[\nu]} = \mathcal{K}_x^{[\nu]} \widehat{w}_x^{[\nu]} + \mathcal{K}_y^{[\nu]} \widehat{w}_y^{[\nu]}$ can be used to represent extra information. Like **3-node CLS** for 1D problems, we study here two cases of $\widehat{e}^{[\nu]}$. For the first case, the vector $\widehat{e}^{[\nu]}$ is used to represent nodal values of the governing equation at the four nodes $\mathbf{x}_1$, $\mathbf{x}_3$, $\mathbf{x}_7$ and $\mathbf{x}_9$. Hereafter, this stencil is referred to as **3×3-node CLS with GE**. For the second case, the vector $\widehat{e}^{[\nu]}$ is set to null. Hereafter, this stencil is referred to as **3×3-node CLS without GE**.

A mapping from the physical space into the RBF-coefficient space is obtained by

solving (2.43)

$$\begin{pmatrix} \widehat{w}_x^{[\nu]} \\ \widehat{w}_y^{[\nu]} \end{pmatrix} = (\mathcal{C}^{[\nu]})^{-1} \begin{pmatrix} \widehat{\nu} \\ \widehat{0} \\ \widehat{e}^{[\nu]} \end{pmatrix}. \tag{2.44}$$

Making use of (2.44), one can express the PDE (2.41) at the central point of the stencil as

$$\underbrace{\left[\mathcal{H}_x^{(2)}(5,:), \quad \mathcal{H}_y^{(2)}(5,:) \right] \left(\mathcal{C}^{[\nu]}\right)^{-1}}_{\mathcal{D}^{[\nu]}} \begin{pmatrix} \widehat{\nu} \\ \widehat{0} \\ \widehat{e}^{[\nu]} \end{pmatrix} = f(\mathbf{x}_5). \tag{2.45}$$

It can reduce to

$$\mathcal{D}_1^{[\nu]} \widehat{\nu} + \mathcal{D}_2^{[\nu]} \widehat{e}^{[\nu]} = f(\mathbf{x}_5), \tag{2.46}$$

where $\mathcal{D}_1^{[\nu]}$ and $\mathcal{D}_2^{[\nu]}$ are the first 9 entries and the last 4 entries of $\mathcal{D}^{[\nu]}$, respectively. In (2.46), $\mathcal{D}_2^{[\nu]} \widehat{e}_\nu$ and $f(\mathbf{x}_5)$ are known values.

Discretisation of equation (2.42)

Unlike equation (2.41), we consider nodal values of the field variable at grid nodes, $\partial u/\partial x$ at $\mathbf{x}_2$ and $\mathbf{x}_8$, and $\partial u/\partial y$ at $\mathbf{x}_4$ and $\mathbf{x}_6$ as unknowns in the discretisation of (2.42).

The conversion matrix is thus formed as

$$\begin{pmatrix} \widehat{u} \\ \widehat{0} \\ \widehat{\partial u_x} \\ \widehat{\partial u_y} \end{pmatrix} = \underbrace{\begin{bmatrix} \mathcal{H}_x^{(0)}, & \mathcal{O} \\ \mathcal{H}_x^{(0)}, & -\mathcal{H}_y^{(0)} \\ \mathcal{H}_x^{(1)}([2,8],:), & \mathcal{O} \\ \mathcal{O}, & \mathcal{H}_y^{(1)}([4,6],:) \end{bmatrix}}_{\mathcal{C}^{[u]}} \begin{pmatrix} \widehat{w}_x^{[u]} \\ \widehat{w}_y^{[u]} \end{pmatrix}, \tag{2.47}$$

where $\widehat{\partial u_x} = (\partial u(\mathbf{x}_2)/\partial x, \partial u(\mathbf{x}_8)/\partial x)^T$ and $\widehat{\partial u_y} = (\partial u(\mathbf{x}_4)/\partial y, \partial u(\mathbf{x}_6)/\partial y)^T$. It is noted that the present additional unknowns $\widehat{\partial u_x}$ and $\widehat{\partial u_y}$ are defined and located in the same way as in the FDM work (Stephenson, 1984).

Solving (2.47) results in

$$\begin{pmatrix} \widehat{w}_x^{[u]} \\ \widehat{w}_y^{[u]} \end{pmatrix} = \left(\mathcal{C}^{[u]}\right)^{-1} \begin{pmatrix} \widehat{u} \\ \widehat{0} \\ \widehat{\partial u_x} \\ \widehat{\partial u_y} \end{pmatrix}. \tag{2.48}$$

Equation (2.48) can be split into

$$\widehat{w}_x^{[u]} = \left(\mathcal{C}_x^{[u]}\right)^{-1} \left(\widehat{u}, \quad \widehat{0}, \quad \widehat{\partial u_x}, \quad \widehat{\partial u_y} \right)^T, \tag{2.49}$$

$$\widehat{w}_y^{[u]} = \left(\mathcal{C}_y^{[u]}\right)^{-1} \left(\widehat{u}, \quad \widehat{0}, \quad \widehat{\partial u_x}, \quad \widehat{\partial u_y} \right)^T, \tag{2.50}$$

where $(\mathcal{C}_x^{[u]})^{-1}$ and $(\mathcal{C}_y^{[u]})^{-1}$ are the first and the last 15 rows of $(\mathcal{C}^{[u]})^{-1}$.

Through (2.49) and (2.50), the first derivatives of u at the central point of the stencil can be computed by

$$\frac{\partial u(\mathbf{x}_5)}{\partial x} = \mathcal{H}_x^{(1)}(5,:)\left(\mathcal{C}_x^{[u]}\right)^{-1}\begin{pmatrix}\widehat{u}\\ \widehat{0}\\ \widehat{\partial u_x}\\ \widehat{\partial u_y}\end{pmatrix}, \tag{2.51}$$

$$\frac{\partial u(\mathbf{x}_5)}{\partial y} = \mathcal{H}_y^{(1)}(5,:)\left(\mathcal{C}_y^{[u]}\right)^{-1}\begin{pmatrix}\widehat{u}\\ \widehat{0}\\ \widehat{\partial u_x}\\ \widehat{\partial u_y}\end{pmatrix}. \tag{2.52}$$

Through (2.48), the discrete form of equation (2.42) over the stencil can be written as

$$\underbrace{\begin{bmatrix}\mathcal{H}_x^{(2)}, & \mathcal{H}_y^{(2)}\end{bmatrix}\left(\mathcal{C}^{[u]}\right)^{-1}}_{\mathcal{D}^{[u]}}\begin{pmatrix}\widehat{u}\\ \widehat{0}\\ \widehat{\partial u_x}\\ \widehat{\partial u_y}\end{pmatrix} = \widehat{\nu}. \tag{2.53}$$

Substitution of (2.53) into (2.46) leads to a discrete form of the biharmonic equation (2.34) at the central point of the stencil

$$\mathcal{D}_1^{[\nu]}\mathcal{D}^{[u]}\begin{pmatrix}\widehat{u}\\ \widehat{0}\\ \widehat{\partial u_x}\\ \widehat{\partial u_y}\end{pmatrix} = f(\mathbf{x}_5) - \mathcal{D}_2^{[\nu]}\widehat{f}_k. \tag{2.54}$$

By applying (2.51), (2.52) and (2.54) at every interior node, we will obtain the final system matrix of dimensions $3(N_x-2)(N_y-2)\times 3(N_x-2)(N_y-2)$. The sparsity of the final system is 97.80% with the given grid of 21×21.

It can be seen that the proposed compact local IRBF stencil does not require the calculation of cross derivatives explicitly. Furthermore, there is no need to derive a computational boundary condition for the intermediate variable ν. When applying the proposed **3×3-node CLS** to fluid flow problems, the variables u and ν are replaced with the streamfunction and the vorticity variables, respectively.

2.5 Numerical examples

The accuracy of the solution is measured using the relative discrete L_2 norm

$$Ne(u) = \frac{\sqrt{\sum_{i=1}^{N}(u_i - u_i^e)^2}}{\sqrt{\sum_{i=1}^{N}(u_i^e)^2}}, \tag{2.55}$$

where N is the number of collocation nodes, and u_i and u_i^e are the computed and exact solutions, respectively.

We will study the behavior of the solution u with respect to (i) the grid size h, and (ii) the MQ width β.

2.5.1 One-dimensional problem

Consider the following fourth-order ODE

$$\frac{d^4u}{dx^4} + \frac{d^2u}{dx^2} = 16\pi^4 \sinh(2\pi x) + 4\pi^2 \sinh(2\pi x), \quad 0 \leq x \leq 2. \tag{2.56}$$

Double boundary conditions are defined as $u = 0$ and $du/dx = 2\pi$ at $x = 0$, and $u = 0$ and $du/dx = 2\pi \cosh(4\pi)$ at $x = 2$. The exact solution to this problem can be verified to be $u^e(x) = \sinh(2\pi x)$.

We employ **5-node CLS** and **3-node CLS** without and with GE to discretise (2.56). To assess the performance of the proposed stencils, the standard local 5-node IRBF stencil is also implemented. We conduct the calculations with several uniform grids, $\{7, 9, \cdots, 37\}$.

Figure 2.4 displays the solution accuracy and the matrix condition numbers against the grid size h. In terms of accuracy (Figure 2.4a), the solution converges apparently as $O(h^{1.40})$ for local 5-node stencil, and $O(h^{5.45})$, $O(h^{3.96})$ and $O(h^{4.16})$ for **5-node CLS** and **3-node CLS** without and with GE, respectively. The compact forms, even for the case of 3-nodes, thus outperform the standard form of 5 nodes as indicated by not only the error norm but also the convergence rate. It can be also seen that **3-node CLS with GE** is more accurate than that without GE. In terms of the matrix condition number (Figure 2.4b), the **5-node CLS** and the standard 5-node stencil yield similar values. It can be also seen that the inclusion of first derivatives in the IRBF approximations, i.e **3-node CLSs**, leads to higher condition numbers of the system matrix.

Figure 2.5a shows a comparison of the accuracy between Implementation 1 and Implementation 2 for the case of **5-node CLS**, indicating that both implementations give similar levels of accuracy. However, Figure 2.5b shows that Implementation 2 yields better condition numbers than Implementation 1, probably owing to the fact that the final system matrix of the former is composed of equations derived from the ODE only.

As mentioned earlier, the value of β would have a strong influence on the solution accuracy. Since the exact solution to this problem is available, it is straightforward to obtain the optimal value of β (i.e. at which $Ne(u)$ is minimum). Table 2.1 shows results obtained by a fixed value and the optimal value of β for three different grids. It can be seen that using the optimal value of β significantly enhances the solution accuracy.

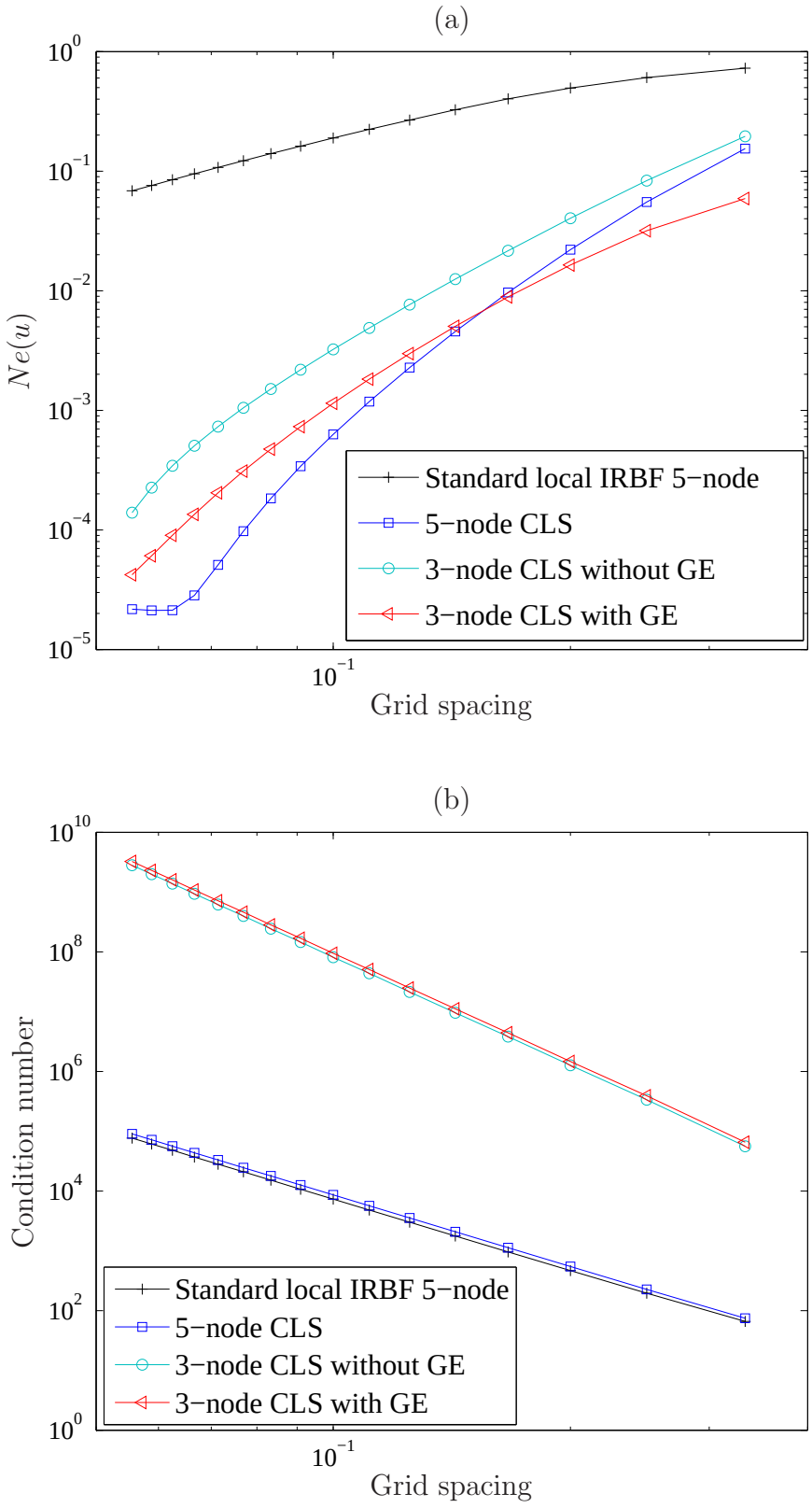

Figure 2.4 ODE: Relative L_2 errors of the solution u and condition numbers of the system matrix against the grid size by the proposed stencils and the standard local IRBF one. It is noted that we employ $\beta = 24$ for local and compact local 5-node stencils, $\beta = 34$ for **3-node CLS without GE**, and $\beta = 5.6$ for **3-node CLS with GE**.

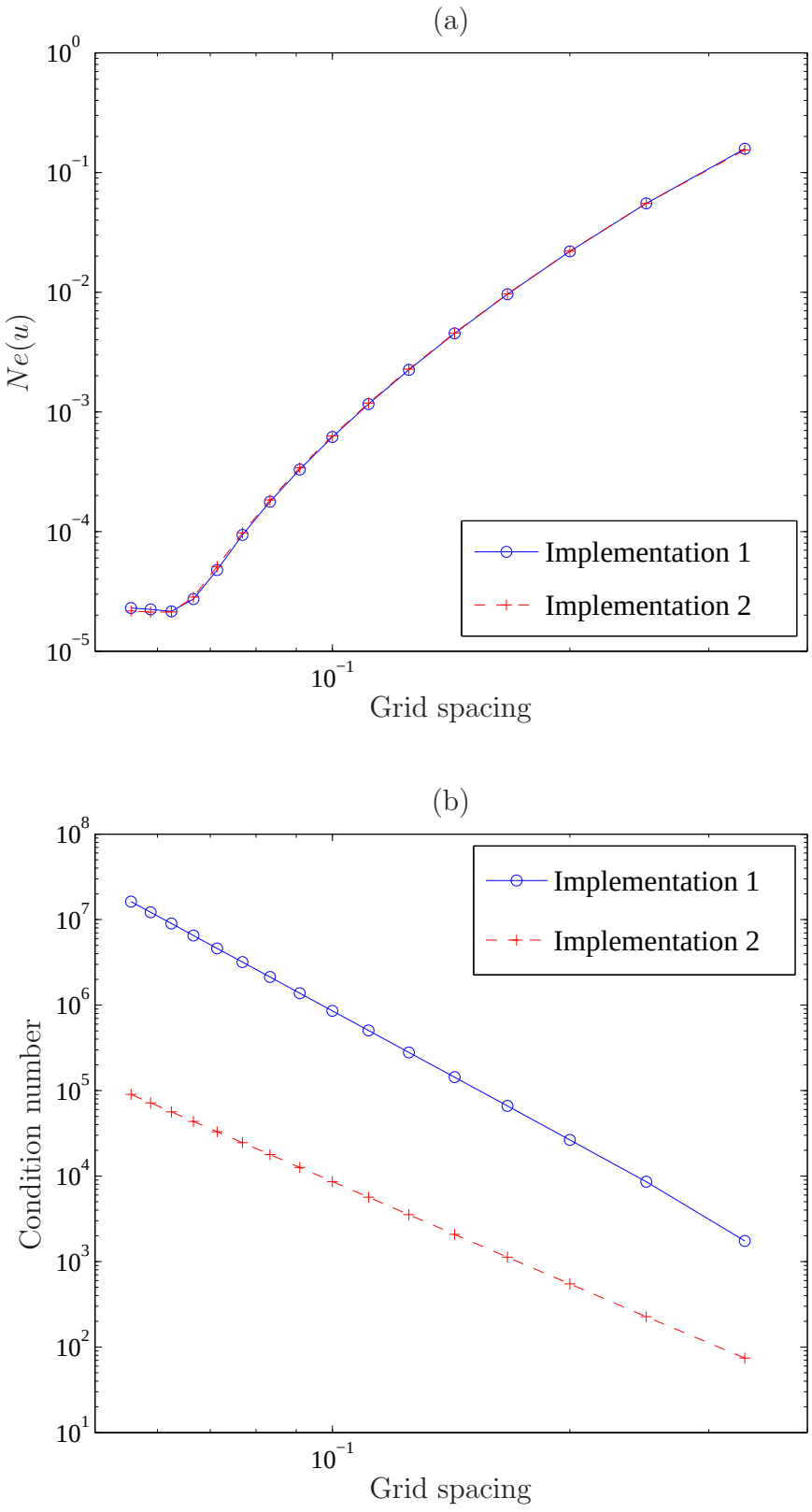

Figure 2.5 ODE, **5-node CLS**, $\beta = 24$: The solution accuracy and matrix condition number against the grid size by Implementation 1 and Implementation 2.

Table 2.1 ODE, **5-node CLS**, **3-node CLS with GE** and **3-node CLS without GE**: Relative L_2 errors of the solution u using some fixed and the optimal values of β for three grids.

	5-node CLS			**3-node CLS**					
				Without GE			With GE		
h	Fixed β=24	Optimal β		Fixed β=77	Optimal β		Fixed β=10	Optimal β	
	$Ne(u)$	β	$Ne(u)$	$Ne(u)$	β	$Ne(u)$	$Ne(u)$	β	$Ne(u)$
1/20	6.30E-4	1.2	4.04E-4	3.46E-3	6	9.50E-4	1.60E-3	2.6	2.10E-4
1/50	1.59E-5	29.5	7.18E-6	5.85E-5	57	2.17E-5	2.31E-5	7	1.06E-5
1/70	6.39E-6	30.3	3.93E-7	8.22E-6	77	8.22E-6	2.97E-6	10	2.97E-6
	$O(h^{4.21})$			$O(h^{4.27})$			$O(h^{4.30})$		

2.5.2 Two-dimensional problems

Example 1

Consider the biharmonic problem with the source function as follow.

$$f(x,y) = 64\pi^4 \sin(2\pi x)\sin(2\pi y) \tag{2.57}$$

The domain of interest as $0 \leq x, y \leq 1$ and boundary conditions of the Dirichlet type. The exact solution is $u^e(x,y) = \sin(2\pi x)\sin(2\pi y)$.

Figure 2.6 shows the behaviour of the solution u using the proposed **13-node CLS** ($\beta = 18$) with respect to the grid size h. Results obtained by the FD 13-node stencil are also included for comparison purposes.

The IRBF method (Implementation 2) is much more accurate and converges much faster than the FDM (Figure 2.6a). The rate of convergence is 4.90 for the former and 1.99 for the latter. On the other hand, the IRBF matrix has higher condition numbers but grows slightly slower than the FD matrix (Figure 2.6b). The rate of growth is 3.25 for the former and 3.97 for the latter. Figure 2.7 indicates that Implementation 2 slightly outperforms Implementation 1 in terms of the matrix condition and accuracy. However, an improvement in the matrix condition here is not as significant as in the case of 1D problems.

Table 2.2 presents results by the proposed **5×5-node CLS** for a fixed value and the optimal value of β. It can be seen that the MQ width has more influence on the solution accuracy than on the system matrix condition number. It is noted that a chosen fixed value $\beta = 2.5$ is the optimal value for the grid with $h = 1/50$.

Table 2.2 PDE, Example 1, **5×5-node CLS**: Condition numbers of the system matrix A and relative L_2 errors of the solution u using a fixed value and the optimal value of β for several grids.

	Fixed $\beta = 2.5$		Optimal β		
h	Cond(A)	$Ne(u)$	β	Cond(A)	$Ne(u)$
1/10	6.15E+2	1.54E-3	1	6.12E+2	1.44E-3
1/20	9.52E+3	1.65E-4	6.2	1.21E+4	7.59E-5
1/30	4.79E+4	8.24E-5	6.4	5.54E+4	1.34E-5
1/40	1.51E+5	4.41E-5	5	1.85E+5	1.35E-5
1/50	3.69E+5	6.47E-6	2.5	3.69E+5	6.47E-6
		$O(h^{3.04})$			$O(h^{3.34})$

Table 2.3 shows the accuracy and matrix condition number against the grid size by the proposed **3×3-node CLS** without and with GE. The solution converges as $O(h^{3.36})$ for the former and $O(h^{3.88})$ for the latter. It can be seen that the incorporation of nodal values of the governing equation into the approximations results in an accuracy improvement.

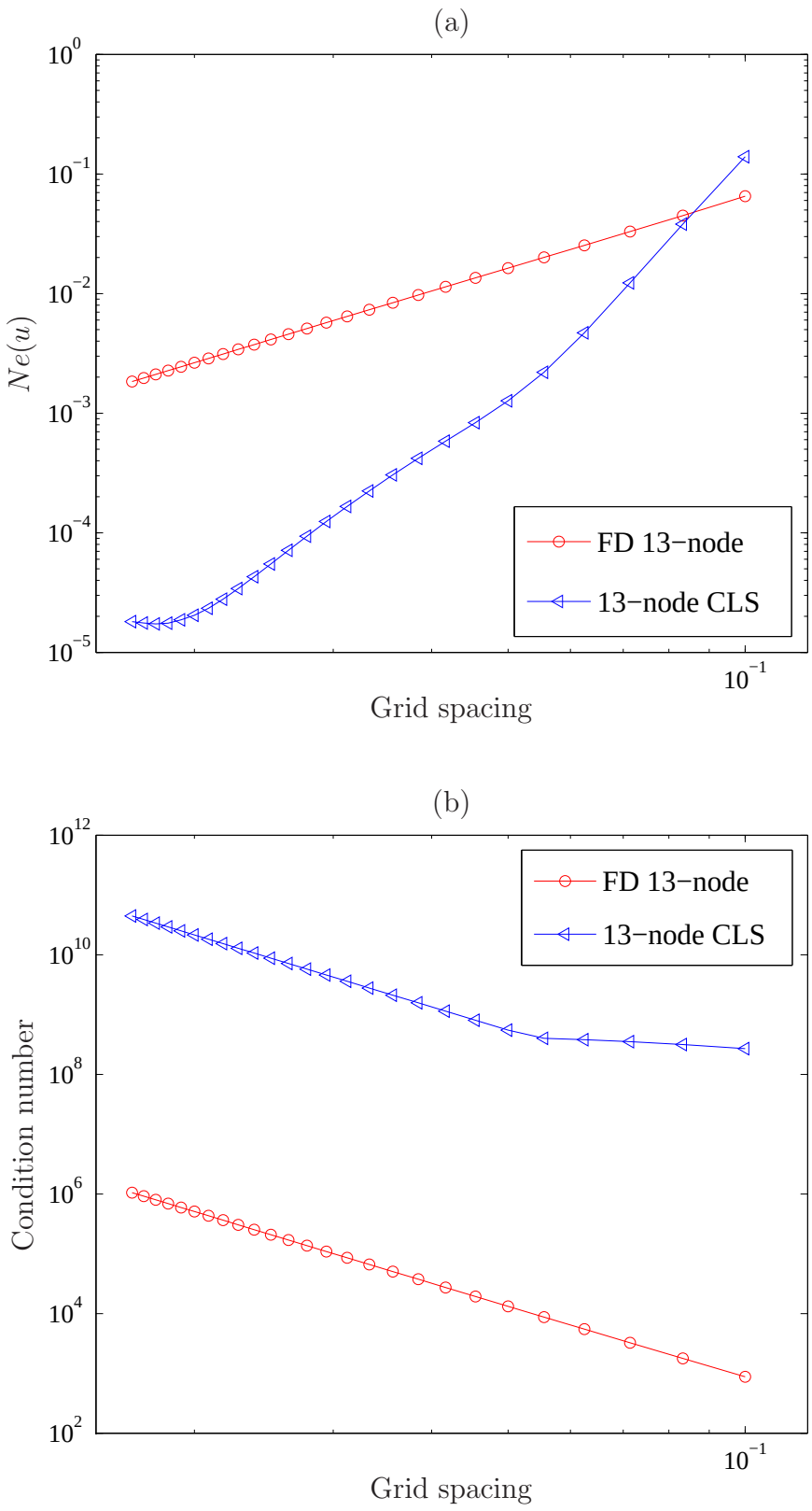

Figure 2.6 PDE , Example 1, **13-node CLS**, $\beta = 18$: The solution accuracy and matrix condition number against the grid size. Results by the FD 13-node stencil are also included.

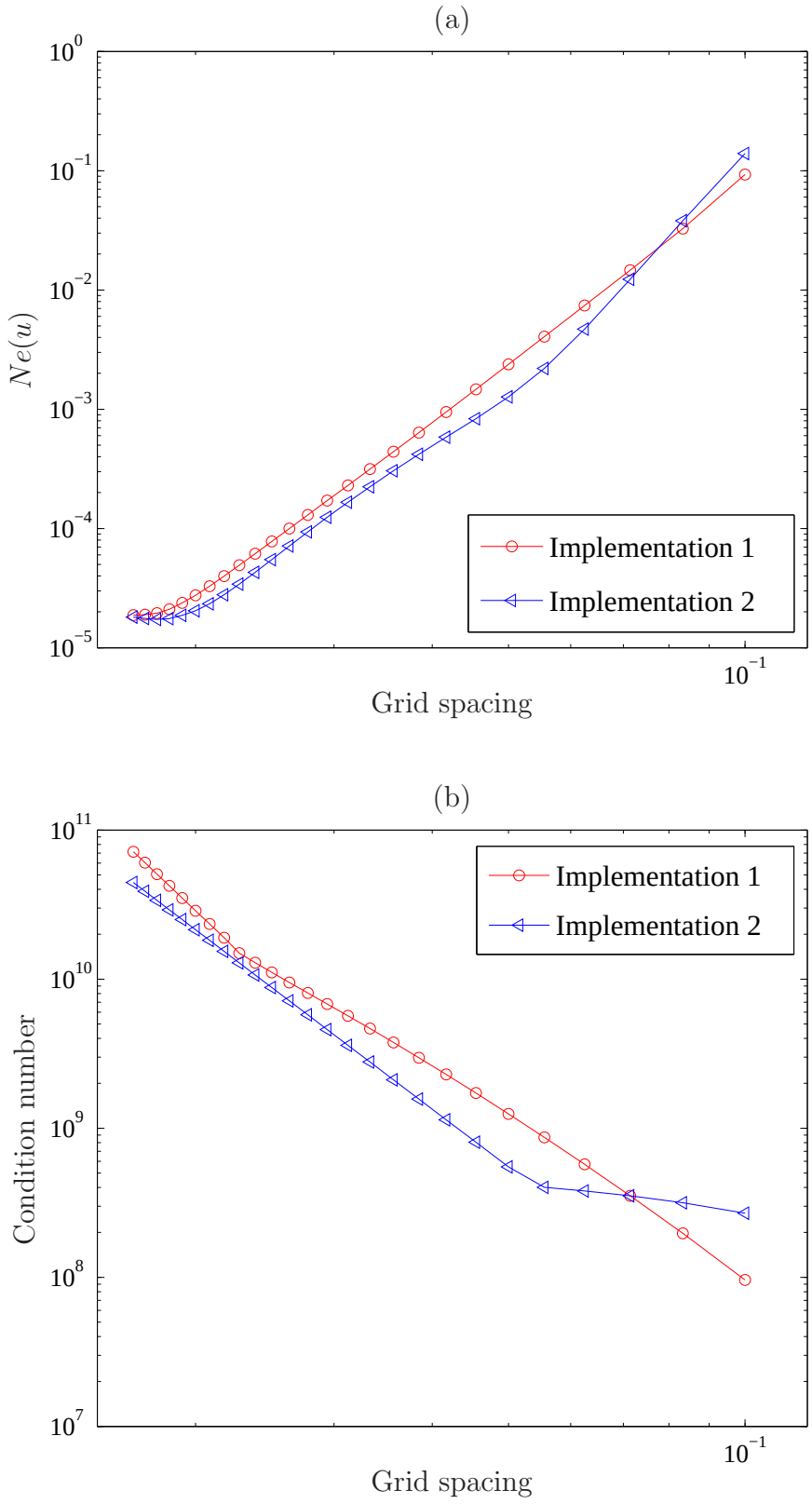

Figure 2.7 PDE, Example 1, **13-node CLS**, $\beta = 18$: The solution accuracy and matrix condition number against the grid size by Implementation 1 and Implementation 2.

Table 2.3 PDE, Example 1, **3×3-node CLS**: relative L_2 errors of the solution u for several grids.

h	Without GE, $\beta = 14.5$	With GE, $\beta = 16.6$
1/10	1.71E-02	1.29E-02
1/20	3.70E-03	3.43E-03
1/30	1.29E-03	1.23E-03
1/40	4.32E-04	4.05E-04
1/50	4.35E-05	8.13E-06
	$O(h^{3.36})$	$O(h^{3.88})$

Example 2

Among our proposed compact stencils, the **3×3-node CLS** does not require special treatments for interior nodes close to the boundary. This stencil is applied here to obtain the structure of the steady-state lid-driven cavity flow in the streamfunction-vorticity formulation

$$\frac{\partial\psi}{\partial y}\frac{\partial\omega}{\partial x} - \frac{\partial\psi}{\partial x}\frac{\partial\omega}{\partial y} = \frac{1}{\mathrm{Re}}\left(\frac{\partial^2\omega}{\partial x^2} + \frac{\partial^2\omega}{\partial y^2}\right), \tag{2.58}$$

$$-\omega = \frac{\partial^2\psi}{\partial x^2} + \frac{\partial^2\psi}{\partial y^2}, \tag{2.59}$$

where Re is the Reynolds number, ψ is the streamfunction and ω is the vorticity. One can compute the $x-$ and $y-$ velocity components according to the following definitions

$$v_x = \frac{\partial\psi}{\partial y} \text{ and } v_y = -\frac{\partial\psi}{\partial x}.$$

The boundary conditions are prescribed in terms of the streamfunction as

$$\psi = 0, \quad \frac{\partial\psi}{\partial x} = 0 \quad \text{at x=0 and x=1,} \tag{2.60}$$

$$\psi = 0, \quad \frac{\partial\psi}{\partial y} = 0 \quad \text{at y=0,} \tag{2.61}$$

$$\psi = 0, \quad \frac{\partial\psi}{\partial y} = 1 \quad \text{at y=1.} \tag{2.62}$$

We employ several grids, $(21\times 21, 31\times 31, \cdots, 111\times 111)$, in the simulation of the flow. A wide range of Re, $(0, 100, 400, 1000, 3200, 5000)$, is considered and the resultant nonlinear set of algebraic equations is solved using the Picard iteration scheme

$$\widehat{\zeta} = \theta\widehat{\zeta}^{(k)} + (1-\theta)\widehat{\zeta}^{(k-1)}, \tag{2.63}$$

where the superscript (k) is used to indicate the current iteration, θ is the relaxation factor $(0 < \theta \leq 1)$ and $\widehat{\zeta} = (\widehat{\psi}, \dfrac{\widehat{\partial\psi}}{\partial x}, \dfrac{\widehat{\partial\psi}}{\partial y})^T$.

The flow is considered to reach a steady state when

$$\frac{\sqrt{\sum\left(\widehat{\zeta}^{(k)}-\widehat{\zeta}^{(k-1)}\right)^2}}{\sqrt{\sum\left(\widehat{\zeta}^{(k)}\right)^2}}<10^{-9}. \tag{2.64}$$

As shown in Section 2.4.3, the proposed formulation does not require the derivation of a computational boundary condition for the vorticity and nodal values of the velocity components are obtained directly from solving the final system.

The value of β is chosen to be 20 for all simulations, while the value of θ is employed in the range of 0.8 to 10^{-5}. The higher the value of Re the smaller the value of θ will be.

The profile of the $x-$component of the velocity vector along the vertical centreline and of the $y-$component along the horizontal centreline for $Re = 1000$ using several grids are demonstrated in Figure 2.8 and Figure 2.9, respectively. To provide the base for assessment, results obtained by the multi-grid FDM (Ghia et al., 1982), which are widely cited in the literature, are included. It can be seen that a convergence with grid refinement is obtained for both velocity profiles.

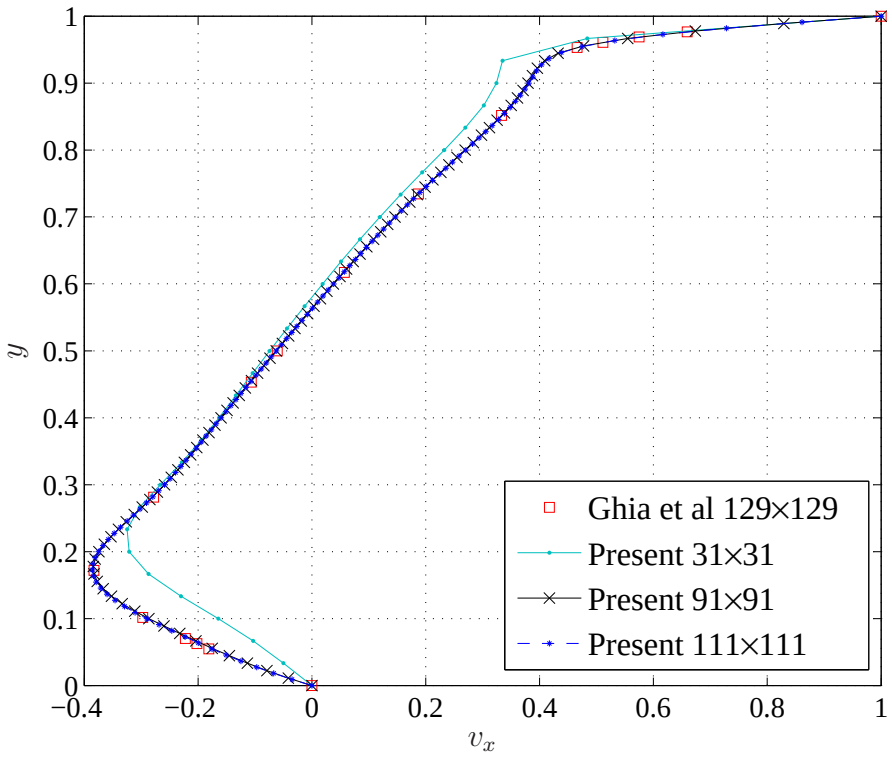

Figure 2.8 PDE, Example 2, $Re = 1000$: Profiles of the $x-$component of the velocity vector along the vertical centerline for several grids. Results by the FDM (Ghia et al., 1982) are also included.

Tables 2.4 and 2.5 give a comparison of the extreme values of the velocity profile on the centrelines obtained by the proposed method, FDM (Ghia et al., 1982),

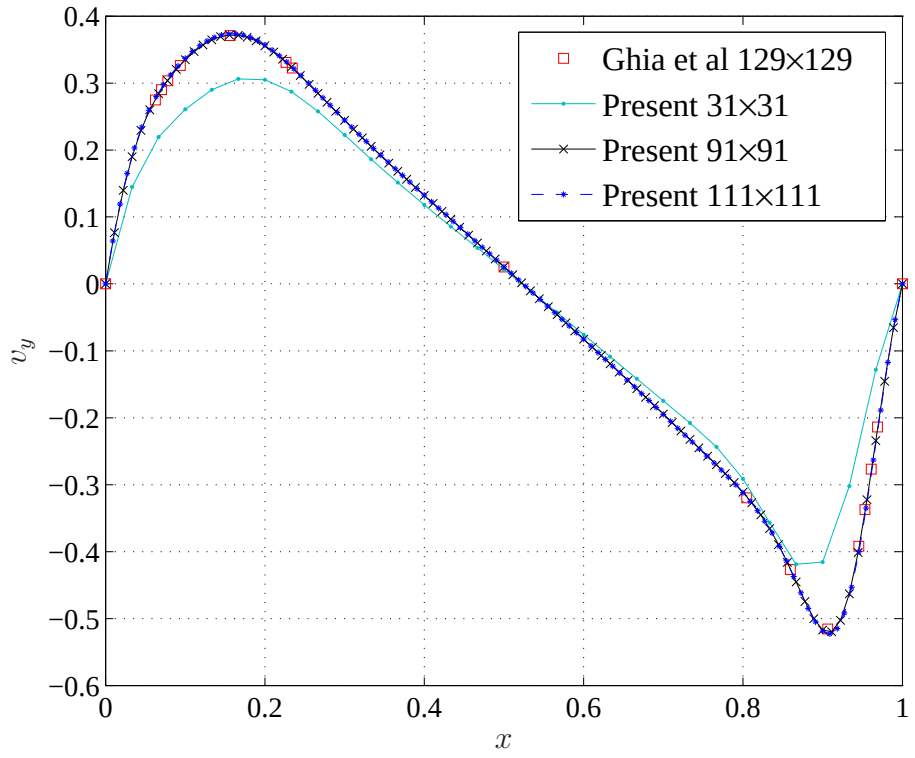

Figure 2.9 PDE, Example 2, $Re = 1000$: Profiles of the $y-$component of the velocity vector along the horizontal centerline for several grids. Results by the FDM (Ghia et al., 1982) are also included.

FVM (Deng et al., 1994) and the pseudo-spectral method (Botella and Peyret, 1998). It can be seen that the present results are in better agreement with the benchmark spectral solution than the others even for 'coarse' grids, e.g. 51×51 in the case of $Re = 100$ and 91×91 in the case of $Re = 1000$.

Table 2.4 PDE, Example 2, $Re = 100$, $\beta = 20$: Extreme values of the velocity profiles on the centerlines by the proposed method and several other methods. It is noted that N is the polynomial degree.

Reference	Grid	$v_{x\ max}$	$v_{y\ max}$	$v_{y\ min}$
Present	31×31	0.21252	0.17675	-0.24908
Present	51×51	0.21354	0.17863	-0.25221
Present	71×71	0.21378	0.17910	-0.25302
Present	91×91	0.21386	0.17928	-0.25334
Present	111×111	0.21390	0.17937	-0.25350
FVM	64×64	0.21315	0.17896	-0.25339
FDM	129×129	0.21090	0.17527	-0.24533
Pseudo-spectral	$N = 96$	0.21404	0.17957	-0.25380

FVM, FDM and Pseudo-spectral refer to finite volume, finite difference and pseudo-spectral methods results in (Deng et al., 1994), (Ghia et al., 1982), and (Botella and Peyret, 1998), respectively.

Table 2.5 PDE, Example 2, $Re = 1000$, $\beta = 20$: Extreme values of the velocity profiles on the centerlines by the proposed method and several other methods. It is noted that N is the polynomial degree.

Reference	Grid	$v_{x\ max}$	$v_{y\ max}$	$v_{y\ min}$
Present	31×31	0.32684	0.30773	-0.42971
Present	51×51	0.37061	0.35703	-0.50010
Present	71×71	0.38056	0.36802	-0.51530
Present	91×91	0.38411	0.37195	-0.52063
Present	111×111	0.38573	0.37376	-0.52305
FVM	128×128	0.38511	0.37369	-0.52280
FDM	129×129	0.38289	0.37095	-0.51550
Pseudo-spectral	$N = 96$	0.3885698	0.3796447	-0.5270771

FVM, FDM and Pseudo-spectral refer to finite volume, finite difference and pseudo-spectral methods results in (Deng et al., 1994), (Ghia et al., 1982), and (Botella and Peyret, 1998), respectively.

Results concerning the distribution of of the streamfunction and vorticity over the flow domain are shown in Figures 2.10 and 2.11, respectively. They look feasible in comparison with those in literature (e.g. (Ghia et al., 1982; Botella and Peyret, 1998; Deng et al., 1994)).

2.6 Concluding remarks

This chapter is concerned with the development of several compact local IRBF stencils for solving fourth-order ODEs and PDEs. The IRBF approximations are expressed in terms of not only nodal values of the field variable but also nodal values of the ODE/PDE and, in some cases, of first derivative(s). The latter is incorporated through the conversion system with the help of the integration constants. In the case of 3×3-node stencil, the resultant discretisation system is constructed through a set of two second-order PDEs, but there is no need to derive a computational boundary condition for the intermediate variable and no requirement for the calculation of cross derivatives explicitly. The proposed stencils are successfully verified using problems with analytic solution, showing that high rates of convergence and high levels of accuracy are obtained. For the lid-driven cavity flow, a convergent solution is obtained for high Re numbers and the obtained results are in very good agreement with the benchmark solutions.

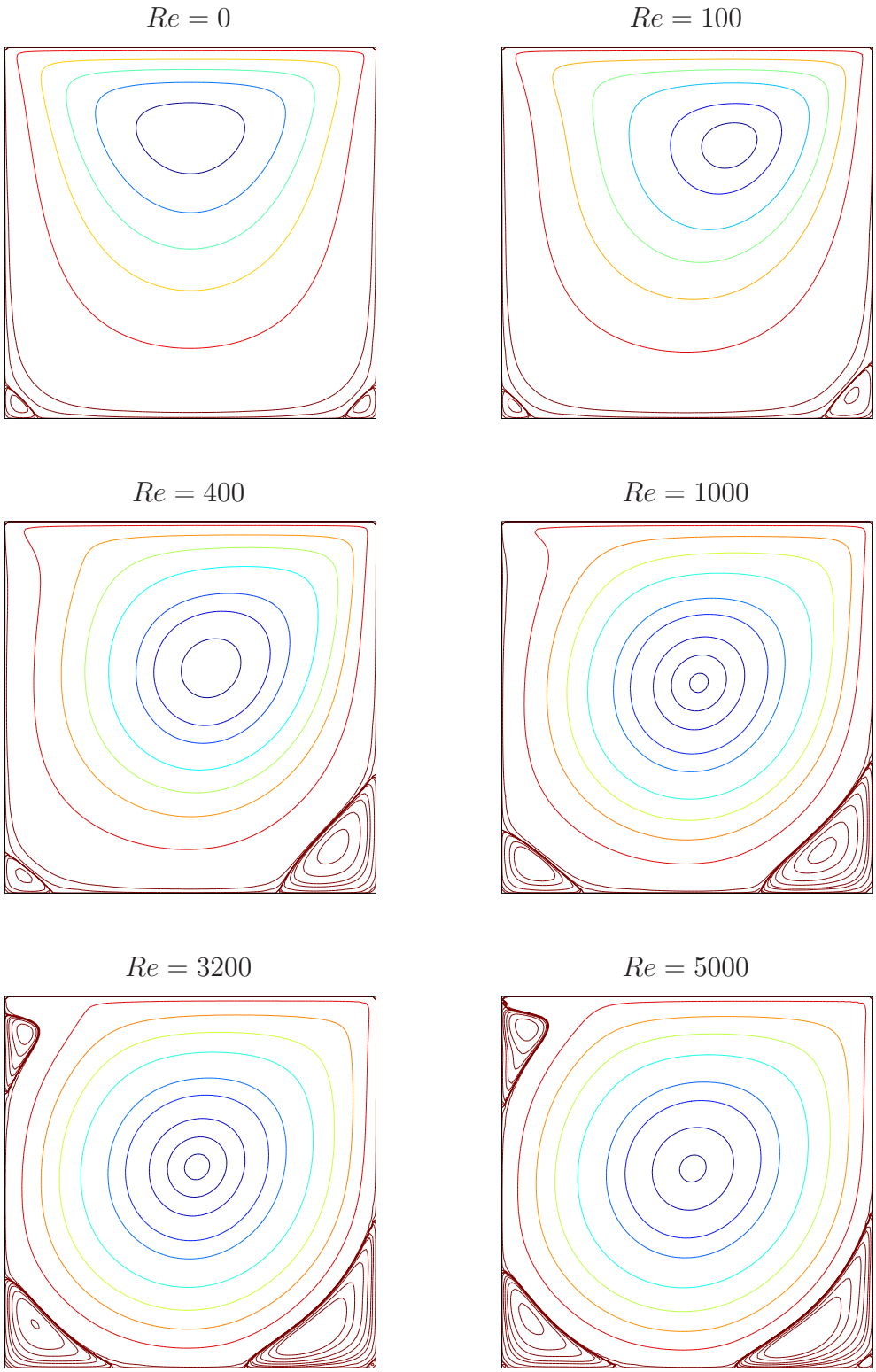

Figure 2.10 PDE, Example 2, **3×3-node CLS**, a grid of 111×111: Streamlines of the flow at several Reynolds numbers. It can be seen that secondary vortices are clearly captured.

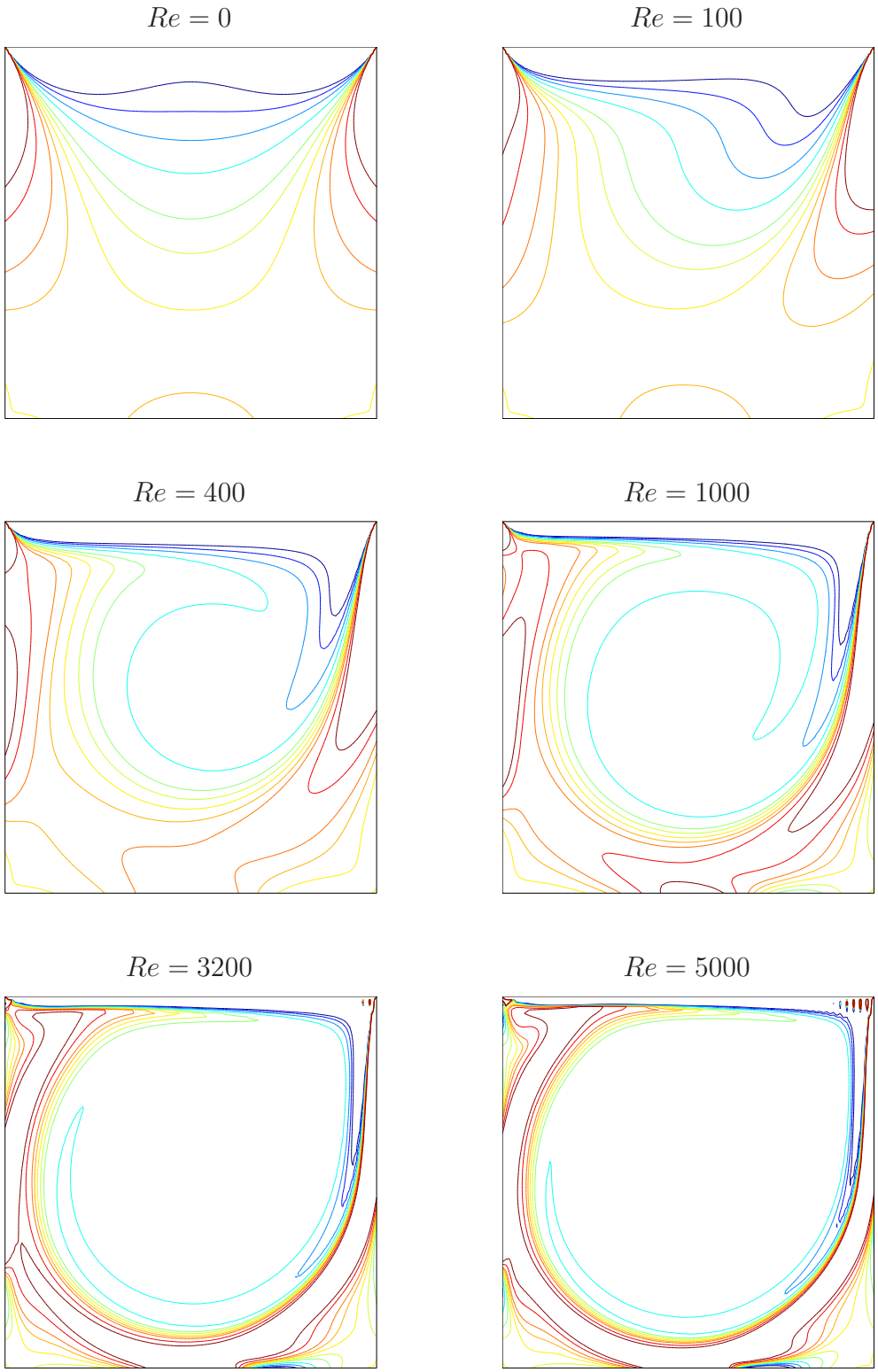

Figure 2.11 PDE, Example 2, **3×3-node CLS**, a grid of 111×111: Iso-vorticity lines of the flow at several Reynolds numbers.

Chapter 3

Compact local IRBF stencils and point collocation for second-order differential problems

In the previous chapter, compact local IRBF stencils were developed for the discretisation of fourth-order ODEs/PDEs. In this chapter, we are interested in second-order PDEs governing fluid flows, namely the convection-diffusion equation and the streamfunction-vorticity formulation. The governing equations are discretised by means of point collocation. We will develop compact RBF approximations based on 3×3 stencils to represent the convection and diffusion terms. Salient features here are that (i) integration is employed to construct local RBF approximations; and (ii) through the constants of integration, values of the convection-diffusion equation at several selected nodes on the stencil are also enforced. Numerical results indicate that (i) the inclusion of the governing equation into the stencil leads to a significant improvement in accuracy; (ii) when the convection dominates, accurate solutions are obtained at a regime of the RBF width which makes the RBFs peaked; and (iii) high levels of accuracy are achieved using relatively coarse grids.

3.1 Introduction

It is known that some RBFs such as the Gaussian and multiquadric basis functions exhibit a spectral accuracy (e.g., (Madych and Nelson, 1990; Madych, 1992; Wendland, 2005)). These RBFs contain a width (shape) parameter. Increasing the RBF width and/or the number of RBFs can lead to an enhancement in the quality of the approximations. On the other hand, the condition number of an interpolation RBF matrix is an increasing function of the RBF width and the number of RBFs. In this sense, at large values of the RBF width and/or the number of RBFs, the severe ill-conditioning of RBF matrices may prevent the method from achieving a high rate of convergence. This relation between numerical stability and error was discussed in (Schaback, 1995) - the so-called uncertainty or trade-off principle. Recently, Fornberg and his co-workers (Fornberg and Wright, 2004; Fornberg et al., 2011) proposed techniques that allow for

a stable calculation of very large values of the RBF width. It was shown that the ill-conditioning problem of the RBF methods can be overcome. It was demonstrated in (Fornberg and Wright, 2004) that the highest accuracy is often found at values of the RBF width that cause the direct (traditional) computation of RBF matrices to suffer from severe ill-conditioning.

In this chapter, compact IRBF 3×3 stencils are developed for the convection-diffusion equation governing heat transfer and fluid flow problems defined on rectangular and non-rectangular domains. The RBF width is chosen as $a = \beta h$, where β is a given number and h is a grid size. Let R be the ratio of the convection to diffusion. When the convection dominates (i.e., large values of R), the solution involves some steep gradients which usually occur near the boundary, and the corresponding computation becomes very challenging. It will be shown later that the optimal value of β is a decreasing function of R. Accurate results for large values of R are obtained at a regime of β that makes RBF peaked (not flat), and one can thus simply apply a direct (traditional) way to compute the corresponding IRBF interpolants.

This chapter is organised as follows. A brief overview of integrated-RBF approximations is given in Section 2. Section 3 describes new compact IRBF 3×3 stencils for the convection-diffusion equation. In Section 4, the method is verified through an analytic example governed by the convection-diffusion equation and two benchmark fluid flow problems (i.e., lid-driven cavity and natural convection flows) governed by the streamfunction-vorticity formulation. Section 5 gives some concluding remarks.

3.2 Integrated-RBF approximations

Consider a function $u(\mathbf{x})$ with $\mathbf{x} = (x, y)^T$. The IRBF expressions representing u and its derivatives are constructed as follows (Mai-Duy and Tran-Cong, 2001, 2003).

In the x direction, the second derivative of u is first decomposed into RBFs

$$\frac{\partial^2 u(\mathbf{x})}{\partial x^2} = \sum_{i=1}^{N} w_i^{[x]} I_{[x]i}^{(2)}(\mathbf{x}), \tag{3.1}$$

where N is the number of RBFs; $\left\{w_i^{[x]}\right\}_{i=1}^{N}$ the set of weights/coefficients; and $\left\{I_{[x]i}^{(2)}(\mathbf{x})\right\}_{i=1}^{N}$ the set of RBFs. Approximations to the first derivative and function are then obtained through integration

$$\frac{\partial u(\mathbf{x})}{\partial x} = \sum_{i=1}^{N} w_i^{[x]} I_{[x]i}^{(1)}(\mathbf{x}) + C_1^{[x]}(y), \tag{3.2}$$

$$u^{[x]}(\mathbf{x}) = \sum_{i=1}^{N} w_i^{[x]} I_{[x]i}^{(0)}(\mathbf{x}) + x C_1^{[x]}(y) + C_2^{[x]}(y), \tag{3.3}$$

where $I^{(1)}_{[x]i}(\mathbf{x}) = \int I^{(2)}_{[x]i}(\mathbf{x})dx$; $I^{(0)}_{[x]i}(\mathbf{x}) = \int I^{(1)}_{[x]i}(\mathbf{x})dx$; and $C^{[x]}_1(y)$ and $C^{[x]}_2(y)$ are the constants of integration which are univariate functions of the variable y. For points that have the same y coordinate, their corresponding integration constants will have the same value.

For the y direction, in the same way, one has

$$\frac{\partial^2 u(\mathbf{x})}{\partial y^2} = \sum_{i=1}^{N} w_i^{[y]} I^{(2)}_{[y]i}(\mathbf{x}), \tag{3.4}$$

$$\frac{\partial u(\mathbf{x})}{\partial y} = \sum_{i=1}^{N} w_i^{[y]} I^{(1)}_{[y]i}(\mathbf{x}) + C^{[y]}_1(x), \tag{3.5}$$

$$u^{[y]}(\mathbf{x}) = \sum_{i=1}^{N} w_i^{[y]} I^{(0)}_{[y]i}(\mathbf{x}) + yC^{[y]}_1(x) + C^{[y]}_2(x). \tag{3.6}$$

It can be seen that there are two approximate values of the function u at point $\mathbf{x}$, namely $u^{[x]}(\mathbf{x})$ and $u^{[y]}(\mathbf{x})$. These two values need be forced to be identical. It is noted that the integration constants are univariate functions and they arise in a natural way.

3.3 Proposed method

The PDE to be solved is of the form

$$\frac{\partial^2 u}{\partial x^2} + \frac{\partial^2 u}{\partial y^2} + p(x,y)\frac{\partial u}{\partial x} + q(x,y)\frac{\partial u}{\partial y} = f(x,y), \tag{3.7}$$

where p, q and f are some given functions. The magnitudes of p and q decide the value of R. We restrict our attention to regions which may be partitioned into rectangular subregions. A Cartesian grid is used to represent the problem domain.

Consider an interior node, $\mathbf{x}_0$. Its associated 3×3 stencil is defined as

$$\begin{bmatrix} \mathbf{x}_3 & \mathbf{x}_6 & \mathbf{x}_9 \\ \mathbf{x}_2 & \mathbf{x}_5 & \mathbf{x}_8 \\ \mathbf{x}_1 & \mathbf{x}_4 & \mathbf{x}_7 \end{bmatrix}$$

where $\mathbf{x}_0 \equiv \mathbf{x}_5$.

We now utilise IRBFs (3.1)-(3.3) and (3.4)-(3.6) to construct compact approximations over this stencil.

In the x direction, collocating (3.1)-(3.3) at all grid nodes on the stencil yields

$$\widehat{\frac{\partial^2 u}{\partial x^2}} = \mathcal{H}^{(2)}_x \widehat{w}_x, \tag{3.8}$$

$$\widehat{\frac{\partial u}{\partial x}} = \mathcal{H}^{(1)}_x \widehat{w}_x, \tag{3.9}$$

$$\widehat{u^{[x]}} = \mathcal{H}^{(0)}_x \widehat{w}_x, \tag{3.10}$$

where $\widehat{u}^{[x]}$ denotes a vector of nodal values of u,

$$\widehat{w}_x = \left(w_1^{[x]}, \cdots, w_9^{[x]}, C_1^{[x]}(y_1), C_1^{[x]}(y_2), C_1^{[x]}(y_3), C_2^{[x]}(y_1), C_2^{[x]}(y_2), C_2^{[x]}(y_3)\right)^T,$$

$$\left(\mathcal{H}_x^{(2)}\right)_{i,j} = I_{[x]j}^{(2)}(\mathbf{x}_i) \quad i,j = (1,\cdots,9); \quad \left(\mathcal{H}_x^{(2)}\right)_{i,j} = 0 \quad i = (1,\cdots,9),\ j = (10,\cdots,15),$$

$$\left(\mathcal{H}_x^{(1)}\right)_{i,j} = I_{[x]j}^{(1)}(\mathbf{x}_i) \quad i,j = (1,\cdots,9); \quad \left(\mathcal{H}_x^{(1)}\right)_{i,j} = 0 \quad i = (1,\cdots,9),\ j = (10,\cdots,15),$$

$$\begin{aligned}
\text{except for} \quad & \left(\mathcal{H}_x^{(1)}\right)_{1,10} = \left(\mathcal{H}_x^{(1)}\right)_{2,11} = \left(\mathcal{H}_x^{(1)}\right)_{3,12} = 1,\\
& \left(\mathcal{H}_x^{(1)}\right)_{4,10} = \left(\mathcal{H}_x^{(1)}\right)_{5,11} = \left(\mathcal{H}_x^{(1)}\right)_{6,12} = 1,\\
& \left(\mathcal{H}_x^{(1)}\right)_{7,10} = \left(\mathcal{H}_x^{(1)}\right)_{8,11} = \left(\mathcal{H}_x^{(1)}\right)_{9,12} = 1,
\end{aligned}$$

$$\left(\mathcal{H}_x^{(0)}\right)_{i,j} = I_{[x]j}^{(0)}(\mathbf{x}_i) \quad i,j = (1,\cdots,9); \quad \left(\mathcal{H}_x^{(0)}\right)_{i,j} = 0 \quad i = (1,\cdots,9),\ j = (10,\cdots,15),$$

$$\begin{aligned}
\text{except for} \quad & \left(\mathcal{H}_x^{(0)}\right)_{1,10} = x_1;\ \left(\mathcal{H}_x^{(0)}\right)_{2,11} = x_2;\ \left(\mathcal{H}_x^{(0)}\right)_{3,12} = x_3,\\
& \left(\mathcal{H}_x^{(0)}\right)_{4,10} = x_4;\ \left(\mathcal{H}_x^{(0)}\right)_{5,11} = x_5;\ \left(\mathcal{H}_x^{(0)}\right)_{6,12} = x_6,\\
& \left(\mathcal{H}_x^{(0)}\right)_{7,10} = x_7;\ \left(\mathcal{H}_x^{(0)}\right)_{8,11} = x_8;\ \left(\mathcal{H}_x^{(0)}\right)_{9,12} = x_9,\\
& \left(\mathcal{H}_x^{(0)}\right)_{1,13} = \left(\mathcal{H}_x^{(0)}\right)_{2,14} = \left(\mathcal{H}_x^{(0)}\right)_{3,15} = 1,\\
& \left(\mathcal{H}_x^{(0)}\right)_{4,13} = \left(\mathcal{H}_x^{(0)}\right)_{5,14} = \left(\mathcal{H}_x^{(0)}\right)_{6,15} = 1,\\
& \left(\mathcal{H}_x^{(0)}\right)_{7,13} = \left(\mathcal{H}_x^{(0)}\right)_{8,14} = \left(\mathcal{H}_x^{(0)}\right)_{9,15} = 1.
\end{aligned}$$

In the y direction, in a similar fashion, one has

$$\widehat{\frac{\partial^2 u}{\partial y^2}} = \mathcal{H}_y^{(2)}\widehat{w}_y, \tag{3.11}$$

$$\widehat{\frac{\partial u}{\partial y}} = \mathcal{H}_y^{(1)}\widehat{w}_y, \tag{3.12}$$

$$\widehat{u}^{[y]} = \mathcal{H}_y^{(0)}\widehat{w}_y, \tag{3.13}$$

where $\widehat{u}^{[y]}$ denotes a vector of nodal values of u,

$$\widehat{w}_y = \left(w_1^{[y]}, \cdots, w_9^{[y]}, C_1^{[y]}(x_1), C_1^{[y]}(x_4), C_1^{[y]}(x_7), C_2^{[y]}(x_1), C_2^{[y]}(x_4), C_2^{[y]}(x_7)\right)^T,$$

$$\left(\mathcal{H}_y^{(2)}\right)_{i,j} = I_{[y]j}^{(2)}(\mathbf{x}_i) \quad i,j = (1,\cdots,9); \quad \left(\mathcal{H}_y^{(2)}\right)_{i,j} = 0 \quad i = (1,\cdots,9),\ j = (10,\cdots,15),$$

$$\left(\mathcal{H}_y^{(1)}\right)_{i,j} = I_{[y]j}^{(1)}(\mathbf{x}_i) \quad i,j = (1,\cdots,9); \quad \left(\mathcal{H}_y^{(1)}\right)_{i,j} = 0 \quad i = (1,\cdots,9),\ j = (10,\cdots,15),$$

$$\begin{aligned} \text{except for} \quad & \left(\mathcal{H}_y^{(1)}\right)_{1,10} = \left(\mathcal{H}_y^{(1)}\right)_{2,10} = \left(\mathcal{H}_y^{(1)}\right)_{3,10} = 1, \\ & \left(\mathcal{H}_y^{(1)}\right)_{4,11} = \left(\mathcal{H}_y^{(1)}\right)_{5,11} = \left(\mathcal{H}_y^{(1)}\right)_{6,11} = 1, \\ & \left(\mathcal{H}_y^{(1)}\right)_{7,12} = \left(\mathcal{H}_y^{(1)}\right)_{8,12} = \left(\mathcal{H}_y^{(1)}\right)_{9,12} = 1, \end{aligned}$$

$$\left(\mathcal{H}_y^{(0)}\right)_{i,j} = I_{[y]j}^{(0)}(\mathbf{x}_i) \quad i,j = (1,\cdots,9); \quad \left(\mathcal{H}_y^{(0)}\right)_{i,j} = 0 \quad i = (1,\cdots,9),\ j = (10,\cdots,15),$$

$$\begin{aligned} \text{except for} \quad & \left(\mathcal{H}_y^{(0)}\right)_{1,10} = y_1;\ \left(\mathcal{H}_y^{(0)}\right)_{2,10} = y_2;\ \left(\mathcal{H}_y^{(0)}\right)_{3,10} = y_3, \\ & \left(\mathcal{H}_y^{(0)}\right)_{4,11} = y_4;\ \left(\mathcal{H}_y^{(0)}\right)_{5,11} = y_5;\ \left(\mathcal{H}_y^{(0)}\right)_{6,11} = y_6, \\ & \left(\mathcal{H}_y^{(0)}\right)_{7,12} = y_7;\ \left(\mathcal{H}_y^{(0)}\right)_{8,12} = y_8;\ \left(\mathcal{H}_y^{(0)}\right)_{9,12} = y_9, \\ & \left(\mathcal{H}_y^{(0)}\right)_{1,13} = \left(\mathcal{H}_y^{(0)}\right)_{2,13} = \left(\mathcal{H}_y^{(0)}\right)_{3,13} = 1, \\ & \left(\mathcal{H}_y^{(0)}\right)_{4,14} = \left(\mathcal{H}_y^{(0)}\right)_{5,14} = \left(\mathcal{H}_y^{(0)}\right)_{6,14} = 1, \\ & \left(\mathcal{H}_y^{(0)}\right)_{7,15} = \left(\mathcal{H}_y^{(0)}\right)_{8,15} = \left(\mathcal{H}_y^{(0)}\right)_{9,15} = 1. \end{aligned}$$

For an efficient and convenient computation, the two spaces of the RBF coefficients, i.e., $\widehat{w}_x$ and $\widehat{w}_y$, should be converted into a single space of nodal values of the field variable u. In the present study, this conversion is implemented as follows.

The nodal values of u computed from the IRBF approximation in the x direction are forced to be the "exact" nodal values of u, which are known in the representation of a function and unknown in the solution of a differential equation, i.e.,

$$\widehat{u}^{[x]} = (u_1, \cdots, u_9)^T. \tag{3.14}$$

The nodal values of u computed from the IRBF approximation in the y direction are forced to be equal to those from the IRBF approximation in the x direction, i.e.,

$$\widehat{u}^{[x]} - \widehat{u}^{[y]} = \widehat{0}, \tag{3.15}$$

where $\widehat{0}$ is a vector of zeros of length 9.

Owing to the presence of the integration constants, the lengths of $\widehat{w}_x$ and $\widehat{w}_y$ are larger than those of $\widehat{u}^{[x]}$ and $\widehat{u}^{[y]}$, respectively. This facilitates the inclusion of extra equations into the conversion system. Here, extra equations can be used to impose the governing equation (3.7) at several nodes other than $\mathbf{x}_0$ on the stencil,

e.g., at $(\mathbf{x}_2, \mathbf{x}_4, \mathbf{x}_6, \mathbf{x}_8)$,

$$\frac{\partial^2 u}{\partial x^2}(x_2, y_2) + \frac{\partial^2 u}{\partial y^2}(x_2, y_2) + p(x_2, y_2)\frac{\partial u}{\partial x}(x_2, y_2) + q(x_2, y_2)\frac{\partial u}{\partial y}(x_2, y_2) = f(x_2, y_2), \tag{3.16}$$

$$\frac{\partial^2 u}{\partial x^2}(x_4, y_4) + \frac{\partial^2 u}{\partial y^2}(x_4, y_4) + p(x_4, y_4)\frac{\partial u}{\partial x}(x_4, y_4) + q(x_4, y_4)\frac{\partial u}{\partial y}(x_4, y_4) = f(x_4, y_4), \tag{3.17}$$

$$\frac{\partial^2 u}{\partial x^2}(x_6, y_6) + \frac{\partial^2 u}{\partial y^2}(x_6, y_6) + p(x_6, y_6)\frac{\partial u}{\partial x}(x_6, y_6) + q(x_6, y_6)\frac{\partial u}{\partial y}(x_6, y_6) = f(x_6, y_6), \tag{3.18}$$

$$\frac{\partial^2 u}{\partial x^2}(x_8, y_8) + \frac{\partial^2 u}{\partial y^2}(x_8, y_8) + p(x_8, y_8)\frac{\partial u}{\partial x}(x_8, y_8) + q(x_8, y_8)\frac{\partial u}{\partial y}(x_8, y_8) = f(x_8, y_8). \tag{3.19}$$

Conditions (3.14), (3.15) and (3.16)-(3.19) constitute the following conversion system

$$\begin{pmatrix} \widehat{u} \\ \widehat{0} \\ \widehat{f} \end{pmatrix} = \underbrace{\begin{bmatrix} \mathcal{H}_x^{(0)}, & \mathcal{O} \\ \mathcal{H}_x^{(0)}, & -\mathcal{H}_y^{(0)} \\ \mathcal{K}_x, & \mathcal{K}_y \end{bmatrix}}_{\mathcal{C}} \begin{pmatrix} \widehat{w}_x \\ \widehat{w}_y \end{pmatrix}, \tag{3.20}$$

where $\mathcal{C}$ is the conversion matrix; $\widehat{u}$, $\widehat{0}$, $\widehat{w}_x$, $\widehat{w}_y$, $\mathcal{H}_x^{(0)}$ and $\mathcal{H}_y^{(0)}$ are defined as before; $\mathcal{O}$ is a 9×15 matrix of zeros;

$$\widehat{f} = (f(\mathbf{x}_2), f(\mathbf{x}_4), f(\mathbf{x}_6), f(\mathbf{x}_8))^T,$$

$$\mathcal{K}_x = \begin{bmatrix} I^{(2)}_{[x]1}(\mathbf{x}_2) + p(\mathbf{x}_2)I^{(1)}_{[x]1}(\mathbf{x}_2), & \cdots, & I^{(2)}_{[x]9}(\mathbf{x}_2) + p(\mathbf{x}_2)I^{(1)}_{[x]9}(\mathbf{x}_2), & 0, & 1, & 0, & 0, & 0, & 0 \\ I^{(2)}_{[x]1}(\mathbf{x}_4) + p(\mathbf{x}_4)I^{(1)}_{[x]1}(\mathbf{x}_4), & \cdots, & I^{(2)}_{[x]9}(\mathbf{x}_4) + p(\mathbf{x}_4)I^{(1)}_{[x]9}(\mathbf{x}_4), & 1, & 0, & 0, & 0, & 0, & 0 \\ I^{(2)}_{[x]1}(\mathbf{x}_6) + p(\mathbf{x}_6)I^{(1)}_{[x]1}(\mathbf{x}_6), & \cdots, & I^{(2)}_{[x]9}(\mathbf{x}_6) + p(\mathbf{x}_6)I^{(1)}_{[x]9}(\mathbf{x}_6), & 0, & 0, & 1, & 0, & 0, & 0 \\ I^{(2)}_{[x]1}(\mathbf{x}_8) + p(\mathbf{x}_2)I^{(1)}_{[x]1}(\mathbf{x}_8), & \cdots, & I^{(2)}_{[x]9}(\mathbf{x}_8) + p(\mathbf{x}_2)I^{(1)}_{[x]9}(\mathbf{x}_8), & 0, & 1, & 0, & 0, & 0, & 0 \end{bmatrix},$$

$$\mathcal{K}_y = \begin{bmatrix} I^{(2)}_{[y]1}(\mathbf{x}_2) + q(\mathbf{x}_2)I^{(1)}_{[y]1}(\mathbf{x}_2), & \cdots, & I^{(2)}_{[y]9}(\mathbf{x}_2) + q(\mathbf{x}_2)I^{(1)}_{[y]9}(\mathbf{x}_2), & 1, & 0, & 0, & 0, & 0, & 0 \\ I^{(2)}_{[y]1}(\mathbf{x}_4) + q(\mathbf{x}_4)I^{(1)}_{[y]1}(\mathbf{x}_4), & \cdots, & I^{(2)}_{[y]9}(\mathbf{x}_4) + q(\mathbf{x}_4)I^{(1)}_{[y]9}(\mathbf{x}_4), & 0, & 1, & 0, & 0, & 0, & 0 \\ I^{(2)}_{[y]1}(\mathbf{x}_6) + q(\mathbf{x}_6)I^{(1)}_{[y]1}(\mathbf{x}_6), & \cdots, & I^{(2)}_{[y]9}(\mathbf{x}_6) + q(\mathbf{x}_6)I^{(1)}_{[y]9}(\mathbf{x}_6), & 0, & 1, & 0, & 0, & 0, & 0 \\ I^{(2)}_{[y]1}(\mathbf{x}_8) + q(\mathbf{x}_8)I^{(1)}_{[y]1}(\mathbf{x}_8), & \cdots, & I^{(2)}_{[y]9}(\mathbf{x}_8) + q(\mathbf{x}_8)I^{(1)}_{[y]9}(\mathbf{x}_8), & 0, & 0, & 1, & 0, & 0, & 0 \end{bmatrix}.$$

This mapping leads to

$$\begin{pmatrix} \widehat{w}_x \\ \widehat{w}_y \end{pmatrix} = \mathcal{C}^{-1} \begin{pmatrix} \widehat{u} \\ \widehat{0} \\ \widehat{f} \end{pmatrix}, \tag{3.21}$$

or

$$\widehat{w}_x = \mathcal{C}_x^{-1} \left(\widehat{u}, \widehat{0}, \widehat{f}\right)^T, \tag{3.22}$$

$$\widehat{w}_y = \mathcal{C}_y^{-1} \left(\widehat{u}, \widehat{0}, \widehat{f}\right)^T, \tag{3.23}$$

where $\mathcal{C}_x^{-1}$ and $\mathcal{C}_y^{-1}$ denote the first and last 15 rows of the matrix $\mathcal{C}^{-1}$, respectively.

It is noted that the condition of $\mathcal{C}$ is an increasing function of the RBF width. For very large values of the RBF width, a direct way of computing the IRBF interpolant, i.e., (3.20) and (3.21), cannot be carried out, which needs further studies.

When the problem domain is non-rectangular, stencils of the interior nodes close to the irregular boundary may be no longer of rectangular shape. There are two types of nodes in the stencil: regular grid nodes and boundary nodes. The latter is generated by the intersection of the grid lines and the irregular boundary. Special treatment is needed in the construction of the conversion matrix; the governing equation is only enforced at the mentioned nodes that are still regular (i.e., intersection of the two grid lines). It is expected that the ability of RBFs to work with irregular nodes and the inclusion of the governing equation into the approximations will alleviate the loss of accuracy caused by the non-rectangular shapes of stencils.

By substituting (3.22) into (3.8) and (3.9) and (3.23) into (3.11) and (3.12), one has

$$\widehat{\frac{\partial^2 u}{\partial x^2}} = \mathcal{H}_x^{(2)} \mathcal{C}_x^{-1} \left(\widehat{u}, \widehat{0}, \widehat{f} \right)^T, \tag{3.24}$$

$$\widehat{\frac{\partial u}{\partial x}} = \mathcal{H}_x^{(1)} \mathcal{C}_x^{-1} \left(\widehat{u}, \widehat{0}, \widehat{f} \right)^T, \tag{3.25}$$

$$\widehat{\frac{\partial^2 u}{\partial y^2}} = \mathcal{H}_y^{(2)} \mathcal{C}_y^{-1} \left(\widehat{u}, \widehat{0}, \widehat{f} \right)^T, \tag{3.26}$$

$$\widehat{\frac{\partial u}{\partial y}} = \mathcal{H}_y^{(1)} \mathcal{C}_y^{-1} \left(\widehat{u}, \widehat{0}, \widehat{f} \right)^T. \tag{3.27}$$

Nodal derivative values are thus expressed not only in terms of the nodal values of u at all grid nodes on the stencil but also in terms of the nodal values of the governing equation at selected nodes on the stencil.

In this work, the governing equation (3.7) is simply discretised by means of point collocation. The obtained discrete system is then transformed into a set of algebraic equations by making use of (3.24)-(3.27). The algebraic set is sparse so that one can solve it efficiently for the unknown nodal values of the field variable u. The sparsity of the algebraic matrix (i.e. the percentage of zero entries relative to the total matrix entries) is 97.68% with the given grid of 21×21.

It is noted that, unlike the standard finite difference method, the proposed stencils are based on two-dimensional approximations. In this regard, it is possible to extend the stencils to unstructured node layouts.

3.4 Numerical examples

The proposed scheme is implemented with the multiquadric basis function

$$I_i(\mathbf{x}) = \sqrt{(\mathbf{x} - \mathbf{c}_i)^T (\mathbf{x} - \mathbf{c}_i) + a_i^2}, \tag{3.28}$$

where $\mathbf{c}_i$ and a_i are the centre and width, respectively. It is noted that another form of the width (shape) parameter is defined as $\epsilon_i = 1/a_i$ - this form is very convenient and meaningful for the study/use of flat RBFs (i.e., $\epsilon_i \to 0$, Laurent expansions). The present work is mainly concerned with the solution of convection-dominated problems, where the RBF width is found to be small for an accurate simulation (i.e., small a_i and large ϵ_i).

We choose the RBF width according to the simple relation $a_i = \beta h_i$, where β is a given number and h_i is a grid size.

For the simulation of viscous flows, we employ Picard iteration to deal with the resultant nonlinear set of algebraic equations. At each iteration, the solution field is relaxed as

$$\zeta^k = \theta\zeta^k + (1-\theta)\zeta^{k-1}, \tag{3.29}$$

where the superscript k is used to denote a current iteration, ζ a vector whose entries are nodal values of the field variable over the whole domain, and θ a scalar ($0 < \theta \leq 1$). The iteration is set to stop when $CM < 10^{-7}$, where CM (i.e., convergence measure) is defined as

$$CM = \text{norm}(\zeta_k - \zeta_{k-1})/\text{norm}(\zeta_k). \tag{3.30}$$

3.4.1 Example 1: analytic test (rectangular domain)

The proposed method is first verified in the test boundary-value problem governed by

$$\frac{\partial^2 u}{\partial x^2} + \frac{\partial^2 u}{\partial y^2} - R\frac{\partial u}{\partial x} = 0, \tag{3.31}$$

where $0 \leq x, y \leq 1$, subject to

$$u(x,0) = 0 \quad 0 \leq x \leq 1, \tag{3.32}$$
$$u(x,1) = 0 \quad 0 \leq x \leq 1, \tag{3.33}$$
$$u(0,y) = \sin(\pi y) \quad 0 \leq y \leq 1, \tag{3.34}$$
$$u(1,y) = \sin(2\pi y) \quad 0 \leq y \leq 1. \tag{3.35}$$

The exact solution to this problem is

$$u_e(x,y) = \exp(Rx/2)\sin(\pi y)\left[2\exp(-R/2)\sinh(\sigma x) + \sinh(\sigma(1-x))\right]/\sinh(\sigma), \tag{3.36}$$

where $\sigma = \sqrt{\pi^2 + R^2/4}$. As shown in Figure 3.1, the higher the value of R the thinner the boundary layer will be.

To study the effects of using compact approximations on the solution accuracy, the original local IRBF scheme, which is also based on a 3×3 stencil, is employed here. Calculations are carried out at $R = 40$ with two values of β: 0.9 (small) and 2.5 (large) using uniform grids. Results obtained are presented in Tables 3.1 and 3.2. It can be seen that the incorporation of information about the governing equation into the stencil leads to a significant improvement in accuracy, especially for the case of small β.

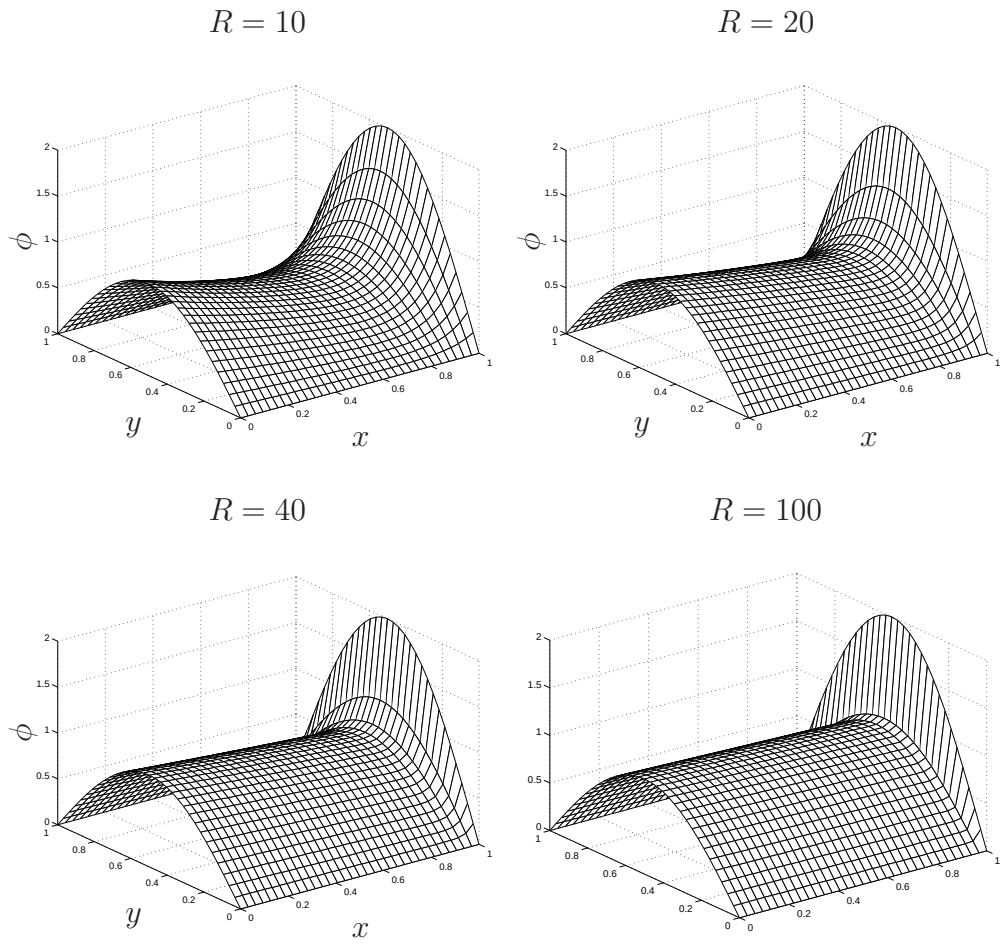

Figure 3.1 Example 1, rectangular domain: exact solutions at several values of R.

Figures 3.2 and 3.3 display the solution accuracy against the RBF width, showing that the optimal value of β is 5.80 for $R = 10$, 2.40 for $R = 20$, 0.91 for $R = 40$ and 0.012 for $R = 100$. It should be pointed out that (i) the optimal value of β is reduced as R increases; and (ii) the optimal values of β are small (i.e., less than 1) for large values of R.

For $R = (10, 20, 40, 100)$, the corresponding condition numbers at the optimal value of β are 2.20×10^6, 1.57×10^4, 2.35×10^3 and 4.53×10^3, respectively for the interpolation matrix in (3.20), and 3.73×10^2, 2.55×10^2, 1.53×10^2 and 9.68×10^1, respectively for the final system matrix. It can be seen that the condition number of the interpolation matrix is significantly reduced as R increases. In other words, calculations are stabler as R increases. As a result, at large values of R where the numerical simulation becomes challenging, one can apply a simple direct (traditional) way to compute the IRBF interpolants for the highest accuracy.

Table 3.3 shows a comparison of accuracy between the present scheme and other techniques. Results by the upwind (UDS), central difference (CDS) and single cell high order (SCHOS) schemes are extracted from (Gupta et al., 1984). High order schemes (i.e., IRBF and SCHOS) perform much better than low order schemes (i.e., UDS and CDS). The presently proposed method yields the most accurate results.

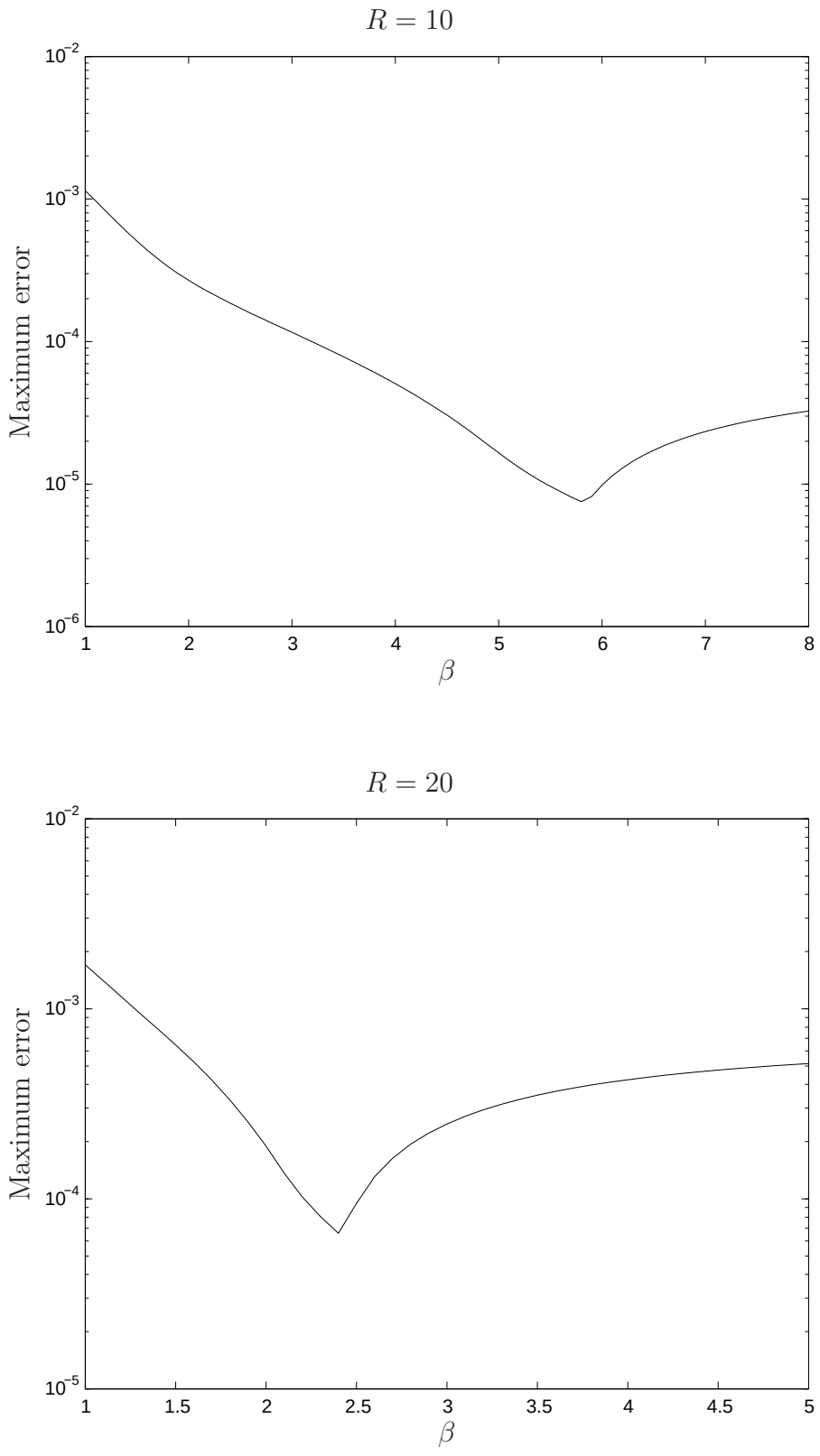

Figure 3.2 Example 1, rectangular domain: the maximum relative error against the RBF width ($\beta = a/h$) at a grid of 33×33. The optimal value of β is a decreasing function of R.

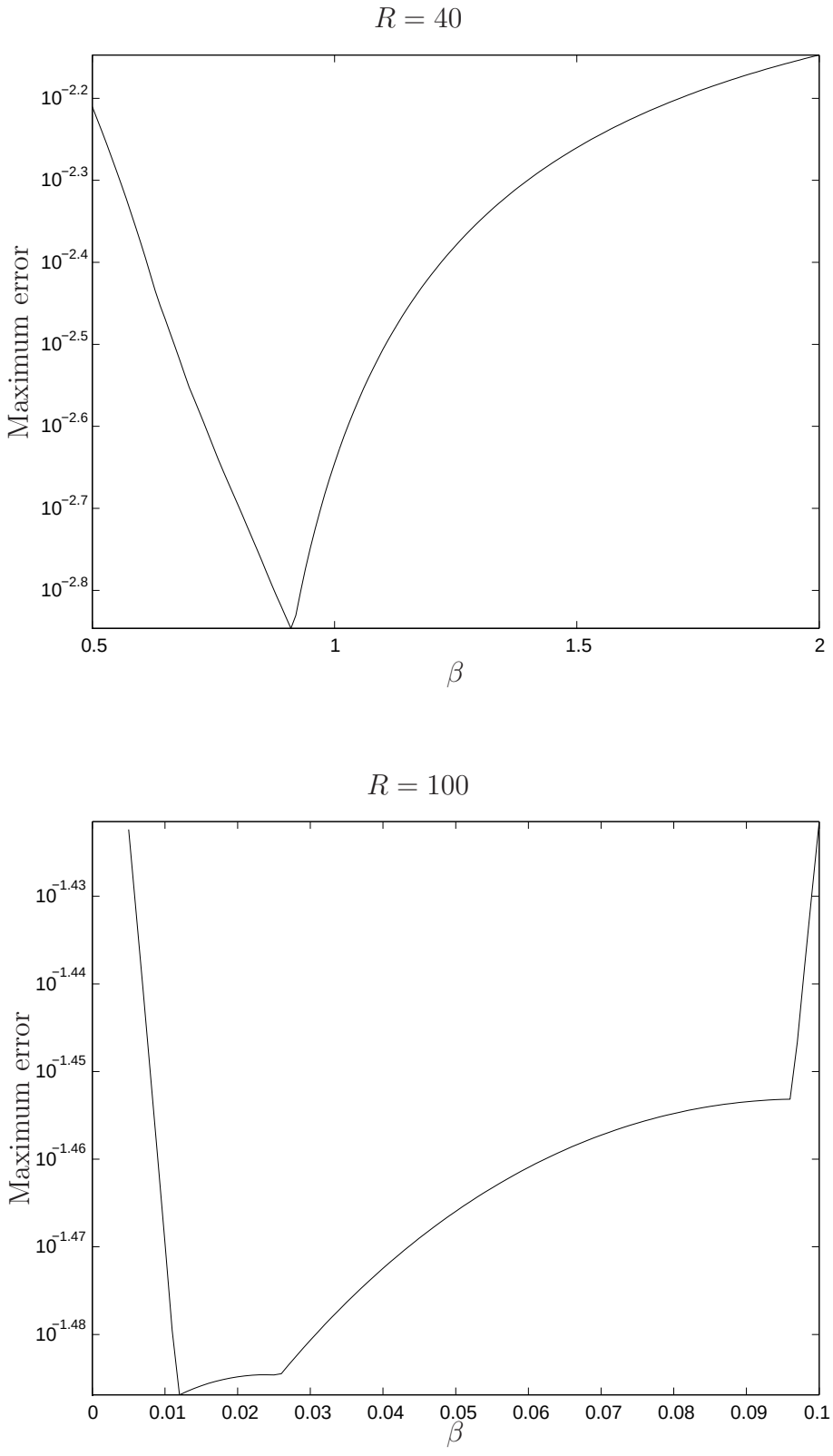

Figure 3.3 Example 1, rectangular domain: the maximum relative error against the RBF width ($\beta = a/h$) at a grid of 33×33. The optimal value of β is a decreasing function of R.

Table 3.1 Example 1, $R = 40$, $\beta = 2.5$: Maximum relative errors and rates of convergence by the original local IRBF and present compact local IRBF methods. The rate presented here is the exponent of $O(h^{\text{rate}})$ that is computed over two successive grids (point-wise) and also over the whole set of grids used. LCR stands for local convergence rate.

$N_x \times N_y$	h	Original IRBFs		Compact IRBFs	
		Error	LCR	Error	LCR
15×15	7.14×10^{-2}	3.64×10^{-1}	-	4.64×10^{-1}	-
17×17	6.25×10^{-2}	2.93×10^{-1}	1.60	2.35×10^{-1}	5.10
19×19	5.55×10^{-2}	2.38×10^{-1}	1.76	1.32×10^{-1}	4.84
21×21	5.00×10^{-2}	1.95×10^{-1}	1.89	8.03×10^{-2}	4.76
23×23	4.54×10^{-2}	1.61×10^{-1}	2.01	5.10×10^{-2}	4.76
25×25	4.16×10^{-2}	1.33×10^{-1}	2.12	3.36×10^{-2}	4.80
27×27	3.84×10^{-2}	1.12×10^{-1}	2.23	2.27×10^{-2}	4.85
29×29	3.57×10^{-2}	9.41×10^{-2}	2.34	1.58×10^{-2}	4.93
31×31	3.33×10^{-2}	7.95×10^{-2}	2.45	1.11×10^{-2}	5.01
33×33	3.12×10^{-2}	6.73×10^{-2}	2.57	8.04×10^{-3}	5.10
Overall convergence rate			2.04		4.86

Table 3.2 Example 1, $R = 40$, $\beta = 0.9$: Maximum relative errors and rates of convergence by the original local IRBF and present compact local IRBF methods. The rate presented here is the exponent of $O(h^{\text{rate}})$ that is computed over two successive grids (point-wise) and also over the whole set of grids used.

$N_x \times N_y$	h	Original IRBFs		Compact IRBFs	
		Error	LCR	Error	LCR
15×15	7.14×10^{-2}	4.26×10^{-1}	-	4.21×10^{-1}	-
17×17	6.25×10^{-2}	3.62×10^{-1}	1.21	2.08×10^{-1}	5.27
19×19	5.55×10^{-2}	3.11×10^{-1}	1.29	1.10×10^{-1}	5.42
21×21	5.00×10^{-2}	2.70×10^{-1}	1.34	6.10×10^{-2}	5.58
23×23	4.54×10^{-2}	2.36×10^{-1}	1.38	3.48×10^{-2}	5.87
25×25	4.16×10^{-2}	2.09×10^{-1}	1.40	2.01×10^{-2}	6.31
27×27	3.84×10^{-2}	1.87×10^{-1}	1.41	1.15×10^{-2}	6.98
29×29	3.57×10^{-2}	1.84×10^{-1}	0.20	6.34×10^{-3}	8.03
31×31	3.33×10^{-2}	1.81×10^{-1}	0.18	3.19×10^{-3}	9.93
33×33	3.12×10^{-2}	1.78×10^{-1}	0.33	1.46×10^{-3}	12.05
Overall convergence rate			1.12		6.60

Table 3.3 Example 1: Maximum relative errors at a grid size of $h = 1/32$. Results by UDS, CDS and SCHOS are extracted from (Gupta et al., 1984).

R	UDS	CDS	SCHOS	Compact IRBFs
10	0.0916	0.4537×10^{-2}	0.6011×10^{-4}	0.7523×10^{-5}
20	0.1262	0.1576×10^{-1}	0.1399×10^{-3}	0.6587×10^{-4}
40	0.1686	0.5925×10^{-1}	0.1511×10^{-2}	0.1424×10^{-2}
100	0.2264	3.0020×10^{-1}	0.3517×10^{-1}	0.3259×10^{-1}

3.4.2 Example 2: analytic test (non-rectangular domain)

Next, we shall verify the proposed stencil with the case of non-rectangular domains. Consider the following PDE

$$\frac{\partial^2 u}{\partial x^2} + \frac{\partial^2 u}{\partial y^2} - R\left(\frac{\partial u}{\partial x} + \frac{\partial u}{\partial y}\right) = f \tag{3.37}$$

defined on a circular domain $x^2 + y^2 \leq 1$ and subjected to Dirichlet boundary conditions. The boundary conditions and the forcing function f are chosen so that the solution to this problem is

$$u_e(x, y) = \frac{e^{R(x^2+y^2)} - 1}{e^R - 1}. \tag{3.38}$$

This analytic solution is a bounded function: $0 \leq u_e(x, y) \leq 1$; the boundary layer is steeper as R increases.

The problem domain is covered by a rectangular Cartesian grid. The grid nodes outside the domain are then removed and the boundary nodes are generated through the intersection of the grid lines and the boundary.

We employ a number of grids, $\{10\times10, 20\times20, \cdots, 150\times150\}$, with three typical values of R, (1,10,25), to study the grid convergence behaviour of the proposed stencil. Figure 3.4 displays the the relative discrete L_2 error, denoted by N_e, against the grid size h. The solution converges apparently as $O(h^{4.24})$ for $R = 1$, $O(h^{3.60})$ for $R = 10$ and $O(h^{3.36})$ for $R = 25$. To capture the boundary layer accurately, the RBF width is chosen smaller as R increases: $\beta = 25$ for $R = 1$, $\beta = 7$ for $R = 10$, and $\beta = 0.5$ for $R = 25$. One advantage of the RBF calculations at low values of β (small RBF widths) is that their matrices have low condition numbers. It is noted that large condition numbers indicate a nearly singular matrix. For $R = (1, 10, 25)$, using a grid of 50×50, the corresponding condition numbers are 6.45×10^9, 3.48×10^8 and 6.31×10^6, respectively for the interpolation matrix in (3.20), and 5.22×10^3, 2.46×10^3, and 1.21×10^3, respectively for the final system matrix. The RBF width needs to be large for diffusion-dominated problems (small R) and small for convection-dominated problems (large R). For example, for $R = 1$, using a grid of 150×150, the error N_e is 5.03×10^{-8} for $\beta = 25$, but increased up to 8.74×10^{-7} for $\beta = 10$. For $R = 25$, the error N_e is 3.91×10^{-3} for $\beta = 0.5$, but increased up to 7.97×10^{-3} for $\beta = 1$.

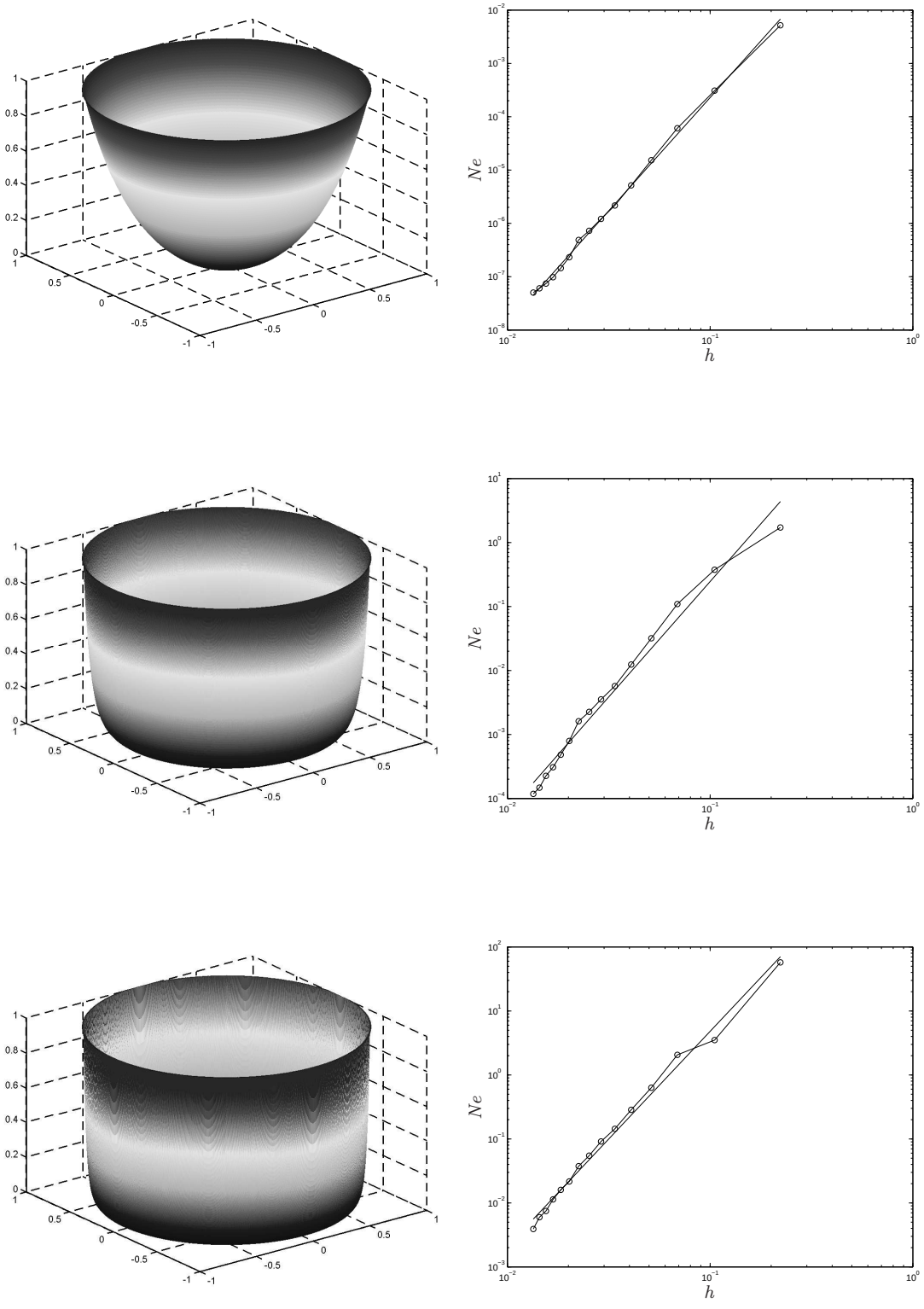

Figure 3.4 Example 2, non-rectangular domain: The exact solution (left) and the grid-convergence behaviour of the proposed stencil (right) for $R = 1$ (top), $R = 10$ (middle) and $R = 25$ (bottom). Grids employed are $(10 \times 10, 20 \times 20, \cdots, 150 \times 150)$. The solution converges apparently as $O(h^{4.24})$ for $R = 1$, $O(h^{3.60})$ for $R = 10$ and $O(h^{3.36})$ for $R = 25$.

3.4.3 Example 3: Natural convection in a square slot

Using the Boussinesq approximation, the 2D dimensionless governing equations for a steady buoyancy-driven flow in terms of the streamfunction ψ, vorticity ω and temperature T can be written as

$$v_x\frac{\partial \omega}{\partial x}+v_y\frac{\partial \omega}{\partial y} = \sqrt{\frac{\mathrm{Pr}}{Ra}}\left(\frac{\partial^2 \omega}{\partial x^2}+\frac{\partial^2 \omega}{\partial y^2}\right)+\frac{\partial T}{\partial x}, \tag{3.39}$$

$$v_x\frac{\partial T}{\partial x}+v_y\frac{\partial T}{\partial y} = \frac{1}{\sqrt{Ra\,\mathrm{Pr}}}\left(\frac{\partial^2 T}{\partial x^2}+\frac{\partial^2 T}{\partial y^2}\right), \tag{3.40}$$

$$-\omega = \frac{\partial^2 \psi}{\partial x^2}+\frac{\partial^2 \psi}{\partial y^2}, \tag{3.41}$$

where v_x and v_y are the x and y components of the velocity vector

$$v_x=\frac{\partial \psi}{\partial y}, \quad v_y=-\frac{\partial \psi}{\partial x},$$

and Pr and Ra are the Prandtl and Rayleigh numbers defined as $Pr=\nu/\alpha$ and $Ra=\beta g\Delta T L^3/\alpha\nu$, respectively in which ν is the kinematic viscosity, α the thermal diffusivity, β the thermal expansion coefficient, g the gravity, and L and ΔT the characteristic length and temperature difference, respectively. In this dimensionless scheme, the velocity scale is taken as $U=\sqrt{gL\beta\Delta T}$ for the purpose of balancing the buoyancy and inertial forces (Ostrach, 1988).

Consider free convection in a unit cavity. The left wall is heated to generate nontrivial motion, while the top and bottom walls are adiabatic. The boundary conditions are given by

$$\psi=0,\ \frac{\partial \psi}{\partial x}=0,\ T=1 \quad \text{on} \qquad x=0, \tag{3.42}$$

$$\psi=0,\ \frac{\partial \psi}{\partial x}=0,\ T=0 \quad \text{on} \qquad x=1, \tag{3.43}$$

$$\psi=0,\ \frac{\partial \psi}{\partial y}=0,\ \frac{\partial T}{\partial y}=0 \quad \text{on} \qquad y=0,\ y=1. \tag{3.44}$$

There are three governing equations that are solved in a coupled manner. Equations (3.39) with $R=\sqrt{Ra/Pr}$ and (3.40) with $R=\sqrt{RaPr}$ are discretised using (3.24)-(3.27), while (3.41) is handled by the compact IRBF 9 point formula in (Mai-Duy and Tran-Cong, 2011). A computational boundary condition for the vorticity is derived here using the scheme proposed in (Ho-Minh et al., 2009).

From the published works, the flow was widely simulated for Ra in the range of 10^3 to 10^6. In this study, a wider range is considered and we use a uniform grid to represent the domain. Table 3.4 and Figure 3.5 show the obtained results for the case of $Ra=10^3$ using $\beta=10$, $Ra=10^5$ using $\beta=1.5$, and $Ra=10^7$ using $\beta=0.8$. Grid convergence is clearly observed for all cases and the obtained solutions are in very good agreement with the benchmark results reported in (Davis, 1983; Quere, 1991) (Table 3.4). Contour plots of the field variables look

feasible even at coarse grids (Figure 3.5). As Ra increases, the pattern of the flow becomes complex. Very thin boundary layers are formed at $Ra = 10^7$. We employ small values of β for the simulation of high Ra flows. If $\beta = 10$ and $\beta = 5$ is used for $Ra = 10^7$, the Picard iteration scheme fails to obtain a convergent solution as shown in Figure 3.6. The matrix conditions of the interpolant, which are recorded when the iteration scheme has achieved convergence, are presented in Table 3.5. Their values are relatively low, allowing the calculation of the interpolant to be conducted in a direct way.

Table 3.4 Natural convection: Grid convergence study. "Benchmark" and "Benchmark*" refer to the finite difference and pseudo spectral results in (Davis, 1983) and (Quere, 1991), respectively.

Grid	$v_{y\ max}$	error(%)	x	$v_{x\ max}$	error(%)	y	$\overline{N_{v_x}}$	error(%)
				$Ra = 10^3$, $\beta = 10$, $\alpha = 0.01$				
21×21	3.7040	0.18	0.178	3.6555	0.17	0.814	1.1183	0.02
31×31	3.7000	0.08	0.178	3.6518	0.07	0.813	1.1180	0.00
41×41	3.6988	0.04	0.178	3.6507	0.04	0.813	1.1179	0.00
Benchmark	3.697		0.178	3.649		0.813	1.118	
				$Ra = 10^5$, $\beta = 1.5$, $\alpha = 0.01$				
31×31	69.071	0.70	0.065	34.892	0.46	0.855	4.5380	0.42
41×41	68.893	0.44	0.066	34.863	0.38	0.855	4.5331	0.31
51×51	68.797	0.30	0.066	34.825	0.27	0.855	4.5296	0.23
Benchmark	68.59		0.066	34.73		0.855	4.519	
				$Ra = 10^7$, $\beta = 0.8$, $\alpha = 0.001$				
61×61	694.68	0.64	0.021	140.17	5.66	0.874	16.207	1.91
71×71	695.70	0.49	0.021	142.97	3.78	0.876	16.233	1.75
81×81	696.05	0.44	0.021	145.33	2.19	0.874	16.269	1.53
Benchmark*	699.179		0.021	148.595		0.879	16.523	

Table 3.5 Natural convection: Condition numbers of the conversion matrix for the vorticity equation (middle column) and the energy equation (last column) which are measured when the Picard iteration scheme has achieved convergence.

$Ra = 10^3,\ \beta = 10$		
21×21	$O(10^7)$	$O(10^7)$
31×31	$O(10^7)$	$O(10^7)$
41×41	$O(10^7)$	$O(10^7)$
$Ra = 10^5,\ \beta = 1.5$		
31×31	$O(10^3)$	$O(10^3)$
41×41	$O(10^3)$	$O(10^3)$
51×51	$O(10^3)$	$O(10^3)$
$Ra = 10^7,\ \beta = 0.8$		
61×61	$O(10^4)$	$O(10^4)$
71×71	$O(10^4)$	$O(10^4)$
81×81	$O(10^4)$	$O(10^4)$

3.4.4 Example 4: Lid-driven cavity flow

The governing equations employed here are the steady-state Navier-Stokes equations written in the stream function ψ and vorticity ω as

$$v_x \frac{\partial \omega}{\partial x} + v_y \frac{\partial \omega}{\partial y} = \frac{1}{Re}\left(\frac{\partial^2 \omega}{\partial x^2} + \frac{\partial^2 \omega}{\partial y^2}\right), \tag{3.45}$$

$$-\omega = \frac{\partial^2 \psi}{\partial x^2} + \frac{\partial^2 \psi}{\partial y^2}. \tag{3.46}$$

where Re is the Reynolds number. The cavity is taken as a unit square with the lid sliding from left to right at a unit velocity. The boundary conditions for v_x and v_y become

$$\psi = 0,\ \frac{\partial \psi}{\partial x} = 0 \quad \text{on} \qquad x = 0,\ x = 1, \tag{3.47}$$

$$\psi = 0,\ \frac{\partial \psi}{\partial y} = 0 \quad \text{on} \qquad y = 0, \tag{3.48}$$

$$\psi = 0,\ \frac{\partial \psi}{\partial y} = 1 \quad \text{on} \qquad y = 1. \tag{3.49}$$

At each top corner, there are two values of v_x, making the solution singular. In the early paper by Ghia et al. (Ghia et al., 1982), the flow was simulated by the finite-difference method using very fine grids (i.e., 129×129 and 257×257). The obtained results are very accurate and often cited in the literature for comparison purposes. Later on, in the work of Botella and Peyret (Botella and Peyret, 1998), simulations were carried out by using a Chebyshev collocation method for handling a regular part of the solution and a substraction method for dealing with the singularity part. Spectral results for the flow at $Re = 100$ and $Re = 1000$ were reported.

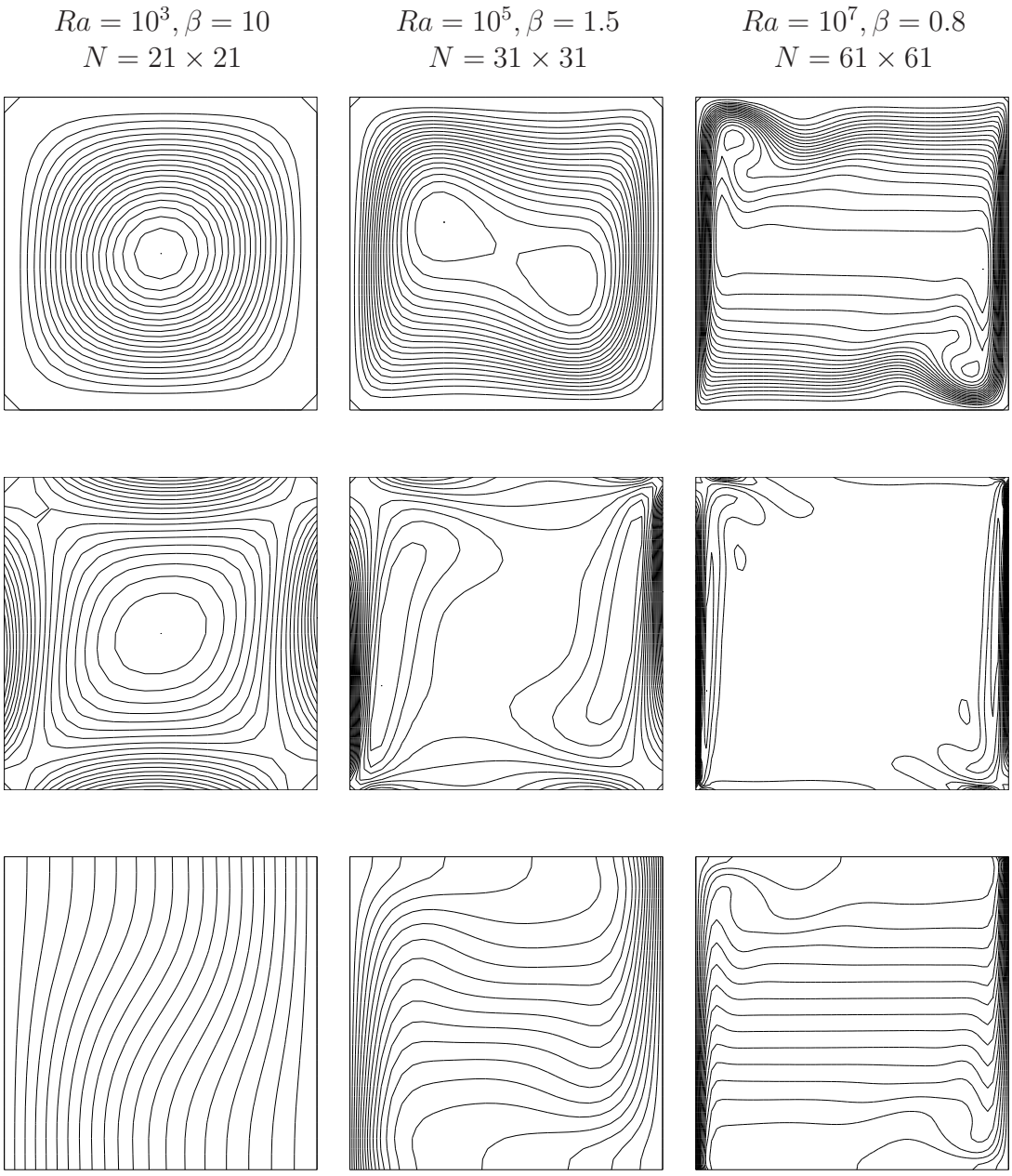

Figure 3.5 Natural convection: Contour plots of the streamfunction (top), vorticity (middle) and temperature (bottom) at coarse grids. Each plot contains 21 contour lines whose values vary linearly.

In the present work, the domain is simply discretised using a uniform Cartesian grid. For stencils involving a top corner, we remove such a point from both sets of RBF centres and collocation points. Grid convergence study of the present method for $Re = 100$ and $Re = 1000$ are presented in Table 3.6 for extreme values of the velocity profiles and in Table 3.7 for features of the primary vortex. Apart from the finite-difference and spectral benchmark solutions, results by Li et al. (Li et al., 1995) using a compact fourth-order finite difference scheme are also included. It can be seen that the present solutions converge very fast and consistently. Results by the present method using a grid 81×81 and those by the compact finite difference method using a grid 129×129 (Li et al., 1995) are in excellent agreement with the spectral benchmark solutions (Table 3.7). In addition, results by the present technique are in closer agreement with the

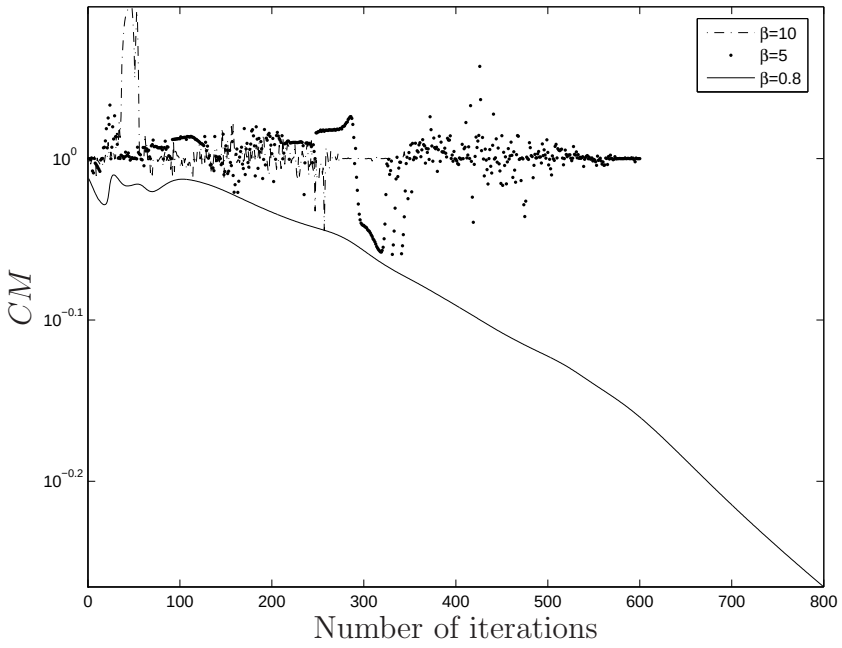

Figure 3.6 Natural convection, $Ra = 10^7$, $N = 61 \times 61$, $\alpha = 0.001$, solution at $Ra = 10^6$ used as initial solution: the convergence behaviour of the Picard iteration scheme for $\beta = 10$, $\beta = 5$ and $\beta = 0.8$. The first two fail to give a convergent solution.

spectral benchmark solutions than the finite difference benchmark ones (Tables 3.6 and 3.7). Figure 3.7 shows contour plots of the streamfunction and vorticity, and the velocity profiles on the centrelines for $Re = 5000$. Other observations here are similar to those for the natural convection problem. The value of β needs be smaller for higher Re solution. If larger values of β are used, the Picard scheme may not achieve convergence as shown in Figure 3.8.

3.5 Conclusions

Compact local stencils based on integrated RBFs are developed for the convection-diffusion equation defined on rectangular and non-rectangular domains. Like standard local stencils, the system of algebraic equations is sparse. Unlike standard local stencils, a high level of accuracy is achieved using relatively coarse grids. For convection-dominant flows whose patterns are quite complex due to the presence of steep gradients, it is observed that the most accurate results are obtained at small values of the RBF width. This suggests that one can consider a simple direct (traditional) way for computing the IRBF interpolants in the simulation of highly-nonlinear heat transfer and fluid flow problems.

Table 3.6 Lid-driven cavity flow: Grid convergence study for extreme values of the velocity profiles. "Benchmark" and "Benchmark*" refer to the finite difference and pseudo spectral results in (Ghia et al., 1982) and (Botella and Peyret, 1998), respectively.

Grid	$v_{x\ min}$	error(%)	y	$v_{y\ max}$	error(%)	x	$v_{y\ min}$	error(%)	x
				$Re = 100,\ \beta = 5,\ \alpha = 0.01$					
11×11	-0.18325	14.38	0.476	0.15895	11.48	0.223	-0.20049	21.01	0.796
21×21	-0.20979	1.99	0.462	0.17566	2.18	0.236	-0.24609	3.04	0.809
31×31	-0.21356	0.22	0.458	0.17922	0.19	0.237	-0.25292	0.35	0.810
41×41	-0.21400	0.02	0.458	0.17961	0.02	0.237	-0.25372	0.03	0.810
Benchmark	-0.21090		0.453	0.17527		0.234	-0.24533		0.805
Benchmark*	-0.21404		0.458	0.17957		0.237	-0.25380		0.810
				$Re = 1000,\ \beta = 1,\ \alpha = 0.01$					
11×11	-0.24017	38.19	0.253	0.23700	37.12	0.150	-0.31896	39.48	0.886
21×21	-0.30445	21.64	0.240	0.28406	24.64	0.187	-0.38808	26.37	0.877
31×31	-0.34565	11.04	0.202	0.33195	11.93	0.170	-0.45790	13.12	0.892
41×41	-0.36710	5.52	0.184	0.35531	5.73	0.163	-0.49400	6.27	0.902
51×51	-0.37690	3.00	0.178	0.36514	3.13	0.161	-0.50989	3.26	0.906
61×61	-0.38198	1.69	0.175	0.37016	1.79	0.160	-0.51786	1.74	0.908
71×71	-0.38473	0.98	0.173	0.37292	1.06	0.159	-0.52207	0.95	0.909
Benchmark	-0.38289		0.172	0.37095		0.156	-0.51550		0.906
Benchmark*	-0.38857		0.172	0.37694		0.158	-0.52708		0.909

Table 3.7 Lid-driven cavity flow: Grid convergence study for features of the primary vortex. "Benchmark" and "Benchmark*" refer to the finite difference and pseudo spectral results in (Ghia et al., 1982) and (Botella and Peyret, 1998), respectively.

Grid	ψ-value	ω-value	location
	$Re = 100$, $\beta = 5$, $\alpha = 0.01$		
11×11	-0.089672	-2.84550	0.5799, 0.7494
21×21	-0.101767	-3.13748	0.6142, 0.7397
31×31	-0.103337	-3.16448	0.6153, 0.7376
41×41	-0.103506	-3.16602	0.6155, 0.7373
Benchmark	-0.103423	-3.16646	0.6172, 0.7344
	$Re = 1000$, $\beta = 1$, $\alpha = 0.01$		
11×11	-0.0831278	-1.530614	0.5414, 0.6066
21×21	-0.0950666	-1.810049	0.5370, 0.5952
31×31	-0.1070562	-1.940676	0.5315, 0.5790
41×41	-0.1131694	-2.003820	0.5311, 0.5708
51×51	-0.1158241	-2.033826	0.5312, 0.5677
61×61	-0.1171839	-2.050214	0.5312, 0.5665
71×71	-0.1179237	-2.059308	0.5312, 0.5659
81×81	-0.1183359	-2.064312	0.5311, 0.5655
Li et al. (Li et al., 1995) (129×129)	-0.118448	-2.05876	0.5313, 0.5625
Benchmark	-0.117929	-2.04968	0.5313, 0.5625
Benchmark*	-0.1189366	-2.067753	0.5308, 0.5652

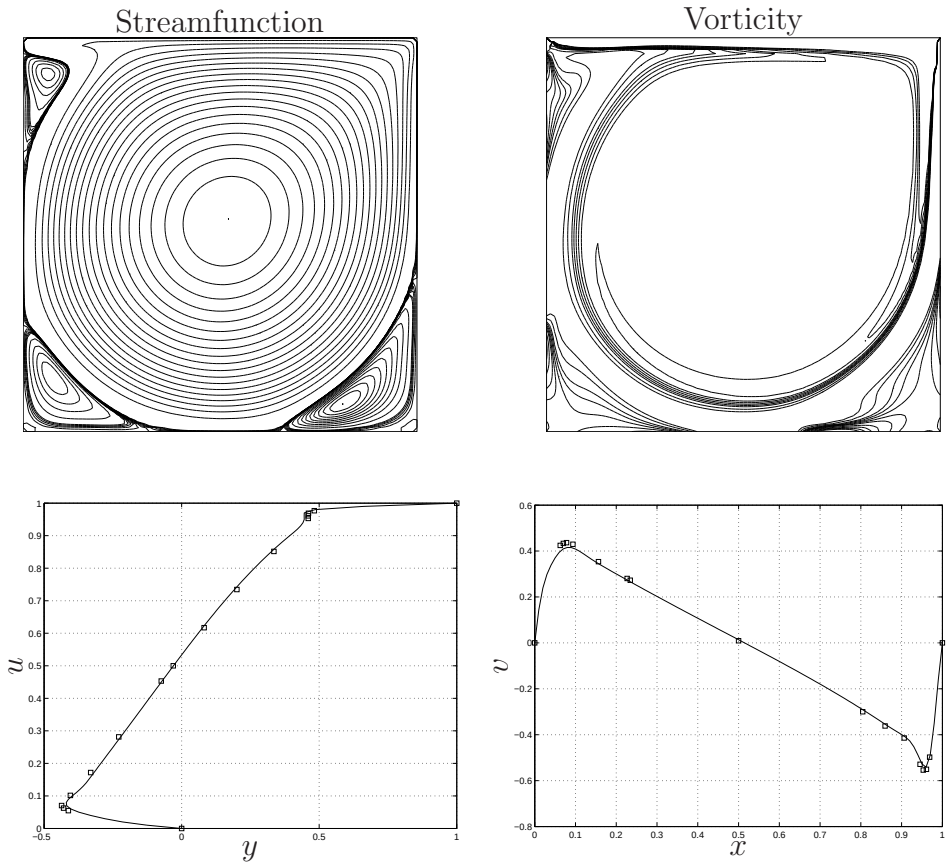

Figure 3.7 Lid driven cavity flow, $Re = 5000$, $N = 101 \times 101$, $\beta = 0.1$, $\alpha = 0.01$: Contour plots of the streamfunction and vorticity (top), and plots of the velocity profiles on the centrelines (bottom). Finite-difference results at a dense grid of 257×257 [31], denoted by $\square$, are also included.

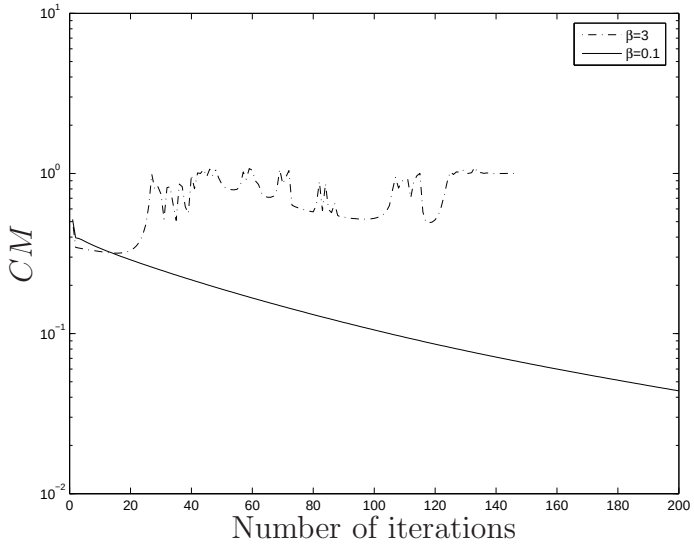

Figure 3.8 Lid-driven cavity flow, $Re = 5000$, $N = 101 \times 101$, $\alpha = 0.01$, solution at $Re = 3200$ used as initial solution: the convergence behaviour of the Picard iteration scheme for $\beta = 3$ and $\beta = 0.1$. Using $\beta = 3$ fails to give a convergent solution.

Chapter 4

Compact local IRBF stencils and subregion collocation for second-order differential problems

In Chapters 2 and 3, CLIRBF stencils are deployed in the context of point collocation methods, which we refer to as CLIRBF-PCM. In this Chapter, CLIRBF stencils will be introduced into the subregion-collocation (finite-volume) formulation for the discretisation of second-order ODEs/PDEs governing heat transfer and fluid flows. For the latter, the streamfunction-vorticity formulation is employed. We refer to present approach as CLIRBF-FVM. The problem domain can be rectangular or non-rectangular, and is simply represented by a Cartesian grid, over which overlapping compact local IRBF stencils are utilised to approximate the field variable and its derivatives. The governing differential equation is integrated over non-overlapping control volumes associated with grid nodes, and the divergence theorem is then applied to convert volume integrals into surface/line integrals. Line integrals are evaluated by means of the middle point rule (i.e. second-order integration scheme) and three-point Gaussian quadrature rule (i.e. high-order integration scheme). The accuracy of the proposed method is numerically investigated through the solution of several test problems including natural convection in an annulus. Numerical results indicate that (i) the proposed method produces accurate results using relatively coarse grids and (ii) the three-point integration scheme is generally more accurate than the middle point scheme.

4.1 Introduction

Finite volume methods (FVMs), which conserve mass, momentum and energy over any control volume and can work effectively with complex geometry problems, are widely used in computational fluid dynamic (CFD) (Patankar, 1980; Eymard et al., 2000; Huilgol and Phan-Thien, 1997; Pereira et al., 2001). It should be pointed out that the accuracy of a finite-volume solution is decided not only by the way to approximate the field variable but also by numerical integration schemes used for evaluating line/surface integrals in the formulation.

Epperson (Epperson, 2002) has shown that, given exact nodal function values, using a n-point Gaussian quadrature rule can lead to a solution whose error is $O(h^{2n})$, where h is the discretisation size. As a result, the error is of order up to h^2 only if one uses the middle point rule (i.e. one point Gaussian quadrature rule). Toroney and Turner (Moroney and Turner, 2006) proposed a FVM method, where differentiated RBFs are employed as a means of local gradient interpolation and the underlying line integrals are evaluated using the three-point Gaussian quadrature rule. Numerical results showed that the method yields accuracy several orders of magnitude better than simpler methods based on shape functions for both linear and nonlinear diffusion problems.

RBFs have emerged as a powerful high-order approximation tool for scattered data (Kansa, 1990; Haykin, 1999). The application of RBFs for the solution of ODEs and PDEs has received a great deal of attention over the last twenty years (Fasshauer, 2007). In recent years, research effort has been focused on constructing the RBF approximations in local form (to obtain sparse system matrices) (Shu et al., 2003; Lee et al., 2003; Sarler, 2005; Mai-Duy and Tran-Cong, 2009) and in compact local form (to obtain both sparse system matrices and high rates of convergence of the approximate solution) (Tolstykh and Shirobokov, 2005; Wright and Fornberg, 2006; Mai-Duy and Tran-Cong, 2011; Thai-Quang et al., 2012; Hoang-Trieu et al., 2012). It is known that the width of RBFs (shape parameter) strongly affects the quality of the approximations (Kansa, 1990; Rippa, 1999; Fornberg and Wright, 2004; Larsson and Fornberg, 2005). Numerical experiments show that, to yield a well-conditioned system matrix, one should choose small RBF widths for global methods, but can take small and large values for local methods. The accuracy of local RBF methods can thus be effectively controlled not only by the spatial discretisation size but also by the RBF width.

In this chapter, compact local integrated RBF stencils will be incorporated into the FV formulation to discretise second-order differential equations in one (1D) and two (2D) dimensions. Two numerical integration schemes, namely the middle point rule and 3-point Gaussian quadrature rule, are employed and their effects on the solution accuracy are investigated. We also study the accuracy behaviour against the RBF width. Results obtained are compared with standard FVMs as well as point collocation methods employed with compact local IRBF stencils.

The remainder of this chapter is organised as follows. A brief review of integrated RBFs including compact local approximations is given in Section 4.2. The proposed method is described for 1D and 2D problems in Section 4.3 and then verified in Section 4.4. Section 4.5 concludes the chapters.

4.2 Brief review of integrated RBFs

Consider a function $u(\mathbf{x})$. The integral formulation starts with the decomposition of highest-order derivatives under consideration into a set of RBFs. For second-

order differential problems, one has

$$\frac{\partial^2 u(\mathbf{x})}{\partial \eta^2} = \sum_{i=1}^{N} w_i^{[\eta]} I_{[\eta]i}^{(2)}(\mathbf{x}), \quad \mathbf{x} \in \Omega, \tag{4.1}$$

where η is used to denote a component of the position vector $\mathbf{x}$ (e.g. η can be x for 1D problems, and x or y for 2D problems); Ω is the domain of interest; $\{w_i\}_{i=1}^N$ is the set of unknown RBF coefficients; and $\left\{I_{[\eta]i}^{(2)}(\mathbf{x})\right\}_{i=1}^N$ is the set of RBFs. We will implement (4.1) with the multiquadric RBF (MQ)

$$I_i^{(2)}(\mathbf{x}) = \sqrt{(\mathbf{x} - c_i)^2 + a_i^2}, \tag{4.2}$$

where c_i and a_i are the centre and the width of the ith MQ, respectively.

Approximate expressions for first-order derivatives and the function u itself are then obtained by integrating expression (4.1)

$$\frac{\partial u(\mathbf{x})}{\partial \eta} = \sum_{i=1}^{N} w_i^{[\eta]} I_{[\eta]i}^{(1)}(\mathbf{x}) + C_1^{[\eta]}, \tag{4.3}$$

$$u(\mathbf{x}) = \sum_{i=1}^{N} w_i^{[\eta]} I_{[\eta]i}^{(0)}(\mathbf{x}) + \eta C_1^{[\eta]} + C_2^{[\eta]}, \tag{4.4}$$

where $I_{[\eta]i}^{(1)}(\mathbf{x}) = \int I_{[\eta]i}^{(2)}(\mathbf{x}) d\eta$; $I_{[\eta]i}^{(0)}(\mathbf{x}) = \int I_{[\eta]i}^{(1)}(\mathbf{x}) d\eta$; and $C_1^{[\eta]}$ and $C_2^{[\eta]}$ are the "constants" of integration. $C_1^{[\eta]}$ and $C_2^{[\eta]}$ will be constants for 1D problems, functions in one variable for 2D problems, and in two variables for 3D problems. These functions are unknown and can be approximated as linear combinations of basis functions.

The approximations (4.1)-(4.4) are called a global IRBF scheme if one employs these expressions over the entire domain, a 1D-IRBF scheme if they are employed along grid lines, and a local IRBF scheme if they are employed over small overlapping subregions. Global schemes can yield a high rate of convergence, but their matrices are fully populated and thus very costly for solving large-scale problems. On the other hand, local schemes result in sparse matrices that can be handled in a very efficient way, but their accuracies are deteriorated significantly. Several treatments were proposed to improve the solution accuracy of local IRBF schemes. One simple but effective way is to incorporate, through the constants of integration, nodal values of the governing equation or of first/second derivatives into the local approximations. Such approximations are called a compact local IRBF scheme. It was shown numerically that compact local IRBF schemes are superior to local IRBF ones regarding both the computational cost and the accuracy in the context of point-collocation formulation. In the present work, compact local IRBF stencils are introduced into the subregion-collocation/finite-volume formulation for the solution of second-order differential problems defined on rectangular and non-rectangular domains.

4.3 Proposed method

The proposed finite-volume method, which is based on compact local IRBF stencils, (CLIRBF-FVM) is first described for 1D problems and then extended to 2D problems.

4.3.1 One dimensional problems

Consider a 1D problem governed by

$$\frac{d^2u(x)}{dx^2} + \frac{du(x)}{dx} + u(x) = f(x), \quad x \in \Omega, \tag{4.5}$$

where $u(x)$ and $f(x)$ are continuous and prescribed functions, respectively. The domain Ω is subdivided into a set of non-overlapping line segments (control volumes) that are associated with grid nodes. Figure 4.1 shows a full control volume for an interior grid node x_i, ($i \in \{2, 3, \ldots, N-1\}$) and a half control volume for a boundary node x_i ($i \in \{1, N\}$). Integrating (4.5) over the full control volume

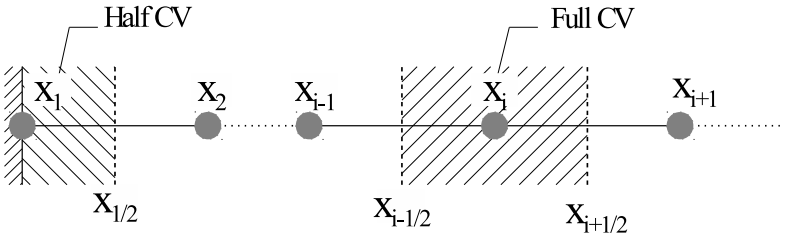

Figure 4.1 A schematic diagram for the CV formulation in 1D.

Ω_i results in

$$\int_{\Omega_i} \left(\frac{d^2u(x)}{dx^2} + \frac{du(x)}{dx} + u(x) \right) d\Omega_i = \int_{\Omega_i} f(x) d\Omega_i, \tag{4.6}$$

or

$$\frac{du(x_{i+1/2})}{dx} - \frac{du(x_{i-1/2})}{dx} + u(x_{i+1/2}) - u(x_{i-1/2}) + \int_{x_{i-1/2}}^{x_{i+1/2}} u(x)dx = \int_{x_{i-1/2}}^{x_{i+1/2}} f(x)dx. \tag{4.7}$$

The integrals on the left and right sides of equation (4.7) are evaluated using the middle point rule and also the three point Gaussian quadrature rule.

For the former, the integrals are expressed as

$$\int_{x_{i-1/2}}^{x_{i+1/2}} u(x)dx = u(x_i)\Delta x, \tag{4.8}$$

$$\int_{x_{i-1/2}}^{x_{i+1/2}} f(x)dx = f(x_i)\Delta x, \tag{4.9}$$

where $\Delta x = x_{i+1/2} - x_{i-1/2}$.

For the latter, the integrals are expressed as

$$\int_{x_{i-1/2}}^{x_{i+1/2}} u(x)dx = \frac{\Delta x}{2}\sum_{k=1}^{3}\gamma_k u(\frac{x_{i+1/2}-x_{i-1/2}}{2}\zeta_k + \frac{x_{i+1/2}+x_{i-1/2}}{2}), \tag{4.10}$$

$$\int_{x_{i-1/2}}^{x_{i+1/2}} f(x)dx = \frac{\Delta x}{2}\sum_{k=1}^{3}\gamma_k f(\frac{x_{i+1/2}-x_{i-1/2}}{2}\zeta_k + \frac{x_{i+1/2}+x_{i-1/2}}{2}), \tag{4.11}$$

$$\{\gamma_k\}_{k=1}^{3} = \left\{\frac{5}{9}, \frac{8}{9}, \frac{5}{9}\right\}, \quad \{\zeta_k\}_{k=1}^{3} = \left\{-\sqrt{\frac{3}{5}}, 0, +\sqrt{\frac{3}{5}}\right\}, \tag{4.12}$$

where γ_k and ζ_k are the weights and Gauss points, respectively.

We now approximate the field variable u and its derivatives in equations (4.7), (4.8) - (4.11) using compact local IRBFs. Over a 3-node stencil $[x_{i-1}, x_i, x_{i+1}]$ associated with grid node x_i, the relation between the physical space and the RBF weight space can be established as

$$\begin{pmatrix} u_{i-1} \\ u_i \\ u_{i+1} \\ f_{i-1} \\ f_{i+1} \end{pmatrix} = \underbrace{\begin{bmatrix} \mathcal{H}^{(0)} \\ \mathcal{K} \end{bmatrix}}_{\mathcal{C}} \begin{pmatrix} w_1 \\ w_2 \\ w_3 \\ c_1 \\ c_2 \end{pmatrix}, \tag{4.13}$$

where nodal values of the governing equation at grid nodes x_{i-1} and x_{i+1} (i.e. f_{i-1} and f_{i+1}) are also included, $\mathcal{C}$ is the conversion matrix, and $\mathcal{H}^{(0)}$ and $\mathcal{K}$ are submatrices defined as

$$\mathcal{H}^{(0)} = \begin{bmatrix} I_1^{(0)}(x_{i-1}), & I_2^{(0)}(x_{i-1}), & I_3^{(0)}(x_{i-1}), & x_{i-1}, & 1 \\ I_1^{(0)}(x_i), & I_2^{(0)}(x_i), & I_3^{(0)}(x_i), & x_i, & 1 \\ I_1^{(0)}(x_{i+1}), & I_2^{(0)}(x_{i+1}), & I_3^{(0)}(x_{i+1}), & x_{i+1}, & 1 \end{bmatrix},$$

$$\mathcal{K} = \begin{bmatrix} \mathcal{G}_1(x_{i-1}), & \mathcal{G}_2(x_{i-1}), & \mathcal{G}_3(x_{i-1}), & x_{i-1}+1, & 1 \\ \mathcal{G}_1(x_{i+1}), & \mathcal{G}_2(x_{i+1}), & \mathcal{G}_3(x_{i+1}), & x_{i+1}+1, & 1 \end{bmatrix},$$

in which $\mathcal{G}_k(x) = I_k^{(2)}(x) + I_k^{(1)}(x) + I_k^{(0)}(x)$ with $k \in \{1, 2, 3\}$. It is noted that the subscripts $i-1, i$ and $i+1$ are used to represent the nodes of the stencil in a global definition, while $1, 2$ and 3 denote the nodes of the stencil in a local definition.

Solving (4.13) yields

$$\begin{pmatrix} w_1 \\ w_2 \\ w_3 \\ c_1 \\ c_2 \end{pmatrix} = \mathcal{C}^{-1} \begin{pmatrix} u_{i-1} \\ u_i \\ u_{i+1} \\ f_{i-1} \\ f_{i+1} \end{pmatrix}. \tag{4.14}$$

Values of the field variable and its derivatives at an arbitrary point on the stencil can thus be calculated in the physical space as

$$u(x) = \left[\begin{array}{ccccc} I_1^{(0)}(x), & I_2^{(0)}(x), & I_3^{(0)}(x), & x, & 1 \end{array} \right] \mathcal{C}^{-1} \begin{pmatrix} \widehat{u} \\ \widehat{f} \end{pmatrix}, \tag{4.15}$$

$$\frac{du(x)}{dx} = \left[\begin{array}{ccccc} I_1^{(1)}(x), & I_2^{(1)}(x), & I_3^{(1)}(x), & 1, & 0 \end{array} \right] \mathcal{C}^{-1} \begin{pmatrix} \widehat{u} \\ \widehat{f} \end{pmatrix}, \tag{4.16}$$

$$\frac{d^2u(x)}{dx^2} = \left[\begin{array}{ccccc} I_1^{(2)}(x), & I_2^{(2)}(x), & I_3^{(2)}(x), & 0, & 0 \end{array} \right] \mathcal{C}^{-1} \begin{pmatrix} \widehat{u} \\ \widehat{f} \end{pmatrix}, \tag{4.17}$$

where $x_{i-1} < x < x_{i+1}$, $\widehat{u} = (u_{i-1}, u_i, u_{i+1})^T$, and $\widehat{f} = (f_{i-1}, f_{i+1})^T$.

We consider two types of boundary conditions

(i) Dirichlet boundary conditions: Since values of u are given at x_1 and x_n, the discretisation is carried out for full control volumes only.

(ii) Dirichlet and Neumann boundary conditions: Since the first derivative du/dx instead of the field variable u is given at a boundary node, one needs to generate one additional algebraic equation for the value of u at that node. This can be achieved by conducting the discretisation over a half control volume associated with the boundary node.

4.3.2 Two dimensional problems

Poisson equation

The governing equation here takes the form

$$\nabla^2 u(\mathbf{x}) = f(\mathbf{x}), \quad \mathbf{x} \in \Omega. \tag{4.18}$$

Rectangular domains:

We discretise the problem domain using a Cartesian grid of density $N_x \times N_y$. Control volumes associated with grid nodes are of rectangular shapes that do not overlap each other. Consider an interior node $\mathbf{x}_{i,j}$ $(2 \leq i \leq N_x - 1; 2 \leq j \leq N_y - 1)$. Its associated 9-node stencil is defined globally as

$$\begin{bmatrix} \mathbf{x}_{i-1,j+1} & \mathbf{x}_{i,j+1} & \mathbf{x}_{i+1,j+1} \\ \mathbf{x}_{i-1,j} & \mathbf{x}_{i,j} & \mathbf{x}_{i+1,j} \\ \mathbf{x}_{i-1,j-1} & \mathbf{x}_{i,j-1} & \mathbf{x}_{i+1,j-1} \end{bmatrix},$$

and locally as

$$\begin{bmatrix} \mathbf{x}_3 & \mathbf{x}_6 & \mathbf{x}_9 \\ \mathbf{x}_2 & \mathbf{x}_5 & \mathbf{x}_8 \\ \mathbf{x}_1 & \mathbf{x}_4 & \mathbf{x}_7 \end{bmatrix},$$

where the grid nodes are numbered from bottom to top and from left to right. Figure 4.2 shows a schematic diagram for a full control volume associated with an interior node and a half control volume associated with a boundary node.

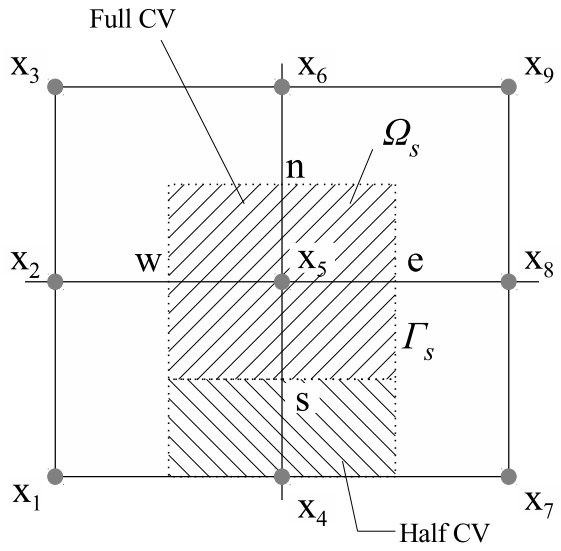

Figure 4.2 A schematic diagram for the CV formulation in 2D.

Integrating (4.18) over a full control volume Ω_s yields

$$\int_{\Omega_s} \nabla^2 u(\mathbf{x}) d\Omega_s = \int_{\Omega_s} f(\mathbf{x}) d\Omega_s. \tag{4.19}$$

By means of the divergence theorem, (4.19) reduces to

$$\oint_{\Gamma_s} \nabla u(\mathbf{x}) \cdot \widehat{n} d\Gamma_s = \int_{\Omega_s} f(\mathbf{x}) d\Omega_s, \tag{4.20}$$

or

$$\int_{y_s}^{y_n} \left.\frac{\partial u(\mathbf{x})}{\partial x}\right|_e dy - \int_{y_s}^{y_n} \left.\frac{\partial u(\mathbf{x})}{\partial x}\right|_w dy + \int_{x_w}^{x_e} \left.\frac{\partial u(\mathbf{x})}{\partial y}\right|_n dx - \int_{x_w}^{x_e} \left.\frac{\partial u(\mathbf{x})}{\partial y}\right|_s dx = \int_{\Omega_s} f(\mathbf{x}) d\Omega_s, \tag{4.21}$$

where Γ_s is the interface of the control volume, $\widehat{n}$ is the outward unit normal vector, and $|_e$, $|_w$, $|_n$ and $|_s$ denote the east, west, north and south faces of the control volume, respectively.

If the middle point rule is applied to (4.20), one obtains

$$\left(\frac{\partial u(\mathbf{x}_e)}{\partial x} - \frac{\partial u(\mathbf{x}_w)}{\partial x}\right) \Delta y + \left(\frac{\partial u(\mathbf{x}_n)}{\partial y} - \frac{\partial u(\mathbf{x}_s)}{\partial y}\right) \Delta x = \Delta x \Delta y f(\mathbf{x}), \tag{4.22}$$

where the subscripts e, w, n and s are used to indicate the intersections of the grid lines with the east, west, north and south faces of the control volume, respectively; $\Delta x = x_e - x_w$ and $\Delta y = y_n - y_s$.

If the three-point Gaussian quadrature rule is applied to (4.20), one obtains

$$\frac{\Delta y}{2}\sum_{j=1}^{3}\gamma_j\frac{\partial u(y(\zeta_j))}{dx}\bigg|_e-\frac{\Delta y}{2}\sum_{j=1}^{3}\gamma_j\frac{\partial u(y(\zeta_j))}{dx}\bigg|_w+\frac{\Delta x}{2}\sum_{i=1}^{3}\gamma_i\frac{\partial u(x(\zeta_i))}{dy}\bigg|_n$$
$$-\frac{\Delta x}{2}\sum_{i=1}^{3}\gamma_i\frac{\partial u(x(\zeta_i))}{dy}\bigg|_s=\frac{\Delta x\Delta y}{4}\sum_{i=1}^{3}\sum_{j=1}^{3}\gamma_i\gamma_j f\left(x(\zeta_i),y(\zeta_j)\right), \quad (4.23)$$

where γ_i and ζ_i are defined as before.

Now we approximate gradients in (4.22) and (4.23) using compact local IRBF approximations defined over overlapping 3×3 stencils. The conversion matrix for each stencil is constructed as

$$\begin{pmatrix}\widehat{u}\\ \widehat{0}\\ \widehat{f}\end{pmatrix}=\underbrace{\begin{bmatrix}\mathcal{H}_x^{(0)}, & \mathcal{O}\\ \mathcal{H}_x^{(0)}, & -\mathcal{H}_y^{(0)}\\ \mathcal{K}_x, & \mathcal{K}_y\end{bmatrix}}_{\mathcal{C}}\begin{pmatrix}\widehat{w}_x\\ \widehat{w}_y\end{pmatrix}, \quad (4.24)$$

where $\widehat{0}$ and $\mathcal{O}$ are a zero vector and zero matrix, respectively; $\widehat{u}$ and $\widehat{0}$ are vectors of length 9; $\widehat{w}_x$ and $\widehat{w}_y$ are the RBF coefficient vectors of length 15; $\mathcal{O}, \mathcal{H}_x^{(0)}, \mathcal{H}_y^{(0)}$ are matrices of dimensions 9×15, and $\mathcal{K}_x$ and $\mathcal{K}_y$ are matrices of dimensions 4×15. Equations $\widehat{u}=\mathcal{H}_x^{(0)}\widehat{w}_x$ are employed to collocate the variable u over the stencil; equations $\mathcal{H}_x^{(0)}\widehat{w}_x-\mathcal{H}_y^{(0)}\widehat{w}_y=\widehat{0}$ are employed to enforce nodal values of u obtained from the integration with respect to x and y to be identical; equations $\mathcal{K}_x\widehat{w}_x+\mathcal{K}_y\widehat{w}_y=\widehat{f}$ are employed to represent values of the PDE (4.18) at selected nodes;

$$\widehat{u}=\left(u_1,\cdots,u_9\right)^T,$$
$$\widehat{w}_x=\left(w_1^{[x]},\cdots,w_9^{[x]},c_1^{[x]}(y_1),c_1^{[x]}(y_2),c_1^{[x]}(y_3),c_2^{[x]}(y_1),c_2^{[x]}(y_2),c_2^{[x]}(y_3)\right)^T,$$
$$\widehat{w}_y=\left(w_1^{[y]},\cdots,w_9^{[y]},c_1^{[y]}(x_1),c_1^{[y]}(x_4),c_1^{[y]}(x_7),c_2^{[y]}(x_1),c_2^{[y]}(x_4),c_2^{[y]}(x_7)\right)^T,$$

$$\mathcal{H}_x^{(0)} = \begin{bmatrix} I_{[x]1}^{(0)}(\mathbf{x_1}), & \cdots, & I_{[x]9}^{(0)}(\mathbf{x_1}), & x_1, & 0, & 0, & 1, & 0, & 0 \\ I_{[x]1}^{(0)}(\mathbf{x_2}), & \cdots, & I_{[x]9}^{(0)}(\mathbf{x_2}), & 0, & x_2, & 0, & 0, & 1, & 0 \\ I_{[x]1}^{(0)}(\mathbf{x_3}), & \cdots, & I_{[x]9}^{(0)}(\mathbf{x_3}), & 0, & 0, & x_3, & 0, & 0, & 1 \\ I_{[x]1}^{(0)}(\mathbf{x_4}), & \cdots, & I_{[x]9}^{(0)}(\mathbf{x_4}), & x_1, & 0, & 0, & 1, & 0, & 0 \\ I_{[x]1}^{(0)}(\mathbf{x_5}), & \cdots, & I_{[x]9}^{(0)}(\mathbf{x_5}), & 0, & x_2, & 0, & 0, & 1, & 0 \\ I_{[x]1}^{(0)}(\mathbf{x_6}), & \cdots, & I_{[x]9}^{(0)}(\mathbf{x_6}), & 0, & 0, & x_3, & 0, & 0, & 1 \\ I_{[x]1}^{(0)}(\mathbf{x_7}), & \cdots, & I_{[x]9}^{(0)}(\mathbf{x_7}), & x_1, & 0, & 0, & 1, & 0, & 0 \\ I_{[x]1}^{(0)}(\mathbf{x_8}), & \cdots, & I_{[x]9}^{(0)}(\mathbf{x_8}), & 0, & x_2, & 0, & 0, & 1, & 0 \\ I_{[x]1}^{(0)}(\mathbf{x_9}), & \cdots, & I_{[x]9}^{(0)}(\mathbf{x_9}), & 0, & 0, & x_3, & 0, & 0, & 1 \end{bmatrix},$$

$$\mathcal{H}_y^{(0)} = \begin{bmatrix} I_{[y]1}^{(0)}(\mathbf{x_1}), & \cdots, & I_{[y]9}^{(0)}(\mathbf{x_1}), & y_1, & 0, & 0, & 1, & 0, & 0 \\ I_{[y]1}^{(0)}(\mathbf{x_2}), & \cdots, & I_{[y]9}^{(0)}(\mathbf{x_2}), & y_2, & 0, & 0, & 1, & 0, & 0 \\ I_{[y]1}^{(0)}(\mathbf{x_3}), & \cdots, & I_{[y]9}^{(0)}(\mathbf{x_3}), & y_3, & 0, & 0, & 1, & 0, & 0 \\ I_{[y]1}^{(0)}(\mathbf{x_4}), & \cdots, & I_{[y]9}^{(0)}(\mathbf{x_4}), & 0, & y_4, & 0, & 0, & 1, & 0 \\ I_{[y]1}^{(0)}(\mathbf{x_5}), & \cdots, & I_{[y]9}^{(0)}(\mathbf{x_5}), & 0, & y_5, & 0, & 0, & 1, & 0 \\ I_{[y]1}^{(0)}(\mathbf{x_6}), & \cdots, & I_{[y]9}^{(0)}(\mathbf{x_6}), & 0, & y_6, & 0, & 0, & 1, & 0 \\ I_{[y]1}^{(0)}(\mathbf{x_7}), & \cdots, & I_{[y]9}^{(0)}(\mathbf{x_7}), & 0, & 0, & y_7, & 0, & 0, & 1 \\ I_{[y]1}^{(0)}(\mathbf{x_8}), & \cdots, & I_{[y]9}^{(0)}(\mathbf{x_8}), & 0, & 0, & y_8, & 0, & 0, & 1 \\ I_{[y]1}^{(0)}(\mathbf{x_9}), & \cdots, & I_{[y]9}^{(0)}(\mathbf{x_9}), & 0, & 0, & y_9, & 0, & 0, & 1 \end{bmatrix}.$$

In this study, selected nodes for $\mathcal{K}_x\widehat{w}_x + \mathcal{K}_y\widehat{w}_y = \widehat{f}$ are chosen as $(\mathbf{x}_2, \mathbf{x}_4, \mathbf{x}_6, \mathbf{x}_8)$ so that

$$\mathcal{K}_x = \begin{bmatrix} I_{[x]1}^{(2)}(\mathbf{x_2}), & \cdots, & I_{[x]9}^{(2)}(\mathbf{x_2}), & 0, & 0, & 0, & 0, & 0, & 0 \\ I_{[x]1}^{(2)}(\mathbf{x_4}), & \cdots, & I_{[x]9}^{(2)}(\mathbf{x_4}), & 0, & 0, & 0, & 0, & 0, & 0 \\ I_{[x]1}^{(2)}(\mathbf{x_6}), & \cdots, & I_{[x]9}^{(2)}(\mathbf{x_6}), & 0, & 0, & 0, & 0, & 0, & 0 \\ I_{[x]1}^{(2)}(\mathbf{x_8}), & \cdots, & I_{[x]9}^{(2)}(\mathbf{x_8}), & 0, & 0, & 0, & 0, & 0, & 0 \end{bmatrix},$$

$$\mathcal{K}_y = \begin{bmatrix} I_{[y]1}^{(2)}(\mathbf{x_2}), & \cdots, & I_{[y]9}^{(2)}(\mathbf{x_2}), & 0, & 0, & 0, & 0, & 0, & 0 \\ I_{[y]1}^{(2)}(\mathbf{x_4}), & \cdots, & I_{[y]9}^{(2)}(\mathbf{x_4}), & 0, & 0, & 0, & 0, & 0, & 0 \\ I_{[y]1}^{(2)}(\mathbf{x_6}), & \cdots, & I_{[y]9}^{(2)}(\mathbf{x_6}), & 0, & 0, & 0, & 0, & 0, & 0 \\ I_{[y]1}^{(2)}(\mathbf{x_8}), & \cdots, & I_{[y]9}^{(2)}(\mathbf{x_8}), & 0, & 0, & 0, & 0, & 0, & 0 \end{bmatrix}.$$

Solving (4.24) yields

$$\begin{pmatrix} \widehat{w}_x \\ \widehat{w}_y \end{pmatrix} = \mathcal{C}^{-1}\left(\widehat{u}, \widehat{0}, \widehat{f}\right)^T, \tag{4.25}$$

or $\widehat{w}_x = \mathcal{C}_x^{-1}(\widehat{u}, \widehat{0}, \widehat{f})^T$ and $\widehat{w}_y = \mathcal{C}_y^{-1}(\widehat{u}, \widehat{0}, \widehat{f})^T$, where $\mathcal{C}_x^{-1}$ and $\mathcal{C}_y^{-1}$ are the first and the last 15 rows of matrix $\mathcal{C}^{-1}$. Substitution of $\widehat{w}_x$ and $\widehat{w}_y$ into (4.3) defined over the stencil leads to

$$\frac{\partial u(\mathbf{x})}{\partial x} = \mathcal{H}_x^{(1)}(\mathbf{x})\mathcal{C}_x^{-1}(\widehat{u}, \widehat{0}, \widehat{f})^T, \tag{4.26}$$

$$\frac{\partial u(\mathbf{x})}{\partial y} = \mathcal{H}_y^{(1)}(\mathbf{x})\mathcal{C}_y^{-1}(\widehat{u}, \widehat{0}, \widehat{f})^T, \tag{4.27}$$

where

$$\mathcal{H}_x^{(1)}(\mathbf{x}) = \left[I_{[x]1}^{(1)}(\mathbf{x}), \cdots, I_{[x]9}^{(1)}(\mathbf{x}), J_{[y]1}(y), J_{[y]2}(y), J_{[y]3}(y), 0, 0, 0\right], \tag{4.28}$$

$$\mathcal{H}_y^{(1)}(\mathbf{x}) = \left[I_{[y]1}^{(1)}(\mathbf{x}), \cdots, I_{[y]9}^{(1)}(\mathbf{x}), J_{[x]1}(x), J_{[x]2}(x), J_{[x]3}(x), 0, 0, 0\right], \tag{4.29}$$

in which $\{J_{[y]1}(y), J_{[y]2}(y), J_{[y]3}(y)\}$ and $\{J_{[x]1}(x), J_{[x]2}(x), J_{[x]3}(x)\}$ are sets of basis functions used for the approximation of integration "constants" $C_1^{[x]}(y)$ and $C_1^{[y]}(x)$ in equations (4.3)-(4.4), respectively

$$C_1^{[x]}(y) = c_1^{[x]}(y_1)J_{[y]1}(y) + c_1^{[x]}(y_2)J_{[y]2}(y) + c_1^{[x]}(y_3)J_{[y]3}(y), \tag{4.30}$$

$$C_1^{[y]}(x) = c_1^{[y]}(x_1)J_{[x]1}(x) + c_1^{[y]}(x_4)J_{[x]2}(x) + c_1^{[y]}(x_7)J_{[x]3}(x). \tag{4.31}$$

In a similar way, values of the field variable and its second derivatives are obtained by substituting $\widehat{w}_x$ and $\widehat{w}_y$ into (4.4) and (4.1), respectively.

It can be seen that the approximations for u and its derivatives are expressed in terms of nodal values of the field variable and of the governing equation. For Dirichlet boundary conditions only, the discretisation is carried out over full control volumes associated with interior grid nodes. For Neumann boundary conditions, extra equations are needed and they are generated from half control volumes associated with the boundary nodes.

Non-rectangular domains:

We embed the problem domain in a rectangular domain and then discretise it using a Cartesian grid of density $N_x \times N_y$. Only Dirichlet boundary conditions are considered here. There are three types of nodes, namely (i) the boundary nodes (the intersections of the grid lines and the boundary); (ii) normal interior nodes, where their associated stencils lie within the problem domain entirely; and (iii) special interior nodes, where their associated stencils are cut by the boundary. For the third type, which is typically illustrated in Figure 4.3, some special treatments are required. We employ nodes $[\mathbf{x}_1, \mathbf{x}_{2'}, \mathbf{x}_3, \mathbf{x}_4, \mathbf{x}_{5'}, \mathbf{x}_6, \mathbf{x}_7, \mathbf{x}_8]$ for the IRBF approximations with respect to the x direction, and $[\mathbf{x}_1, \mathbf{x}_2, \mathbf{x}_3, \mathbf{x}_4, \mathbf{x}_5, \mathbf{x}_6, \mathbf{x}_7, \mathbf{x}_8]$ for the y direction. Furthermore, in the conversion process (4.24), the governing equation is collocated at regular grid nodes only (e.g. $\mathbf{x}_3$ and $\mathbf{x}_7$). Note that the intersections of the x and y grid lines are considered as regular nodes, while the intersections of the grid lines and the non-rectangular boundaries are considered as irregular nodes. The remaining tasks here are similar to those of the rectangular-domain case.

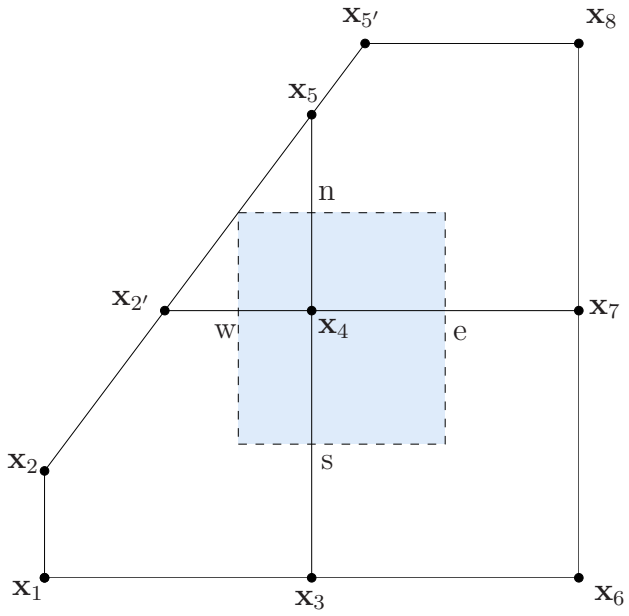

Figure 4.3 A schematic diagram for the CV formulation in 2D, where the stencil is cut by the boundary.

Natural convection flow

The dimensionless governing equations for natural convection flow can be written in terms of the streamfunction ψ, vorticity ω, and temperature T as

$$\frac{\partial T}{\partial t} + \sqrt{RaPr}\left(\frac{\partial (v_x T)}{\partial x} + \frac{\partial (v_y T)}{\partial y}\right) = \frac{\partial^2 T}{\partial x^2} + \frac{\partial^2 T}{\partial y^2}, \tag{4.32}$$

$$-\omega = \frac{\partial^2 \psi}{\partial x^2} + \frac{\partial^2 \psi}{\partial y^2}, \tag{4.33}$$

$$\frac{\partial \omega}{\partial t} + \sqrt{\frac{Ra}{Pr}}\left(\frac{\partial (v_x \omega)}{\partial x} + \frac{\partial (v_y \omega)}{\partial y} - \frac{\partial T}{\partial x}\right) = \frac{\partial^2 \omega}{\partial x^2} + \frac{\partial^2 \omega}{\partial y^2}, \tag{4.34}$$

where $v_x = \dfrac{\partial \psi}{\partial y}$ and $v_y = -\dfrac{\partial \psi}{\partial x}$, Ra is the Rayleigh number, and Pr is the Prandtl number. Integrating (4.32)-(4.34) over a control volume Ω_s results in

$$\frac{\partial}{\partial t}\int_{\Omega_s} T d\Omega_s + \sqrt{RaPr}\int_{\Omega_s}\left(\frac{\partial (v_x T)}{\partial x} + \frac{\partial (v_y T)}{\partial y}\right) d\Omega_s = \int_{\Omega_s}\left(\frac{\partial^2 T}{\partial x^2} + \frac{\partial^2 T}{\partial y^2}\right) d\Omega_s, \tag{4.35}$$

$$-\int_{\Omega_s} \omega d\Omega_s = \int_{\Omega_s}\left(\frac{\partial^2 \psi}{\partial x^2} + \frac{\partial^2 \psi}{\partial y^2}\right) d\Omega_s, \tag{4.36}$$

$$\frac{\partial}{\partial t}\int_{\Omega_s} \omega d\Omega_s + \sqrt{\frac{Ra}{Pr}}\int_{\Omega_s}\left(\frac{\partial (v_x \omega)}{\partial x} + \frac{\partial (v_y \omega)}{\partial y} - \frac{\partial T}{\partial x}\right) d\Omega_s = \int_{\Omega_s}\left(\frac{\partial^2 \omega}{\partial x^2} + \frac{\partial^2 \omega}{\partial y^2}\right) d\Omega_s. \tag{4.37}$$

Assume that T and ω are linear over the time interval $(t^{(n-1)}, t^{(n)})$, the time derivative terms in (4.35) and (4.37) reduce to

$$\frac{\partial}{\partial t}\int_{\Omega_s} T d\Omega_s = \frac{\int_{\Omega_s} T^{(n)} d\Omega_s - \int_{\Omega_s} T^{(n-1)} d\Omega_s}{\Delta t}, \tag{4.38}$$

$$\frac{\partial}{\partial t}\int_{\Omega_s} \omega d\Omega_s = \frac{\int_{\Omega_s} \omega^{(n)} d\Omega_s - \int_{\Omega_s} \omega^{(n-1)} d\Omega_s}{\Delta t}, \tag{4.39}$$

where the superscript (n) is used to indicate the current time level. Using the middle point rule, expressions (4.38) and (4.39) further reduce to

$$\frac{\partial}{\partial t}\int_{\Omega_s} T d\Omega_s = \frac{A}{\Delta t}\left(T^{(n)} - T^{(n-1)}\right), \tag{4.40}$$

$$\frac{\partial}{\partial t}\int_{\Omega_s} \omega d\Omega_s = \frac{A}{\Delta t}\left(\omega^{(n)} - \omega^{(n-1)}\right), \tag{4.41}$$

where A is the area of Ω_s.

We calculate the convection terms in the form

$$\int_{\Omega_s}\left(\frac{\partial(v - xT)}{\partial x} + \frac{\partial(v_y T)}{\partial y}\right) d\Omega_s = \int_{x_w}^{x_e} (v_y T)\Big|_n dx - \int_{x_w}^{x_e} (v_y T)\Big|_s dx + \int_{y_s}^{y_n} (v_x T)\Big|_e dy - \int_{y_s}^{y_n} (v_x T)\Big|_w dy, \tag{4.42}$$

$$\int_{\Omega_s}\left(\frac{\partial(v_x\omega)}{\partial x} + \frac{\partial(v_y\omega)}{\partial y} - \frac{\partial(T)}{\partial x}\right) d\Omega_s = \int_{x_w}^{x_e} (v_y \omega)\Big|_n dx - \int_{x_w}^{x_e} (v_y \omega)\Big|_s dx + \int_{y_s}^{y_n} (v_x\omega - T)\Big|_e dy - \int_{y_s}^{y_n} (v_x\omega - T)\Big|_w dy, \tag{4.43}$$

and treat the diffusion terms in the same way as for Poisson equation in Section 3.2.1.

Boundary conditions for the vorticity equation (4.34) are not given explicitly. One can compute them through equation (4.33) using given derivative boundary conditions for the streamfunction. In the case of rectangular boundaries, values of $\partial\psi/\partial n$ are incorporated into the computational boundary conditions for ω by means of the integration constants (Mai-Duy, 2005; Mai-Duy and Tanner, 2005b). In the case of irregular boundaries, we apply the equations reported in (Le-Cao et al., 2009)

$$\omega_b = -\left[1 + \left(\frac{t_x}{t_y}\right)^2\right]\frac{\partial^2\psi_b}{\partial x^2} - q_y, \tag{4.44}$$

$$\omega_b = -\left[1 + \left(\frac{t_y}{t_x}\right)^2\right]\frac{\partial^2\psi_b}{\partial y^2} - q_x, \tag{4.45}$$

where $t_x = \partial x/\partial s$, $t_y = \partial y/\partial s$, s is the tangential direction of boundary, and q_x, q_y are the known quantities defined as

$$q_x = -\frac{t_y}{t_x^2}\frac{\partial^2\psi_b}{\partial y\partial s} + \frac{1}{t_x}\frac{\partial^2\psi_b}{\partial x\partial s}, \tag{4.46}$$

$$q_y = -\frac{t_x}{t_y^2}\frac{\partial^2\psi_b}{\partial x\partial s} + \frac{1}{t_y}\frac{\partial^2\psi_b}{\partial y\partial s}. \tag{4.47}$$

The solution procedure involves the following steps

1. Solve equation (4.36) for ψ, subject to Dirichlet conditions
2. Compute the velocity components v_x and v_y, and the boundary values for the vorticity ω
3. Solve equation (4.35) for T, subject to Dirichlet and Neumann boundary conditions for natural convection in a square slot (Example 4.4.4), and to Dirichlet boundary conditions for natural convection in an annulus (Example 4.4.4)
4. Solve equation (4.37) for ω, subject to Dirichlet conditions
5. Repeat the above steps until the solution has reached the steady state.

4.4 Numerical examples

The proposed CLIRBF-FVM is verified in a series of 1D and 2D problems. If the exact solution is available, the accuracy of the approximate solution is measured using the relative discrete L_2 norm

$$Ne(u) = \frac{\sqrt{\sum_{i=1}^{N} (u_i - u_i^e)^2}}{\sqrt{\sum_{i=1}^{N} (u_i^e)^2}}, \tag{4.48}$$

where N is the number of collocation nodes, and u_i and u_i^e are the computed and exact solutions, respectively. We simply choose the MQ width as $a_i = \beta h$, where β is a given number, and h is a grid spacing. Results by the standard FVM (Patankar, 1980) and the point-collocation method employed with compact local IRBF stencils (CLIRBF-PCM) (Mai-Duy and Tran-Cong, 2011) are also included to provide the base for the assessment of the performance of the present method.

4.4.1 Example 1 (1D problem)

Consider the following ODE

$$\frac{\partial^2 u}{\partial x^2} + \frac{\partial u}{\partial x} + u = -\exp(-5x)\left[9979\sin(100x) + 900\cos(100)\right], \quad 0 \le x \le 1. \tag{4.49}$$

The exact solution to this problem is taken as $u^e(x) = \exp(-5x)\sin(100x)$. We discretise the domain using $\{71, 73, \ldots, 591\}$ uniformly distributed nodes. The solution accuracy and the matrix condition number versus the grid size are shown in Figure 4.4 for Dirichlet boundary conditions only and in Figure 4.5 for Dirichlet and Neumann boundary conditions.

It can be seen that the proposed CLIRBF-FVM (1 Gauss point) outperforms the standard FVM, and the proposed CLIRBF-FVM (3 Gausss point) outperforms

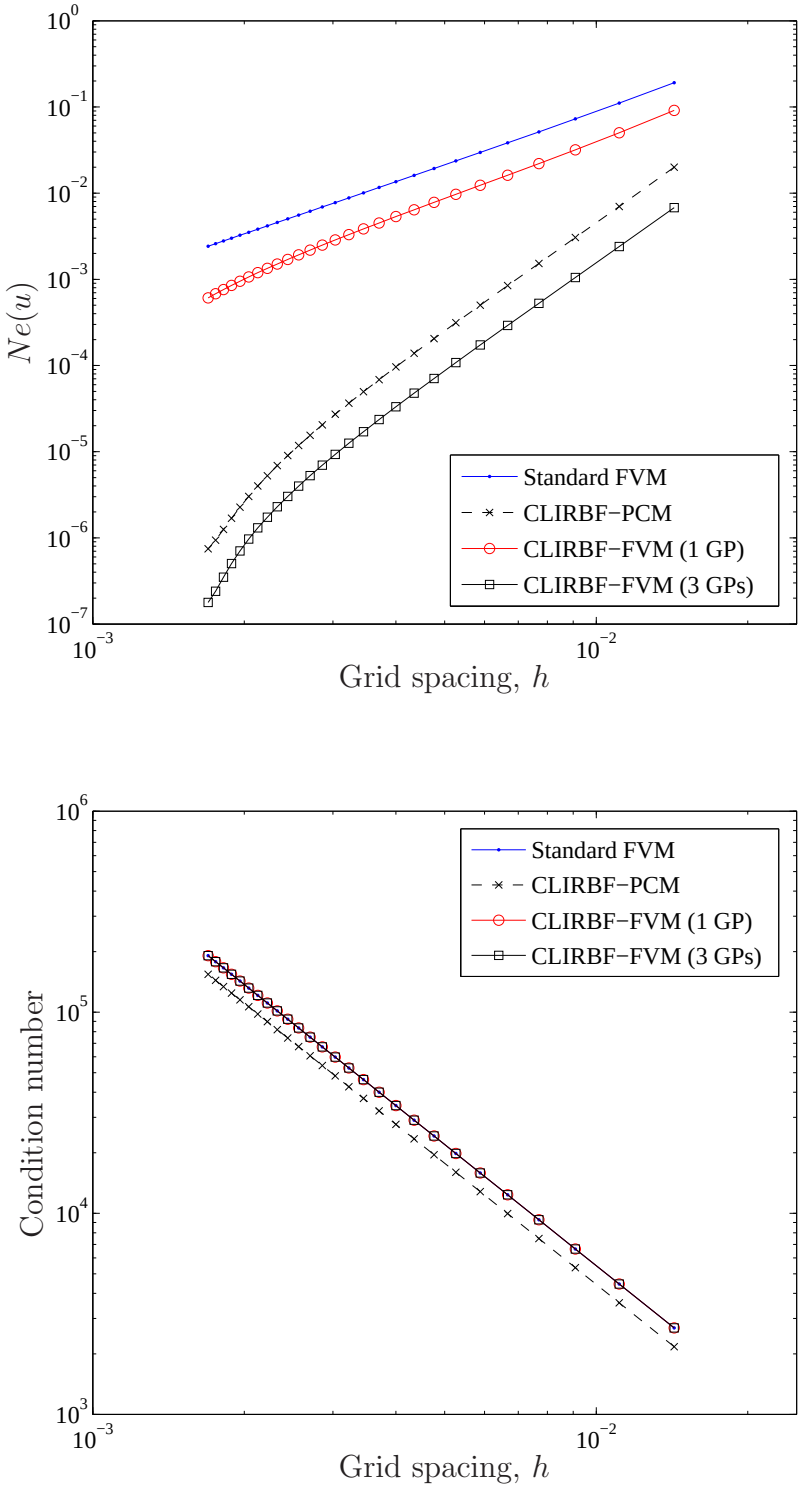

Figure 4.4 Example 1, ODE, Dirichlet boundary conditions: Relative L_2 errors of the solution u (top) and condition numbers of the system matrix (bottom) against the grid size by the standard FVM, CLIRBF-PCM, CLIRBF-FVM (1 Gauss point) and CLIRBF-FVM (3 Gauss points). Their behaviours are, respectively, $O(h^{2.03})$, $O(h^{4.72})$, $O(h^{2.30})$ and $O(h^{4.81})$ for the solution accuracy, and $O(h^{2.00})$, $O(h^{2.00})$, $O(h^{2.00})$ and $O(h^{2.00})$ for the matrix condition number.

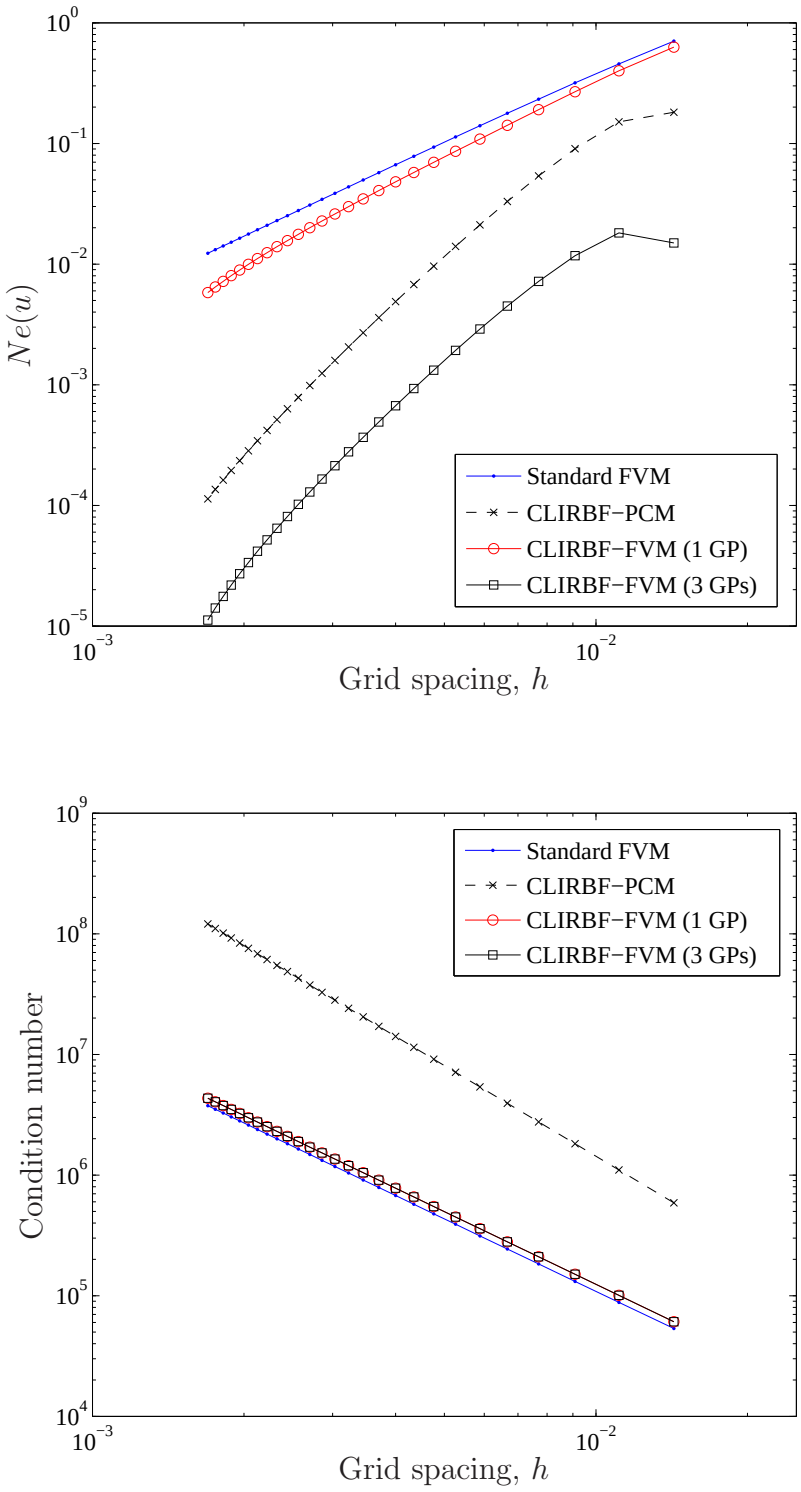

Figure 4.5 Example 1, ODE, Dirichlet and Neumann boundary conditions: Relative L_2 errors of the solution u (top) and condition numbers of the system matrix (bottom) against the grid size by the standard FVM, CLIRBF-PCM, CLIRBF-FVM (1 Gauss point) and CLIRBF-FVM (3 Gauss points). Their behaviours are, respectively, $O(h^{1.93})$, $O(h^{3.83})$, $O(h^{2.22})$ and $O(h^{3.88})$ for the solution accuracy, and $O(h^{2.00})$, $O(h^{2.50})$, $O(h^{2.00})$ and $O(h^{2.00})$ for the matrix condition number.

CLIRBF-PCM regarding both the solution accuracy and convergence rate. High rates of convergence are obtained with CLIRBF-FVM employed with the 3-point Gaussian quadrature rule as expected. The control-volume formulation is much more accurate than the point-collocation formulation, especially for the case of Neumann boundary conditions. Regarding the numerical stability, the condition numbers of the system matrix by the present method are similar to those by the standard FVM and CLIRBF-PCM for the case of Dirichlet boundary conditions only, but much lower than those by CLIRBF-PCM for the case of Dirichlet and Neumann boundary conditions.

4.4.2 Example 2 (2D problem, rectangular domain)

We take the following Poisson equation to verify the present method

$$\frac{\partial^2 u}{\partial x^2} + \frac{\partial^2 u}{\partial y^2} = 4(1-\pi^2)\sin(2\pi x)\sinh(2y) + 16(1-\pi^2)\cosh(4x)\cos(4\pi y), \quad (4.50)$$

where $-0.5 \leq x, y \leq 0.5$. Its exact solution is given by $u^e(x,y) = \sin(2\pi x)\sinh(2y) + \cosh(4x)\cos(4\pi y)$. The calculation is carried out with several grid densities $\{7\times 7, 9\times 9, \ldots, 71\times 71\}$. The solution accuracy and condition number by CLIRBF-FVM and CLIRBF-PCM are shown in Figures 4.6 and 4.7. The former is for Dirichlet boundary conditions, while the latter is for Dirichlet and Neumann boundary conditions, where u is specified on the left and right boundaries ($x = -0.5$ and $x = 0.5$) and $\partial u/\partial x$ is prescribed on the bottom and top boundaries ($y = -0.5$ and $y = 0.5$). Remarks here are similar to the 1D problems, using the middle-point rule is able to lead to a solution $O(h^2)$, while the 3-point Gaussian quadrature rule results in a solution with a very high rate of convergence, up to $O(h^{5.03})$.

Figure 4.8 shows the influence of the MQ width measured via β on the solution accuracy, which is investigated on three grids $\{31\times 31, 41\times 41, 51\times 51\}$. It can be seen that the present scheme can work well for a wide range of β. However, the optimal value of β and its stable range (e.g. 20 to 60 in this particular example) are problem-dependent. Generally, one needs to choose small values of β when the solution involves steep gradients.

4.4.3 Example 3 (2D problem, non-rectangular domain)

Consider the same PDE as in Example 2. However, the domain of interest is of circular shape of radius 1/2 and the boundary conditions are of Dirichlet type (Figure 4.9). Results obtained are presented in Figure 4.10. It shows that the numerical solution converges fast - apparently as $O(h^4)$ - for both CLIRBF-PCM and CLIRBF-FVM (3 Gauss points), and CLIRBF-FVM is more stable than CLIRBF-PCM. It also shows that the 1-point Gaussian quadrature scheme results in larger error than 3-point scheme. The error of the former is of order h^2 only at fine grids.

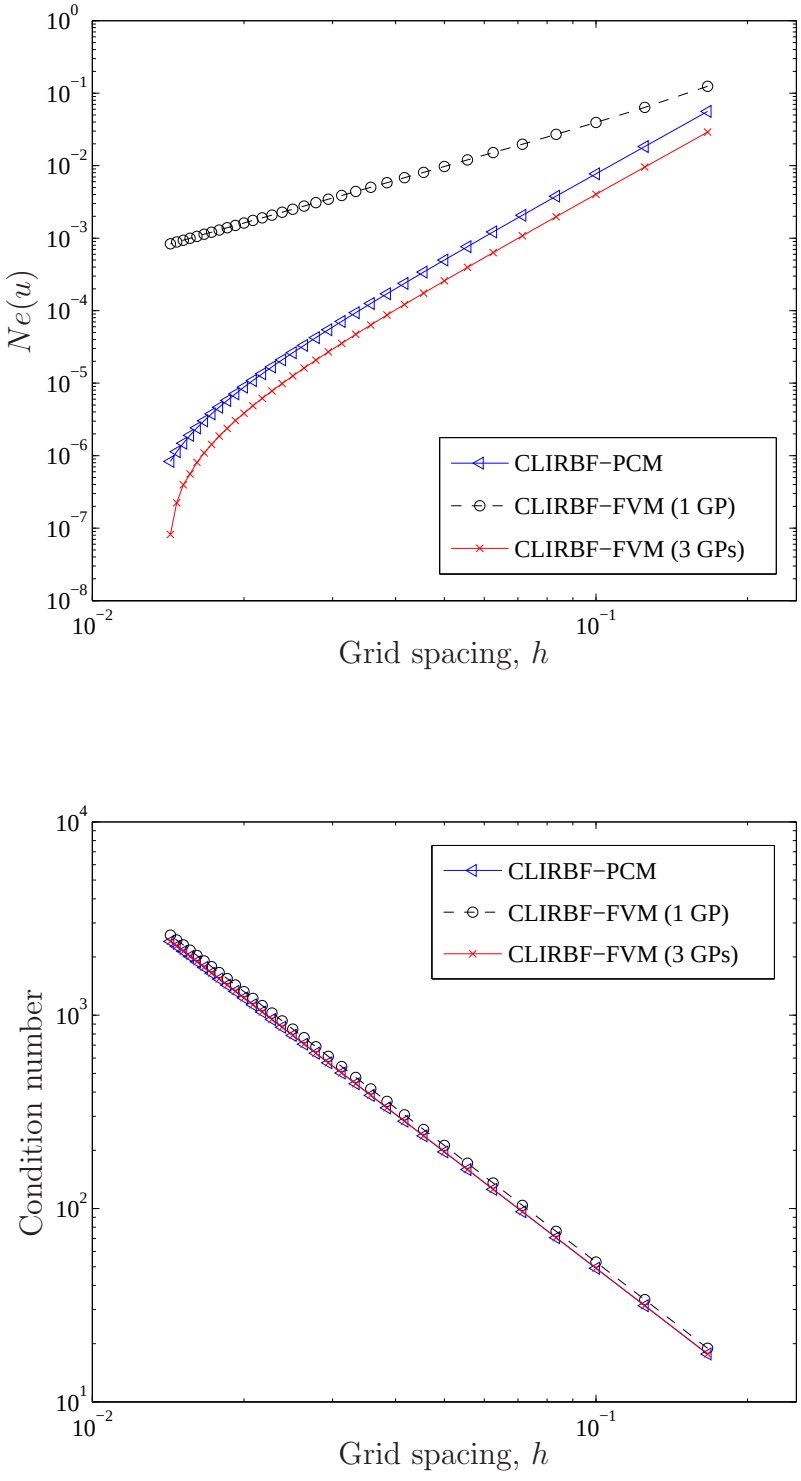

Figure 4.6 Example 2, PDE, rectangular domain, Dirichlet boundary condition: Relative L_2 errors of the solution u (top) and condition numbers of the system matrix (bottom) against the grid size by the CLIRBF-PCM, CLIRBF-FVM (1 Gauss point) and CLIRBF-FVM (3 Gauss points). Their behaviours are, respectively, $O(h^{4.42})$, $O(h^{2.00})$ and $O(h^{4.72})$ for the solution accuracy, and $O(h^{2.00})$, $O(h^{2.00})$ and $O(h^{2.00})$ for the matrix condition number.

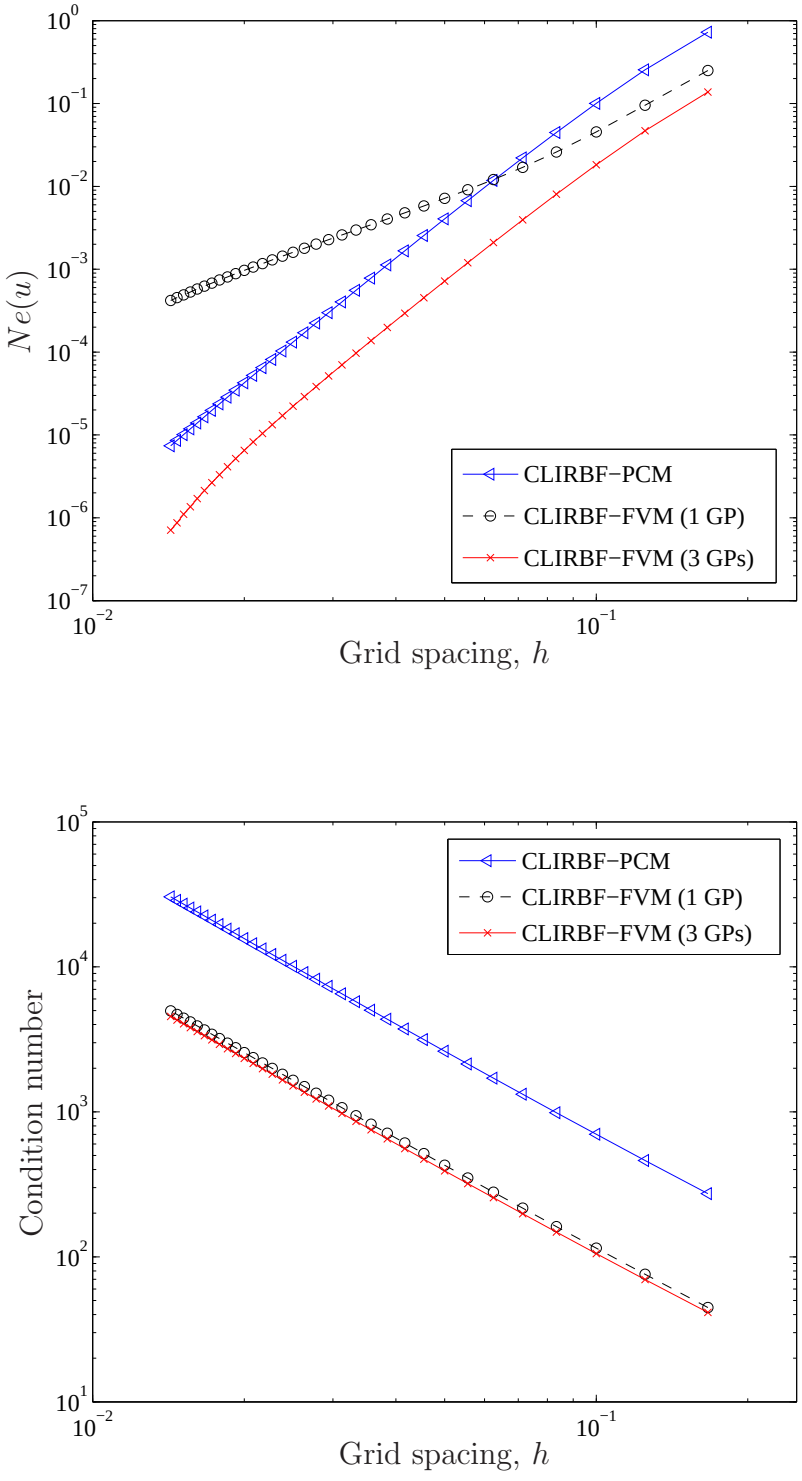

Figure 4.7 Example 2, PDE, rectangular domain, Dirichlet and Neumann boundary conditions: Relative L_2 errors of the solution u (top) and condition numbers of the system matrix (bottom) against the grid size by the CLIRBF-PCM, CLIRBF-FVM (1 Gauss point) and CLIRBF-FVM (3 Gauss points). Their behaviours are, respectively, $O(h^{4.82})$, $O(h^{2.42})$ and $O(h^{5.03})$ for the solution accuracy, and $O(h^{1.93})$, $O(h^{1.93})$ and $O(h^{1.93})$ for the matrix condition number.

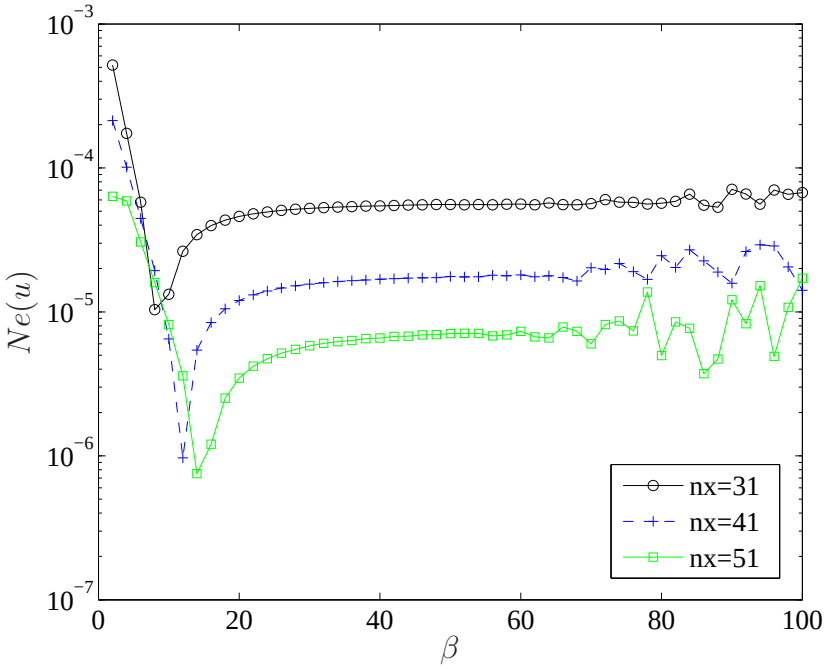

Figure 4.8 Example 2, PDE, rectangular domain, $N = \{31 \times 31, 41 \times 41, 51 \times 51\}$: the effect of the MQ width on the solution accuracy.

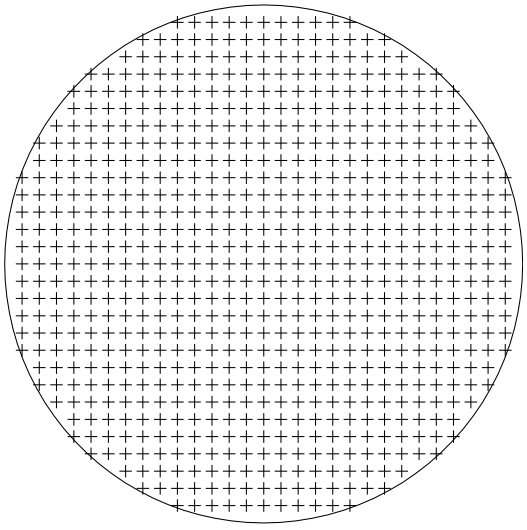

Figure 4.9 Non-rectangular domain: circular domain and its discretisation

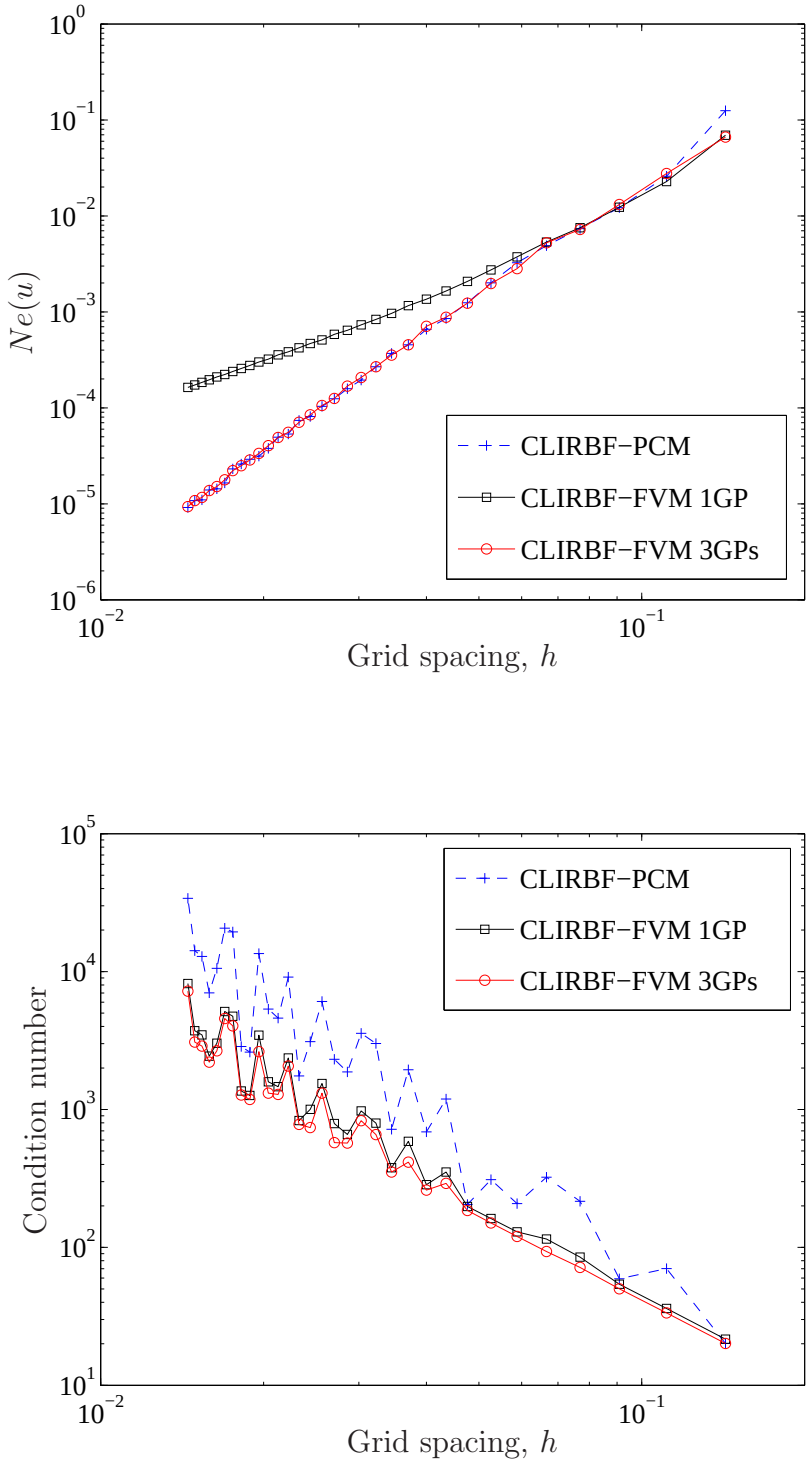

Figure 4.10 Example 3, PDE, non-rectangular domain, Dirichlet boundary condition: Relative L_2 errors of the solution u and condition numbers of the system matrix against the grid size by the CLIRBF-PCM, CLIRBF-FVM (1 Gauss point) and CLIRBF-FVM (3 Gauss points). Their behaviours are, respectively, $O(h^{4.03})$, $O(h^{2.44})$ and $O(h^{3.98})$ for the solution accuracy, and $O(h^{2.85})$, $O(h^{2.39})$ and $O(h^{2.37})$ for the matrix condition number.

4.4.4 Example 4: Thermally-Driven Cavity Flow Problem

Natural convection in a square slot

Consider a flow in a stationary unit square cavity ($0 \leq x, y \leq 1$), where the two side walls are heated with $T = 1$ at $x = 0$ and $T = 0$ at $x = 1$, while the top and the bottom walls are insulated ($\partial T/\partial y = 0$ at $y = 0$ and $y = 1$) (Figure 4.11). The no-slip boundary conditions lead to $\psi = 0$ and $\partial\psi/\partial n = 0$ on the four walls.

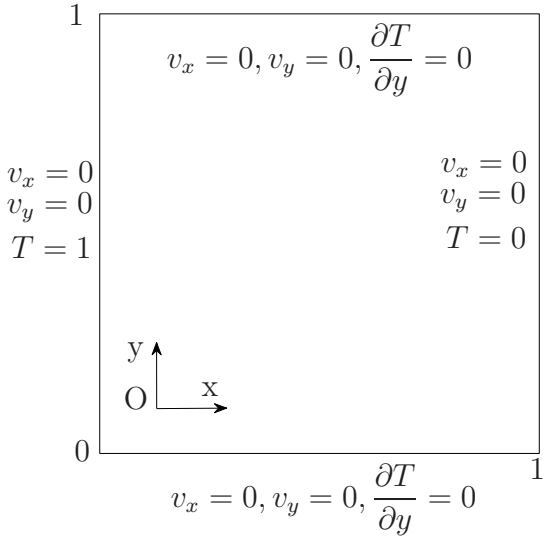

Figure 4.11 Geometry and boundary conditions for natural convection in a square slot.

Some important measures associated with this type of flow are

- Maximum horizontal velocity $v_{x\ max}$ on the vertical mid-plane and its location
- Maximum vertical velocity $v_{y\ max}$ on the horizontal mid-plane and its location
- The average Nusselt number throughout the cavity, which is defined as

$$\overline{Nu} = \int_0^1 Nu(x)dx, \tag{4.51}$$

$$Nu(x) = \int_0^1 \left(v_x T - \frac{\partial T}{\partial x}\right) dy, \tag{4.52}$$

  in which $(v_x T - \partial T/\partial x)$ is the local heat flux in the horizontal direction
- The average Nusselt number on the vertical plane at $x = 0$ (left wall) and at $x = 1/2$ (middle cross-section), which are defined by

$$Nu_0 = Nu(x = 0, y)$$
$$Nu_{1/2} = Nu(x = 1/2, y)$$

A wide range of Ra, $(10^3, 10^4, \ldots, 10^7)$, and $Pr = 0.71$ are considered. The initial solution is taken from the computed solution at the lower and nearest value of Ra. For $Ra = 10^3$, the simulation starts with the fluid at rest.

Table 4.1 shows results obtained by the present method using the 3-point Gaussian quadrature rule, the benchmark solutions provided by G. De Vahl Davis (Davis, 1983) for $10^3 \leq Ra \leq 10^6$, and by P. Le Quere (Quere, 1991) for $Ra \geq 10^6$, and some other numerical results. It can be seen that (i) very good agreement is achieved between these results; and (ii) the present solutions are in better agreement with the benchmark ones than those obtained by the Galerkin-RBF approach (Ho-Minh et al., 2009), and the thermal BGK lattice Boltzmann (Hao-Chueh et al., 2010). Figure 4.12 displays the distribution of the streamfunction, vorticity and temperature over the flow domain. They look feasible in comparison with those reported in the literature.

Natural convection in a concentric annulus between an outer square cylinder and an inner circular cylinder

The geometry and boundary condition of the problem are displayed in Figure 4.13. We take the ratio between the radius R of the inner cylinder and the side length L of the outer square to be 0.2. The Prandtl number is fixed at 0.71 and the Rayleigh number is varied in a range of $(10^4, 5 \times 10^4, 10^5, 5 \times 10^5, 10^6)$. The average Nusselt number is defined by

$$Nu = -\frac{1}{k} \oint \frac{\partial T}{\partial n} ds, \tag{4.53}$$

where k is the thermal conductivity.

Results concerning the average Nusselt number at the outer walls Nu_o and at the inner walls Nu_i are presented in Table 4.2. They agree well with other results ((Le-Cao et al., 2009; Moukalled and Acharya, 1996; Shu and Zhu, 2002; Ngo-Cong et al., 2012a)).

Figure 4.14 shows the contours of the streamfunction, vorticity, and temperature of the flow for several values of the Rayleigh number. At $Ra = 10^4$, their distributions are nearly symmetric about the horizontal axis across the cylinder centre. These distributions become more unsymmetric with increasing Ra (higher convection strength).

4.5 Concluding remarks

This chapter presents a new finite-volume method for the simulation of heat transfer and fluid flow problems on rectangular and nonrectangular domains. The use of compact local IRBF approximations instead of the usual linear interpolations to represent the field variable and the employment of high-order integration schemes rather than the middle-point rule can lead to a significant improvement in accuracy for a finite-volume solution. The method is verified in analytic test problems for which high rates of convergence of the solution are achieved and in natural convection flows for which a convergent and accurate solution at high Ra number is obtained.

Table 4.1 Natural convection in a square slot: Maximum velocities on the middle planes and the average Nusselt number by the present CLIRBF-FVM (3 Gauss points) and by some other methods.

Ra	Density	$v_{x\ max}$	x	$v_{y\ max}$	y	$\overline{Nu}$	$Nu_{1/2}$	Nu_0
10^3	11×11	3.612	0.814	3.693	0.177	1.121	1.117	1.120
	21×21	3.648	0.813	3.698	0.179	1.118	1.118	1.117
	GRBF[a]	-	-	-	-	1.118	1.119	1.117
	LBM[b]	3.648	0.810	3.697	0.180	1.116	-	-
	FDM[c]	3.649	0.813	3.697	0.178	1.118	1.118	1.117
10^4	31×31	16.059	0.823	19.612	0.118	2.247	2.240	2.246
	41×41	16.164	0.823	19.643	0.119	2.247	2.245	2.247
	GRBF[a]	-	-	-	-	2.247	2.248	2.244
	LBM[b]	16.138	0.820	19.602	0.120	2.230	-	-
	FDM[c]	16.178	0.823	19.617	0.119	2.243	2.243	2.238
10^5	41×41	34.61	0.854	68.98	0.065	4.535	4.530	4.527
	51×51	34.73	0.855	68.93	0.066	4.527	4.526	4.509
	GRBF[a]	-	-	-	-	4.529	4.530	4.521
	LBM[b]	34.459	0.855	68.551	0.065	4.488	-	-
	FDM[c]	34.73	0.855	68.59	0.066	4.519	4.519	4.509
10^6	61×61	64.44	0.851	222.73	0.0372	8.833	8.821	8.809
	71×71	64.59	0.850	222.12	0.0375	8.849	8.840	8.840
	GRBF [a]	-	-	-	-	8.864	8.865	8.827
	LBM[b]	63.413	0.848	219.708	0.036	8.745	-	-
	FDM[c]	64.63	0.8507	219.36	0.0379	8.800	8.799	8.817
	SM[d]	64.83	0.850	220.6	0.038	8.825	8.825	-
10^7	91×91	155.057	0.864	749.835	0.021	16.555	16.536	16.815
	GRBF[a]	-	-	-	-	16.661	16.661	-
	SM[d]	148.595	0.879	699.179	0.021	16.523	16.523	-

[a] Galerkin-RBF method (Ho-Minh et al., 2009)
[b] Thermal BGK lattice Boltzmann model (Hao-Chueh et al., 2010)
[c] Finite difference method (Davis, 1983)
[d] Spectral method (Quere, 1991)

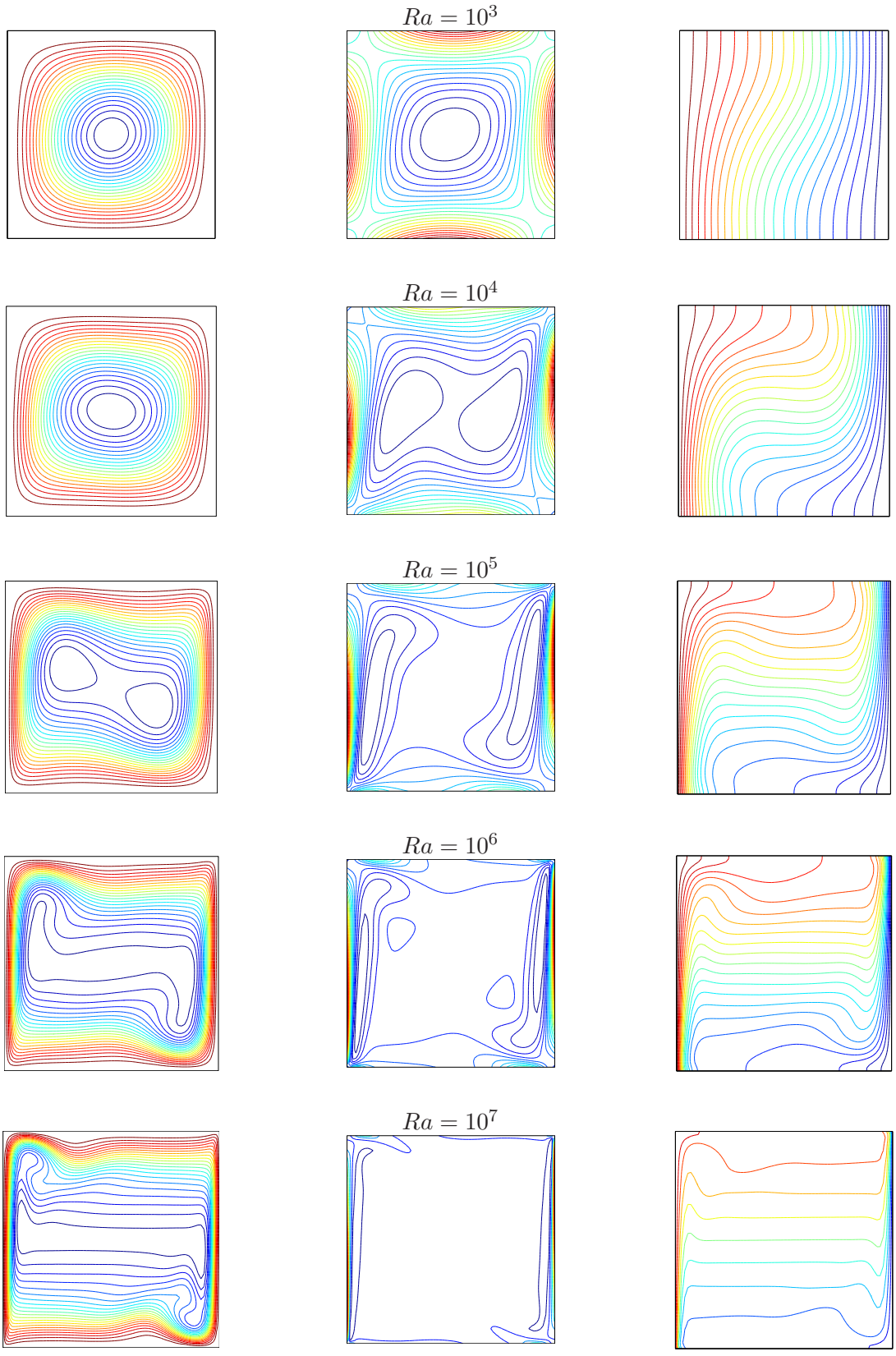

Figure 4.12 Natural convection in a square slot, $N = 71 \times 71$: Contour plots for the streamfunction (left), vorticity (middle), and temperature (right) for several Ra numbers.

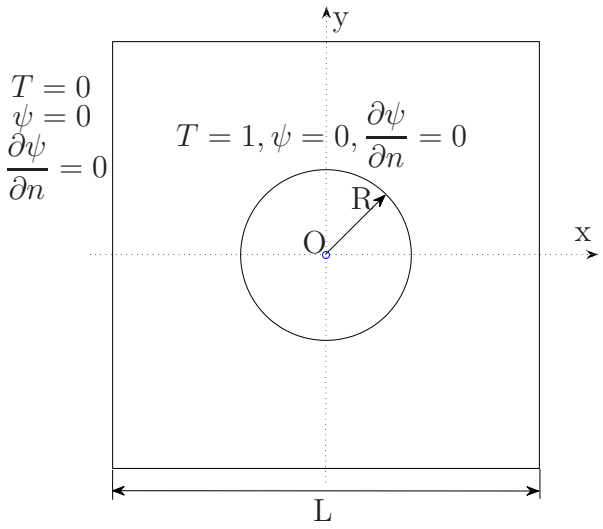

Figure 4.13 Geometry and boundary conditions for natural convection in a concentric annulus between an outer square cylinder and an inner circular cylinder.

Table 4.2 Natural convection in an annulus defined by concentric outer square and inner circular cylinders: the average Nusselt number on the outer (Nu_o) and inner (Nu_i) cylinders by the present CLIRBF-FVM (1 Gauss point) and by some other methods (RBF, FVM and DQM).

Ra	10^4	5×10^4	10^5	5×10^5	10^6
Grid			Nu_o		
32×32	3.22	3.98	4.78	7.30	8.67
42×42	3.22	4.01	4.83	7.38	8.63
52×52	3.22	4.04	4.88	7.52	8.77
62×62	3.22	4.04	4.88	7.51	8.93
1D-IRBF [a]	3.22	4.04	4.89	7.43	8.70
LMLS-IRBF [b]	3.23	4.05	4.91	7.43	8.67
DQM [c]	3.24		4.86		8.90
FVM [d]	3.33		5.08		9.37
Grid			Nu_i		
32×32	3.21	3.97	4.77	7.49	8.89
42×42	3.21	4.00	4.83	7.45	8.78
52×52	3.22	4.02	4.86	7.55	8.98
62×62	3.22	4.03	4.88	7.51	8.90
1D-IRBF [a]	3.21	4.04	4.89	7.51	8.85
LMLS-IRBF [b]	3.23	4.06	4.92	7.55	8.90
DQM [c]	3.24		4.86		8.90
FVM [d]	3.33		5.08		9.37

[a] One dimensional integrated-RBF (Le-Cao et al., 2009)
[b] Local moving least square - one-dimensional IRBF (Ngo-Cong et al., 2012a)
[c] Differential quadrature method (Shu and Zhu, 2002)
[d] Finite volume method (Moukalled and Acharya, 1996)

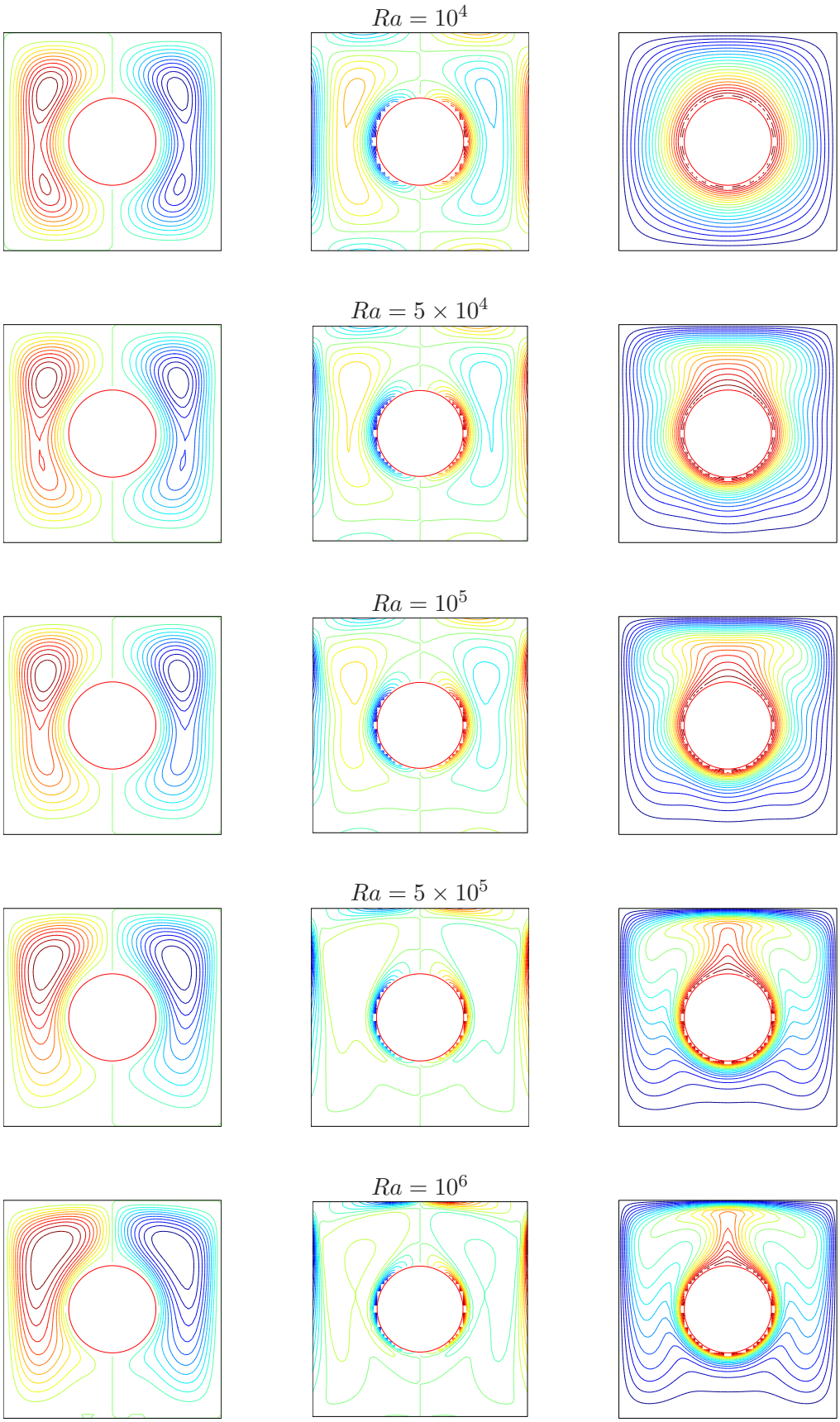

Figure 4.14 Natural convection in a concentric annulus between an outer square cylinder and an inner circular cylinder, $N = 62 \times 62$: Contour plots for the streamfunction (left), vorticity (middle), and temperature (right) for several Ra numbers.

Chapter 5

Compact local IRBF stencils for viscoelastic fluid flows

This chapter is concerned with the use of compact local IRBF stencils in the simulation of viscoelastic fluid flows. We solve the Navier-Stokes equation, where the streamfunction-vorticity formulation is employed, and constitutive equation, where Oldroyd-B model is taken, in a coupled manner, with Newton iteration. Poiseuille and corrugated tube flows are considered to verify the present method. Highly nonlinear and accurate solutions are obtained.

5.1 Introduction

Non-Newtonian fluid flows are known to be more difficult to simulate numerically than Newtonian fluid flows. This can be attributed to the following reasons (Keunings, 1990; Walters and Webster, 2003). Firstly, viscoelastic fluids are more complex than Newtonian fluids. Constitutive equations relating stresses to strain rates are linear for Newtonian fluids but nonlinear for viscoelastic fluids. Secondly, the mathematical model for a viscoelastic fluid consists of the continuity and momentum equations, which possess an elliptic character, and the constitutive equation, which possesses a hyperbolic character. Due to the characteristic mixture in the governing equations, one needs to pay more attention in the simulation of viscoelastic flows (Walters and Webster, 2003; Barnes et al., 1989; Macosko, 1994; Grillet et al., 1999). For example, the behaviour of geometric singularities in a flow is much more severe if the fluid is viscoelastic (Keunings, 1986) and consequently, treatments other than the standard ones (i.e. those associated with the Newtonian case) are normally required here. Thirdly, the stress grows exponentially with convection, leading to the great numerical difficulty in obtaining a convergent solution at high Weissenberg numbers - the so-called high Weissenberg number problem (HWNP).

Viscoelastic fluid problems have been solved by different numerical methods, for example, Finite Element methods (FEMs) (Crochet et al., 1984; Keunings and Crochet, 1984; Guenette and Fortin, 1995; Hulsen et al., 2005), Finite Volume methods (FVMs) (Xue et al., 1995; Oliveira et al., 1998; Oliveira, 2001; Yapici

et al., 2009) and spectral methods (SMs) (Pilitsis and Beris, 1989). A set of continuity, momentum and constitutive equations can be solved by a coupled or decoupled approach. For the former, the three equations are solved simultaneously, while for the latter, the continuity and momentum equations and the constitutive equation are solved separately at each iteration. The decoupled approach involves a set of smaller system matrices and thus saving data storage and reducing computational time; however, it suffers from poor convergence. The decoupled approach has been used in (Tanner and Xue, 2002) for computing the transient flows with high elasticity, and in (Xue et al., 1995) for the study of secondary flows of viscoelastic fluid in straight pipes. The coupled approach is more stable than decoupled one, but it leads to large single matrices. One advantage of the coupled approach is that its resultant system can be solved by means of a Newton iterative scheme, which gives a relatively fast convergence. The implementation of the coupled approach has been reported in many papers (Momeni-Masuleh and Phillips, 2004; Pilitsis and Beris, 1989, 1992; Ho-Minh et al., 2010). The two approaches may be mixed (Harlen et al., 1995). Further details can be found in (Tanner and Xue, 2002).

The employment of radial basis functions for solving ODEs/PDEs was proposed by Kansa in 1990 (Kansa, 1990). Since then, RBFs have been increasingly used in the simulation of engineering applications. In the context of viscoelastic flows, several RBF works were reported, including (Mai-Duy and Tran-Cong, 2008a; Ho-Minh et al., 2010), where global RBF approximations are employed to represent the field variables. Global methods lead to dense matrices and therefore only well suit problems whose solutions can be captured with a relatively small number of nodes. Local methods are a preferred option for solving problems whose solutions involve complex variations (e.g. steep gradients). In this chapter, compact local IRBF stencils will be applied for the simulation of flows of a viscoelastic fluid modelled by the Oldroyd-B model. Poiseuille flows between two parallel plates and in a straight circular tube, and flows through a corrugated tube are considered to verify the present CLIRBF method. For Poiseuille flows, certain analytic solutions are available. For corrugated tube flows, they were simulated with Newtonian fluid (Lahbabi and Chang, 1986) and viscoelastic fluid using the pseudospectral technique (Pilitsis and Beris, 1992), spectral method (Momeni-Masuleh and Phillips, 2004), mixed pseudospectral/finite difference method (PSFD), modified PSFD in a stretched cylindrical coordinate system (PCFD) method (Pilitsis and Beris, 1989), 2D-IRBF method (Mai-Duy and Tanner, 2005a), 1D-IRBF method (Ho-Minh et al., 2010), etc. Results obtained by spectral methods are considered as benchmark solutions. Here, we employ Newton iteration to solve the resultant CLIRBF systems and compare our results with the analytic and benchmark spectral solutions to test the performance of CLIRBF stencils.

The chapter is organised as follows. In Section 5.2, the governing equations and Newton's iteration scheme are briefly reviewed. In Section 5.3, compact local IRBF stencils are described. The present CLIRBF method is verified in Section 5.4. Section 5.5 concludes the chapter.

5.2 Governing equations and Newton's iteration scheme

5.2.1 Governing equations

As reviewed earlier in Section 5.1, it might be advantageous to simulate viscoelastic flows in a coupled manner, where one includes stresses in the list of dependent variables. Equations for determining these variables are taken from constitutive models such as UCM, PTT and Oldroyd-B. In the present study, the Oldroyd-B model is employed, where the extra stress tensor is decomposed into

$$\boldsymbol{\tau} = 2\eta_s \mathbf{D} + \boldsymbol{\tau}_v, \tag{5.1}$$

where η_s is the solvent viscosity, $\mathbf{D} = 0.5(\nabla \mathbf{v}^T + \nabla \mathbf{v})$, and $\boldsymbol{\tau}_v$ is the elastic stress defined as

$$\boldsymbol{\tau}_v + \lambda \overset{\nabla}{\boldsymbol{\tau}}_v = 2\eta_p \mathbf{D}, \tag{5.2}$$

in which η_p is the polymeric viscosity, λ is the relaxation time and $\overset{\nabla}{\boldsymbol{\tau}}_v$ is the material time derivative given by

$$\overset{\nabla}{\boldsymbol{\tau}}_v = \frac{\partial \boldsymbol{\tau}_v}{\partial t} + \boldsymbol{v} \cdot \nabla \boldsymbol{\tau}_v - (\nabla \boldsymbol{v})^T \cdot \boldsymbol{\tau}_v - \boldsymbol{\tau}_v \cdot \nabla \boldsymbol{v}. \tag{5.3}$$

The governing equations for flows of an Oldroyd-B fluid in dimensionless form can thus be written as

$$\nabla \cdot \mathbf{v} = 0, \tag{5.4}$$

$$\frac{\partial \mathbf{v}}{\partial t} + \mathbf{v} \cdot \nabla \mathbf{v} = -\frac{1}{Re} \nabla p + \frac{1}{Re} \nabla \tau_v + \frac{\alpha}{Re} \Delta \mathbf{v}, \tag{5.5}$$

$$\boldsymbol{\tau}_v + We \overset{\nabla}{\boldsymbol{\tau}}_v = 2(1-\alpha)\boldsymbol{D}, \tag{5.6}$$

where We is the Weissenberg number, Re is the Reynolds number and α is the ratio of the solvent (Newtonian) viscosity to the total viscosity of the viscoelastic fluid.

5.2.2 Newton's iteration scheme

For simplicity, we review the Newton's iteration scheme for 1D case. Consider an equation $f(x) = 0$. Figure 5.1 illustrates the way in which the solution is found by using the Newton iteration method. In this figure, the solution is the point where the curve $y = f(x)$ meets the x-axis. Let x_0 be the first guess value of the solution. We can construct a straight line $y = f'(x_0)$ tangent to the curve $y = f(x)$ at the point $x = x_0$. This line intersects the x-axis at the point x_1. The point x_1 is the next guess value. Again, another straight line tangent to $y = f(x)$ is constructed at x_1 to obtain a new guess point x_2. The process continues until the function $f(x) = 0$ is satisfied.

The above procedure can be briefly described as

$$x_i = x_{i-1} - f(x_{i-1})/f'(x_{i-1}). \tag{5.7}$$

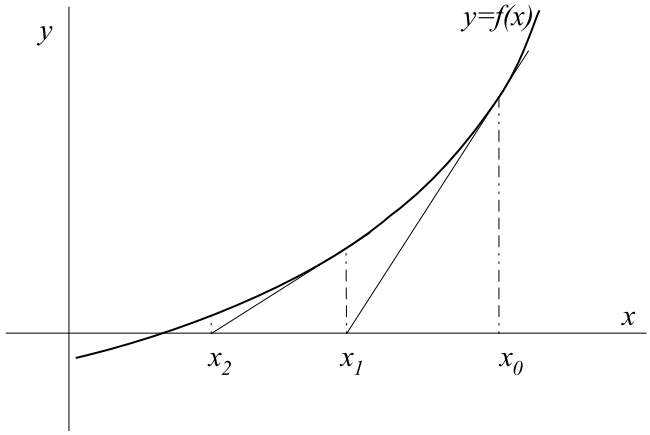

Figure 5.1 Newton's iteration scheme.

One needs to compute equation (5.7) repeatedly until the convergence condition is satisfied

$$|f(x_i)| < \varepsilon, \tag{5.8}$$

where ε is a prescribed tolerance.

5.3 Compact local integrated RBF stencils

The implementation of CLIRBF stencils for solving elliptic equation has been described in the previous chapters. In this section, we will utilise CLIRBF stencils to discretise hyperbolic constitutive equations.

Constitutive equations for the Oldroyd-B model can be rewritten as

$$\xi + u\frac{\partial \xi}{\partial x} + v\frac{\partial \xi}{\partial y} = b(\mathbf{x}), \tag{5.9}$$

where ξ is used to denote a component of the stress tensor, $\mathbf{x} = (x, y)^T$ is the position vector; and u, v and $b(\mathbf{x})$ are given values and function, respectively. We employ CLIRBF stencils of 3×3 nodes to represent the solution. At an arbitrary point in the stencil, the field variable and its first derivatives are computed as

$$\frac{\partial \xi(\mathbf{x})}{\partial x} = \mathcal{H}_x^{(1)}(\mathbf{x})\widehat{w}_x, \quad \xi(\mathbf{x}) = \mathcal{H}_x^{(0)}(\mathbf{x})\widehat{w}_x, \tag{5.10}$$

$$\frac{\partial \xi(\mathbf{x})}{\partial y} = \mathcal{H}_y^{(1)}(\mathbf{x})\widehat{w}_y, \quad \xi(\mathbf{x}) = \mathcal{H}_y^{(0)}(\mathbf{x})\widehat{w}_y, \tag{5.11}$$

where the hat notation is used to denote a vector, superscript (.) the associated derivative order, subscripts x and y the quantities associated with the integration process in the x and y direction, respectively, $\widehat{w}$ is the RBF coefficient vector, $\mathcal{H}$ is the RBF coefficient matrix defined as before (e.g. in Chapter 4), and $\mathcal{H}^{(0)} = \int \mathcal{H}^{(1)}$.

Making use of (5.10) and (5.11), the governing equation (5.9) reduces to

$$\frac{1}{2}\left[\mathcal{H}_x^{(0)}(\mathbf{x})\widehat{w}_x + \mathcal{H}_y^{(0)}(\mathbf{x})\widehat{w}_y\right] + u\mathcal{H}_x^{(1)}(\mathbf{x})\widehat{w}_x + v\mathcal{H}_y^{(1)}(\mathbf{x})\widehat{w}_y = b(\mathbf{x}). \tag{5.12}$$

It is noted that, in (5.12), the value of ξ on the left side is computed in an averaging sense since there are two approximations, one from the x and one from the y directions for the same quantity.

To convert equation (5.12) into the physical space from the RBF coefficient space, we construct the following conversion system

$$\underbrace{\begin{bmatrix} \mathcal{H}_x^{(0)}, & \mathcal{O} \\ \mathcal{H}_x^{(0)}, & -\mathcal{H}_y^{(0)} \\ \frac{1}{2}\mathcal{H}_x^{(0)}(\widehat{\mathbf{x}}) + u\mathcal{H}_x^{(1)}(\widehat{\mathbf{x}}), & \frac{1}{2}\mathcal{H}_y^{(0)}(\widehat{\mathbf{x}}) + v\mathcal{H}_y^{(1)}(\widehat{\mathbf{x}}) \end{bmatrix}}_{\mathcal{C}} \begin{pmatrix} \widehat{w_x} \\ \widehat{w_y} \end{pmatrix} = \begin{pmatrix} \widehat{\xi} \\ \widehat{0} \\ b(\widehat{\mathbf{x}}) \end{pmatrix}, \tag{5.13}$$

where $\mathcal{H}_x^{(0)}$ and $\mathcal{H}_y^{(0)}$ are the RBF coefficient matrices of dimensions 9×15, $\mathcal{C}$ the conversion matrix of dimensions 22×30, the first subset of equations represents the field variable ξ at all grid nodes of the stencil, the second subset is used to force the values of the field variable ξ from the two approximations to be identical, the last subset is employed to include values of (5.12) at four selected nodes $\widehat{\mathbf{x}} = [\mathbf{x}_2, \mathbf{x}_4, \mathbf{x}_6, \mathbf{x}_8]$ into the approximations (i.e. compact form).

Solving equation (5.13) results in

$$\begin{pmatrix} \widehat{w_x} \\ \widehat{w_y} \end{pmatrix} = \mathcal{C}^{-1} \begin{pmatrix} \widehat{\xi} \\ \widehat{0} \\ b(\widehat{\mathbf{x}}) \end{pmatrix}. \tag{5.14}$$

Substitution of (5.14) into (5.12) yields

$$\underbrace{\begin{bmatrix} \frac{1}{2}\mathcal{H}_x^{(0)}(\mathbf{x}) + u\mathcal{H}_x^{(1)}(\mathbf{x}), & \frac{1}{2}\mathcal{H}_y^{(0)}(\mathbf{x}) + v\mathcal{H}_y^{(1)}(\mathbf{x}) \end{bmatrix} \mathcal{C}^{-1}}_{\mathcal{D}} \begin{pmatrix} \widehat{\xi} \\ \widehat{0} \\ b(\widehat{\mathbf{x}}) \end{pmatrix} = b(\mathbf{x}), \tag{5.15}$$

where $\mathcal{D}$ is an array of 22 entries. This equation can be rewritten as

$$\mathcal{D}_1\widehat{\xi} = b(\mathbf{x}) - \mathcal{D}_2 b(\widehat{\mathbf{x}}), \tag{5.16}$$

where $\mathcal{D}_1$ and $\mathcal{D}_2$ are the first 9 columns and the last 4 columns of $\mathcal{D}$, respectively.

Equation (5.16) is the CLIRBF discretisation form of the governing equation (5.9).

5.4 Numerical examples

The present RBF method is verified with Poiseuille flows and corrugated tube flows. Here, we are only interested in the steady state of these flows. The

streamfunction-vorticity formulation is adopted and we solve the coupled system of linear and nonlinear algebraic equations by the Newton's iteration scheme. In the case of Poiseuille flows, where an exact solution is available, the accuracy of the approximate solution is measured using the root mean squared error

$$RMS = \sqrt{\frac{\sum_{i=1}^{N} (u_i - u_i^e)^2}{N}}, \tag{5.17}$$

where N is the number of collocation nodes, and u_i and u_i^e are the computed and exact solutions, respectively.

5.4.1 Fully developed planar Poiseuille Flow

The planar Poiseuille flow is a term used to describe the motion of a fluid between two parallel stationary infinite plates, which is caused by the constant non-zero pressure gradient in one direction parallel to the plates. Such a flow is an idealisation of a real three dimensional flow as depicted in Figure 5.2. The fluid

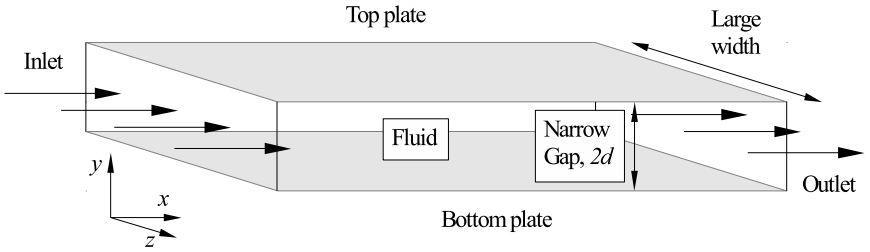

Figure 5.2 Geometry for planar Poiseuille flow. The spacing between the two plates is exaggerated in relation to its length.

flows in the x direction between two rectangular plates, separated by a gap $2d$. Those plates stretch in the z direction and their width is very large relative to the gap. As a result, one can ignore the velocity in the z direction and simply model the flow by a cross section (Wilkes, 2005). Figure 5.3 shows a 2D computational model for this 3D flow. The computational domain can be further reduced to a half (i.e. $0 \leq y \leq d$) if one takes into account the symmetry of the flow.

The dimensionless governing equations for flows of Newtonian and Oldroyd-B fluids take the form

Newtonian fluid:

$$\frac{\partial^2 \psi}{\partial x^2} + \frac{\partial^2 \psi}{\partial y^2} = -\omega, \tag{5.18}$$

$$\frac{\partial^2 \omega}{\partial x^2} + \frac{\partial^2 \omega}{\partial y^2} = Re \left(v_x \frac{\partial \omega}{\partial x} + v_y \frac{\partial \omega}{\partial y} \right), \tag{5.19}$$

where $v_x = \dfrac{\partial \psi}{\partial y}$, $v_y = -\dfrac{\partial \psi}{\partial x}$, and Re is the Reynolds number.

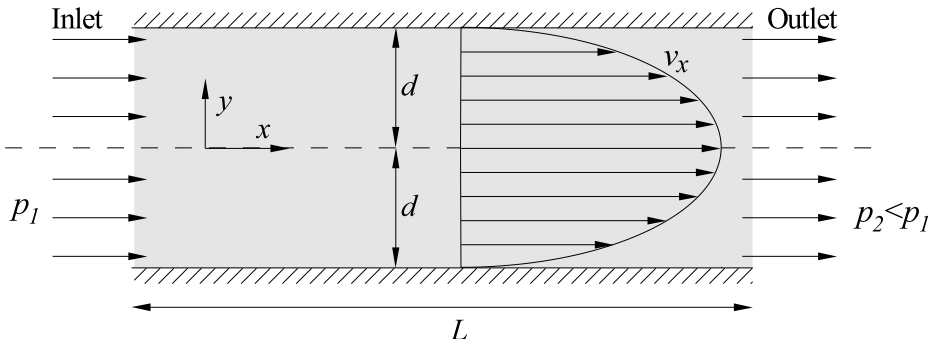

Figure 5.3 A 2D computational model for planar Poiseuille flow.

Oldroyd-B fluid (slow motion):

$$\frac{\partial^2\psi}{\partial x^2}+\frac{\partial^2\psi}{\partial y^2}=-\omega, \tag{5.20}$$

$$\alpha\left(\frac{\partial^2\omega}{\partial x^2}+\frac{\partial^2\omega}{\partial y^2}\right)+\frac{\partial^2\tau_{xy}}{\partial x^2}-\frac{\partial^2\tau_{xy}}{\partial y^2}-\frac{\partial^2\left(\tau_{xx}-\tau_{yy}\right)}{\partial x\partial y}=0 \tag{5.21}$$

$$\tau_{xx}+We\left(v_x\frac{\partial\tau_{xx}}{\partial x}+v_y\frac{\partial\tau_{xx}}{\partial y}-2\frac{\partial v_x}{\partial x}\tau_{xx}-2\frac{\partial v_x}{\partial y}\tau_{xy}\right)=2\left(1-\alpha\right)\frac{\partial v_x}{\partial x}, \tag{5.22}$$

$$\tau_{xy}+We\left(v_x\frac{\partial\tau_{xy}}{\partial x}+v_y\frac{\partial\tau_{xy}}{\partial y}-\frac{\partial v_x}{\partial y}\tau_{yy}-\frac{\partial v_y}{\partial x}\tau_{xx}\right)=\left(1-\alpha\right)\left(\frac{\partial v_x}{\partial y}+\frac{\partial v_y}{\partial x}\right), \tag{5.23}$$

$$\tau_{yy}+We\left(v_x\frac{\partial\tau_{yy}}{\partial x}+v_y\frac{\partial\tau_{yy}}{\partial y}-2\frac{\partial v_y}{\partial x}\tau_{xy}-2\frac{\partial v_y}{\partial y}\tau_{yy}\right)=2\left(1-\alpha\right)\frac{\partial v_y}{\partial y}, \tag{5.24}$$

where We is the Weissenberg number and α is the ratio of the retardation time to the relaxation time. In this study, we employ $\alpha=1/9$.

The exact solution to (5.20)-(5.24) at the steady state is given by

$$\begin{aligned}
v_x &= 1-y^2, & v_y &= 0\\
\psi &= y-1/3y^3, & \omega &= 2y,\\
\tau_{xx} &= 2We(1-\alpha)\left(\frac{\partial v_x}{\partial y}\right)^2=8We\left(1-\alpha\right)y^2,\\
\tau_{xy} &= \left(1-\alpha\right)\left(\frac{\partial v_x}{\partial y}\right)=-2\left(1-\alpha\right)y,\\
\tau_{yy} &= 0.
\end{aligned}$$

Boundary conditions:

Consider a half domain of dimensions $L\times d=1\times 1$. We impose the flow rate $Q=1(m^3/s)$ in the present simulation. The non-slip and symmetric boundary

conditions are applied on the top plate and the centreline, respectively, while the periodic condition is applied on the inlet and outlet (Figure 5.4).

$$\frac{\partial v_x}{\partial y} = 0, \quad v_y = 0, \quad \psi = 0, \quad \omega = 0 \quad \text{at} \quad y = 0; 0 \leq x \leq 1,$$

$$v_x = 0, \quad v_y = 0, \quad \psi = \frac{2}{3}, \quad \frac{\partial \psi}{\partial y} = 0 \quad \text{at} \quad y = 1; 0 \leq x \leq 1,$$

$$\psi^i = \psi^o, \quad \frac{\partial \psi^i}{\partial x} = \frac{\partial \psi^o}{\partial x}, \quad \omega^i = \omega^o, \quad \frac{\partial \omega^i}{\partial x} = \frac{\partial \omega^o}{\partial x}, \quad \text{at} \quad x = [0, 1]; 0 \leq y \leq 1.$$

It is noted that, by taking $\psi = 0$ on the centreline and with the imposed flow rate $Q = 1$, one has $\psi = 2/3$ on the wall.

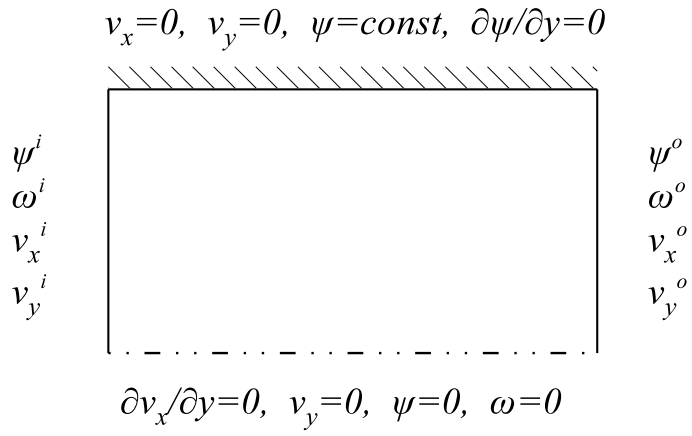

Figure 5.4 Boundary conditions for Poiseuille flows.

On the top plate, the vorticity is computed as $\omega = -\partial^2\psi/\partial y^2$ and we incorporate $\partial\psi/\partial y = 0$ into $\partial^2\psi/\partial n^2$ in the manner as prescribed in Section 4.3.2 of Chapter 4. The symmetric condition leads to $\partial v_x/\partial y = 0$, from which one can derive $\omega = \partial^2\psi/\partial y^2 = 0$ on the centreline.

In the case of Oldroyd-B fluid, one also needs to derive boundary conditions for stresses. Such boundary conditions can be obtained by solving the constitutive equations that are collocated on the wall

$$\tau_{xx} - 2We\frac{\partial v_x}{\partial y}\tau_{xy} = 0, \tag{5.25}$$

$$\tau_{xy} - We\frac{\partial v_x}{\partial y}\tau_{yy} = (1-\alpha)\frac{\partial v_x}{\partial y}, \tag{5.26}$$

$$\tau_{yy} - 2We\frac{\partial v_y}{\partial y}\tau_{yy} = 2(1-\alpha)\frac{\partial v_y}{\partial y}, \tag{5.27}$$

where boundary conditions for velocities are taken into account. At first, equation (5.27) is solved for τ_{yy}, i.e. $\tau_{yy} = \left(2(1-\alpha)\frac{\partial v_y}{\partial y}\right) / \left(1 - 2We\frac{\partial v_y}{\partial y}\right)$. Then, the obtained τ_{yy} is substituted into equation (5.26) to get τ_{xy}. Finally, τ_{xx} is obtained by substituting τ_{xy} into (5.25).

Owing to the periodic condition, stresses on the inlet and outlet are forced to be equal $\xi^i - \xi^o = 0$, where ξ is used to denote τ_{xx}, τ_{xy} and τ_{yy}. On the centerline, the constitutive equations reduce to

$$\tau_{xx} + We\left(v_x\frac{\partial \tau_{xx}}{\partial x} - 2\frac{\partial v_x}{\partial x}\tau_{xx}\right) = 2\left(1-\alpha\right)\frac{\partial v_x}{\partial x} \tag{5.28}$$

$$\tau_{xy} = 0, \tag{5.29}$$

$$\tau_{yy} + We\left(v_x\frac{\partial \tau_{yy}}{\partial x} - 2\frac{\partial v_y}{\partial y}\tau_{yy}\right) = 2\left(1-\alpha\right)\frac{\partial v_y}{\partial y}. \tag{5.30}$$

Table 5.1 shows the RMS errors of the computed solutions in the case of Newtonian fluid for several values of Re. It can be seen that a convergent solution is obtained for high Re numbers and the accuracy is enhanced as the grid is refined. Highly accurate results are achieved even at a coarse grid of 11×11.

Table 5.1 Planar Poiseuille flow of Newtonian fluid: RMS errors of the computed solutions for several values of Re.

Re	Density	$Ne(v_x)$	$Ne(v_y)$	$Ne(\psi)$	$Ne(\omega)$
10^1	11×11	4.839E-05	9.709E-09	1.254E-06	1.683E-05
	21×21	6.478E-06	1.762E-09	1.231E-07	8.207E-07
10^2	11×11	4.838E-05	9.166E-09	1.247E-06	1.685E-05
	21×21	6.480E-06	2.780E-09	1.262E-07	3.598E-07
10^3	11×11	4.831E-05	8.670E-09	1.181E-06	1.704E-05
	21×21	6.478E-06	1.437E-09	1.237E-07	3.883E-07
10^4	11×11	4.762E-05	8.600E-09	5.776E-07	2.194E-05
	21×21	6.455E-06	5.252E-10	9.549E-08	6.131E-07
10^5	11×11	4.747E-05	7.625E-09	6.270E-06	1.375E-04
	21×21	6.336E-06	7.167E-10	1.655E-07	4.560E-06
10^6	11×11	4.766E-05	8.372E-09	2.326E-07	8.752E-05
	21×21	6.430E-06	4.235E-09	2.393E-08	3.482E-06
10^7	11×11	4.727E-05	1.473E-06	2.185E-06	5.456E-04
	21×21	6.446E-06	4.618E-09	6.724E-08	6.029E-06

Tables 5.2 and 5.3 show the computed results for planar Poiseuille flow of Oldroyd-B fluid. In Table 5.2, the present method is shown to yield accurate results at high We numbers using a grid of 21×21. As We increases, the effects of nonlinearity in the constitutive equations become stronger and the solution accuracy is observed to be reduced. In Table 5.3, a clear grid convergence at $We = 9$ is produced, where grids of densities, $\{11 \times 11, 21 \times 21, 31 \times 31, 41 \times 41\}$, are employed.

Table 5.2 Planar Poiseuille flow of Oldroyd-B fluid, grid of 21×21: RMS errors of the computed solutions for several values of We.

We	$Ne(v_x)$	$Ne(\psi)$	$Ne(\omega)$	$Ne(Txx)$	$Ne(Txy)$
0	6.476E-06	1.193E-07	1.543E-06	5.044E-08	1.359E-06
1	6.463E-06	1.009E-07	1.359E-06	4.180E-05	1.100E-06
2	6.388E-06	2.380E-08	1.557E-05	1.267E-04	2.862E-06
3	6.437E-06	1.228E-07	2.842E-05	2.906E-04	8.096E-06
4	7.059E-06	4.650E-07	8.974E-05	1.002E-03	1.560E-05
5	6.656E-06	2.981E-07	4.603E-05	7.523E-04	9.837E-06
6	6.715E-06	2.423E-07	6.781E-05	1.255E-03	1.956E-05
7	6.694E-06	2.523E-07	6.301E-05	1.336E-03	1.916E-05
8	1.239E-05	2.760E-06	1.516E-04	4.492E-03	9.421E-05
9	1.609E-05	3.481E-06	2.035E-04	7.102E-03	1.526E-04

Table 5.3 Planar Poiseuille flow of Oldroyd-B fluid, $We = 9$: Grid convergence study.

Density	$Ne(v_x)$	$Ne(\psi)$	$Ne(\omega)$	$Ne(Txx)$	$Ne(Txy)$
11×11	6.133E-05	1.070E-05	7.953E-04	3.160E-02	6.644E-04
21×21	1.609E-05	3.481E-06	2.035E-04	7.102E-03	1.526E-04
31×31	4.180E-05	1.112E-05	2.998E-04	9.538E-03	2.689E-04
41×41	4.228E-05	1.101E-05	3.350E-04	7.826E-03	2.266E-04

5.4.2 Poiseuille Flows in straight circular tubes

This section is concerned with simulating the Poiseuille flow of Newtonian and Oldroyd-B fluids in a circular tube. We employ the governing equations in the cylindrical coordinate system (Pilitsis and Beris, 1991)

Newtonian fluid:

$$\frac{1}{r}\left(\frac{\partial^2\psi}{\partial z^2}+\frac{\partial^2\psi}{\partial r^2}-\frac{1}{r}\frac{\partial\psi}{\partial r}\right)=-\omega, \tag{5.31}$$

$$\left(\frac{\partial^2\omega}{\partial z^2}+\frac{\partial^2\omega}{\partial r^2}+\frac{1}{r}\frac{\partial\omega}{\partial r}-\frac{\omega}{r^2}\right)=\frac{\pi Re}{2}\left(v_z\frac{\partial\omega}{\partial z}+v_r\frac{\partial\omega}{\partial r}-\frac{v_r}{r}\omega\right), \tag{5.32}$$

where Re is the Reynolds number, $Re=\dfrac{2\rho Q}{\pi R\mu}$, and r is the radial distance.

Oldroyd-B fluid (creeping flows):

$$\frac{1}{r}\left(\frac{\partial^2\psi}{\partial z^2}+\frac{\partial^2\psi}{\partial r^2}-\frac{1}{r}\frac{\partial\psi}{\partial r}\right)=-\omega, \quad (5.33)$$

$$\alpha\left(\frac{\partial^2\omega}{\partial z^2}+\frac{\partial^2\omega}{\partial r^2}+\frac{1}{r}\frac{\partial\omega}{\partial r}-\frac{\omega}{r^2}\right)+\frac{\partial^2\tau_{rr}}{\partial r\partial z}+\frac{1}{r}\frac{\partial\tau_{rr}}{\partial z}-\frac{\partial^2\tau_{rz}}{\partial r^2}+\frac{\partial^2\tau_{rz}}{\partial z^2}$$
$$+\frac{1}{r^2}\tau_{rz}+\frac{1}{r}\frac{\partial\tau_{rz}}{\partial r}-\frac{\partial^2\tau_{zz}}{\partial r\partial z}-\frac{1}{r}\frac{\partial^2\tau_{\theta\theta}}{\partial z}=0, \quad (5.34)$$

$$\tau_{rr}+We\left(v_r\frac{\partial\tau_{rr}}{\partial r}+v_z\frac{\partial\tau_{rr}}{\partial z}-2\frac{\partial v_r}{\partial r}\tau_{rr}-2\frac{\partial v_r}{\partial z}\tau_{rz}\right)=2(1-\alpha)\frac{\partial v_r}{\partial r}, \quad (5.35)$$

$$\tau_{rz}+We\left(v_r\frac{\partial\tau_{rz}}{\partial r}+v_z\frac{\partial\tau_{rz}}{\partial z}+\frac{v_r}{r}\tau_{rz}-\frac{\partial v_z}{\partial r}\tau_{rr}-\frac{\partial v_r}{\partial z}\tau_{zz}\right)=(1-\alpha)\left(\frac{\partial v_r}{\partial z}+\frac{\partial v_z}{\partial r}\right), \quad (5.36)$$

$$\tau_{zz}+We\left(v_r\frac{\partial\tau_{zz}}{\partial r}+v_z\frac{\partial\tau_{zz}}{\partial z}-2\frac{\partial v_z}{\partial r}\tau_{rz}-2\frac{\partial v_z}{\partial z}\tau_{zz}\right)=2(1-\alpha)\frac{\partial v_z}{\partial z}, \quad (5.37)$$

$$\tau_{\theta\theta}+We\left(v_r\frac{\partial\tau_{\theta\theta}}{\partial r}+v_z\frac{\partial\tau_{\theta\theta}}{\partial z}-2\frac{v_r}{r}\tau_{\theta\theta}\right)=2(1-\alpha)\frac{v_r}{r}, \quad (5.38)$$

where α is the ratio of the retardation time to the relaxation time, $v_z=\frac{1}{r}\frac{\partial\psi}{\partial r}, v_r=-\frac{1}{r}\frac{\partial\psi}{\partial z}$. Here, we take $\alpha=0.85$.

The exact solution when the flow reaches the steady state is given by

$$\begin{aligned}
&v_z=1-r^2, && v_r=0\\
&\psi=1/2r^2-1/4r^4, && \omega=2r,\\
&\tau_{rr}=0,\\
&\tau_{rz}=(1-\alpha)\frac{\partial v_z}{\partial r}=-2(1-\alpha)r,\\
&\tau_{zz}=2We(1-\alpha)\left(\frac{\partial v_z}{\partial r}\right)^2=8We(1-\alpha)r^2.
\end{aligned}$$

The boundary conditions here are similar to those for the planar Poiseuille flow (Section 5.4.1). We apply the non-slip condition on the wall, the symmetric condition on the centreline, and the periodic condition on the inlet and outlet.

On the wall: $v_r=0, v_z=0, \psi=0, \frac{\partial\psi}{\partial z}=0, \frac{\partial\psi}{\partial r}=0$, and the constitutive equations reduce to

$$\tau_{rr}-2We\frac{\partial v_r}{\partial r}\tau_{rr}=2(1-\alpha)\frac{\partial v_r}{\partial r}, \quad (5.39)$$

$$\tau_{rz}-We\frac{\partial v_z}{\partial r}\tau_{rr}=(1-\alpha)\frac{\partial v_z}{\partial r}, \quad (5.40)$$

$$\tau_{zz}-2We\frac{\partial v_z}{\partial r}\tau_{rz}=0, \quad (5.41)$$

$$\tau_{\theta\theta}=0. \quad (5.42)$$

On the centreline: $v_r = 0, \tau_{rz} = 0, \dfrac{\partial v_z}{\partial r} = \dfrac{\partial \tau_{rr}}{\partial r} = \dfrac{\partial \tau_{zz}}{\partial r} = \dfrac{\partial \tau_{\theta\theta}}{\partial r} = 0$. It is noted that, due to the involvement of the term $1/r$, special care is needed in the handling of the governing equation and boundary conditions on the centreline (Constantinescu and Lele, 2000). In this study, we directly employ the symmetric conditions instead of the simplified constitutive equations.

For Newtonian fluid, we assume that the flow is laminar. The simulation is conducted for a wide range of Re, $\{10^1, 10^2, \cdots, 10^9\}$. It is noted that simulations at high values of Re are conducted here only for the purpose of testing the convergence of the proposed numerical method. Results concerning $Re = 10$ and $Re = 10^9$ are presented in Table 5.4. Highly nonlinear solutions up to $Re = 10^9$ are achieved using a coarse grid of 11×11. The numerical accuracy is improved with increasing number of nodes used.

Table 5.4 Circular Poiseuille flow of Newtonian fluid: RMS errors of the computed solutions for $Re = \{10, 10^9\}$.

Re	Density	$Ne(v_x)$	$Ne(v_y)$	$Ne(\psi)$	$Ne(\omega)$
10^1	11×11	4.002E-04	4.265E-09	2.331E-05	3.497E-04
	21×21	1.178E-04	8.041E-09	2.956E-06	7.118E-05
10^9	11×11	4.428E-04	3.311E-09	2.351E-05	3.502E-04
	21×21	1.179E-04	6.764E-11	2.958E-06	7.107E-05

For Oldroyd-B fluid, RMS errors of the computed solutions are shown in Table 5.5, where We number in a range of 1 to 9 and a grid of 21×21 are employed. It is observed that the numerical accuracy reduces with increasing We number. Figure 5.5 displays profiles of velocity and shear stress, and Figure 5.6 the normal stress difference. They are in very good agreement with the analytic results. Table 5.6 shows a grid convergence for the velocity, streamfunction, vorticity and stresses at $We = 9$. As the grid is refined, $\{11 \times 11, 21 \times 21, \cdots, 51 \times 51\}$, the solution accuracy is generally enhanced.

5.4.3 Flows in corrugated tubes

The schematic diagram of the flow through a corrugated tube is described in Figure 5.7. The radius of the corrugated tube along the z axis is given by

$$r_w = R\left(1 - \varepsilon \cos(2\pi z/L)\right), \tag{5.43}$$

where R is the average radius of an equivalent straight tube, ε is the amplitude of the corrugation and L is the wavelength. Two parameters, namely ε and the ratio $M = R/L$ are often used to characterise the geometry of the tube. As the flow is symmetric and periodic, one only needs to consider a reduced domain as shown in Figure 5.7 for the numerical analysis.

The governing equations and boundary conditions here are the same as those in Section 5.4.2. We will solve the equations in a stretched cylindrical coordinate system $(\widehat{r}, \theta, \widehat{z})$, where $\widehat{r} = r/r_w$, and $\widehat{z} = z/L$.

Table 5.5 Circular Poiseuille flow of Oldroyd-B fluid, grid of 21×21: RMS errors of the computed solutions for several We numbers.

We	$Ne(v_z)$	$Ne(\psi)$	$Ne(\omega)$	$Ne(Tzz)$	$Ne(Trz)$
1	1.162E-04	2.945E-06	7.291E-05	3.968E-04	1.117E-05
2	1.254E-04	2.924E-06	7.296E-05	5.222E-04	1.688E-05
3	1.178E-04	2.881E-06	7.003E-05	7.654E-04	8.966E-06
4	1.211E-04	2.829E-06	7.527E-05	1.015E-03	2.688E-05
5	1.045E-04	2.759E-06	9.075E-05	1.216E-03	5.216E-05
6	1.739E-04	2.910E-06	1.167E-04	1.277E-03	7.896E-05
7	6.636E-05	2.581E-06	2.373E-04	1.645E-03	1.948E-04
8	1.578E-04	3.221E-06	2.583E-04	1.926E-03	2.124E-04
9	3.524E-05	2.362E-06	3.272E-04	2.037E-03	2.741E-04

Table 5.6 Circular Poiseuille flow of Oldroyd-B fluid, $We = 9$: Grid convergence study.

Density	$Ne(v_z)$	$Ne(\psi)$	$Ne(\omega)$	$Ne(Tzz)$	$Ne(Trz)$
11×11	4.432E-04	2.321E-05	3.386E-04	9.940E-03	4.078E-05
21×21	3.524E-05	2.362E-06	3.272E-04	2.037E-03	2.741E-04
31×31	8.439E-05	1.083E-06	2.601E-04	1.465E-03	2.236E-04
41×41	1.637E-05	7.565E-07	1.171E-04	1.314E-03	1.117E-04
51×51	1.789E-05	3.688E-07	7.740E-05	1.050E-03	7.359E-05

Consider a function $f(r, z)$ in the physical domain. Below are formulas of transforming the function $f(r, z)$ and its derivatives into the computational domain

$$\frac{\partial f}{\partial r} = \frac{1}{r_w}\frac{\partial f}{\partial \widehat{r}}, \tag{5.44}$$

$$\frac{\partial f}{\partial z} = \frac{1}{L}\frac{\partial f}{\partial \widehat{z}} - \frac{1}{L}\frac{\widehat{r}}{r_w}\frac{dr_w}{d\widehat{z}}\frac{\partial f}{\partial \widehat{r}}, \tag{5.45}$$

$$\frac{\partial^2 f}{\partial r^2} = \frac{1}{r_w^2}\frac{\partial^2 f}{\partial \widehat{r}^2}, \tag{5.46}$$

$$\begin{aligned}\frac{\partial^2 f}{\partial z^2} = {} & \frac{1}{L^2}\frac{\partial^2 f}{\partial \widehat{z}^2} + \frac{1}{L^2}\frac{\widehat{r}^2}{r_w^2}\left(\frac{dr_w}{d\widehat{z}}\right)^2\frac{\partial^2 f}{\partial \widehat{r}^2} - \frac{2}{L^2}\frac{\widehat{r}}{r_w}\frac{dr_w}{d\widehat{z}}\frac{\partial^2 f}{\partial \widehat{r}\partial \widehat{z}} \\ & - \frac{\widehat{r}}{L^2}\left(\frac{1}{r_w}\frac{d^2 r_w}{d\widehat{z}^2} - \frac{2}{r_w^2}\left(\frac{dr_w}{d\widehat{z}}\right)^2\right)\frac{\partial f}{\partial \widehat{r}},\end{aligned} \tag{5.47}$$

$$\frac{\partial^2 f}{\partial r \partial z} = -\frac{1}{L}\frac{1}{r_w^2}\frac{dr_w}{d\widehat{z}}\frac{\partial f}{\partial \widehat{r}} + \frac{1}{L}\frac{1}{r_w}\frac{\partial^2 f}{\partial \widehat{r}\partial \widehat{z}} - \frac{1}{L}\frac{\widehat{r}}{r_w^2}\frac{dr_w}{d\widehat{z}}\frac{\partial^2 f}{\partial \widehat{r}^2}. \tag{5.48}$$

One important measure for the study of corrugated tube flows is the flow resistance, which is defined as

$$fRe = \frac{2\pi \Delta P R^4}{L(\mu_n + \mu_p)Q}, \tag{5.49}$$

where ΔP is the constant pressure drop per unit cell.

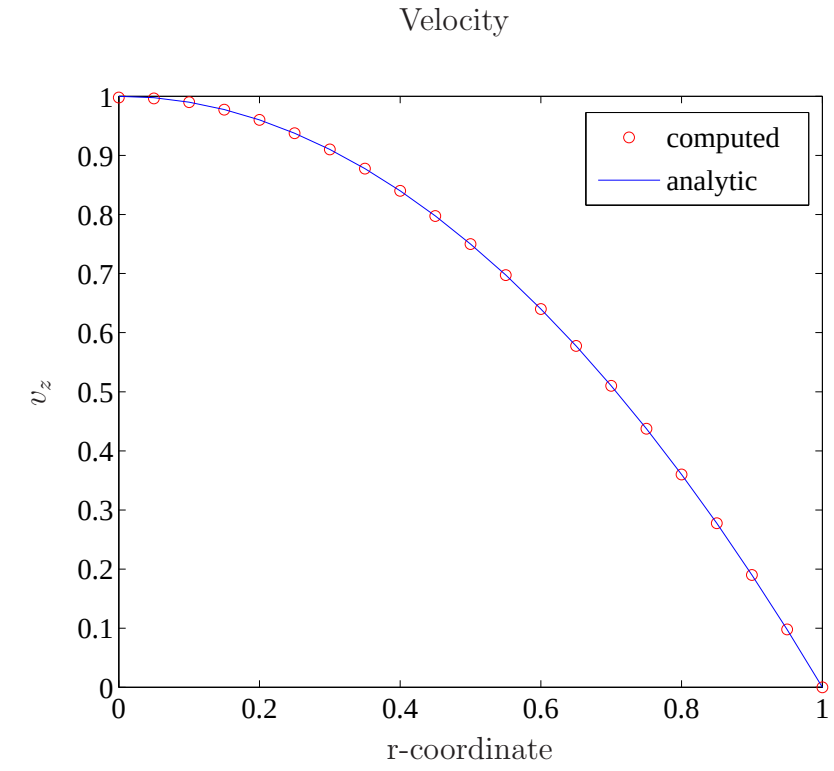

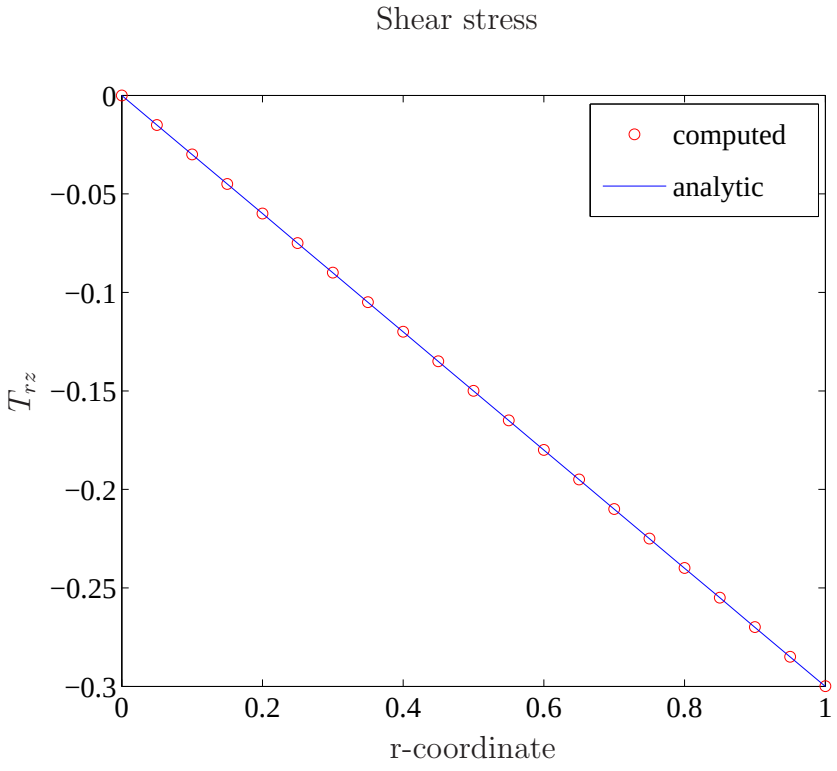

Figure 5.5 Circular Poiseuille flow of Oldroyd-B fluid, grid of 21×21: Computed profiles for velocity.

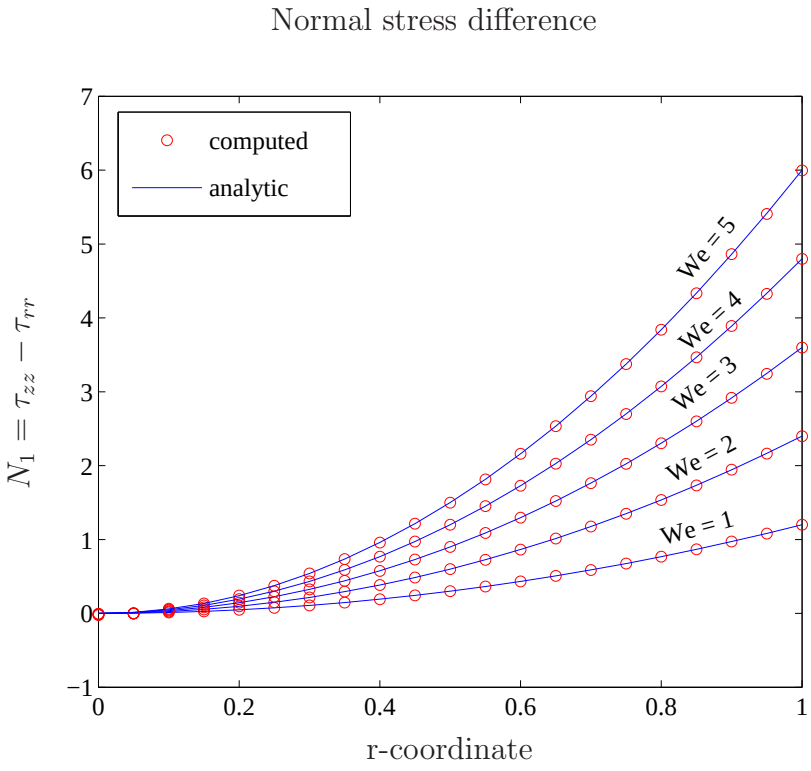

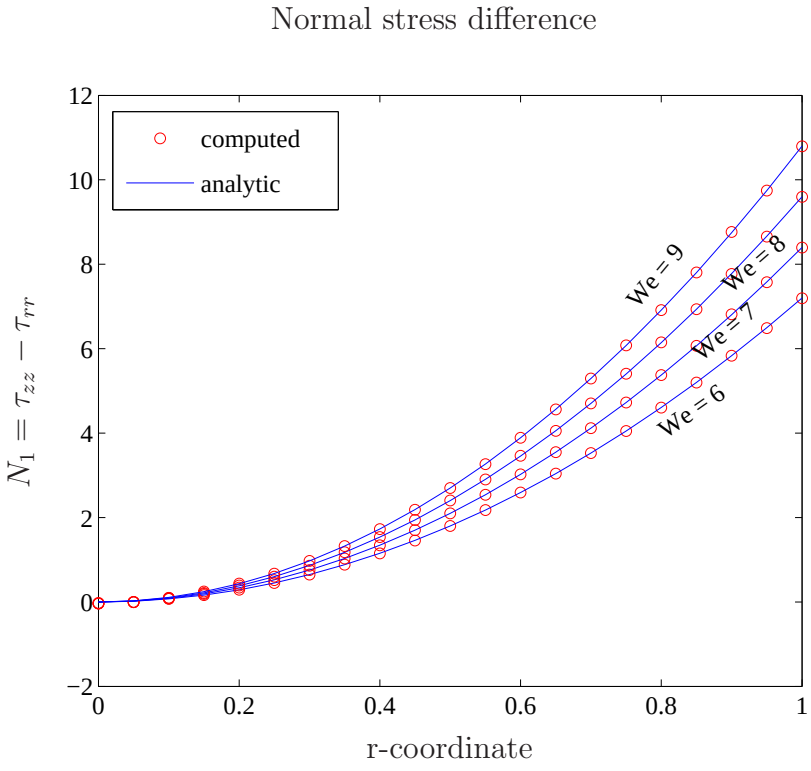

Figure 5.6 Circular Poiseuille flow of Oldroyd-B fluid, grid of 21×21: Computed profiles for stresses.

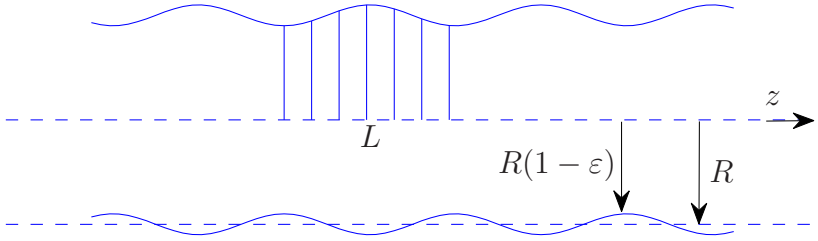

Figure 5.7 Geometry of a corrugated tube.

Newtonian fluid

To obtain the flow resistance, we calculate the pressure gradients

$$\frac{\partial P}{\partial r} = \frac{1}{L}\left(\frac{\partial \omega}{\partial \widehat{z}} - \frac{\widehat{r}}{r_w}\frac{dr_w}{d\widehat{z}}\frac{\partial \omega}{\partial \widehat{r}}\right) - \frac{\pi Re}{2}\left(\frac{v_r}{r_w}\frac{\partial v_r}{\partial \widehat{r}} + \frac{1}{L}v_z\left(\frac{\partial v_r}{\partial \widehat{z}} - \frac{\widehat{r}}{r_w}\frac{dr_w}{d\widehat{z}}\frac{\partial v_r}{\partial \widehat{r}}\right)\right), \tag{5.50}$$

$$\frac{\partial P}{\partial z} = -\frac{1}{r_w}\left(\frac{\partial \omega}{\partial \widehat{r}} + \frac{\omega}{\widehat{r}}\right) - \frac{\pi Re}{2}\left(\frac{v_r}{r_w}\frac{\partial v_z}{\partial \widehat{r}} + \frac{1}{L}v_z\left(\frac{\partial v_z}{\partial \widehat{z}} - \frac{\widehat{r}}{r_w}\frac{dr_w}{d\widehat{z}}\frac{\partial v_z}{\partial \widehat{r}}\right)\right). \tag{5.51}$$

The above equations reduce to

$$\frac{\partial P}{\partial r} = \frac{1}{L}\left(\frac{\partial \omega}{\partial \widehat{z}} - \frac{\widehat{r}}{r_w}\frac{dr_w}{d\widehat{z}}\frac{\partial \omega}{\partial \widehat{r}}\right), \tag{5.52}$$

$$\frac{\partial P}{\partial z} = -\frac{1}{r_w}\left(\frac{\partial \omega}{\partial \widehat{r}} + \frac{\omega}{\widehat{r}}\right), \tag{5.53}$$

on the wall, and

$$\frac{\partial P}{\partial r} = 0, \tag{5.54}$$

$$\frac{\partial P}{\partial z} = -\frac{2}{r_w}\frac{\partial \omega}{\partial \widehat{r}} - \frac{\pi Re}{2}\frac{1}{L}v_z\frac{\partial v_z}{\partial \widehat{z}}, \tag{5.55}$$

on the centreline.

Table 5.7 displayed the flow resistances at $Re = 0$ for different geometries of the corrugated tube. Results obtained by the spectral method (SM) (Momeni-Masuleh and Phillips, 2004), Pseudospectral/ finite element method (PSFD) (Pilitsis and Beris, 1989), Fourier-Chebyshev Collocation (FCC) (Pilitsis and Beris, 1991), modified PSFD in a stretched cylindrical coordinate (PCFD) (Pilitsis and Beris, 1989), global 1D integrated radial basis function method (Ho-Minh et al., 2010) are also included. There is a good agreement between these results. It can be seen that the present solutions are closer to those obtained by the PSFD method. We choose the tube with ($\epsilon = 0.16, M = 0.3$) to study the influence of Re on the flow resistance. Results obtained by the present method and by 1D-IRBF, 2D-IRBF, Galerkin finite element method (GFE) (Pilitsis and Beris, 1992) and Fourier-Chebyshev Collocation (FCC) (Pilitsis and Beris, 1992) are

Table 5.7 Corrugated tube flow of Newtonian fluid, $Re = 0$: Computed flow resistances.

ε	0.1	0.1	0.2	0.286	0.3	0.5
M	0.5	0.1592	0.1042	0.2333	0.1592	0.5
21×21	17.7523	16.9250	19.7620	26.3843	26.4346	95.1881
31×31	17.7516	16.9275	19.7635	26.3820	26.4357	95.6558
41×41	17.7515	16.9284	19.7644	26.3821	26.4359	95.6354
1D-IRBF[a]	17.74106	16.92760	19.76351	26.37759	26.43378	95.61778
SM[b]	17.7514	16.9290	19.7658	26.3724	26.4370	95.6363
FCC[c]	-	-	19.765	26.383	26.437	-
PSFD[d]	-	-	19.765	26.383	26.436	-
PCFD[e]	-	-	19.761	26.377	26.432	-

[a] 1D-Integrated Radial basis function network (Ho-Minh et al., 2010)
[b] Spectral method (Momeni-Masuleh and Phillips, 2004)
[c] Fourier-Chebyshev Collocation (Pilitsis and Beris, 1991)
[d] Pseudospectral/ finite element method (Pilitsis and Beris, 1989)
[e] Modified PSFD in a stretched cylindrical coordinate (Pilitsis and Beris, 1989)

presented in Table 5.8. The present solutions agree well with other solutions, particularly with the predictions produced by the FCC method.

Figure 5.8 displays contour plots for the streamfunction and vorticity at several values of Re, where a grid of 41×41 is employed. They looks feasible when compared with those reported in (Lahbabi and Chang, 1986; Mai-Duy and Tanner, 2005a; Ho-Minh et al., 2010).

Table 5.8 Corrugated tube flow of Newtonian fluid, $\varepsilon = 0.3$, $M = 0.16$: Flow resistances for a wide range of Re.

Re	0	12	22.6	51	73	132	207.4	264	397.2	783
21×21	26.4468	27.1721	28.5503	31.7126	33.4234	36.5206	38.9315	40.2267	42.3418	45.5700
31×31	26.4469	27.1744	28.5533	31.7183	33.4372	36.5244	38.9595	40.2381	42.3469	45.5704
41×41	26.4473	27.1755	28.5538	31.7423	33.4480	36.5262	38.9600	40.2446	42.3479	45.5827
IRBF[a]	26.4445	27.1773	28.5535	31.7511	33.4538	36.5424	38.9996	40.3044	42.4595	45.7402
IRBF[b]	26.46298	27.19314	28.55838	31.76329	33.44396	36.51618	38.97686	40.26089	42.37057	45.60680
GFE[c]	26.4193	27.0911	28.4433	31.6984	33.4039	36.5392	38.9330	40.1544	42.1112	45.0734
FCC[d]	26.4484	27.1791	28.5536	31.7484	33.4488	36.5264	38.9601	40.2446	42.3479	45.5828

[a] Integrated Radial basis function network (Mai-Duy and Tanner, 2005a) with a grid of 25×25

[b] Integrated Radial basis function network (Ho-Minh et al., 2010) with a grid of 51×51

[c] Galerkin finite element method (Pilitsis and Beris, 1992) with the number of elements in the r and z directions being $N_r = 40$, $N_z = 40$, respectively.

[d] Fourier-Chebyshev Collocation (Pilitsis and Beris, 1992) with the number of Fourier and Chebyshev modes being $N_x = 16$, and $N_c = 33$, respectively.

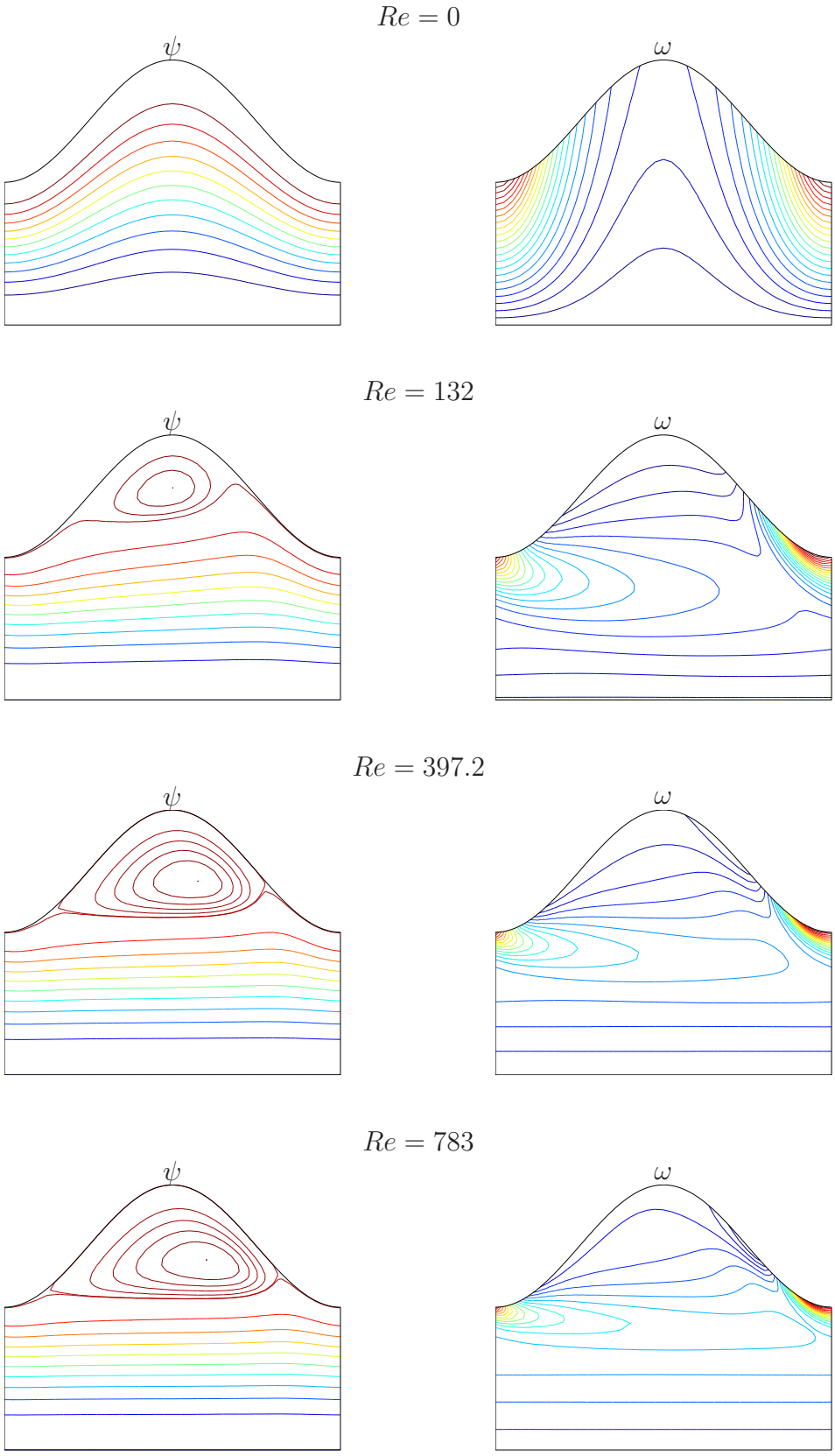

Figure 5.8 Corrugated tube flow of Newtonian fluid, $M = 0.16$, $\epsilon = 0.3$, $N = 41 \times 41$: Contour plots for the streamfunction and vorticity.

Oldroyd-B fluid

The pressure gradients are computed as

$$\frac{\partial P}{\partial r} = \frac{\alpha}{L}\left(\frac{\partial \omega}{\partial \widehat{z}} - \frac{\widehat{r}}{r_w}\frac{dr_w}{d\widehat{z}}\frac{\partial \omega}{\partial \widehat{r}}\right) + \frac{1}{r_w}\frac{\partial \tau_{rr}}{\partial \widehat{r}} + \frac{1}{L}\left(\frac{\partial \tau_{rz}}{\partial \widehat{z}} - \frac{\widehat{r}}{r_w}\frac{dr_w}{d\widehat{z}}\frac{\partial \tau_{rz}}{\partial \widehat{r}}\right) + \frac{1}{r_w \widehat{r}}\left(\tau_{rr} - \tau_{\theta\theta}\right), \tag{5.56}$$

$$\frac{\partial P}{\partial z} = -\frac{\alpha}{r_w}\left(\frac{\partial \omega}{\partial \widehat{r}} + \frac{\omega}{\widehat{r}}\right) + \frac{1}{r_w}\frac{\partial \tau_{rz}}{\partial \widehat{r}} + \frac{\tau_{rz}}{r_w \widehat{r}} + \frac{1}{L}\left(\frac{\partial \tau_{zz}}{\partial \widehat{z}} - \frac{\widehat{r}}{r_w}\frac{dr_w}{d\widehat{z}}\frac{\partial \tau_{zz}}{\partial \widehat{r}}\right). \tag{5.57}$$

On the centreline, they reduce to

$$\frac{\partial P}{\partial r} = 0, \tag{5.58}$$

$$\frac{\partial P}{\partial z} = -\frac{2\alpha}{r_w}\frac{\partial \omega}{\partial \widehat{r}} + \frac{2}{r_w}\frac{\partial \tau_{rz}}{\partial \widehat{r}} + \frac{1}{L}\frac{\partial \tau_{zz}}{\partial \widehat{z}}. \tag{5.59}$$

Table 5.9 shows the computed flow resistances for the tube of $(\epsilon = 1, M = 0.5)$ at $We = \{0, 1.2017, 3.6213\}$ by the present, PCFD and FCC methods. The present solutions are in very good agreement with the benchmark spectral results (Pilitsis and Beris, 1992).

Table 5.9 Corrugated tube flow of Oldroyd-B fluid, $\epsilon = 0.1, M = 0.5$: Computed flow resistances.

We	Present method			PCFD [a]	FCC [b]
	21×21	31×31	41×41	$N_x = 16$, $N_p = 200$	$N_x = 16$, $N_c = 33$
0.0	17.75026	17.75049	17.75020	17.74791	17.75110
1.2017	17.71754	17.68673	17.69261	17.69965	17.70284
3.6213	-	17.70225	17.69329	17.69158	17.69477

[a] Pseudospectral cylindrical finite element method (Pilitsis and Beris, 1992)
[b] Fourier-Chebyshev Collocation (Pilitsis and Beris, 1992)

Contour plots for ψ, ω, v_r, v_z, τ_{rr}, τ_{rz}, τ_{zz} and $\tau_{\theta\theta}$ for the tube of $(M = 0.5, \epsilon = 0.1)$ at $We = 1.2017$ using a grid of 31×31 are displayed in Figure 5.9.

The influence of grid density on the numerical accuracy is illustrated in Figure 5.10. It can be seen that the contours of the velocity become smoother as the grid is refined. When the grid size used is small enough (i.e. 31×31 for v_z and 21×21 for v_r), the maximum and minimum values the velocity fields remain unchanged.

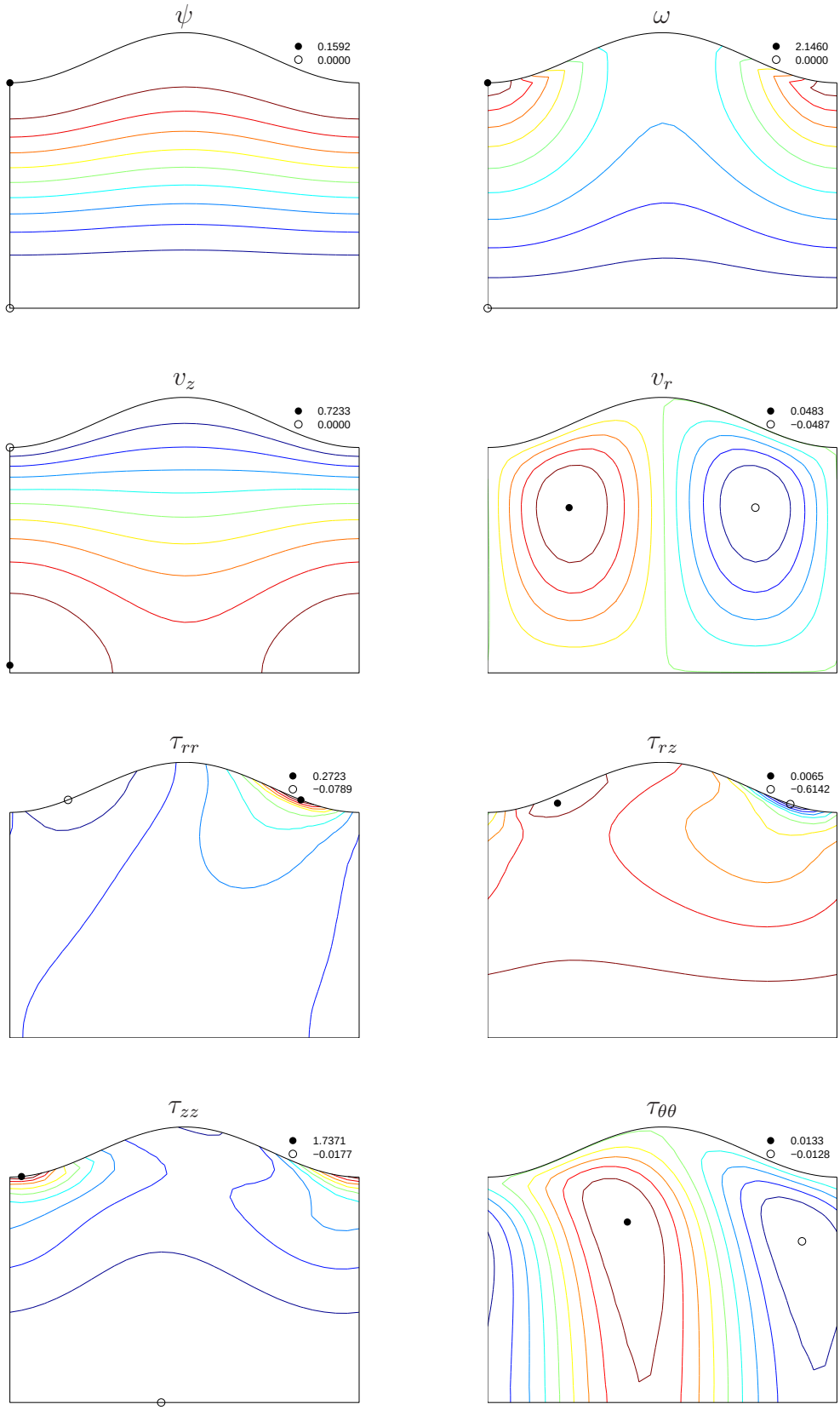

Figure 5.9 Corrugated tube flow of Oldroyd-B fluid, $We = 1.2017, N = 31 \times 31, M = 0.5, \epsilon = 0.1$: Contour plots for the field variables. The maximum and minimum values and their locations are also included.

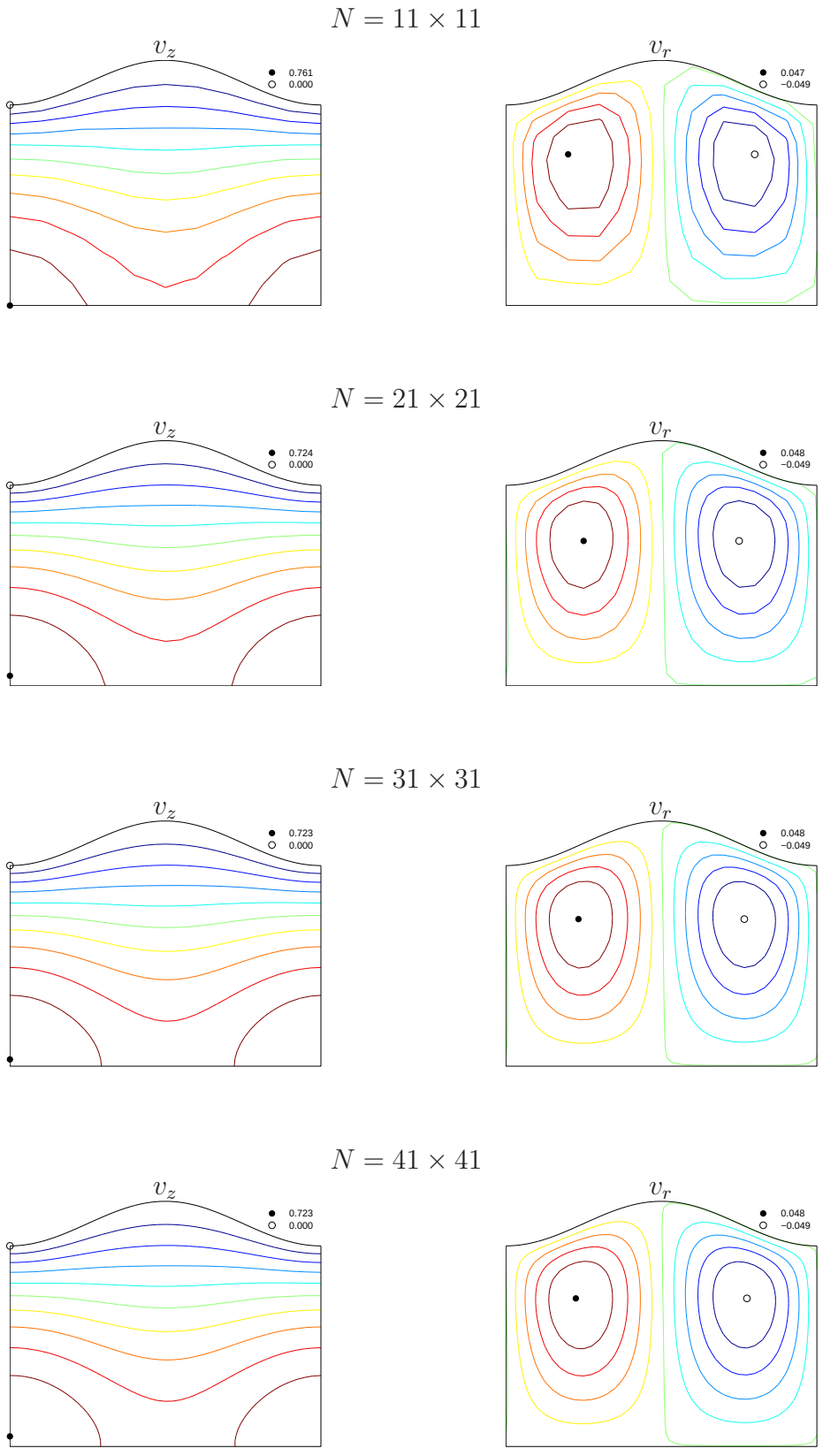

Figure 5.10 Corrugated tube flow of Oldroyd-B fluid, $We = 1.2017, M = 0.5, \epsilon = 0.1$: Contour plots for the velocity v_z (left) and v_r (right). The maximum and minimum values of the velocities and their locations are also included.

5.5 Conclusion

In this chapter, CLIRBF stencils are employed to represent the field variables, including stresses, in the governing equations representing creeping flows of Oldroyd-B fluid. The present method is verified with Poiseuille flows and corrugated tube flows. Grid convergence is studied carefully, including the case of Newtonian fluid. Highly-nonlinear solutions (i.e. high Re solution for Newtonian fluid and high We solution for viscoelastic fluid) are obtained. The CLIRBF results are compared with the analytic solution for Poiseuille flows and with the benchmark solutions for corrugated tub flows. In all cases, very good agreement is achieved and the accuracy of the RBF solutions is clearly observed to be enhanced as the grid is refined.

Chapter 6

Compact local IRBF stencils for transient problems

In this chapter, transient equations are considered. In the discretisation of temporal derivatives, linear and nonlinear terms are treated according to the Crank-Nicolson (CN) and Adams-Bashforth (AB) schemes, respectively. Spatial derivatives are approximated using compact local IRBF stencils. Our numerical scheme is verified with several test problems: heat transfer problems, travelling inviscid cosine wave, 1D and 2D Burger's equations, and start-up planar Poiseuille flows of Newtonian and Oldroyd-B fluids. Results obtained are compared with analytic solutions and those by other numerical methods.

6.1 Introduction

Many mechanics problems are governed by transient equations. The wave equation, diffusion equation, Burger's equation, Navier-Stokes equation and differential constitutive models for viscoelastic fluids are examples of transient equations. As shown in Chapter 1, the Navier-Stokes equations are parabolic equations, while constitutive equations relating stresses and velocity gradients (e.g. Oldroyd-B model and PTT model) for viscoelastic fluids are hyperbolic equations. Even in the case of steady state, to obtain the structure of fluid flows, the time derivative term in the governing equation can be utilised to handle the nonlinear terms - it acts like an under-relaxation process. In this case, simple first-order temporal discretisation schemes are usually employed. When the flow reaches the steady state, the time derivative term vanishes and the solution accuracy is purely decided by the spatial approximation.

For transient flows, the issue about temporal accuracy is generally complex. Oliveira (Oliveira, 2001) studied the effect of the temporal discretisation on numerical accuracy by simulating the time-dependent vortex shedding from a circular cylinder in a viscoelastic fluid flow. Both second-order backward scheme and first-order Euler scheme were utilised. The second-order scheme provided a good time resolution even with a large time step (0.05), while the first-order scheme produced a reduction on the amplitude of the oscillation for both the time-

dependent drag and lift coefficients even with small time steps (e.g. 0.00625). Moreover, when a first-order time discretisation was coupled with first-order spatial discretisation, the numerical diffusion became very strong. This article also pointed out that the use of second-order accuracy scheme for both the temporal and the spatial discretisation is an essential requirement for producing realistic predictions. In addition, the rise of an artificial diffusion caused by the use of low order time truncation schemes can be found in (Kansa, 2007). Due to this transient numerical diffusion, the amplitudes of travelling waves in a transient process can be weakened (Xue et al., 2004). Therefore, the use of temporal discretisation schemes of second order or higher is a preferred option in the simulation of such transient processes. In this study, the Crank-Nicolson/Adams Bashforth (CN-AB) scheme, which produces a second order accuracy, is adopted.

For the spatial discretisation of transient problems, various numerical methods and techniques have been applied, such as the cubic spline function technique (Jain and Holla, 1978), FDM (Srivastava et al., 2011; Bahadir, 2003), adomian decomposition method (Zhu et al., 2010), and radial basis function method (RBF) (Kansa, 2007). We employ compact local IRBF stencils, which produce high-order accuracy, for the spatial discretisation in our study.

The remainder of this chapter is organised as follows. In Section 6.2, compact local IRBF stencils for 1D and 2D problems are described and a brief review of the CN-AB algorithm is given. In Section 6.3, several numerical examples are considered to verify the present method. Section 6.4 concludes the chapter.

6.2 Spatial and temporal discretisations

6.2.1 Spatial discretisation

We employ IRBFs in compact local form to discretise spatial derivatives. In the IRBF approach, the highest-order derivative(s) in the ODE/PDE is (are) approximated by RBFs, and lower-order derivatives and the dependent variable itself are then obtained by integration

$$\frac{\partial^k u(\mathbf{x})}{\partial \eta^k} = \sum_{i=1}^{N} w_i^{[\eta]} g_i(\mathbf{x}) = \sum_{i=1}^{N} w_i^{[\eta]} I_{[\eta]i}^{(k)}(\mathbf{x}), \tag{6.1}$$

$$\frac{\partial^{k-1} u(\mathbf{x})}{\partial \eta^{k-1}} = \sum_{i=1}^{N} w_i^{[\eta]} I_{[\eta]i}^{(k-1)}(\mathbf{x}) + C_1^{[\eta]}, \tag{6.2}$$

$$\cdots$$

$$u(\mathbf{x}) = \sum_{i=1}^{N} w_i^{[\eta]} I_{[\eta]i}^{(0)}(\mathbf{x}) + \frac{\eta^{k-1}}{(k-1)!} C_1^{[\eta]} + \frac{\eta^{k-2}}{(k-2)!} C_2^{[\eta]} + \cdots + C_k^{[\eta]}, \tag{6.3}$$

where $\mathbf{x}$ is the position vector, N is the number of RBFs, $\{w_i\}_{i=1}^{N}$ is the set of network weights, and $\{g_i(\mathbf{x})\}_{i=1}^{N}$ is the set of RBFs, η denotes a component of the position vector $\mathbf{x}$ (e.g. η can be x for 1D problems, and x or y for 2D problems), superscript (k) denotes the order of the derivatives of u, $I_{[\eta]i}^{(k-1)}(\mathbf{x}) = \int I_{[\eta]i}^{(k)}(\mathbf{x}) d\eta$,

$\cdots$, $I^{(0)}_{[\eta]i}(\mathbf{x}) = \int I^{(1)}_{[\eta]i}(\mathbf{x})d\eta$; and $C^{[\eta]}_1, C^{[\eta]}_2, \cdots, C^{[\eta]}_k$ are the "constants" of integration, which will be constants for 1D problems and functions in one variable for 2D problems. With the help of integration constants, one can incorporate information about the ODEs/PDEs into IRBF approximations to enhance their numerical accuracy.

One dimensional problems

For 1D problems, we employ compact 3-node stencils to represent the field variable and its derivatives. Collocating expression (6.3) at $[x_1, x_2, x_3]$ results in

$$\begin{bmatrix} u_1 \\ u_2 \\ u_3 \end{bmatrix} = \underbrace{\begin{pmatrix} I^{(0)}_1(x_1), & I^{(0)}_2(x_1), & I^{(0)}_3(x_1), & \dfrac{x_1^{k-1}}{(k-1)!}, & \dfrac{x_1^{k-2}}{(k-2)!}, & \cdots, & 1 \\ I^{(0)}_1(x_2), & I^{(0)}_2(x_2), & I^{(0)}_3(x_2), & \dfrac{x_2^{k-1}}{(k-1)!}, & \dfrac{x_2^{k-2}}{(k-2)!}, & \cdots, & 1 \\ I^{(0)}_1(x_3), & I^{(0)}_2(x_3), & I^{(0)}_3(x_3), & \dfrac{x_3^{k-1}}{(k-1)!}, & \dfrac{x_3^{k-2}}{(k-2)!}, & \cdots, & 1 \end{pmatrix}}_{\mathcal{H}^{(0)}} \begin{pmatrix} w_1 \\ w_2 \\ w_3 \\ C_1 \\ C_2 \\ \vdots \\ C_k \end{pmatrix}, \tag{6.4}$$

where $u_i = u(x_i)$. Without loss of generality, for simplicity, one can assume the governing equation of the form $\mathcal{K}(u) = f(x)$. We construct the process of converting the RBF space into the physical space as follows

$$\begin{bmatrix} u_1 \\ u_2 \\ u_3 \\ f_1 \\ f_3 \end{bmatrix} = \underbrace{\begin{pmatrix} \mathcal{H}^{(0)} \\ \mathcal{K}(x_1) \\ \mathcal{K}(x_3) \end{pmatrix}}_{\mathcal{C}} \begin{pmatrix} w_1 \\ w_2 \\ w_3 \\ C_1 \\ C_2 \\ \vdots \\ C_k \end{pmatrix}, \tag{6.5}$$

where values of the governing equation at the two end points are also included, and $\mathcal{C}$ is the conversion matrix. Solving equation (6.5) yields

$$\widehat{w} = \mathcal{C}^{-1} \begin{pmatrix} \widehat{u} \\ \widehat{f} \end{pmatrix}, \tag{6.6}$$

where $\widehat{u} = [u_1, u_2, u_3]^T$, $\widehat{w} = [w_1, w_2, w_3, C_1, C_2, \cdots, C_k]^T$, and $\widehat{f} = [f_1, f_3]^T$. Approximate expressions for u and its derivatives in the physical space will be obtained by substituting equation (6.6) into (6.3), (6.2) and (6.1).

Two dimensional problems

For 2D problems, we employ compact 9-node IRBF stencils. The stencil is numbered from bottom to top and from left to right as $\begin{bmatrix} \mathbf{x}_3 & \mathbf{x}_6 & \mathbf{x}_9 \\ \mathbf{x}_2 & \mathbf{x}_5 & \mathbf{x}_8 \\ \mathbf{x}_1 & \mathbf{x}_4 & \mathbf{x}_7 \end{bmatrix}$.

The procedure to construct compact local IRBF approximations associated with $\mathbf{x}_5$ here is similar to that for 1D problem. At first, equations (6.1)-(6.3) are appropriately collocated over the stencil to form the following conversion system

$$\begin{pmatrix} \widehat{u} \\ \widehat{0} \\ \widehat{f} \end{pmatrix} = \underbrace{\begin{bmatrix} \mathcal{H}_x^{(0)} & \mathcal{O} \\ \mathcal{H}_x^{(0)} & -\mathcal{H}_y^{(0)} \\ \mathcal{K}_x & \mathcal{K}_y \end{bmatrix}}_{\mathcal{C}} \begin{pmatrix} \widehat{w}_x \\ \widehat{w}_y \end{pmatrix}, \tag{6.7}$$

where $\widehat{u} = (u_1, u_2, \cdots, u_9)^T$; $\widehat{0}$ is a zero vector of length 9; $\widehat{w}_x$ and $\widehat{w}_x$ are the weight vectors with respect to the x and y directions, respectively; $\mathcal{O}$ is a zero matrix of dimensions 9×15; the second sub-system $\mathcal{H}_x^{(0)}\widehat{w}_x - \mathcal{H}_y^{(0)}\widehat{w}_y = \widehat{0}$ is used to enforce values of u obtained with respect to x direction and those obtained with respect to y direction to be identical; and the last sub-system $\mathcal{K}_x\widehat{w}_x + \mathcal{K}_y\widehat{w}_y = \widehat{f}$ is the discretisation of the governing equation at neighbouring nodes: $[\mathbf{x}_2, \mathbf{x}_4, \mathbf{x}_6, \mathbf{x}_8]$.

Then, expression (6.7) is solved for the weight vector $(\widehat{w}_x, \widehat{w}_y)^T$. Finally, by substituting $(\widehat{w}_x, \widehat{w}_y)^T$ into (6.1)-(6.3), one can obtain approximate expressions of computing the field variable and its derivatives over the stencil.

6.2.2 Temporal discretisation

Equations governing transient problems can be written in a general form

$$\frac{\partial \mathbf{u}}{\partial t} = \mathbf{F}(\mathbf{u}, t), \tag{6.8}$$

where function $\mathbf{F}(\mathbf{u}, t)$ represents linear, denoted by $\mathbf{F}_L(\mathbf{u}, t)$, and non-linear, $\mathbf{F}_{NL}(\mathbf{u}, t)$, terms

$$\mathbf{F}(\mathbf{u}, t) = \mathbf{F}_L(\mathbf{u}, t) + \mathbf{F}_{NL}(\mathbf{u}, t). \tag{6.9}$$

One can discretise equation (6.8) in the form of

$$\mathbf{F}(\mathbf{u}, t)^{(n+1)} = \theta\mathbf{F}(\mathbf{u}, t)^{(n+1)} + (1-\theta)\mathbf{F}(\mathbf{u}, t)^{(n)}, \tag{6.10}$$

where θ is a blending factor, $0 \leq \theta \leq 1$, and the superscript denotes the time level. When $\theta = 0$, the value at the time level $(n+1)$ is explicitly determined by the value at the time (n). This type of scheme, named the fully explicit, produces a first order accuracy with respect to time, and is unconditionally unstable. A stability condition is required for time step to obtain convergence. When $\theta = 1$ we have the fully implicit scheme. In this scheme, the value at the time level $(n+1)$ is implicitly determined by the value at the time (n). This scheme also gives only first-order accuracy in time, but is unconditionally stable. When $0 < \theta < 1$, the value at the time level $(n+1)$ is determined by the value at the time levels (n) and $(n+1)$. When $\theta = 1/2$, the scheme is known as a Crank-Nicolson scheme, which gives second order accuracy in time and unconditionally stable (Tanner and Xue, 2002). It can be seen that the explicit scheme involves simple calculations (low cost), but suffers from unstableness. On the other hand, the implicit scheme is almost unconditionally stable, but one needs to solve the nonlinear system of algebraic equations. The Crank Nicolson/Adams Bashforth (CN-AB) scheme is

designed to take advantages of the explicit and implicit schemes. It is based on an implicit scheme for treating the linear term, and explicit scheme for the non-linear term

$$\mathbf{F}(\mathbf{u},t)^{(n+1)} = \frac{1}{2}\left(\mathbf{F}_L(\mathbf{u},t)^{(n+1)} + \mathbf{F}_L(\mathbf{u},t)^{(n)}\right) + \frac{3}{2}\mathbf{F}_{NL}(\mathbf{u},t)^{(n)} - \frac{1}{2}\mathbf{F}_{NL}(\mathbf{u},t)^{(n-1)}. \tag{6.11}$$

It is noted that the superscripts $(n-1),(n),(n+1)$ in equation (6.10)-(6.11) denote successive time levels. The CN-AB scheme has been increasingly used in engineering applications (He and Sun, 2007; Tone, 2004; Johnston and Liu, 2004).

6.3 Numerical examples

We measure the solution accuracy by means of absolute error and root mean squared error (RMS)

$$\epsilon = \mid u_i - u_i^e \mid, \tag{6.12}$$

$$RMS = \sqrt{\frac{\sum_{i=1}^{N}(u_i - u_i^e)^2}{N}}, \tag{6.13}$$

where N is the number of collocation nodes, and u_i and u_i^e are the computed and exact solutions, respectively.

6.3.1 Example 1: Heat equation

Consider a 1D heat equation $\dfrac{\partial u}{\partial t} = \dfrac{\partial^2 u}{\partial x^2}$ in a domain $0 \le x \le 1$, $t \ge 0$ with the initial condition given as $u(x,0) = \exp(-x^2)$. The exact solution to this problem can be verified to be $u(x,t) = \dfrac{1}{\sqrt{1+4t}}\exp\left(-\dfrac{x^2}{1+4t}\right)$. Using the CN-AB scheme, the heat equation reduces to

$$u^{(n+1)} - \frac{\Delta t}{2}\frac{\partial^2 u^{(n+1)}}{\partial x^2} = u^{(n)} + \frac{\Delta t}{2}\frac{\partial^2 u^{(n)}}{\partial x^2}. \tag{6.14}$$

Boundary conditions for u at $x=0$ and $x=1$ are taken from the exact solution. It is noted that their values change with time. Computed values of u along the x axis at several time levels are displayed in Figure 6.1. Corresponding analytic solutions are also included for comparison purposes. Very good agreement is achieved.

To study the influence of grid size on numerical accuracy, the RMS error is computed using different grid sizes at a fixed time level $t = 1$. A time step $\Delta t = 10^{-3}$ and grids of $\{11, 21, \cdots, 101\}$ nodes are used. The RMS error against the grid size is shown in Figure 6.2, where a high rate of convergence, $O(h^{4.65})$, is observed.

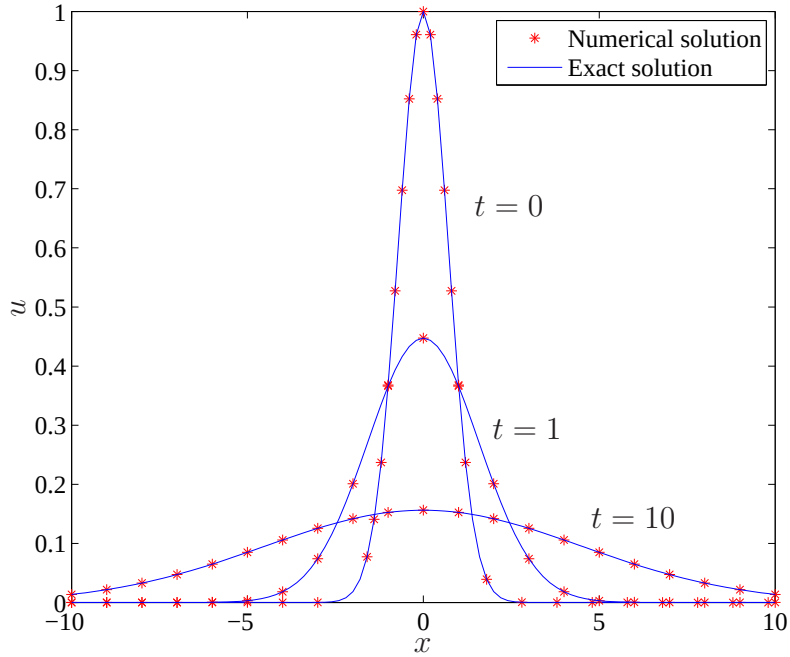

Figure 6.1 Example 1, Heat equation, $N = 101$, $\Delta t = 0.001$. Exact and computed solutions at several time levels.

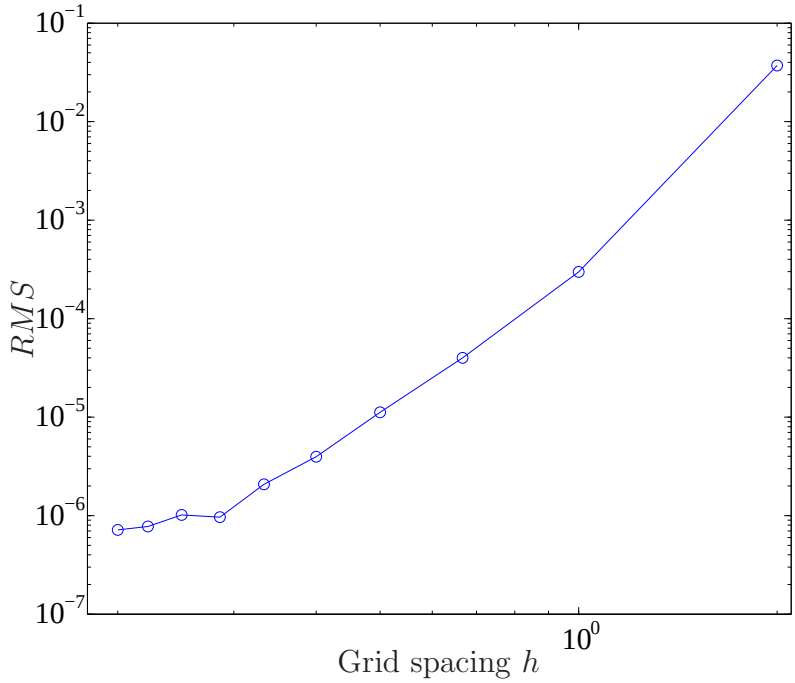

Figure 6.2 Example 1, Heat equation, $N = \{11, 21, \cdots, 101\}$. Error against grid size at $t = 1$. The solution converges apparently as $O(h^{4.65})$.

To analyse the influence of time step on numerical accuracy, the RMS error is computed using different time steps $\{0.1, 0.09, \cdots, 0.01\}$ and a fixed grid of 101 nodes. Figure 6.3 displays the RMS error versus time step at a time level $t = 1$, where a second order rate of convergence is observed. The present method based on compact local IRBF stencils and CN-AB scheme is able to produce a solution that is high order accurate in space and second-order accurate in time.

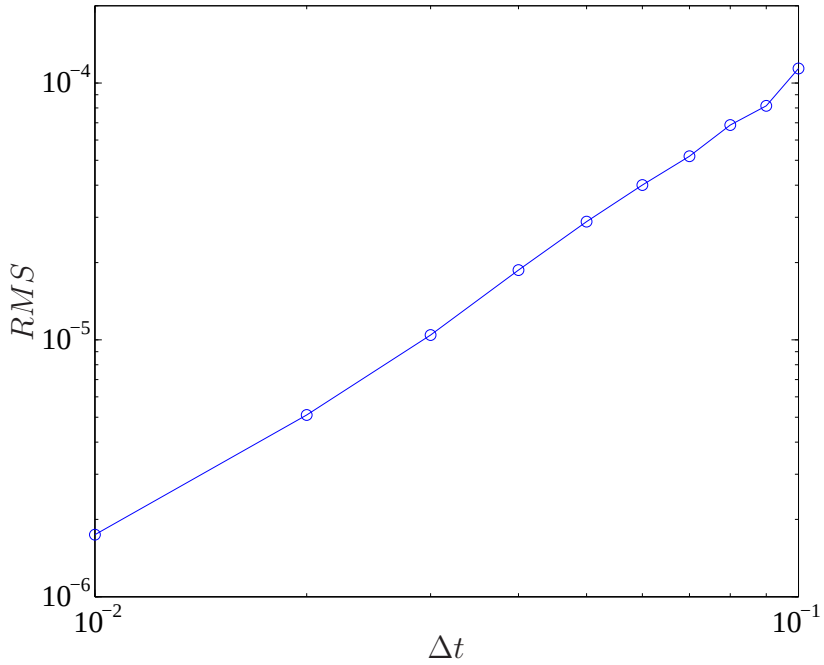

Figure 6.3 Example 1, Heat equation, $N = 101$, $\Delta t = \{10^{-2}, 2 \times 10^{-2}, \cdots, 10^{-1}\}$. Error against time step at $t = 1$. The solution converges apparently as $O(\Delta t^{1.81})$.

6.3.2 Example 2: Travelling inviscid cosine wave

The travelling inviscid cosine wave is governed by a 1D-hyperbolic equation defined as $\dfrac{\partial u}{\partial t} + \dfrac{\partial u}{\partial x} = 0$. The exact solution is taken to be $u(x,t) = \cos(x - t)$. Boundary condition (at $x = 0$) and initial condition (at $t = 0$) are derived from the exact solution. Computed values of u in the domain $[-10\pi, 10\pi]$ at a time level $t = 1.5$ together with the corresponding exact solution are shown in Figure 6.4. Very good agreement is obtained.

Table 6.1 displays the RMS error at several time levels t using a grid of 42 nodes and a time step $\Delta t = 10^{-4}$. Results obtained by RBFs (Kansa, 2007) and local RBFs (Islam et al., 2013) are also included for comparison purposes. The present method yields the most accurate results at all time levels. Figure 6.5 describes the solution behaviour with grid refinement, where the number of grid nodes employed varies in a range of $N = \{11, 21, \cdots, 101\}$. A fast rate of convergence, $O(h^{3.53})$, is observed.

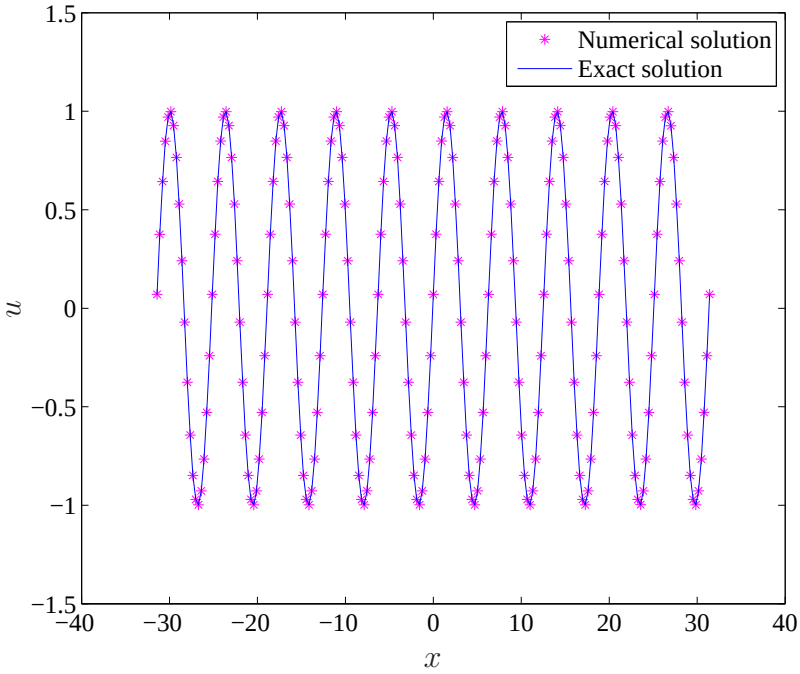

Figure 6.4 Example 2, $N = 201$, $\Delta t = 0.001$, $x \in [-10\pi; 10\pi]$. Exact and numerical solutions at $t = 1.5$.

Table 6.1 Example 2, Hyperbolic equation, $N = 42$, $\Delta t = 10^{-4}$, the root mean squared errors at several time levels t.

t	Present	Kansa (Kansa, 2007)	Islam (Islam et al., 2013)
0.002	5.856E-08	3.6E-03	1.06E-06
$\pi/2$	1.225E-05	6.7E-05	2.50E-04
$3\pi/2$	1.670E-05	2.7E-04	1.06E-04
2π	1.886E-05	7.3E-05	3.32E-04

6.3.3 Example 3: 1D-Burgers' Equation

The Burgers' equations have a wide range of applicability, e.g. in the modelling of shock wave and heat conduction. As a result, solutions to 1D and 2D Burgers' equations have received a great deal of attention.

Consider a 1D-Burgers' equation $\dfrac{\partial u}{\partial t} - \dfrac{\partial^2 u}{\partial x^2} + u\dfrac{\partial u}{\partial x} = 0$ with the exact solution being $u(x,t) = -\dfrac{2\sinh(x)}{\cosh(x) - e^{-t}}$. The analytic solution at various time levels are tabulated in Table 6.2 and displayed in Figure 6.6. The domain of interest is $-9 \leq x \leq 9$.

The initial condition chosen at $t = 0.1$ is taken from the analytic solution: $u(x,t) = -\dfrac{2\sinh(x)}{\cosh(x) - e^{-0.1}}$. We assume that the boundary conditions are fixed,

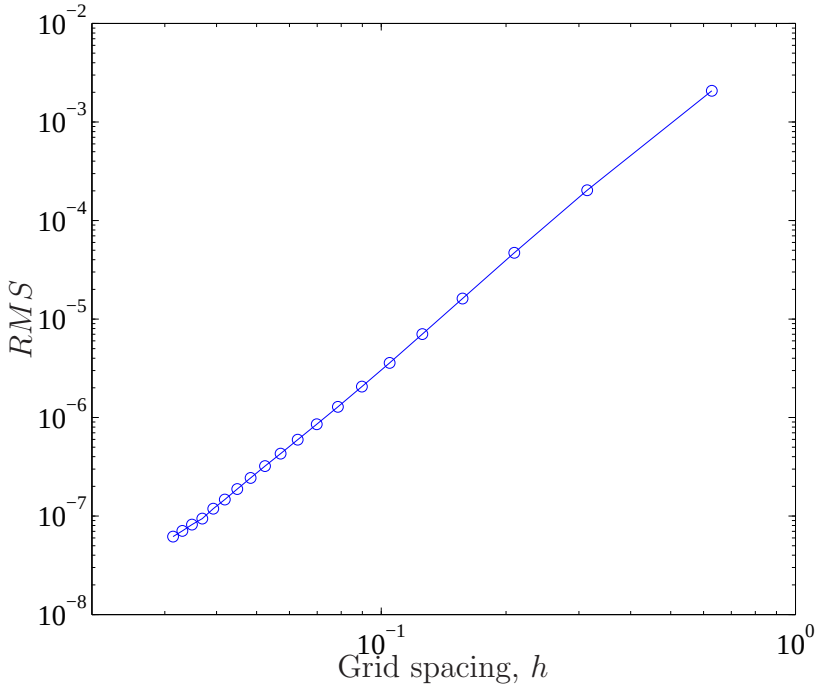

Figure 6.5 Example 2, Hyperbolic equation, $N = \{11, 21, \cdots, 201\}$, $\Delta t = 0.001$, $x \in [0; 2\pi]$. RMS error against grid size at $t = 2$. The solution converges as $O(h^{3.53})$

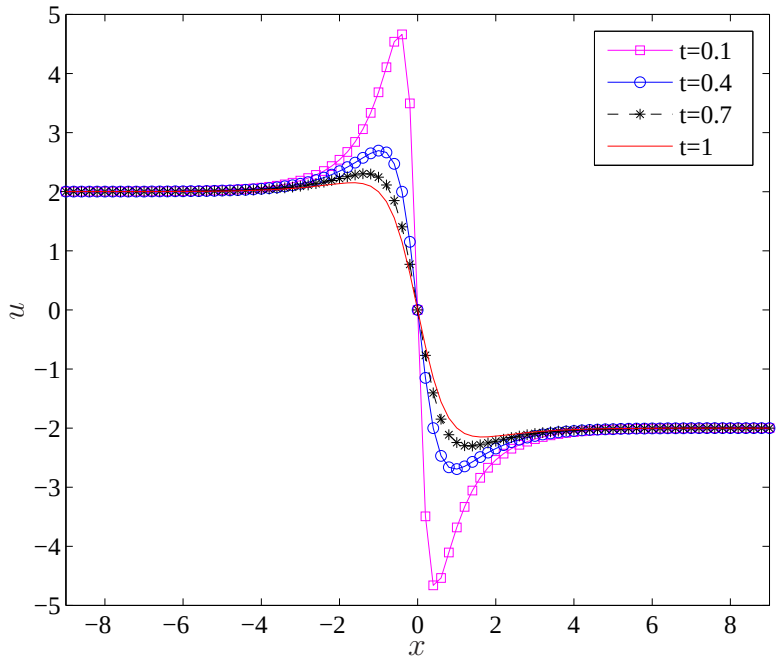

Figure 6.6 Example 3, 1D-Burgers' Equation. Analytic solution of Burger equation at various time levels.

i.e. $u(-9,t)=2$ and $u(9,t)=-2$ instead of changing with time. Time step and grid size are chosen as $\Delta t=0.01$ and $h=0.2$. They are taken to be same as those reported in (Hoffmann and Chiang, 2000) for comparison purposes.

The Burgers' equation is discretised as follows

$$\frac{u^{(n+1)}-u^{(n)}}{\Delta t}-\frac{1}{2}\left(\frac{\partial^2 u^{(n+1)}}{\partial x^2}+\frac{\partial^2 u^{(n)}}{\partial x^2}\right)+\left(\frac{3}{2}u^{(n)}\frac{\partial u^{(n)}}{\partial x}-\frac{1}{2}u^{(n-1)}\frac{\partial u^{(n-1)}}{\partial x}\right)=0, \tag{6.15}$$

or

$$u^{(n+1)}-\frac{\Delta t}{2}\frac{\partial^2 u^{(n+1)}}{\partial x^2}=u^{(n)}+\frac{\Delta t}{2}\frac{\partial^2 u^{(n)}}{\partial x^2}-\frac{\Delta t}{2}\left(3u^{(n)}\frac{\partial u^{(n)}}{\partial x}-u^{(n-1)}\frac{\partial u^{(n-1)}}{\partial x}\right). \tag{6.16}$$

Results obtained at several time levels are presented in Table 6.3, showing a good agreement with the exact solution. We also compare the present results with those by the finite difference methods employed with the DuFort-Frankel explicit (D/F), forward time/central space (FTCS) explicit, modified Runge-Kutta (MRK) and second order Total Variation Diminishing (TVD) schemes (Hoffmann and Chiang, 2000). Figures 6.7 and 6.8 display the error distribution over the spatial domain at two time levels using the same time step and grid size. The present method is seen to perform much better than the finite difference methods. It is noted that the error presented is simply taken as the difference between the analytic solution and the numerical solution.

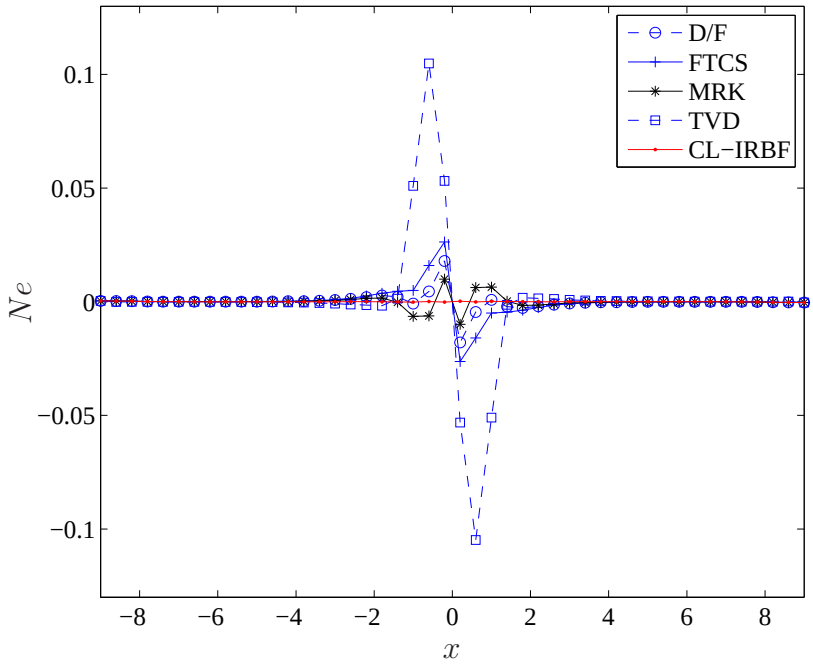

Figure 6.7 Example 3, 1D Burger's equation. Distribution of error over the spatial domain at $t=0.4$ by the DuFort-Frankel explicit (D/F), FTCS explicit, modified Runge-Kutta (MRK), second order TVD scheme (TVD), and present (CL-IRBF) methods.

Table 6.2 Example 3. Exact solution

x	$t=0.1$	$t=0.4$	$t=0.7$	$t=1$
-9.0	2.0004	2.0003	2.0002	2.0002
-8.6	2.0007	2.0005	2.0004	2.0003
-8.2	2.0010	2.0007	2.0005	2.0004
-7.8	2.0015	2.0011	2.0008	2.0006
-7.4	2.0022	2.0016	2.0012	2.0009
-7.0	2.0033	2.0024	2.0018	2.0013
-6.6	2.0049	2.0036	2.0027	2.0020
-6.2	2.0074	2.0054	2.0040	2.0030
-5.8	2.0110	2.0081	2.0060	2.0044
-5.4	2.0164	2.0121	2.0089	2.0066
-5.0	2.0245	2.0180	2.0133	2.0098
-4.6	2.0366	2.0269	2.0198	2.0145
-4.2	2.0549	2.0401	2.0293	2.0214
-3.8	2.0823	2.0597	2.0434	2.0315
-3.4	2.1237	2.0889	2.0639	2.0457
-3.0	2.1866	2.1321	2.0934	2.0656
-2.6	2.2833	2.1955	2.1347	2.0917
-2.2	2.4335	2.2871	2.1895	2.1224
-1.8	2.6715	2.4144	2.2538	2.1479
-1.4	3.0565	2.5724	2.3022	2.1360
-1.0	3.6826	2.6931	2.2460	2.0000
-0.6	4.5374	2.4717	1.8484	1.5574
-0.2	3.4945	1.1513	0.7692	0.6174
0.2	-3.4945	-1.1513	-0.7692	-0.6174
0.6	-4.5374	-2.4717	-1.8484	-1.5574
1.0	-3.6826	-2.6931	-2.2460	-2.0000
1.4	-3.0565	-2.5724	-2.3022	-2.1360
1.8	-2.6715	-2.4144	-2.2538	-2.1479
2.2	-2.4335	-2.2871	-2.1895	-2.1224
2.6	-2.2833	-2.1955	-2.1347	-2.0917
3.0	-2.1866	-2.1321	-2.0934	-2.0656
3.4	-2.1237	-2.0889	-2.0639	-2.0457
3.8	-2.0823	-2.0597	-2.0434	-2.0314
4.2	-2.0549	-2.0401	-2.0293	-2.0214
4.6	-2.0366	-2.0269	-2.0198	-2.0145
5.0	-2.0245	-2.0180	-2.0133	-2.0098
5.4	-2.0164	-2.0121	-2.0089	-2.0066
5.8	-2.0110	-2.0081	-2.0060	-2.0044
6.2	-2.0074	-2.0054	-2.0040	-2.0030
6.6	-2.0049	-2.0036	-2.0027	-2.0020
7.0	-2.0033	-2.0024	-2.0018	-2.0013
7.4	-2.0022	-2.0016	-2.0012	-2.0009
7.8	-2.0015	-2.0011	-2.0008	-2.0006
8.2	-2.0010	-2.0007	-2.0005	-2.0004
8.6	-2.0007	-2.0005	-2.0004	-2.0003
9.0	-2.0004	-2.0003	-2.0002	-2.0002

Table 6.3 Example 3. Solution by CLIRBF

x	$t=0.1$	$t=0.4$	$t=0.7$	$t=1$
-9.0	2.0000	2.0000	2.0000	2.0000
-8.6	2.0007	2.0002	2.0001	2.0001
-8.2	2.0010	2.0005	2.0003	2.0002
-7.8	2.0015	2.0010	2.0006	2.0004
-7.4	2.0022	2.0016	2.0011	2.0007
-7.0	2.0033	2.0024	2.0017	2.0012
-6.6	2.0049	2.0037	2.0026	2.0019
-6.2	2.0074	2.0054	2.0040	2.0029
-5.8	2.0110	2.0081	2.0060	2.0044
-5.4	2.0164	2.0121	2.0089	2.0066
-5.0	2.0245	2.0181	2.0133	2.0098
-4.6	2.0366	2.0269	2.0198	2.0145
-4.2	2.0549	2.0401	2.0293	2.0214
-3.8	2.0823	2.0597	2.0434	2.0315
-3.4	2.1237	2.0889	2.0639	2.0458
-3.0	2.1866	2.1321	2.0934	2.0656
-2.6	2.2833	2.1955	2.1347	2.0918
-2.2	2.4335	2.2871	2.1896	2.1225
-1.8	2.6715	2.4144	2.2538	2.1480
-1.4	3.0565	2.5725	2.3023	2.1361
-1.0	3.6826	2.6932	2.2461	2.0001
-0.6	4.5374	2.4716	1.8484	1.5575
-0.2	3.4945	1.1515	0.7693	0.6175
0.2	-3.4945	-1.1515	-0.7694	-0.6175
0.6	-4.5374	-2.4716	-1.8484	-1.5575
1.0	-3.6826	-2.6932	-2.2461	-2.0001
1.4	-3.0565	-2.5725	-2.3023	-2.1361
1.8	-2.6715	-2.4144	-2.2538	-2.1480
2.2	-2.4335	-2.2871	-2.1896	-2.1225
2.6	-2.2833	-2.1955	-2.1347	-2.0918
3.0	-2.1866	-2.1321	-2.0934	-2.0656
3.4	-2.1237	-2.0889	-2.0639	-2.0458
3.8	-2.0823	-2.0597	-2.0434	-2.0315
4.2	-2.0549	-2.0401	-2.0293	-2.0214
4.6	-2.0366	-2.0269	-2.0198	-2.0145
5.0	-2.0245	-2.0181	-2.0133	-2.0098
5.4	-2.0164	-2.0121	-2.0089	-2.0066
5.8	-2.0110	-2.0081	-2.0060	-2.0044
6.2	-2.0074	-2.0054	-2.0040	-2.0029
6.6	-2.0049	-2.0037	-2.0026	-2.0019
7.0	-2.0033	-2.0024	-2.0017	-2.0012
7.4	-2.0022	-2.0016	-2.0011	-2.0007
7.8	-2.0015	-2.0010	-2.0006	-2.0004
8.2	-2.0010	-2.0005	-2.0003	-2.0002
8.6	-2.0007	-2.0002	-2.0001	-2.0001
9.0	-2.0000	-2.0000	-2.0000	-2.0000

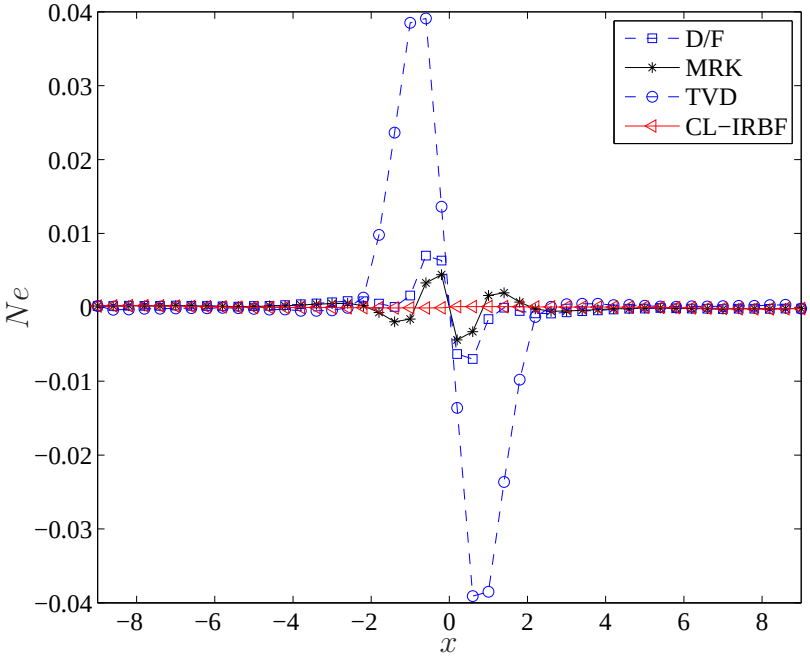

Figure 6.8 Example 3, 1D Burger's equation. Distribution of error over the spatial domain at $t = 1$ by the DuFort-Frankel explicit (D/F), FTCS explicit, modified Runge-Kutta (MRK), second order TVD scheme (TVD), and present (CL-IRBF) methods.

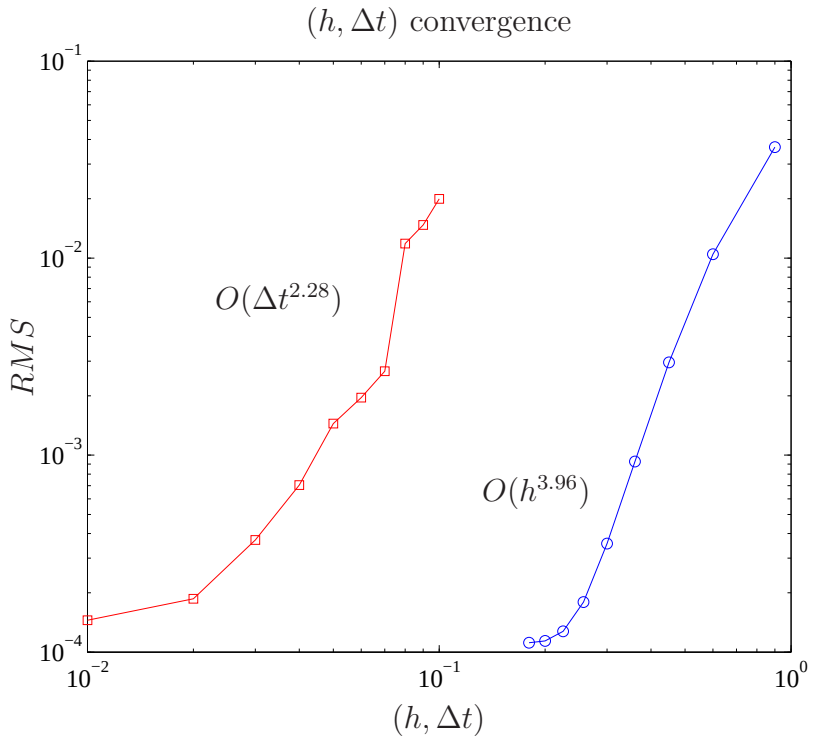

Figure 6.9 Example 3, 1D Burger's equation. Variations of the RMS error of the solution as time step and grid size are reduced.

Figure 6.9 shows the behaviour of the CLIRBF solution with respect to time-step and grid refinements. For the former, a fixed grid of 71 nodes and a number of time steps, $\{0.1, 0.09, \cdots, 0.01\}$, are employed. For the latter, a fixed time step $\Delta t = 0.01$ and a number of grids, $\{21, 31, \cdots, 101\}$, are employed. The error is computed at a time level $t = 0.5$. The solution converges as $O(h^{3.96})$ in space and $O(\Delta t^{2.28})$ in time.

6.3.4 Example 4: 2D-Burger's equation

Consider a 2D-Burgers' equation:

$$\frac{\partial u}{\partial t} + u\frac{\partial u}{\partial x} + v\frac{\partial u}{\partial y} = \frac{1}{Re}\left(\frac{\partial^2 u}{\partial x^2} + \frac{\partial^2 u}{\partial y^2}\right), \tag{6.17}$$

$$\frac{\partial v}{\partial t} + u\frac{\partial v}{\partial x} + v\frac{\partial v}{\partial y} = \frac{1}{Re}\left(\frac{\partial^2 v}{\partial x^2} + \frac{\partial^2 v}{\partial y^2}\right), \tag{6.18}$$

where $a \le x \le b$, $c \le y \le d$ and $t \ge 0$.

Using the CN-AB scheme, the two equations (6.17)-(6.18) reduce to

$$u^{(n+1)} - \frac{\Delta t}{2Re}\left(\frac{\partial^2 u^{(n+1)}}{\partial x^2} + \frac{\partial^2 u^{(n+1)}}{\partial y^2}\right) = u^{(n)} + \frac{\Delta t}{2Re}\left(\frac{\partial^2 u^{(n)}}{\partial x^2} + \frac{\partial^2 u^{(n)}}{\partial y^2}\right)$$
$$-\frac{3\Delta t}{2}\left(u^{(n)}\frac{\partial u^{(n)}}{\partial x} + v^{(n)}\frac{\partial u^{(n)}}{\partial y}\right) + \frac{\Delta t}{2}\left(u^{(n-1)}\frac{\partial u^{(n-1)}}{\partial x} + v^{(n-1)}\frac{\partial u^{(n-1)}}{\partial y}\right), \tag{6.19}$$

$$v^{(n+1)} - \frac{\Delta t}{2Re}\left(\frac{\partial^2 v^{(n+1)}}{\partial x^2} + \frac{\partial^2 v^{(n+1)}}{\partial y^2}\right) = v^{(n)} + \frac{\Delta t}{2Re}\left(\frac{\partial^2 v^{(n)}}{\partial x^2} + \frac{\partial^2 v^{(n)}}{\partial y^2}\right)$$
$$-\frac{3\Delta t}{2}\left(u^{(n)}\frac{\partial v^{(n)}}{\partial x} + v^{(n)}\frac{\partial v^{(n)}}{\partial y}\right) + \frac{\Delta t}{2}\left(u^{(n-1)}\frac{\partial v^{(n-1)}}{\partial x} + v^{(n-1)}\frac{\partial v^{(n-1)}}{\partial y}\right), \tag{6.20}$$

and we employ compact local IRBF stencils to approximate spatial derivatives. The present method is verified with the following two problems.

Problem 1: This problem has the exact solution

$$u(x, y, t) = \frac{3}{4} - \frac{1}{4\left(1 + exp\left(Re(-t - 4x - 4y)/32\right)\right)}, \tag{6.21}$$

$$v(x, y, t) = \frac{3}{4} + \frac{1}{4\left(1 + exp\left(Re(-t - 4x - 4y)/32\right)\right)}, \tag{6.22}$$

where $0 \le x, y \le 1$ and $t \ge 0$. The initial conditions and boundary conditions for u and v are specified by using the exact solution, i.e. equations (6.21)- (6.22). The simulation is conducted for $Re = 100$ with a time step $\Delta t = 10^{-4}$ and a grid of density 21×21. The absolute errors of u and v by the present method and fully implicit FDM (Bahadir, 2003), and fully implicit FDM with discrete Adomian decomposition (Zhu et al., 2010) are displayed in Table 6.4 for $t = 0.01$ and in Table 6.5 for $t = 0.5$. It can be seen that, for both cases, the present method is much more accurate than the FDMs and yields a very high level of accuracy.

Table 6.4 Example 4, Problem 1, $Re = 100$, $t = 0.01$, $\Delta t = 10^{-4}$, $N = 21 \times 21$. Comparison of absolute errors for u and v at several mesh points.

(x, y)	Error of u			Error of v		
	Present	Bahadir (Bahadir, 2003)	Zhu et.al. (Zhu et al., 2010)	Present	Bahadir (Bahadir, 2003)	Zhu et.al. (Zhu et al., 2010)
(0.1,0.1)	$1.14911e{-6}$	$5.29661e{-5}$	$5.91368e{-5}$	$1.14908e{-6}$	$7.29661e{-5}$	$5.91368e{-5}$
(0.5,0.1)	$2.29430e{-8}$	$1.20674e{-5}$	$4.84030e{-6}$	$2.30915e{-8}$	$7.93260e{-6}$	$4.84030e{-6}$
(0.9,0.1)	$1.71473e{-7}$	$1.10003e{-5}$	$3.41000e{-8}$	$1.71541e{-7}$	$8.99970e{-6}$	$3.41000e{-8}$
(0.3,0.3)	$3.66283e{-7}$	$6.29661e{-5}$	$5.91368e{-5}$	$3.66776e{-7}$	$6.29661e{-5}$	$5.91368e{-5}$
(0.7,0.3)	$2.53254e{-9}$	$2.06740e{-6}$	$4.84030e{-6}$	$3.01732e{-9}$	$2.06740e{-6}$	$4.84030e{-6}$
(0.1,0.5)	$1.89259e{-8}$	$4.04048e{-6}$	$1.64290e{-6}$	$1.86997e{-8}$	$5.95952e{-6}$	$1.64290e{-6}$
(0.5,0.5)	$3.65917e{-7}$	$6.29661e{-5}$	$5.91368e{-5}$	$3.66422e{-7}$	$6.29661e{-5}$	$5.91368e{-5}$
(0.9,0.5)	$1.24917e{-8}$	$2.06740e{-6}$	-	$1.27592e{-8}$	$2.06740e{-6}$	-
(0.3,0.7)	$2.78012e{-9}$	$4.04048e{-6}$	-	$2.30865e{-9}$	$4.04048e{-6}$	-
(0.7,0.7)	$3.73489e{-7}$	$6.29661e{-5}$	-	$3.73943e{-7}$	$6.29661e{-5}$	-
(0.1,0.9)	$4.50360e{-8}$	$8.29028e{-6}$	-	$4.48990e{-8}$	$1.70972e{-6}$	-
(0.5,0.9)	$3.14502e{-10}$	$4.04048e{-6}$	-	$1.97235e{-10}$	$4.04048e{-6}$	-
(0.9,0.9)	$9.85985e{-7}$	$6.29661e{-5}$	-	$9.85766e{-7}$	$6.29661e{-5}$	-

Table 6.5 Example 4, Problem 1, $Re = 100$, $t = 0.5$, $\Delta t = 10^{-2}$, $N = 21 \times 21$.: Comparison of absolute errors for u and v at several mesh points.

(x, y)	Error of u			Error of v		
	Present	Bahadir (Bahadir, 2003)	Zhu et.al. (Zhu et al., 2010)	Present	Bahadir (Bahadir, 2003)	Zhu et.al. (Zhu et al., 2010)
(0.1,0.1)	$8.50334e{-6}$	$9.72051e{-4}$	$2.77664e{-4}$	$8.50020e{-6}$	$9.07949e{-4}$	$2.77664e{-4}$
(0.5,0.1)	$1.56541e{-7}$	$7.12590e{-4}$	$4.52081e{-4}$	$1.51181e{-7}$	$1.37741e{-3}$	$4.52081e{-4}$
(0.9,0.1)	$2.44263e{-6}$	$6.92379e{-4}$	$3.37430e{-6}$	$2.44726e{-6}$	$1.38762e{-3}$	$3.37400e{-6}$
(0.3,0.3)	$1.69270e{-5}$	$1.25205e{-3}$	$2.77664e{-4}$	$1.69221e{-5}$	$7.17949e{-4}$	$2.77664e{-4}$
(0.7,0.3)	$2.38233e{-7}$	$7.42590e{-4}$	$4.52081e{-4}$	$2.43770e{-7}$	$1.37741e{-3}$	$4.52081e{-4}$
(0.1,0.5)	$6.92799e{-6}$	$9.14042e{-4}$	$2.86553e{-4}$	$6.93219e{-6}$	$7.95958e{-4}$	$2.86553e{-4}$
(0.5,0.5)	$4.52579e{-6}$	$1.10205e{-3}$	$2.77664e{-4}$	$4.52359e{-6}$	$1.72051e{-4}$	$2.77664e{-4}$
(0.9,0.5)	$3.06627e{-7}$	$3.82590e{-4}$	-	$3.04792e{-7}$	$6.17410e{-4}$	-
(0.3,0.7)	$5.81910e{-6}$	$7.54042e{-4}$	-	$5.82246e{-6}$	$5.55958e{-4}$	-
(0.7,0.7)	$2.64176e{-6}$	$8.92051e{-4}$	-	$2.64221e{-6}$	$7.82051e{-4}$	-
(0.1,0.9)	$3.68561e{-7}$	$8.15864e{-4}$	-	$3.65375e{-7}$	$8.14136e{-4}$	-
(0.5,0.9)	$4.33886e{-6}$	$2.04042e{-4}$	-	$4.33811e{-6}$	$2.40424e{-5}$	-
(0.9,0.9)	$1.49306e{-5}$	$1.00205e{-3}$	-	$1.49326e{-5}$	$1.09205e{-3}$	-

To investigate the order of accuracy of CLIRBF stencils, the RMS error is calculated upon four grids, $\{11 \times 11, 21 \times 21, 31 \times 31, 41 \times 41\}$, and the time step is chosen very small (i.e. $\Delta t = 10^{-4}$) to minimise its effects. To investigate the order of accuracy of the CN-AB scheme, we employ a fixed grid of density 21×21 and several time steps, $\{0.1, 0.05, 0.01, 0.005\}$. Results obtained at a time level $t = 0.05$ are shown in Figure 6.10, where the solution is seen to be about second-order accurate in time and fourth-order accurate in space.

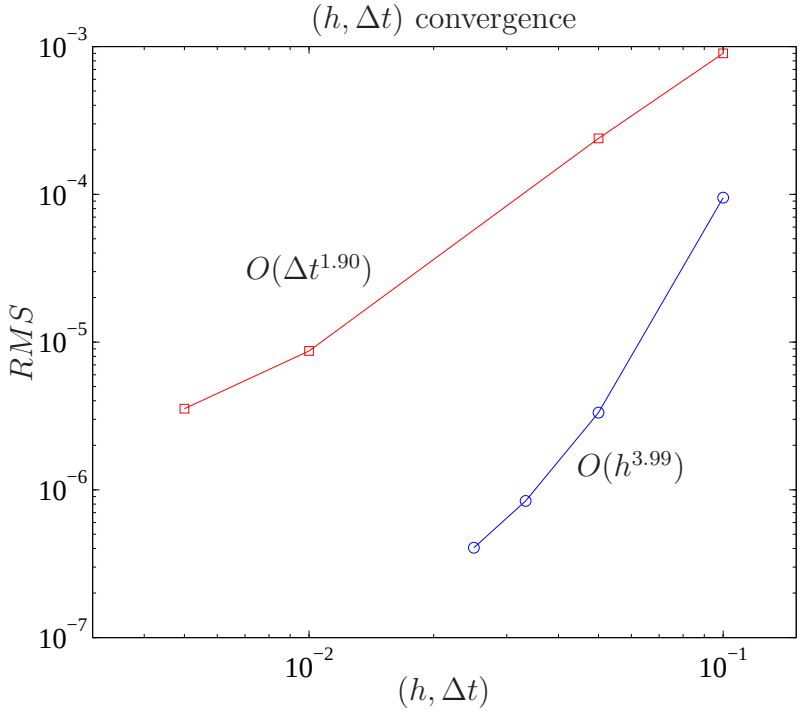

Figure 6.10 Example 4, Problem 1, $t = 0.05$. Spatial and temporal convergence rates.

Problem 2: The computational domain is taken as $0 \leq x \leq 0.5$ and $0 \leq y \leq 0.5$. The initial and boundary conditions are given below

Initial conditions:

$$\left.\begin{array}{l} u(x, y, 0) = \sin(\pi x) + \cos(\pi y) \\ v(x, y, 0) = x + y \end{array}\right\} 0 \leq x \leq 0.5, \quad 0 \leq y \leq 0.5. \tag{6.23}$$

Boundary conditions:

$$\left.\begin{array}{ll} u(0, y, t) = \cos(\pi y), & u(0.5, y, t) = 1 + \cos(\pi y) \\ v(0, y, t) = y, & v(0.5, y, t) = 0.5 + y \end{array}\right\} 0 \leq y \leq 0.5, t \geq 0, \tag{6.24}$$

$$\left.\begin{array}{ll} u(x, 0, t) = 1 + \sin(\pi x), & u(x, 0.5, t) = \sin(\pi x) \\ v(x, 0, t) = x, & v(x, 0.5, t) = x + 0.5 \end{array}\right\} 0 \leq x \leq 0.5, t \geq 0. \tag{6.25}$$

Two values of the Reynolds number, $Re = 50$ and $Re = 500$, are considered. The simulation is performed with a time step $\Delta t = 10^{-4}$ and two grids (21×21 for $Re = 50$ and 41×41 for $Re = 500$). Results obtained are compared with those

produced by Jain and Holla, 1978 (Jain and Holla, 1978) and by Bahadir, 2003 (Bahadir, 2003) in Table 6.6 for $Re = 50$ and in Table 6.7 for $Re = 500$. It can be seen that a very good agreement is achieved between these results.

Table 6.6 Example 4, Problem 2, $t = 0.625$: Solutions at $Re = 50$.

(x, y)	Values of u			Values of v		
	Present CN-AB	Bahadir (Bahadir, 2003)	Jain and Holla (Jain and Holla, 1978)	Present CN-AB	Bahadir (Bahadir, 2003)	Jain and Holla (Jain and Holla, 1978)
(0.1,0.1)	0.96940	0.96688	0.97258	0.09803	0.09824	0.09773
(0.3,0.1)	1.14967	1.14827	1.16214	0.14034	0.14112	0.14039
(0.2,0.2)	0.86191	0.85911	0.86281	0.16710	0.16681	0.16660
(0.4,0.2)	0.97868	0.97637	0.96483	0.17109	0.17065	0.17397
(0.1,0.3)	0.66337	0.66019	0.66318	0.26367	0.26261	0.26294
(0.3,0.3)	0.77189	0.76932	0.77030	0.22624	0.22576	0.22463
(0.2,0.4)	0.58245	0.57966	0.58070	0.32849	0.32745	0.32402
(0.4,0.4)	0.75981	0.75678	0.74435	0.32617	0.32441	0.31822

Table 6.7 Example 4, Problem 2. $t = 0.625$: Solutions at $Re = 500$.

(x, y)	Value of u		Value of v	
	Present 41×41	Jain and Holla (Jain and Holla, 1978) $N = 40$	Present 41×41	Jain and Holla (Jain and Holla, 1978) $N = 40$
(0.15,0.1)	0.95586	0.96066	0.08419	0.08612
(0.3,0.1)	0.96657	0.96852	0.07569	0.07712
(0.1,0.2)	0.83973	0.84104	0.17639	0.17828
(0.2,0.2)	0.86454	0.86866	0.16034	0.16202
(0.1,0.3)	0.67517	0.67792	0.25939	0.26094
(0.3,0.3)	0.77123	0.77254	0.21460	0.21542
(0.15,0.4)	0.54487	0.54543	0.31275	0.31360
(0.2,0.4)	0.58525	0.58564	0.29708	0.29776

6.3.5 Example 5. Start-up planar Poiseuille flows

The present method is further tested with transient Poiseuille flows between two parallel plates. The start-up flow occurs when one makes a sudden imposition of a constant pressure gradient ($\Delta p = p_2 - p_1$) to a stationary fluid. In CFD, owing to the existence of their analytic solutions, start-up planar Poiseuille flows are often used to verify new numerical solvers, particularly in the context of viscoelastic flows (e.g. (Waters and King, 1970; Carew et al., 1994; Duarte et al., 2008; Os and Phillips, 2004; Webster et al., 2004; Miranda and Oliveira, 2010; Xue et al., 2004)), where the velocity-pressure formulation is widely employed.

Figure 6.11 displays the geometry of the planar Poiseuille flow. Consider the nondimensional case, where the velocity and length are normalised by the velocity on the centreline and the gap between the two plates, respectively. The analytic solution for the steady state flow thus takes the form $v_x(y) = 4(1-y)y$, with $0 \leq y \leq 1$ (the maximum velocity on the centreline $y = 0.5$ is 1). Due to symmetry, we consider only a half domain (i.e. $[0,1] \times [0.5,1]$) in the present calculation.

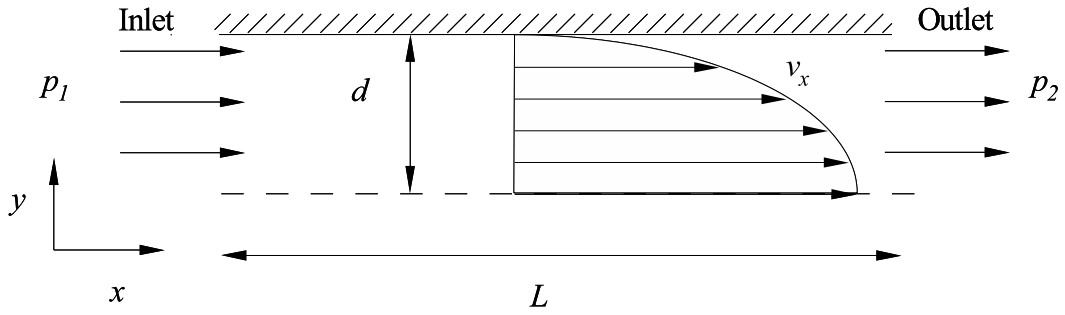

Figure 6.11 Example 5, Schematic of planar Poiseuille flow.

Problem 1. Start up planar Poiseuille flow of Newtonian fluid

The Navier-Stokes equation in the streamfunction-vorticity formulation is given by

$$\frac{\partial^2 \psi}{\partial x^2} + \frac{\partial^2 \psi}{\partial y^2} = -\omega, \tag{6.26}$$

$$\frac{1}{Re}\left(\frac{\partial^2 \omega}{\partial x^2} + \frac{\partial^2 \omega}{\partial y^2}\right) = \frac{\partial \omega}{\partial t} + v_x \frac{\partial \omega}{\partial x} + v_y \frac{\partial \omega}{\partial y}, \tag{6.27}$$

where Re is the Reynolds number, $v_x = \partial\psi/\partial y$ and $v_y = -\partial\psi/\partial x$. The exact solution for this flow takes the form ((Waters and King, 1970))

$$v_x(y,t) = 4y(1-y) - 32\sum_{n=1}^{\infty} \frac{\sin(Ny)}{N^3} e^{-N^2 t}, \tag{6.28}$$

$$v_y(y,t) = 0, \tag{6.29}$$

where $N = (2n-1)\pi$. They lead to the following exact solutions for the streamfunction and vorticity

$$\psi = 4\left(\frac{y^2}{2} - \frac{y^3}{3}\right) - \frac{1}{3} + 32\sum_{n=1}^{\infty}\frac{\cos(Ny)}{N^4}e^{-N^2t}, \tag{6.30}$$

$$\omega = 4(2y-1) + 32\sum_{n=1}^{\infty}\frac{\cos(Ny)}{N^2}e^{-N^2t}. \tag{6.31}$$

We impose velocities on the inlet and outlet, non-slip boundary condition on the wall ($v_x = 0, v_y = 0$) and symmetric conditions ($v_y = 0, \partial v_x/\partial y = 0$) on the centreline. It is noted that the imposed inlet and outlet boundary conditions are functions of time, taken from the exact solution for the velocity v_x - our imposition here is similar to that of Van Os and Phillips (Os and Phillips, 2004).

Boundary conditions for the streamfunction ψ and the vorticity ω are derived as follows. On the centreline, the conditions $\partial v_x/\partial y = 0, v_y = 0$ lead to $\psi = 0, \omega = 0$. On the wall, the velocities $v_x = 0, v_y = 0$ lead to $\psi = const$, which is taken from the analytic solution. The vorticity on the wall is computed as $\omega = -\partial^2\psi/\partial y^2$ and we incorporate $\partial\psi/\partial y = 0$ into $\partial^2\psi/\partial y^2$. On the inlet and outlet, the exact values of the streamfunction are given while the periodic condition is applied for the vorticity, i.e. $\omega^i = \omega^o$ and $\partial\omega^i/\partial x = \partial\omega^o/\partial x$.

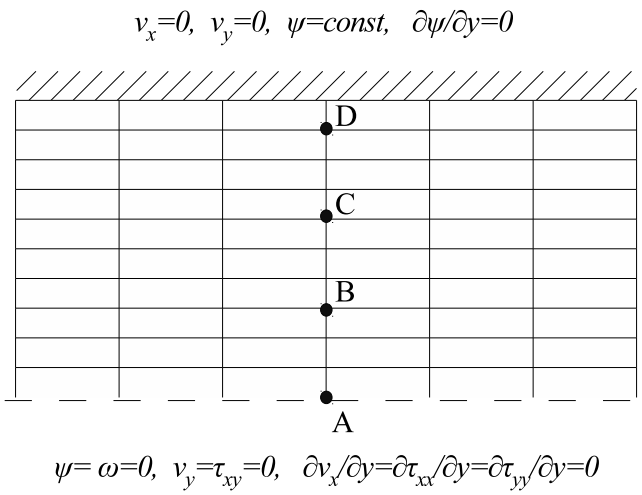

Figure 6.12 Example 5, Grid used for calculating the start-up planar Poiseuille flow. Notice that the boundary conditions for stresses are used for the flow of Oldroyd-B fluid.

The computational domain is represented by a Cartesian grid as shown in Figure 6.12. We also indicate four sample nodes A, B, C and D, at which the evolution of the field variables will be recorded. Figure 6.13 shows the velocity evolution at these indicated sample nodes, while Figure 6.14 illustrates the evolution of the velocity profile. In both figures, the numerical result is displayed by a symbol '$*$', and the analytic solution is displayed by a continuous line. It can be seen that the obtained results lie on the curves of the analytic solution. The value of velocity remains unchanged when $t > 1$ (Figure 6.13), and the velocity profiles at time levels $t = 1$ and $t = 5$ cannot be distinguished (Figure 6.14). Hence, at $t = 1$, it appears that the flow reaches the steady state.

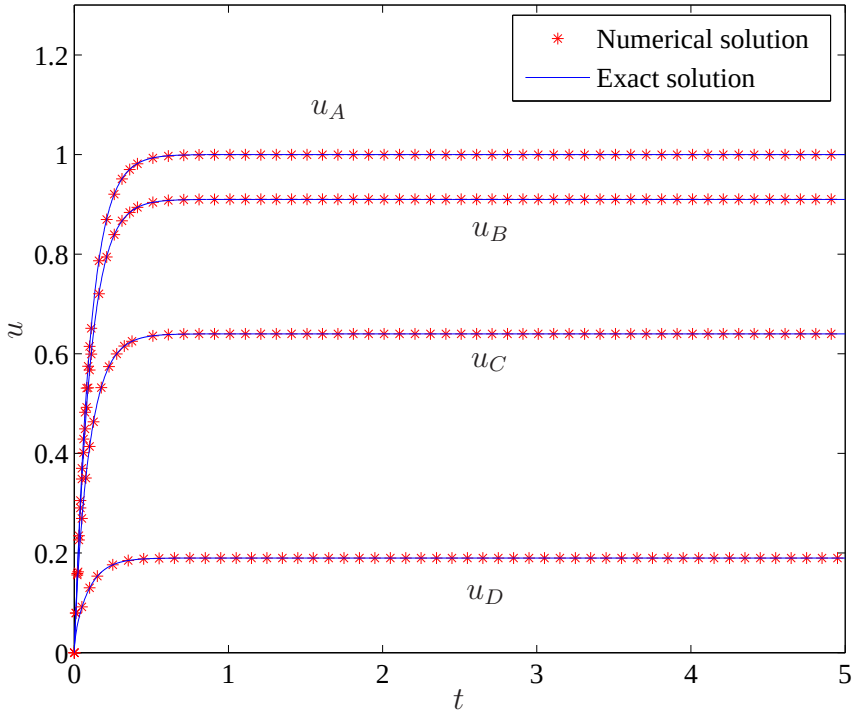

Figure 6.13 Example 5, Problem 1, planar Poiseuille flow of Newtonian fluid, grid spacing $h = 0.05$. Evolution of velocity at nodes indicated in Figure 6.12.

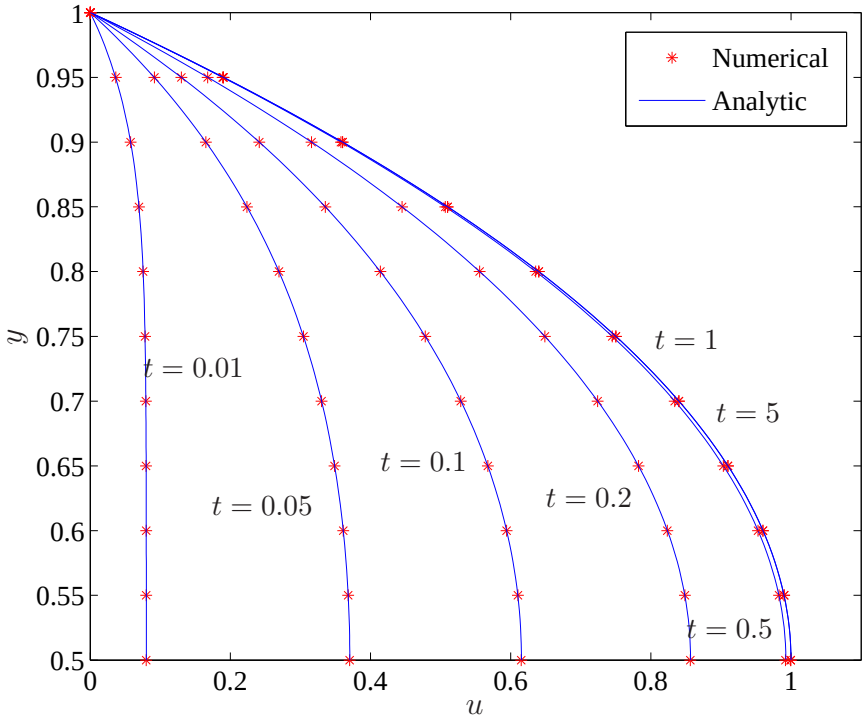

Figure 6.14 Example 5, Problem 1, planar Poiseuille flow of Newtonian fluid, $h = 0.05$. Velocity profiles at different non-dimensional times. Notice that the velocity profiles at $t = 1$ and $t = 5$ are indistinguishable.

We also study convergence rates of the spatial and temporal discretisations of the present method. The obtained results computed at $t = 0.5$ are shown in Figure 6.15. For the the spatial discretisation, the time step $\Delta t = 10^{-4}$ is employed, while the grid sizes used are $h = \{0.1, 0.05, 0.033, 0.025\}$. For the temporal discretisation, the grid size is fixed at $h = 0.05$, and the time steps used are $\Delta t = \{10^{-3}, 7 \times 10^{-4}, 4 \times 10^{-4}, 10^{-4}\}$. The solution converges apparently as $O(h^{3.28})$ and $O(\Delta t^{1.49})$. It can be seen that the rate is relatively high for the spatial discretisation, but lower than the expected value of 2 for the temporal discretisation.

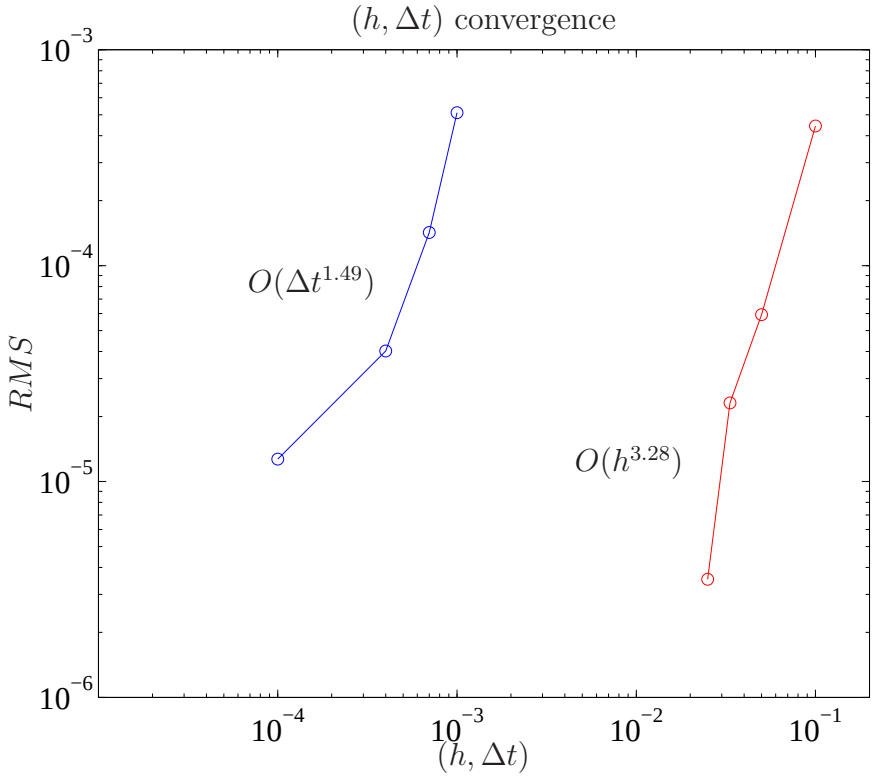

Figure 6.15 Example 5, Problem 1, planar Poiseuille flow of Newtonian fluid, $t = 0.5$: convergence rates of the present method in time and space.

Problem 2: Start up planar Poiseuille flow of Oldroyd-B fluid

The equations governing the motion of an Oldroyd-B fluid are given by

$$\frac{\partial^2 \psi}{\partial x^2} + \frac{\partial^2 \psi}{\partial y^2} = -\omega, \tag{6.32}$$

$$\frac{\alpha}{Re}\left(\frac{\partial^2 \omega}{\partial x^2} + \frac{\partial^2 \omega}{\partial y^2}\right) + \frac{1}{Re}\left(\frac{\partial^2 \tau_{xy}}{\partial x^2} - \frac{\partial^2 \tau_{xy}}{\partial y^2} - \frac{\partial^2 (\tau_{xx} - \tau_{yy})}{\partial x \partial y}\right) = \frac{\partial \omega}{\partial t} + \left(v_x \frac{\partial \omega}{\partial x} + v_y \frac{\partial \omega}{\partial y}\right), \tag{6.33}$$

$$\frac{\partial \tau_{xx}}{\partial t} + v_x \frac{\partial \tau_{xx}}{\partial x} + v_y \frac{\partial \tau_{xx}}{\partial y} - 2\frac{\partial v_x}{\partial x}\tau_{xx} - 2\frac{\partial v_x}{\partial y}\tau_{xy} + \frac{\tau_{xx}}{We} = \frac{2\,(1-\alpha)}{We}\frac{\partial v_x}{\partial x}, \tag{6.34}$$

$$\frac{\partial \tau_{xy}}{\partial t} + v_x \frac{\partial \tau_{xy}}{\partial x} + v_y \frac{\partial \tau_{xy}}{\partial y} - \frac{\partial v_x}{\partial y}\tau_{yy} - \frac{\partial v_y}{\partial x}\tau_{xx} + \frac{\tau_{xy}}{We} = \frac{(1-\alpha)}{We}\left(\frac{\partial v_x}{\partial y} + \frac{\partial v_y}{\partial x}\right), \tag{6.35}$$

$$\frac{\partial \tau_{yy}}{\partial t} + v_x \frac{\partial \tau_{yy}}{\partial x} + v_y \frac{\partial \tau_{yy}}{\partial y} - 2\frac{\partial v_y}{\partial x}\tau_{xy} - 2\frac{\partial v_y}{\partial y}\tau_{yy} + \frac{\tau_{yy}}{We} = \frac{2\,(1-\alpha)}{We}\frac{\partial v_y}{\partial y}, \tag{6.36}$$

where We is the Weissenberg number, and α is the ratio of the retardation time to the relaxation time. Here, we take $\alpha = 1/9$. The analytic solution for this flow takes the form (Waters and King, 1970; Carew et al., 1994)

Velocities:

$$v_x(y,t) = A(y) - 32\sum_{n=1}^{\infty}\frac{\sin(Ny)}{N^3}G_N(E,t), \tag{6.37}$$

$$v_y(y,t) = 0, \tag{6.38}$$

where $N = (2n-1)\pi$, $A(y) = 4(1-y)y$, $E = We/Re$ (elasticity number), and

$$G_N = \begin{cases} \dfrac{1}{2}\left[a_N \exp(p_N t) + b_N \exp\left(q_N t\right)\right], & \text{if} \quad \gamma_N \geq 0, \\ \exp(-\alpha_N^* t)\left(\cos(\beta_N^* t) + (s_N/\beta_N)\sin(\beta_N^* t)\right), & \text{if} \quad \gamma_N < 0, \end{cases} \tag{6.39}$$

in which

$$\begin{aligned} &\alpha_N = 1 + \alpha N^2 E, && \gamma_N = \alpha_N^2 - 4EN^2, && s_N = 1 + (\alpha - 2)N^2 E, \\ &\beta_N = \sqrt{|\gamma_N|}, && \alpha_N^* = \alpha_N/(2E), && \beta_N^* = \beta_N/(2E), \\ &a_N = 1 + s_N/\beta_N, && b_N = 1 - s_N/\beta_N, \\ &p_N = -\alpha_N^* + \beta_N^*, && q_N = -(\alpha_N^* + \beta_N^*). \end{aligned}$$

It will be shown shortly that the elasticity number E has a strong influence on the transient behavior of the fluid.

Stresses:

$$\tau_{yy} = 0, \tag{6.40}$$

$$\tau_{xy} = \frac{(1-\alpha)}{E}\left[EA'(y) - 32\sum_{n=1}^{\infty}\frac{\cos(Ny)}{N^2}H_N(E,t)\right] + C_{xy}(E,y)\exp\left(\frac{-t}{E}\right), \tag{6.41}$$

$$\begin{aligned}\tau_{xx} = {} & 2ReC_{xy}(E,y)\left[A'(y)\exp\left(\frac{-t}{E}\right)t - 32\sum_{n=1}^{\infty}\frac{\cos(Ny)}{N^2}I_N(S_1,t)\right] \\ & + 2ReA'(y)(1-\alpha)\left[EA'(y) - 32\sum_{n=1}^{\infty}\frac{\cos(Ny)}{N^2}H_N(E,t)\right] \\ & - \frac{64ReA'(y)(1-\alpha)}{E}\sum_{n=1}^{\infty}\frac{\cos(Ny)}{N^2}J_N(E,t) \\ & + \frac{2048Re(1-\alpha)}{E}\sum_{n,m=1}^{\infty}\frac{\cos(Ny)}{N^2}\frac{\cos(My)}{M^2}K_{NM}(E,t) \\ & + C_{xx}(E,y)\exp\left(\frac{-t}{E}\right),\end{aligned} \tag{6.42}$$

where $A'(y) = dA(y)/dy = 4(1-2y)$, $M = (2m-1)\pi$, $C_{xy}(E,y)$ and $C_{xx}(E,y)$ are time-dependent functions defined by the requirement that τ_{xy} and τ_{xx} are zeros at $t = 0$, respectively. All coefficients $\{C_{xx}, C_{xy}, H_N, I_N, J_M, K_{NM}\}$ are given in (Carew et al., 1994) and are rewritten in Appendix D.

Because the flow is symmetric, only half domain $[0,1] \times [0.5,1]$ is considered. Boundary conditions for the streamfunction and vorticity here are the same as those for the case of Newtonian fluid. We impose the periodic condition on the inlet and outlet for all the stress components. The stress values at the wall are computed by solving the constitutive equations that are collocated on the wall, where the non-slip boundary conditions are taken into account. It is noted that, for some other studies (e.g. (Xue et al., 2004; Os and Phillips, 2004)), the inlet values of stresses are specified at each time step.

Figures 6.16 - 6.18 displays the time evolution of the field variables, i.e. for the streamfunction in Figure 6.16, velocity in Figure 6.17 and shear stress in Figure 6.18. These results correspond to $We = 0.5$, $E = 0.5$, $h = 0.05$ and $\Delta t = 10^{-3}$. It is noted that, values of the velocity and shear stress are recorded at two sample points, and all the sample points in this example lie on the vertical centreline.

There is a clear difference in behaviour between the Newtonian and non-Newtonian fluids during the transient regime. For the Oldroyd-B fluid, the velocity overshoot (peak 1 and 3) and undershoot (peak 2) occur in reaching the steady state. In these three figures, the corresponding analytic solutions are also included for comparison purposes. The numerical results clearly lie on the analytic curves.

In Figure 6.19, the computed and analytic velocity profiles at different time levels are displayed. They are obtained at times shortly after start-up (t=0.2), during the first peak (t=0.3 and t=0.5), the second peak (t=1), the third peak (t=2), at t=3, when the flow nearly reaches the steady state, and at t=5 when the flow

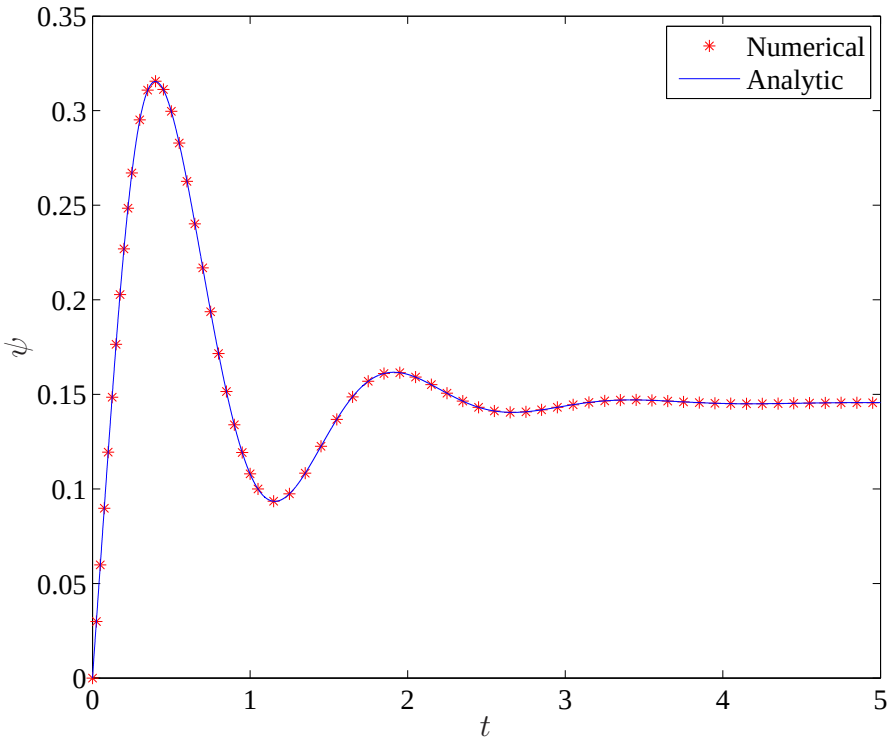

Figure 6.16 Example 5, Problem 2, planar Poiseuille flow of Oldroyd-B fluid, $We = 0.5$: Evolution of the streamfunction at an interior sample node.

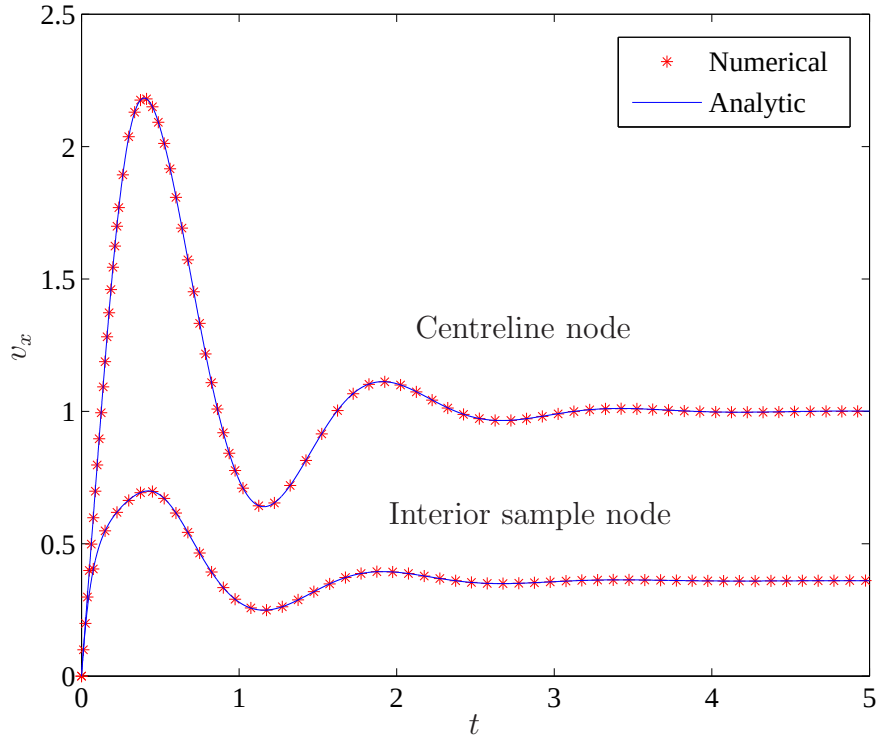

Figure 6.17 Example 5, Problem 2, planar Poiseuille flow of Oldroyd-B fluid, $We = 0.5$: Evolution of the velocity at the centreline node and an interior sample node.

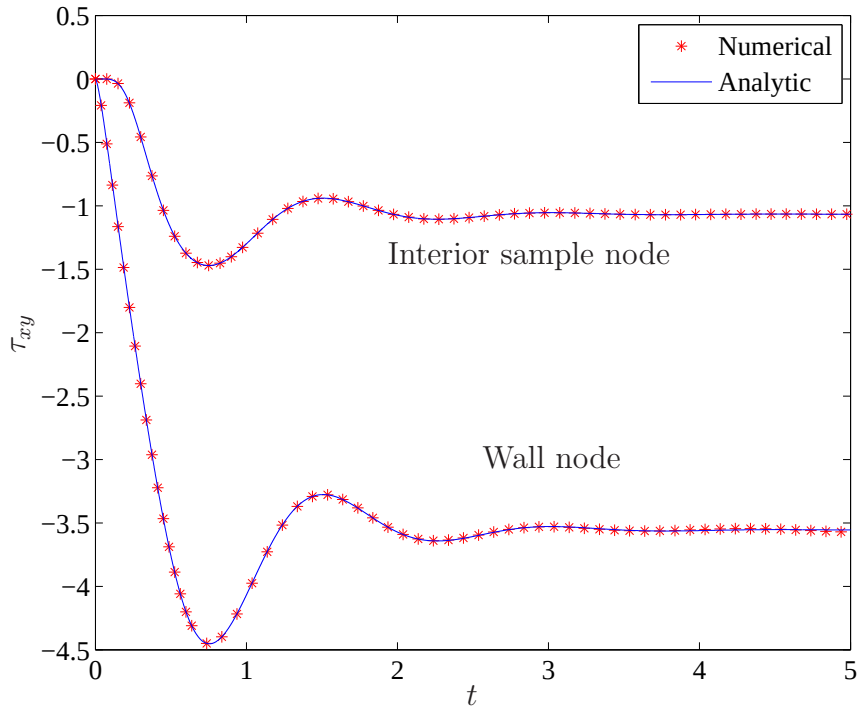

Figure 6.18 Example 5, Problem 2, planar Poiseuille flow of Oldroyd-B fluid, $We = 0.5$. Evolution of shear stress at the wall and an interior sample node.

reaches the steady state. It can be seen that the computed velocity agrees well with the analytic solution.

The present method yields a convergent solution for high values of the elasticity number E. Figure 6.20 shows the evolution of the velocity over time at several elasticity numbers: $E = \{0.1, 0.5, 1, 2, 5\}$. We use $\Delta t = 10^{-3}$, $h = 0.1$, and $Re = 1$ for the calculation. The evolution of the shear stress τ_{xy} and normal stress τ_{xx} with time at the above elasticity numbers are also displayed in Figures 6.21 and 6.22. It can be seen that the elasticity number strongly affects the fluid behaviour. The fluid quickly reaches the steady state when the elasticity number is small. In addition, the velocity overshoot level increases with the increase of the elasticity number (e.g. the velocity overshoot level will be $23.27\%, 118.16\%, 178.15\%, 248.99\%$, and 356.08% with the elasticity $E = \{0.1, 0.5, 1, 2, 5\}$, respectively.), where the overshoot level is calculated as $\left(v_{x\ \text{peak}} - v_{x\ \text{fully developed}}\right) / v_{x\ \text{fully developed}} \times 100$.

6.4 Conclusion

In this chapter, transient equations in one and two dimensions are considered. They are discretised using the Crank-Nicolson and Adams-Bashforth scheme and compact local IRBF stencils. The present method is verified with parabolic and hyperbolic equations. Several examples with analytic solutions are chosen, where numerical results show that the method yields a solution that is about second-order accurate in time and fourth-order accurate in space. Some other examples without exact solutions are also considered, where the present results are found to be in good agreement with those by other numerical methods.

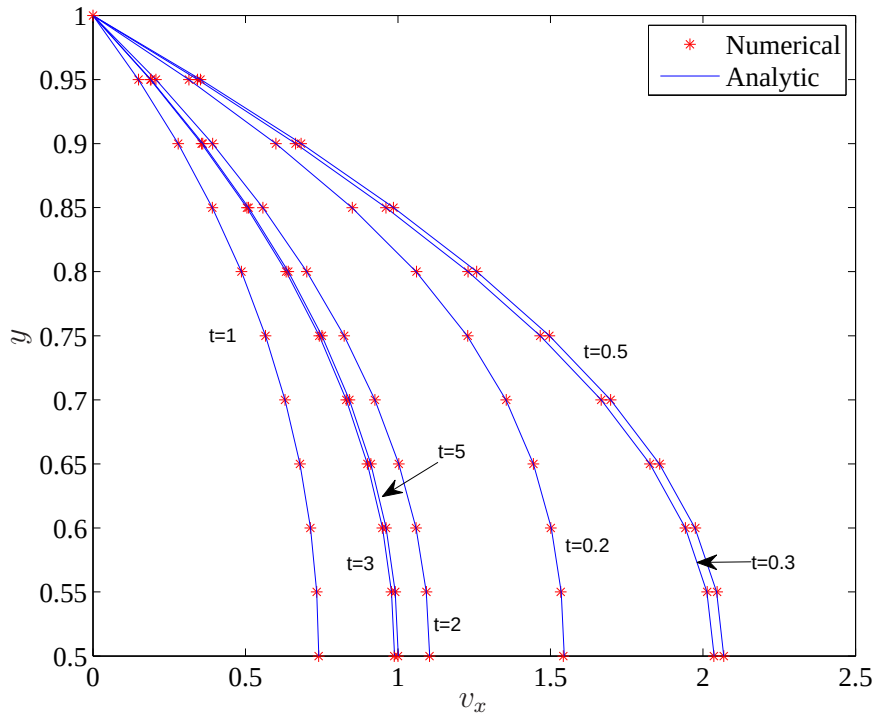

Figure 6.19 Example 5, Problem 2, planar Poiseuille flow of Oldroyd-B fluid, $We = 0.5, E = 0.5, h = 0.05$. Velocity profiles at different time levels.

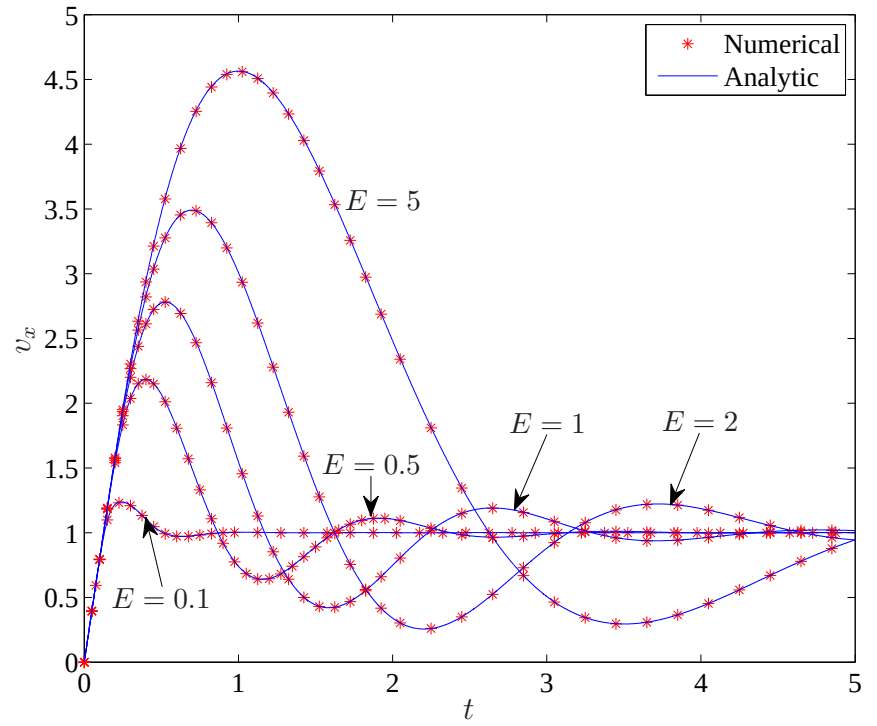

Figure 6.20 Example 5, Problem 2, planar Poiseuille flow of Oldroyd-B fluid, $Re = 1$: Evolution of the centreline velocity over time with different values of the elasticity E.

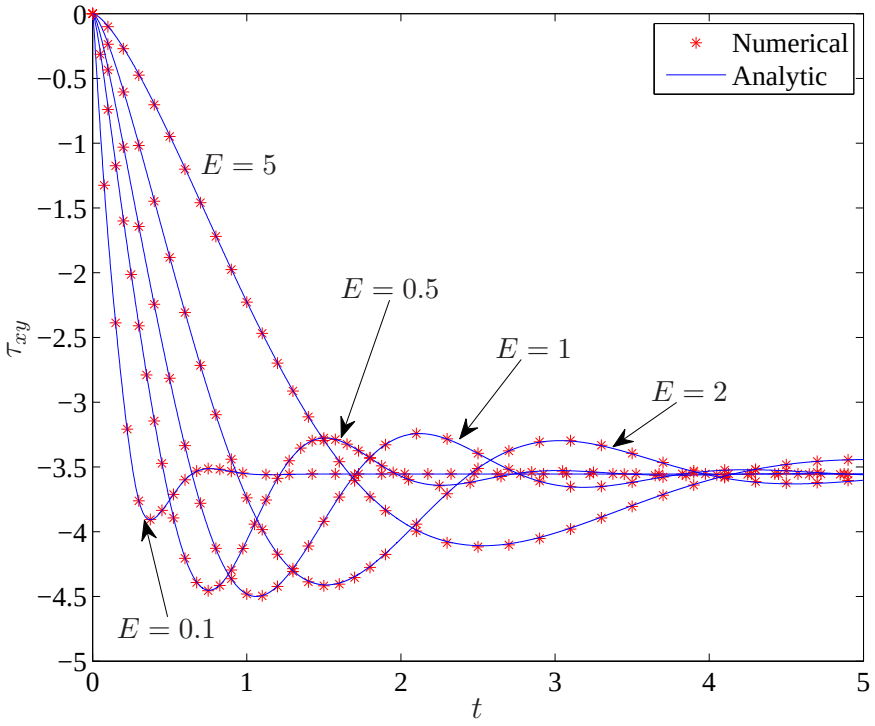

Figure 6.21 Example 5, Problem 2, planar Poiseuille flow of Oldroyd-B fluid, $Re = 1$: Evolution of the shear stress at the wall over time with different values of the elasticity E.

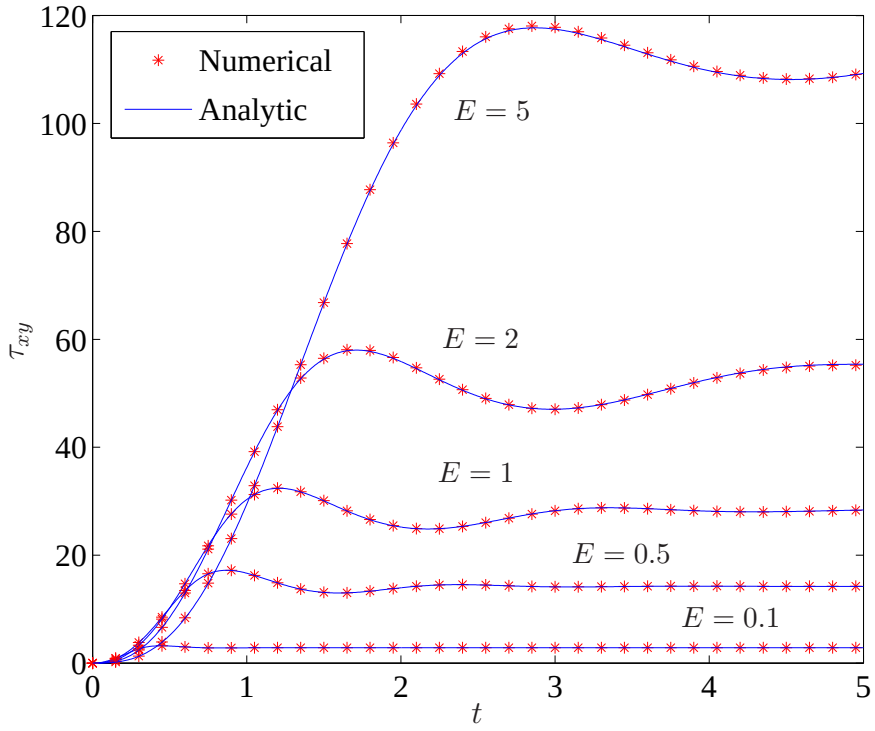

Figure 6.22 Example 5, Problem 2, planar Poiseuille flow of Oldroyd-B fluid, $Re = 1$: Evolution of the normal stress at the wall over time with different values of the elasticity E.

Chapter 7

Conclusions

This chapter concludes the thesis. In this thesis, compact local integrated RBF (CLIRBF) stencils are developed for solving second- and high-order ODEs and PDEs. They overcome some of the weaknesses of local schemes (i.e. low-order accuracy) and global schemes (i.e. fully populated systems). High orders of accuracy of the proposed stencils are achieved owing to

- the use of radial basis functions. We employ the multiquadric functions that possess an exponential rate of convergence. Since RBFs do not require an underlying structured nodes for their approximations, our stencils can also work for problems defined on nonrectangular domains;
- the use of the integral approximation formulation. We decompose highest derivatives in the ODE/PDE into RBFs and then integrate them to obtain approximate expressions for low-order derivatives and the variable itself. Through integration, the discrete solution is more stable and the reduction in rate of convergence caused by differentiation can be avoided;
- the use of compact approximations. The present RBF approximations are expressed in terms of not only nodal values of the field variable but also nodal values of the ODE/PDE and, in some cases, of first derivative(s). The incorporation of the extra information about the governing equation into the RBF approximations is conducted through the conversion process of the multiple RBF spaces into the physical space, with the help of the integration constants.

Contributions of Chapters can be summarised as follows.

In Chapter 2, CLIRBF stencils are incorporated into the point collocation formulation for the discretisation of high-order ODEs/PDEs. For lid-driven cavity fluid flows, the streamfunction formulation is adopted but constructed through a set of two second-order PDEs. Unlike the streamfunction-vorticity formulations, there is no need to derive a computational boundary condition for the intermediate variable and no requirement for the calculation of cross derivatives explicitly. A drawback of compact 3×3 stencils is the production of large interpolant matrices.

In Chapter 3 and 4, CLIRBF stencils are incorporated into the point collocation and subregion collocation formulations, respectively, for the discretisation

of second-order ODEs/PDEs defined on rectangular and non-rectangular domains. Governing equations employed are the convection-diffusion equation and the streamfunction-vorticity formulation. It has been found that, for convection-dominant flows, the most accurate results are obtained at small values of the RBF width and thus allowing for the use of a simple direct (traditional) way to construct the IRBF interpolants. For a finite-volume solution, the employment of high-order integration schemes is shown to be much more accurate than the use of the middle-point rule.

In Chapter 5, CLIRBF stencils are applied for the simulation of steady state viscoelastic fluid flows. The Oldroyd-B model is considered. Verifications are conducted in flows through channels and corrugated tubes.

In Chapter 6, CLIRBF stencils are employed in transient problems. Time derivatives are discretised using second-order temporal schemes. Verifications are conducted for different transient equations, including parabolic equations, hyperbolic nature, 1D and 2D Burgers' equations, start-up planar Poiseuille flows of Newtonian and Oldroyd-B fluids.

Numerical results indicate that (i) compact local IRBF forms are much more accurate than local forms and more efficient than global forms; (ii) highly accurate results are obtained using relatively coarse grids; and (iii) convergent solutions are obtained for highly nonlinear flows and they are in very good agreement with the benchmark solutions.

Below is a brief summary of our future work on CLIRBF stencils, which we would like to pursue, to enhance their performance

- To analyse the influence of the RBF width on the solution accuracy in order to find its optimal value
- To discretise other constitutive equations such as the PTT model
- To extent CLIRBF stencils to three dimensional problems
- To extent CLIRBF stencils to practical fluid flows, where the calculation is carried out in parallel

Appendix A

Summary of Differential Operations

A.1 Differential operations in Cartesian coordinate (x, y, z)

$$(\nabla \cdot \mathbf{v}) = \frac{\partial v_x}{\partial x} + \frac{\partial v_y}{\partial y} + \frac{\partial v_z}{\partial z} \tag{A.1}$$

$$(\mathbf{v} \cdot \nabla) = v_x \frac{\partial}{\partial x} + v_y \frac{\partial}{\partial y} + v_z \frac{\partial}{\partial z} \tag{A.2}$$

A.2 Differential operations in cylindrical coordinate (r, θ, z)

$$(\nabla \cdot \mathbf{v}) = \frac{1}{r}\frac{\partial}{\partial r}(r v_r) + \frac{1}{r}\frac{\partial v_\theta}{\partial \theta} + \frac{\partial v_z}{\partial z} \tag{A.3}$$

$$(\mathbf{v} \cdot \nabla) = v_r \frac{\partial}{\partial r} + \frac{v_\theta}{r}\frac{\partial}{\partial \theta} + v_z \frac{\partial}{\partial z} \tag{A.4}$$

Appendix B

Two-dimensional formulation of governing equations

B.1 Governing equations in Cartesian coordinate

In 2D Cartesian coordinates, the isothermal flow of a viscoelastic fluid is governed by

$$\frac{\partial v_x}{\partial x} + \frac{\partial v_y}{\partial y} = 0, \tag{B.1}$$

$$\rho\left(\frac{\partial v_x}{\partial t} + v_x\frac{\partial v_x}{\partial x} + v_y\frac{\partial v_x}{\partial y}\right) = -\frac{\partial P}{\partial x} + \eta_s\left(\frac{\partial^2 v_x}{\partial x^2} + \frac{\partial^2 v_x}{\partial y^2}\right) + \frac{\partial \tau_{xx}}{\partial x} + \frac{\partial \tau_{xy}}{\partial y}, \tag{B.2}$$

$$\rho\left(\frac{\partial v_y}{\partial t} + v_x\frac{\partial v_y}{\partial x} + v_y\frac{\partial v_y}{\partial y}\right) = -\frac{\partial P}{\partial y} + \eta_s\left(\frac{\partial^2 v_y}{\partial x^2} + \frac{\partial^2 v_y}{\partial y^2}\right) + \frac{\partial \tau_{xy}}{\partial x} + \frac{\partial \tau_{yy}}{\partial y}. \tag{B.3}$$

$$\tau_{xx} + \lambda_1\left(\frac{\partial \tau_{xx}}{\partial t} + v_x\frac{\partial \tau_{xx}}{\partial x} + v_y\frac{\partial \tau_{xx}}{\partial y} - 2\frac{\partial v_x}{\partial x}\tau_{xx} - 2\frac{\partial v_x}{\partial y}\tau_{xy}\right) = 2\eta_p\frac{\partial v_x}{\partial x}, \tag{B.4}$$

$$\tau_{xy} + \lambda_1\left(\frac{\partial \tau_{xy}}{\partial t} + v_x\frac{\partial \tau_{xy}}{\partial x} + v_y\frac{\partial \tau_{xy}}{\partial y} - \frac{\partial v_x}{\partial y}\tau_{yy} - \frac{\partial v_y}{\partial x}\tau_{xx}\right) = \eta_p\left(\frac{\partial v_x}{\partial y} + \frac{\partial v_y}{\partial x}\right), \tag{B.5}$$

$$\tau_{yy} + \lambda_1\left(\frac{\partial \tau_{yy}}{\partial t} + v_x\frac{\partial \tau_{yy}}{\partial x} + v_y\frac{\partial \tau_{yy}}{\partial y} - 2\frac{\partial v_y}{\partial x}\tau_{xy} - 2\frac{\partial v_y}{\partial y}\tau_{yy}\right) = 2\eta_p\frac{\partial v_y}{\partial y} \tag{B.6}$$

The dimensionless form of conservation equations is

$$\frac{\partial v_x^*}{\partial x^*} + \frac{\partial v_y^*}{\partial y^*} = 0, \tag{B.7}$$

$$Re\left(\frac{\partial v_x^*}{\partial t^*} + v_x^*\frac{\partial v_x^*}{\partial x^*} + v_y^*\frac{\partial v_x^*}{\partial y^*}\right) = -\frac{\partial p^*}{\partial x^*} + \alpha\left(\frac{\partial^2 v_x^*}{\partial x^{*2}} + \frac{\partial^2 v_x^*}{\partial y^{*2}}\right) + \frac{\partial \tau_{xx}^*}{\partial x^*} + \frac{\partial \tau_{xy}^*}{\partial y^*}, \tag{B.8}$$

$$Re\left(\frac{\partial v_y^*}{\partial t^*} + v_x^*\frac{\partial v_y^*}{\partial x^*} + v_y^*\frac{\partial v_y^*}{\partial y^*}\right) = -\frac{\partial p^*}{\partial y^*} + \alpha\left(\frac{\partial^2 v_y^*}{\partial x^{*2}} + \frac{\partial^2 v_y^*}{\partial y^{*2}}\right) + \frac{\partial \tau_{xy}^*}{\partial x^*} + \frac{\partial \tau_{yy}^*}{\partial y^*}, \tag{B.9}$$

where

$$
\begin{aligned}
&Re = \frac{\rho V L}{\eta_0}, \quad \alpha = \frac{\lambda_2}{\lambda_1} = \frac{\eta_s}{\eta_0}, \\
&x^* = \frac{x}{L}, \quad y^* = \frac{y}{L}, \quad v_x^* = \frac{v_x}{V}, \quad v_y^* = \frac{v_y}{V}, \\
&p^* = \frac{P}{\eta_0 V/L}, \quad \tau^* = \frac{\tau}{\eta_0 V/L}, \quad t^* = \frac{t}{L/V}
\end{aligned}
$$

B.2 Governing equations in cylindrical coordinate

In 2D (axi-symmetric) cylindrical coordinates, the isothermal flow of a viscoelastic fluid is governed by

$$\frac{1}{r}\frac{\partial}{\partial r}\left(r v_r\right) + \frac{\partial v_z}{\partial z} = 0, \tag{B.10}$$

$$\begin{aligned}
\rho\left(\frac{\partial v_r}{\partial t} + v_r\frac{\partial v_r}{\partial r} + v_z\frac{\partial v_r}{\partial z}\right) &= -\frac{\partial p}{\partial r} + \eta_s\left[\frac{\partial}{\partial r}\left(\frac{1}{r}\frac{\partial}{\partial r}\left(r v_r\right)\right) + \frac{\partial^2 v_r}{\partial z^2}\right] \\
&\quad - \left[\frac{1}{r}\frac{\partial}{\partial r}\left(r\tau_{rr}\right) + \frac{\partial \tau_{zr}}{\partial z} - \frac{\tau_{\theta\theta}}{r}\right],
\end{aligned} \tag{B.11}$$

$$\begin{aligned}
\rho\left(\frac{\partial v_z}{\partial t} + v_r\frac{\partial v_z}{\partial r} + v_z\frac{\partial v_z}{\partial z}\right) &= -\frac{\partial p}{\partial z} + \eta_s\left[\frac{1}{r}\frac{\partial}{\partial r}\left(r\frac{\partial v_z}{\partial r}\right) + \frac{\partial^2 v_z}{\partial z^2}\right] \\
&\quad - \left[\frac{1}{r}\frac{\partial}{\partial r}\left(r\tau_{rz}\right) + \frac{\partial \tau_{zz}}{\partial z}\right].
\end{aligned} \tag{B.12}$$

$$\tau_{rr} + \lambda_1\left(\frac{\partial \tau_{rr}}{\partial t} + v_r\frac{\partial \tau_{rr}}{\partial r} + v_z\frac{\partial \tau_{rr}}{\partial z} - 2\frac{\partial v_r}{\partial r}\tau_{rr} - 2\frac{\partial v_r}{\partial z}\tau_{rz}\right) = 2\eta_p\frac{\partial v_r}{\partial r}, \tag{B.13}$$

$$\begin{aligned}
\tau_{rz} + \lambda_1\left(\frac{\partial \tau_{rz}}{\partial t} + v_r\frac{\partial \tau_{rz}}{\partial r} + v_z\frac{\partial \tau_{rz}}{\partial z} + \frac{v_r}{r}\tau_{rz} - \frac{\partial v_z}{\partial r}\tau_{rr} - \frac{\partial v_r}{\partial z}\tau_{zz}\right) &= \\
\eta_p\left(\frac{\partial v_r}{\partial z} + \frac{\partial v_z}{\partial r}\right),
\end{aligned} \tag{B.14}$$

$$\tau_{zz} + \lambda_1\left(\frac{\partial \tau_{zz}}{\partial t} + v_r\frac{\partial \tau_{zz}}{\partial r} + v_z\frac{\partial \tau_{zz}}{\partial z} - 2\frac{\partial v_z}{\partial r}\tau_{rz} - 2\frac{\partial v_z}{\partial z}\tau_{zz}\right) = 2\eta_p\frac{\partial v_z}{\partial z}, \tag{B.15}$$

$$\tau_{\theta\theta} + \lambda_1\left(\frac{\partial \tau_{\theta\theta}}{\partial t} + v_r\frac{\partial \tau_{\theta\theta}}{\partial r} + v_z\frac{\partial \tau_{\theta\theta}}{\partial z} - 2\frac{v_r}{r}\tau_{\theta\theta}\right) = 2\eta_p\frac{v_r}{r}. \tag{B.16}$$

The dimensionless form of conservation equations is

$$\frac{\partial v_r^*}{\partial r^*} + \frac{v_r^*}{r^*} + \frac{\partial v_z^*}{\partial z^*} = 0, \tag{B.17}$$

$$\frac{\pi Re}{2}\left(\frac{\partial v_r^*}{\partial t^*} + v_r^*\frac{\partial v_r^*}{\partial r^*} + v_z^*\frac{\partial v_r^*}{\partial z^*}\right) = -\frac{\partial p^*}{\partial r^*} + \alpha\left(\frac{\partial^2 v_r^*}{\partial r^{*2}} + \frac{1}{r^*}\frac{\partial v_r^*}{\partial r^*} + \frac{\partial^2 v_r^*}{\partial z^{*2}} - \frac{v_r^*}{r^{*2}}\right) - \frac{\partial \tau_{rr}^*}{\partial r^*} - \frac{\partial \tau_{rz}^*}{\partial z^*} - \frac{\tau_{rr}^* - \tau_{\theta\theta}^*}{r^*}, \tag{B.18}$$

$$\frac{\pi Re}{2}\left(\frac{\partial v_z^*}{\partial t^*} + v_r^*\frac{\partial v_z^*}{\partial r^*} + v_z^*\frac{\partial v_z^*}{\partial z^*}\right) = -\frac{\partial p^*}{\partial z^*} + \alpha\left(\frac{\partial^2 v_z^*}{\partial r^{*2}} + \frac{1}{r^*}\frac{\partial v_z^*}{\partial r^*} + \frac{\partial^2 v_z^*}{\partial z^{*2}}\right) - \frac{\partial \tau_{rz}^*}{\partial r^*} - \frac{\tau_{rz}^*}{r^*} - \frac{\partial \tau_{zz}^*}{\partial z^*}, \tag{B.19}$$

where

$$Re = \frac{2\rho Q}{\pi R\eta_0}, \quad \alpha = \frac{\lambda_2}{\lambda_1} = \frac{\eta_s}{\eta_0},$$
$$v_r^* = \frac{v_r}{Q/R^2}, \quad v_z^* = \frac{v_z}{Q/R^2}, \quad r^* = \frac{r}{R}, \quad z^* = \frac{z}{R},$$
$$p^* = \frac{P}{\eta_0 Q/R^3}, \quad \tau^* = \frac{\tau}{\eta_0 Q/R^3}, \quad t^* = \frac{t}{R^3/Q}.$$

Appendix C

Analytic form of the integrated MQ basis functions

The analytic form of the integrated MQ basis functions used is given below

$$I^{(1)}_{[x]i}(\mathbf{x}) = \frac{(x - x_i^\dagger)}{2} Q + \frac{S_x}{2} R_x \tag{C.1}$$

$$I^{(1)}_{[y]i}(\mathbf{x}) = \frac{(y - y_i^\dagger)}{2} Q + \frac{S_y}{2} R_y \tag{C.2}$$

$$I^{(0)}_{[x]i}(\mathbf{x}) = \left(\frac{(x - x_i^\dagger)^2}{6} - \frac{S_x}{3} \right) Q + \frac{S_x (x - x_i^\dagger)}{2} R_x \tag{C.3}$$

$$I^{(0)}_{[y]i}(\mathbf{x}) = \left(\frac{(y - y_i^\dagger)^2}{6} - \frac{S_y}{3} \right) Q + \frac{S_y (y - y_i^\dagger)}{2} R_y \tag{C.4}$$

where $\mathbf{x} = (x, y)^T$; $\mathbf{c}_i = (x_i^\dagger, y_i^\dagger)^T$; $r = \|\mathbf{x} - \mathbf{c}_i\|$;

$$Q = \sqrt{r^2 + a_i^2} \tag{C.5}$$

$$R_x = \ln \Big((x - x_i^\dagger) + Q \Big) \tag{C.6}$$

$$R_y = \ln \Big((y - y_i^\dagger) + Q \Big) \tag{C.7}$$

$$S_x = r^2 - (x - x_i^\dagger)^2 + a_i^2 \tag{C.8}$$

$$S_y = r^2 - (y - y_i^\dagger)^2 + a_i^2 \tag{C.9}$$

Appendix D

Analytic Solution of the start-up planar Poiseuille Flow of Oldroyd-B fluid

The analytic velocity is given in the form

$$v_x(y,t) = A(y) - 32\sum_{n=1}^{\infty}\frac{\sin(Ny)}{N^3}G_N(E,t), \tag{D.1}$$

$$v_y(y,t) = 0, \tag{D.2}$$

where $N=(2n-1)\pi$, $A(y)=4(1-y)y$, $E=We/Re$ (elasticity number), and

$$G_N = \begin{cases} \dfrac{1}{2}\left[a_N\exp(p_N t) + b_N\exp\left(q_N t\right)\right], & \text{if} \quad \gamma_N \geq 0, \\ \exp(-\alpha_N^* t)\left(\cos(\beta_N^* t) + (s_N/\beta_N)\sin(\beta_N^* t)\right), & \text{if} \quad \gamma_N < 0, \end{cases} \tag{D.3}$$

in which

$$\begin{aligned} \alpha_N &= 1+\alpha N^2 E, & \gamma_N &= \alpha_N^2 - 4EN^2 \\ \beta_N &= \sqrt{|\gamma_N|}, & s_N &= 1+(\alpha-2)N^2E, \\ \alpha_N^* &= \alpha_N/(2E), & \beta_N^* &= \beta_N/(2E), \\ a_N &= 1+s_N/\beta_N, & b_N &= 1-s_N/\beta_N, \\ p_N &= -\alpha_N^*+\beta_N^*, & q_N &= -(\alpha_N^*+\beta_N^*). \end{aligned}$$

The shear stress is as

$$\tau_{xy} = \frac{(1-\alpha)}{E}\left[EA'(y) - 32\sum_{n=1}^{\infty}\frac{\cos(Ny)}{N^2}H_N(E,t)\right] + C_{xy}(E,y)\exp\left(\frac{-t}{E}\right), \tag{D.4}$$

where

$$H_N = \begin{cases} \dfrac{1}{2}\left[\dfrac{a_N}{p_N+1/E}\exp(p_N t) + \dfrac{b_N}{q_N+1/E}\exp\left(q_N t\right)\right], & \text{if} \quad \gamma_N \geq 0, \\ \dfrac{\exp(-\alpha_N^* t)}{c_N^2}\left[\left(\beta_N^* + h_N\dfrac{s_N}{\beta_N}\right)\sin(\beta_N^* t) + \left(h_N - \beta_N^*\dfrac{s_N}{\beta_N}\right)\sin(\beta_N^* t)\right], & \\ & \text{if} \quad \gamma_N < 0, \end{cases} \tag{D.5}$$

with $h_N = -\alpha_N^* + 1/E$, and $c_N^2 = h_N^2 + (\beta_N^*)^2$.

Analytic solution of normal stress

$$\begin{aligned}\tau_{xx} &= 2ReC_{xy}(E,y)\left[A'(y)\exp\left(\frac{-t}{E}\right)t - 32\sum_{n=1}^{\infty}\frac{\cos(Ny)}{N^2}I_N(S_1,t)\right]\\ &+ 2ReA'(y)(1-\alpha)\left[EA'(y) - 32\sum_{n=1}^{\infty}\frac{\cos(Ny)}{N^2}H_N(E,t)\right]\\ &- \frac{64ReA'(y)(1-\alpha)}{E}\sum_{m=1}^{\infty}\frac{\cos(Ny)}{N^2}J_N(E,t)\\ &+ \frac{2048Re(1-\alpha)}{E}\sum_{n,m=1}^{\infty}\frac{\cos(Ny)}{N^2}\frac{\cos(My)}{M^2}K_{NM}(E,t)\\ &+ C_{xx}(E,y)\exp\left(\frac{-t}{E}\right),\end{aligned} \tag{D.6}$$

where

$$I_N = \frac{1}{2}\left[\frac{a_N}{p_N}\exp\left(\left(p_N - 1/E\right)t\right) + \frac{b_N}{q_N}\exp\left(\left(q_N - 1/E\right)t\right)\right], \quad \text{if} \quad \gamma_N \geq 0, \tag{D.7}$$

$$I_N = \frac{\exp((-\alpha_N^* - 1/E)t)}{(\alpha_N^*)^2 + (\beta_N^*)^2}\left[\left(\beta_N^* - \alpha_N^*\frac{s_N}{\beta_N}\right)\sin(\beta_N^* t) + \left(-\alpha_N^* - \beta_N^*\frac{s_N}{\beta_N}\right)\cos(\beta_N^* t)\right], \quad \text{if} \quad \gamma_N < 0, \tag{D.8}$$

$$J_N = \frac{1}{2}\left[\frac{a_N}{(p_N + 1/E)^2}\exp(p_N t) + \frac{b_N}{(q_N + 1/E)^2}\exp\left(q_N t\right)\right], \quad \text{if} \quad \gamma_N \geq 0, \tag{D.9}$$

$$\begin{aligned}J_N = \frac{\exp(-\alpha_N^* t)}{c_N^2}&\left[\left\{h_N\left(\beta_N^* + h_N\frac{s_N}{\beta_N}\right) + \beta_N^*\left(h_N - \beta_N^*\frac{s_N}{\beta_N}\right)\right\}\sin(\beta_N^* t)\right.\\ &\left.\left\{h_N\left(h_N - \beta_N^*\frac{s_N}{\beta_N}\right) - \beta_N^*\left(\beta_N^* + h_N\frac{s_N}{\beta_N}\right)\right\}cos(\beta_N^*)\right], \quad \text{if} \quad \gamma_N < 0,\end{aligned} \tag{D.10}$$

$$K_{NM}(E,t) = \exp\left(\frac{-t}{E}\right)\int_0^t G_N(E,t)H_M(E,t)\exp\left(\frac{t}{E}\right)dt, \tag{D.11}$$

and C_{xy} and C_{xx} are time-independent functions defined by the requirement that τ_{xy} and τ_{xx} are zero at $t = 0$, respectively.

References

Altas, I., Dym, J., Gupta, M., and Manohar, R. (1998). Multigrid solution of automatically generated high-order discretizations for the biharmonic equation. *SIAM Journal on Scientific Computing*, 19:1575–1585.

Bahadir, A. (2003). A fully implicit finite-difference scheme for two-dimensional burgers equations. *Applied Mathematics and Computation*, 137:131–137.

Barnes, H., Hutton, J., and Walters, K. (1989). *An Introduction to Rheology*, volume 3. Elsevier Science Limited.

Bernardi, C., Coppoletta, G., and Maday, Y. (1992). Some spectral approximations of two-dimensional fourth-order problems. *Mathematics of Computation*, 59(199):63–76.

Bialecki, B. and Karageorghis, A. (2010). Spectral Chebyshev collocation for the Poisson and biharmonic equations. *SIAM Journal on Scientific Computing*, 32(5):2995–3019.

Bishko, G., Harlen, O., McLeish, T., and Nicholson, T. (1999). Numerical simulation of the transient flow of branched polymer melts through a planar contraction using the 'pom-pom' model. *Journal of Non-Newtonian Fluid Mechanics*, 82:255–273.

Bjrstad, P. (1983). Fast numerical solution of the biharmonic Dirichlet problem on rectangles. *SIAM Journal on Numerical Analysis*, 20(1):59–71.

Botella, O. and Peyret, R. (1998). Benchmark spectral results on the lid-driven cavity flow. *Computers and Fluids*, 27:421–433.

Bourantas, G., Skouras, E., Loukopoulos, V., and Nikiforidis, G. (2010). Numerical solution of non-isothermal fluid flows using local radial basis functions (LRBF) interpolation and a velocity-correction method. *CMES Computer Modeling in Engineering and Sciences*, 64(2):187–212.

Bueno-Orovio, A., Perez-Garcia, V., and Fenton, F. (2006). Spectral methods for partial differential equations in irregular domains: the spectral smoothed boundary method. *SIAM Journal on Scientific Computing*, 28(3):886–900.

Carew, E., Townsend, P., and Webster, M. (1994). Taylor-galerkin algorithms for viscoelastic flow: application to a model problem. *Numerical Methods for Partial Differential Equations*, 10(2):171–190.

Chantasiriwan, S. (2007). Solutions to harmonic and biharmonic problems with discontinuous boundary conditions by collocation methods using multiquadrics as basis functions. *International Communications in Heat and Mass Transfer*, 34(3):313–320.

Constantinescu, G. and Lele, S. (2000). A new method for accurate treatment of flow equations in cylindrical coordinates using series expansions. *CTR Annual Research Briefs 2000*, page 199.

Conte, S. and Dames, R. (1958). An alternating direction method for solving the biharmonic equation. *Mathematical Tables and Other Aids to Computation*, 12(63):198–205.

Covas, J., Agassant, J., Diogo, A., Vlachopoulos, J., and Walters, K. (1995). *Rheological fundamentals of polymer processing*. Springer.

Crochet, M., Davies, A., and Walters, K. (1984). *Numerical simulation of Non-Newtonian flow*, volume 1. Elsevier Science Limited.

Davis, G. (1983). Natural convection of air in a square cavity: a benchmark numerical solution. *International Journal for Numerical Methods in Fluids*, 3:249–264.

Deng, G., Piquet, J., Queutey, P., and Visonneau, M. (1994). Incompressible flow calculations with a consistent physical interpolation finite volume approach. *Computers and Fluids*, 23:1029–1047.

Duarte, A., Miranda, A., and Oliveira, P. (2008). Numerical and analytical modeling of unsteady viscoelastic flows: The start-up and pulsating test case problems. *Journal of Non-Newtonian Fluid Mechanics*, 154:153–169.

Emdadi, A., Kansa, E., Libre, N., Rahimian, M., and Shekarchi, M. (2008). Stable PDE solution methods for large multiquadric shape parameters. *CMES Computer Modeling in Engineering and Sciences*, 25(1):23–41.

Epperson, J. (2002). *An introduction to numerical methods and analysis*. John Wiley, New York.

Eymard, R., Gallouet, T., and Herbin, R. (2000). Finite volume methods: Schemes and analysis. *Handbook of numerical analysis*, 7:713–1018.

Fan, Y., Tanner, R., and Phan-Thien, N. (1999). Galerkin/least-square finite-element methods for steady viscoelastic flows. *Journal of Non-Newtonian Fluid Mechanics*, 84:233–256.

Fasshauer, G. (2007). *Meshfree Approximation Methods With Matlab*. World Scientific Publishing, Singapore.

Fornberg, B., Larsson, E., and Flyer, N. (2011). Stable computations with gaussian radial basis functions. *SIAM Journal on Scientific Computing*, 33(2):869–892.

Fornberg, B. and Wright, G. (2004). Stable computation of multiquadric interpolants for all values of the shape parameter. *Computers & Mathematics with Applications*, 48(5-6):853867.

Franke, R. (1982). Scattered data interpolation: Tests of some methods. *Mathematics of Computation*, 38(157):181–200.

Ghia, U., Ghia, K., and Shin, C. (1982). High-Re solutions for incompressible flow using the Navier-Stokes equations and a multigrid method. *Journal of Computational Physics*, 48:387–411.

Grillet, A., Yang, B., Khomami, B., and Shaqfeh, E. (1999). Modeling of viscoelastic lid driven cavity flow using finite element simulations. *Journal of Non-Newtonian Fluid Mechanics*, 88:99–131.

Guenette, R. and Fortin, M. (1995). A new mixed finite element method for computing viscoelastic flows. *Journal of Non-Newtonian Fluid Mechanics*, 60:27–52.

Gupta, M. and Manohar, R. (1979). Direct solution of the biharmonic equations using noncoupled approach. *Journal of Computational Physics*, 33:236–248.

Gupta, M., Manohar, R., and Stephenson, J. (1984). A single cell high order scheme for the convection-diffusion equation with variable coefficients. *International Journal for Numerical Methods in Fluids*, 4(7):641–651.

Hao-Chueh, M., Kuen-Hau, L., Cheng-Hsiu, Y., and Chao-An, L. (2010). A thermal lattice boltzmann model for flows with viscous heat dissipation. *CMES Computer Modeling in Engineering and Sciences*, 61(1):45–63.

Harlen, O., Rallison, J., and Szabo, P. (1995). A split Lagrangian-Eulerian method for simulating transient viscoelastic flows. *Journal of Non-Newtonian Fluid Mechanics*, 60:81–104.

Haykin, S. (1999). *Neural Networks: A Comprehensive Foundation (second Edition)*, volume 842. Prentice Hall.

He, Y. and Sun, W. (2007). Stability and convergence of the Crank-Nicolson/Adams-Bashforth scheme for the time-dependent Navier-Stokes equations. *SIAM Journal on Numerical Analysis*, 45(2):837–869.

Heinrichs, W. (1992). A spectral multigrid method for the stokes problem in streamfunction formulation. *Journal of Computational Physics*, 102(2):310–318.

Ho-Minh, D., Mai-Duy, N., and Tran-Cong, T. (2009). A Galerkin-RBF approach for the streamfunction-vorticity-temperature formulation of natural convection in 2D enclosured domains. *CMES Computer Modeling in Engineering and Sciences*, 44(3):219–248.

Ho-Minh, D., Mai-Duy, N., and Tran-Cong, T. (2010). Galerkin/collocation methods based on 1D-integrated-RBFNs for viscoelastic flows. *CMES Computer Modeling in Engineering and Sciences*, 70(3):217–251.

Hoang-Trieu, T.-T., Mai-Duy, N., and Tran-Cong, T. (2012). Several compact local stencils based on integrated RBFs for fourth-order ODEs and PDEs. *CMES Computer Modeling in Engineering and Sciences*, 84(2):171–203.

Hoffmann, K. and Chiang, S. (2000). *Computational Fluid Dynamic, Volume 1*. Wichita, KS: Engineering Education System.

Huilgol, R. and Phan-Thien, N. (1997). *Fluid Mechanics of Viscoelasticity*, volume 6. Elsevier Science Limited.

Hulsen, M., Fattal, R., and Kupferman, R. (2005). Flow of viscoelastic fluids past a cylinder at high Weissenberg number: Stabilized simulations using matrix-logarithms. *Journal of Non-Newtonian Fluid Mechanics*, 127:27–39.

Islam, S.-I., Vertnik, R., and arler, B. (2013). Local radial basis function collocation method along with explicit time stepping for hyperbolic partial differential equations. *Applied Numerical Mathematics*, 67:136–151.

Jain, P. and Holla, D. (1978). Numerical solution of coupled Burgers equations. *International Journal of Non-Linear Mechanics*, 13(4):213–222.

Johnston, H. and Liu, J.-G. (2004). Accurate, stable and efficient Navier-Stokes solvers based on explicit treatment of the pressure term. *Journal of Computational Physics*, 199(1):221–259.

Kansa, E. (1990). Multiquadrics - A scattered data approximation scheme with applications to computational fluid-dynamics - I Surface approximations and partial derivative estimates. *Computers & Mathematics with Applications*, 19(8-9):127–145.

Kansa, E. (2007). Exact explicit time integration of hyperbolic partial differential equations with mesh free radial basis functions. *Engineering Analysis with Boundary Elements*, 31:577–585.

Kansa, E. and Hon, Y. (2000). Circumventing the ill-conditioning problem with multiquadric radial basis functions: Applications to elliptic partial differential equations. *Computers & Mathematics with Applications*, 39(7-8):123–137.

Kansa, E., Power, H., Fasshauer, G., and Ling, L. (2004). A volumetric integral radial basis function method for time-dependent partial differential equations: I. Formulation. *Engineering Analysis with Boundary Elements*, 28:1191–1206.

Keunings, R. (1986). On the high Weissenberg number problem. *Journal of Non-Newtonian Fluid Mechanics*, 20:209–226.

Keunings, R. (1990). Progress and challenges in computational rheology. *Rheologica Acta*, 29:556–570.

Keunings, R. and Crochet, M. (1984). Numerical simulation of the flow of a viscoelastic fluid through an abrupt contraction. *Journal of Non-Newtonian Fluid Mechanics*, 14:279–299.

Kosec, G. and Sarler, B. (2008). Local RBF collocation method for Darcy flow. *CMES Computer Modeling in Engineering and Sciences*, 25:197–208.

Kosec, G. and Sarler, B. (2011). *Numerical Solution of Natural Convection Problems by a Meshless Method*, chapter 5, pages 107–132. InTech.

Lahbabi, A. and Chang, H.-C. (1986). Flow in periodically constricted tubes:

transition to inertial and nonsteady flows. *Chemical Engineering Science*, 41(10):2487–2505.

Larsson, E. and Fornberg, B. (2005). Theoretical and computational aspects of multivariate interpolation with increasingly flat radial basis functions. *Computers & Mathematics with Applications*, 49:103–130.

Le-Cao, K., Mai-Duy, N., and Tran-Cong, T. (2009). An effective intergrated-RBFN Cartesian-grid discretization for the streamfunction-vorticity-temperature formulation in nonrectangular domains. *Numerical Heat Transfer, Part B: Fundamentals*, 55(6):480–502.

Lee, C. K., Liu, X., and Fan, S. C. (2003). Local multiquadric approximation for solving boundary value problems. *Computational Mechanics*, 30(5-6):396–409.

Lele, S. (1992). Compact finite difference schemes with spectral-like resolution. *Journal of Computational Physics*, 103:16–42.

Li, M., Tang, T., and Fornberg, B. (1995). A compact fourth-order finite difference scheme for the steady incompressible Navier-Stokes equations. *International Journal for Numerical Methods in Fluids*, 20:1137–1151.

Liu, X.-D., Osher, S., and Chan, T. (1994). Weighted essentially non-oscillatory schemes. *Journal of Computational Physics*, 115(1):200–212.

Liu, Y., Vinokur, M., and Wang, Z. (2006). Spectral difference method for unstructured grids I: Basic formulation. *Journal of Computational Physics*, 216:780–801.

Macosko, C. (1994). *Rheology: Principles, Measurements, and Applications*. VCH New York.

Madych, W. (1992). Miscellaneous error bounds for multiquadric and related interpolators. *Computers & Mathematics with Applications*, 24(12):121–138.

Madych, W. R. and Nelson, S. A. (1990). Multivariate interpolation and conditionally positive definite functions. II. *Mathematics of Computation*, 54:211–230.

Mai-Duy, N. (2005). Solving high order ordinary differential equations with radial basis function networks. *International Journal for Numerical Methods in Engineering*, 62(6):824–852.

Mai-Duy, N., Ho-Minh, D., and Tran-Cong, T. (2009a). A Galerkin approach incorporating integrated radial basis function networks for the solution of biharmonic equations in two dimensions. *International Journal of Computer Mathematics*, 86(10-11):1746–1759.

Mai-Duy, N., See, H., and Tran-Cong, T. (2009b). A spectral collocation technique based on integrated Chebyshev polynomials for biharmonic problems in irregular domains. *Applied Mathematical Modelling*, 33(1):284–299.

Mai-Duy, N. and Tanner, R. (2005a). Computing non-Newtonian fluid flow with radial basis function networks. *International Journal for Numerical Methods in Fluids*, 48(12):1309–1336.

Mai-Duy, N. and Tanner, R. (2005b). Solving high-order partial differential equations with indirect radial basis function networks. *International Journal for Numerical Methods in Engineering*, 63(11):1636–1654.

Mai-Duy, N. and Tanner, R. (2007). A spectral collocation method based on integrated Chebyshev polynomials for two-dimensional biharmonic boundary-value problems. *Journal of Computational and Applied Mathematics*, 201(1):30–47.

Mai-Duy, N. and Tran-Cong, T. (2001). Numerical solution of differential equations using multiquadric radial basis function networks. *Neural Networks*, 14:185–199.

Mai-Duy, N. and Tran-Cong, T. (2003). Approximation of function and its derivatives using radial basis function networks. *Applied Mathematical Modelling*, 27:197–220.

Mai-Duy, N. and Tran-Cong, T. (2006). Solving biharmonic problems with scattered-point discretization using indirect radial-basis-function networks. *Engineering Analysis with Boundary Elements*, 30:77–87.

Mai-Duy, N. and Tran-Cong, T. (2008a). Integrated radial-basis-function networks for computing Newtonian and non-Newtonian fluid flows. *Computers and Structures*, 87(11-12):642–650.

Mai-Duy, N. and Tran-Cong, T. (2008b). A multidomain integrated-radial-basis-function collocation method for elliptic problems. *Numerical Methods for Partial Differential Equations*, 24(5):1301–1320.

Mai-Duy, N. and Tran-Cong, T. (2009). A Cartesian-grid discretisation scheme based on local integrated RBFNs for two-dimensional elliptic problems. *CMES Computer Modeling in Engineering and Sciences*, 51(3):213–238.

Mai-Duy, N. and Tran-Cong, T. (2010). A numerical study of 2D integrated RBFNs incorporating Cartesian grids for solving 2D elliptic differential problems. *Numerical Methods for Partial Differential Equations*, 26:1443–1462.

Mai-Duy, N. and Tran-Cong, T. (2011). Compact local integrated-RBF approximations for second-order elliptic differential problems. *Journal of Computational Physics*, 230(12):4772–4794.

Miranda, A. and Oliveira, P. (2010). Start-up times in viscoelastic channel and pipe flows. *Korea-Australia Rheology Journal*, 22:65–73.

Moin, P. and Kim, J. (1997). Tackling turbulence with supercomputers. *Scientific American*, 276(1):46–52.

Momeni-Masuleh, S. and Phillips, T. (2004). Viscoelastic flow in an undulating tube using spectral methods. *Computers and Fluids*, 33:10751095.

Moroney, T. and Turner, I. (2006). A finite volume method based on radial basis functions for two-dimensional nonlinear diffusion equations. *Applied Mathematical Modelling*, 30:1118–1133.

Moukalled, F. and Acharya, S. (1996). Natural convection in the annulus between

concentric horizontal circular and square cylinders. *Journal of Thermophysics and Heat Transfer*, 10(3):524–531.

Ngo-Cong, D., Mai-Duy, N., Karunasena, W., and Tran-Cong, T. (2012a). Local moving least square - one-dimensional IRBFN technique: Part I - natural convection flows in concentric and eccentric annuli. *CMES Computer Modeling in Engineering and Sciences*, 83(3):275–310.

Ngo-Cong, D., Mai-Duy, N., Karunasena, W., and Tran-Cong, T. (2012b). A numerical procedure based on 1D-IRBFN and local MLS-1D-IRBFN methods for fluid-structure interaction analysis. *CMES Computer Modeling in Engineering and Sciences*, 83(5):459–498.

Oliveira, P. (2001). Method for time-dependent simulations of viscoelastic flows: vortex shedding behind cylinder. *Journal of Non-Newtonian Fluid Mechanics*, 101:113–137.

Oliveira, P., Pinho, F., and Pinto, G. (1998). Numerical simulation of non-linear elastic flows with a general collocated finite-volume method. *Journal of Non-Newtonian Fluid Mechanics*, 79:1–43.

Os, R. V. and Phillips, T. (2004). Spectral element methods for transient viscoelastic flow problems. *Journal of Computational Physics*, 201(1):286–314.

Osswald, T. and Hernandez-Ortiz, J. (2006). *Polymer processing - Modeling and simulation*. Hanser Gardner Publications.

Ostrach, S. (1988). Natural convection in enclosures. *Journal of Heat Transfer*, 110(4b):1175–1190.

Park, J. and Sandberg, I. (1991). Universal approximation using radial-basis-function networks. *Neural Computation*, 3:246–257.

Pastor, M., Peraire, J., and Zienkiewicz, O. (1991). Adaptive remeshing for shear band localization problems. *Archive of Applied Mechanics*, 61(1):30–39.

Patankar, S. (1980). *Numerical Heat Transfer and Fluid Flow*. Taylor and Francis Group.

Pereira, J., Kobayashi, M., and Pereira, J. (2001). A fourth-order-accurate finite volume compact method for the incompressible Navier-Stokes solutions. *Journal of Computational Physics*, 167:217–243.

Persson, P.-O. (2013). A sparse and high-order accurate line-based discontinuous galerkin method for unstructured meshes. *Journal of Computational Physics*, 233:414–429.

Phan-Thien, N. and Tanner, R. (1977). A new constitutive equation derived from network theory. *Journal of Non-Newtonian Fluid Mechanics*, 2(4):353–365.

Pilitsis, S. and Beris, A. (1989). Calculations of steady-state viscoelastic flow in an undulating tube. *Journal of Non-Newtonian Fluid Mechanics*, 31(3):231–287.

Pilitsis, S. and Beris, A. (1991). Viscoelastic flow in an undulating tube. Part II.

Effects of high elasticity, large amplitude of undulation and inertia. *Journal of Non-Newtonian Fluid Mechanics*, 39:375–405.

Pilitsis, S. and Beris, A. (1992). Pseudospectral calculations of viscoelastic flow in a periodically constricted tube. *Computer Methods in Applied Mechanics and Engineering*, 98:307–328.

Quartapelle, L. (1993). *Numerical Solution of the Incompressible Navier-Stokes Equations*, volume 113 of *International Series of Numerical mathematics*. Springer.

Quere, P. (1991). Accurate solutions to the square thermally driven cavity at high Rayleigh number. *Computers Fluids*, 20(1):29–41.

Rasmussen, H. (1999). Time-dependent finite-element method for the simulation of three-dimensional viscoelastic flow with integral models. *Journal of Non-Newtonian Fluid Mechanics*, 84(2):217–232.

Reddy, J. and Gartling, D. (1994). *The Finite Element method in heat transfer and fluid dynamics*. CRC Pressl Llc.

Rippa, S. (1999). An algorithm for selecting a good value for the parameter c in radial basis function interpolation. *Advances in Computational Mathematics*, 11:193–210.

Sadat, H. and Couturier, S. (2000). Performance and accuracy of a meshless method for laminar natural convection. *Numerical Heat Transfer, Part B*, 37:455–467.

Sarler, B. (2005). A radial basis function collocation approach in computational fluid dynamics. *CMES Computer Modeling in Engineering and Sciences*, 7(2):185–193.

Schaback, R. (1995). Error estimates and condition numbers for radial basis function interpolation. *Advances in Computational Mathematics*, 3(3):251–264.

Shu, C., Ding, H., and Yeo, K. (2003). Local radial basis function-based differential quadrature method and its application to solve two-dimensional incompressible Navier-Stokes equations. *Computer Methods in Applied Mechanics and Engineering*, 192:941–954.

Shu, C. and Zhu, Y. (2002). Efficient computation of natural convection in a concentric annulus between an outer square cylinder and an inner circular cylinder. *International Journal for Numerical Methods in Fluids*, 38:429–445.

Smith, G. (1985). *Numerical solution of partial differential equations: finite difference methods*. Oxford University Press.

Srivastava, V., Tamsir, M., Bhardwaj, U., and Sanyasiraju, Y. (2011). Crank-Nicolson scheme for numerical solutions of two dimensional coupled Burgers equations. *International Journal of Scientific & Engineering Research*, 2(5):44–50.

Stephenson, J. (1984). Single cell discretizations of order two and four for biharmonic problems. *Journal of Computational Physics*, 55:65–88.

Sun, J., Smith, M., Armstrong, R., and Brown, R. (1999). Finite element method for viscoelastic flows based on the discrete adaptive viscoelastic stress splitting and the discontinuous Galerkin method: DAVSS-G/DG. *Journal of Non-Newtonian Fluid Mechanics*, 86:281–307.

Tanner, R. (2000). *Engineering Rheology (second edition)*, volume 52. OUP Oxford.

Tanner, R. and Xue, S.-C. (2002). Computing transient flows with high elasticity. *Korea-Australia Rheology Journal*, 14(4):143–159.

Thai-Quang, N., Le-Cao, K., Mai-Duy, N., and Tran-Cong, T. (2012). A high-order compact local integrated-RBF scheme for steady-state incompressible viscous flows in the primitive variables. *CMES Computer Modeling in Engineering and Sciences*, 84(6):528–557.

Thom, A. (1933). The flow past circular cylinders at low speeds. In *Proceedings of the Royal Society of London. Series A, Containing Papers of a Mathematical and Physical Character*, volume 141, pages 651–669. The Royal Society.

Tolstykh, A. and Shirobokov, D. (2005). Using radial basis functions in a finite difference mode. *CMES Computer Modeling in Engineering and Sciences*, 7:207–222.

Tone, F. (2004). Error analysis for a second order scheme for the Navier-Stokes equations. *Applied Numerical Mathematics*, 50(1):93–119.

Walters, K. and Webster, M. F. (2003). The distinctive CFD challenges of computational Rheology. *International Journal for Numerical Methods in Fluids*, 43:577–596.

Wang, Z. (2002). Spectral (finite) volume method for conservation laws on unstractured grids I: basic formulation. *Journal of Computational Physics*, 178:210–251.

Wapperom, P., Keunings, R., and Legat, V. (2000). The backward-tracking Lagrangian particle method for transient viscoelastic flows. *Journal of Non-Newtonian Fluid Mechanics*, 91:273–295.

Waters, N. and King, M. (1970). Unsteady flow of an elastico-viscous liquid. *Rheologica Acta*, 9(3):345–355.

Webster, M., Tamaddon-Jahromi, H., and Aboubacar, M. (2004). Transient viscoelastic flows in planar contractions. *Journal of Non-Newtonian Fluid Mechanics*, 118:83–101.

Wendland, H. (2005). *Scattered Data Approximation*. Cambridge university press.

Wilkes, J. (2005). *Fluid Mechanics for Chemical Engineers with Microfluidics and CFD*, chapter 6 - Solution of viscos-flow problem, pages 272–320. Prentice Hall.

Wright, G. and Fornberg, B. (2006). Scattered node compact finite difference-type formulas generated from radial basis functions. *Journal of Computational Physics*, 212(1):99–123.

Xue, S.-C., Phan-Thien, N., and Tanner, R. (1995). Numerical study of secondary flows of viscoelastic fluid in straight pipes by an implicit finite volume method. *Journal of Non-Newtonian Fluid Mechanics*, 59:191–213.

Xue, S.-C., Tanner, R., and Phan-Thien, N. (2004). Numerical modelling of transient viscoelastic flows. *Journal of Non-Newtonian Fluid Mechanics*, 123:33–58.

Yapici, K., Karasozen, B., and Uludag, Y. (2009). Finite volume simulation of viscoelastic laminar flow in a lid-driven cavity. *Journal of Non-Newtonian Fluid Mechanics*, 164:51–65.

Yurun, F. and Crochet, M. (1995). High-order finite element methods for steady. *Journal of Non-Newtonian Fluid Mechanics*, 27:283–311.

Zerroukat, M., Power, H., and Chen, C. S. (1998). A numerical method for heat transfer problems using collocation and radial basis functions. *International Journal for Numerical Methods in Engineering*, 42(7):1263–1278.

Zhu, H., Shu, H., and Ding, M. (2010). Numerical soluions of two-dimensional burgers equations by discrete Adomian decomposition method. *Computers & Mathematics with Applications*, 60:840–848.